

Basic Investigation of Turbulent Structures and Blobs of Relevance for Magnetic Fusion Plasmas

THÈSE N° 5228 (2011)

PRÉSENTÉE LE 9 DÉCEMBRE 2011
À LA FACULTÉ DES SCIENCES DE BASE
CRPP - PHYSIQUE DES PLASMAS DE BASE
PROGRAMME DOCTORAL EN PHYSIQUE

ÉCOLE POLYTECHNIQUE FÉDÉRALE DE LAUSANNE

POUR L'OBTENTION DU GRADE DE DOCTEUR ÈS SCIENCES

PAR

Christian Gabriel THEILER

acceptée sur proposition du jury:

Prof. O. Schneider, président du jury
Prof. A. Fasoli, Dr I. Furno, directeurs de thèse
Prof. S. Krasheninnikov, rapporteur
Dr R. Pitts, rapporteur
Prof. P. Ricci, rapporteur




ÉCOLE POLYTECHNIQUE
FÉDÉRALE DE LAUSANNE

Suisse
2011

An electronic version is available for download from either

 <http://library.epfl.ch/theses/?nr=5228>

or

 <http://dx.doi.org/10.5075/epfl-thesis-5228>

This document was last revised on Thursday 10th November, 2011 and has been compiled using pdfL^AT_EX with a template developed by Dr. Christian Schlatter.

Please cite this publication as:

Christian Theiler, **Basic Investigation of Turbulent Structures and Blobs of Relevance for Magnetic Fusion Plasmas**, Ph.D. thesis, no. 5228, Ecole Polytechnique Fédérale de Lausanne (EPFL), CH-1015 Lausanne, Switzerland, November 2011.

Abstract

Similarly to neutral fluids, plasmas often exhibit turbulent behavior. Turbulence in plasmas is usually more complex than in neutral fluids due to long range interactions via electric and magnetic fields, and kinetic effects. It gives rise to many interesting phenomena such as self-generated magnetic fields (dynamos), zonal-flows, transport barriers, or particle pinches. Plasma turbulence plays a crucial role for the success of nuclear fusion as a potentially clean, safe, and long-term source for electric power production.

Turbulent processes in the edge and scrape-off layer (SOL) of magnetic fusion plasmas determine, to a large extent, the overall confinement properties. They also influence the life time of plasma facing components, impurity production and influx, main chamber recycling, tritium retention, and helium ash removal. Edge turbulence is often dominated by *blobs* or *filaments*, magnetic-field-aligned plasma structures observed in the edge of virtually all magnetized plasmas.

This thesis investigates basic aspects of edge turbulence and blobs in simple magnetized toroidal TORPEX plasmas. TORPEX includes important ingredients of SOL physics, such as pressure gradients, " ∇B " and curvature of the magnetic field, together with open field lines. A relatively simple magnetic geometry, full diagnostics access and the possibility of controlled parameter scans allow isolating and studying instabilities and turbulence effects that occur in more complicated forms in fusion and astrophysical plasmas.

Using a number of optimized probe diagnostic methods, the mechanisms for the generation of blobs from ideal interchange waves and for their subsequent propagation are elucidated. A blob velocity scaling law is introduced that takes into account several damping effects of blob cross-field velocity. This scaling law is in good agreement both with blob simulations and experiments on TORPEX. Studies on blob parallel dynamics shed light on blob induced parallel currents and the transport of parallel momentum. Based on this understanding of blob motion, several tools to influence blobs and turbulence as a whole are developed. A methodology for plasma turbulence code validation is established. Using a large set of observables, the agreement between experiments and both 2D and global 3D two-fluid simulations is quantified.

Keywords:

plasma physics, plasma turbulence, nuclear fusion, transport properties, intermittency, interchange instability, blobs, filaments, plasma diagnostics, Langmuir probes, code validation, TORPEX.

Zusammenfassung

Ähnlich wie neutrale Fluide weisen Plasmen oft turbulentes Verhalten auf. Ist Turbulenz schon in neutralen Fluiden eine komplexe Erscheinung, so gilt dies infolge langreichweitiger Wechselwirkungen durch elektromagnetische Felder sowie kinetischer Effekte erst recht für Plasmen. Es kommt zu vielen interessanten Phänomenen, wie der Bildung und Erhaltung grossräumiger magnetischer Felder (Dynamoeffekt), Zonalströmungen, Transportbarrieren oder Teilchen-Pinchs. Plasmaturbulenz spielt eine zentrale Rolle für den Erfolg der Kernfusion als potentiell saubere, sichere und nachhaltige Energiequelle.

Turbulenz im Randbereich und der Abschälsschicht von Fusionsplasmen bestimmt in hohem Maße die Einschlusseigenschaften. Sie beeinflusst auch die Lebensdauer der Wandkomponenten, die Entstehung und den Transport von Verunreinigungen, das Recycling an der Reaktorwand, die Rückhaltung von Tritium und das Abführen der Heliumasche. Dabei spielen *Blobs* eine wichtige Rolle. Dies sind entlang dem Magnetfeld ausgedehnte Strukturen erhöhter Plasmadichte, die im Randbereich verschiedenster magnetisierter Plasmen auftreten.

In dieser Doktorarbeit werden grundlegende Aspekte von Plasmarand-Turbulenz und Blobs in den "einfach" magnetisierten, toroidalen Plasmen in TORPEX untersucht. Das TORPEX Experiment weist wichtige Bestandteile für die Dynamik in der Abschälsschicht auf, wie Druckgradienten im Plasma, Krümmung und Gradienten im Magnetfeld und offene Feldlinien. Eine relativ einfache Geometrie des Magnetfeldes, ein direkter Zugang mit Sonden sowie die Möglichkeit, Parameter im Experiment kontrolliert zu variieren, erlaubt es, Instabilitäten und turbulente Effekte, die in komplizierterer Form in Fusions- und astrophysikalischen Plasmen auftreten, isoliert zu studieren.

Mithilfe optimierter Meßmethoden wird die Entstehung der Blobs von Interchange-Wellen und ihre weitere Dynamik erklärt. Es wird eine Formel für die Geschwindigkeit der Blobs hergeleitet, welche mehrere Bremsmechanismen berücksichtigt. Sie zeigt gute Übereinstimmung mit Simulationen und Experimenten in TORPEX. Die Untersuchung der Blobs parallel zum Magnetfeld gibt Einblicke in die durch Blobs erzeugten Ströme sowie in den Transport von parallelem Impuls. Aufgrund solcher Erkenntnisse werden mehrere Methoden zur Beeinflussung der Blobs und der Turbulenz als Ganzes entwickelt. Ferner wird eine Methodik für die Code-Validation eingeführt. Anhand einer bedeutenden Menge an Observablen wird die Übereinstimmung von Experiment und 2D sowie globalen 3D Zwei-Fluid-Simulationen quantifiziert.

Stichwörter:

Plasmaphysik, Plasmaturbulenz, Kernfusion, Transporteigenschaften, Intermittenz, Interchange Instabilität, Blobs, Plasmadiagnostik, Langmuir Sonden, Code-Validierung, TORPEX.

Contents

1	Introduction	1
1.1	Motivation and outline	6
2	Experimental setup	9
2.1	TORPEX device	9
2.2	Overview of the main diagnostics	11
2.3	Plasma production	14
2.4	The dominant instabilities on TORPEX	16
2.5	Plasmas in the ideal interchange mode regime	19
3	Experimental techniques	21
3.1	Probe theory used on TORPEX	22
3.2	Analysis of swept LPs	23
3.3	Considerations on the validity of the simple probe theory on TORPEX	26
3.4	Conditional average sampling techniques	29
3.5	The triple probe on TORPEX	31
3.5.1	Triple probe principle	31
3.5.2	Novel guarding circuit to reduce stray capacitance	35
3.5.3	Triple probe and guarding circuitry construction	36
3.5.4	Consistency tests	37
3.5.5	Cross-checks with other LP-based techniques	39
3.5.6	Measurements of fluctuations and transport with the triple probe	41
3.6	Conclusions	44
4	Blob formation	47
4.1	Blob formation from ideal interchange waves	48
4.2	Gradient steepening in the blob formation process	51
4.2.1	Spatio-temporal ITE dynamics from CAS	51
4.2.2	Link between the inverse radial density scale length and ITEs at P_1	55
4.2.3	ITEs at probe tip P_2	58
4.3	Conclusions	60

5	Blob motion	63
5.1	Simple 2D models for blob motion	64
5.1.1	Blob motion damped by parallel currents	65
5.1.2	Blob motion damped by neutrals	66
5.1.3	Blob motion damped by ion-polarization currents	66
5.1.4	Generalized expression for blob velocity	67
5.1.5	Comparison with seeded blob simulations	68
5.2	Blob motion in TORPEX and comparison with theory	71
5.2.1	Ion mass scan	73
5.2.2	Effect of changes in the connection length	77
5.2.3	Effect of changes in the neutral gas pressure	80
5.2.4	Some open questions and outlook for future experiments	82
5.3	Conclusions	83
6	Blob parallel dynamics	85
6.1	Measurements of blob parallel currents	85
6.1.1	Direct measurements of the parallel current density to the limiter	86
6.1.2	Origin and importance of asymmetric parallel current structures	90
6.1.3	Importance of the parallel current in damping the charge separation	91
6.2	Blob induced transport of parallel momentum	93
6.3	Proposal for measurements of the pre-sheath density drop inside blobs	97
6.4	Conclusions	100
7	Blob control	103
7.1	Variation of wall tilt	103
7.1.1	Predicted effects of wall tilt	104
7.1.2	Experimental setup	105
7.1.3	Results and discussion	107
7.2	Experiments with a glass limiter	110
7.3	Biasing experiments: introduction and main results	111
7.3.1	Experimental setup	112
7.3.2	Effect of biasing on mode and blobs	113
7.3.3	Time averaged effects of biasing	116
7.4	Conclusions	125
8	Code validation on TORPEX	129
8.1	Methodology of turbulence code validation	131
8.1.1	Validation observables and primacy hierarchy	131
8.1.2	Quantification of the agreement of each observable	133
8.1.3	Metric	136
8.1.4	Quality	137
8.2	Simulation-experiment comparison	137

8.2.1	Global agreement and quality of the comparison	139
8.2.2	Comparison of individual observables	139
8.3	Conclusions	141
9	Conclusions	145
A	Notation	151
A.1	Repeatedly used symbols/variables	151
A.2	Abbreviations	152
B	Estimates of collision frequencies	153
B.1	Estimate of the ion-neutral collision frequency	153
B.2	Estimate of the electron-neutral collision frequency	154
	Acknowledgements	175
	Curriculum Vitae	177

C H A P T E R

1

Introduction

When atomic nuclei collide with sufficiently high energy to overcome the mutual Coulomb repulsion, they can "fuse" to form a heavier nucleus. For elements lighter than iron, this process generally leads to a reduction of the total mass and consequently a release of energy. It is this nuclear fusion energy that powers the Sun and other stars. If achieved at a sufficient rate and in a controlled manner on Earth, fusion has the potential to become a clean, safe, and virtually inexhaustible source for electric power production. To reach fusion relevant conditions, particles and energy need to be confined at high enough density and temperature (of the order of 100 million degrees Celsius for deuterium-tritium fusion reactions). At these temperatures, electrons are stripped from the nuclei and positively charged ions and negatively charged electrons form a fully ionized *plasma*, i.e., an ensemble of charged particles, which is globally neutral and exhibits collective behavior. Therefore, fusion research is intrinsically linked to plasma physics. A non-technical overview of this fascinating field of modern physics can be found in [1].

Due to their electric charge, plasma particles can be influenced by magnetic fields. Indeed, a single particle spirals around a magnetic field line and can move freely only in the direction of the field. Therefore, while the plasma is confined by enormous gravitational forces in the Sun, magnetic fields can be used to confine the plasma in the laboratory. During more than 50 years of fusion research, different magnetic confinement concepts have been developed and tested [2, 3]. The most advanced

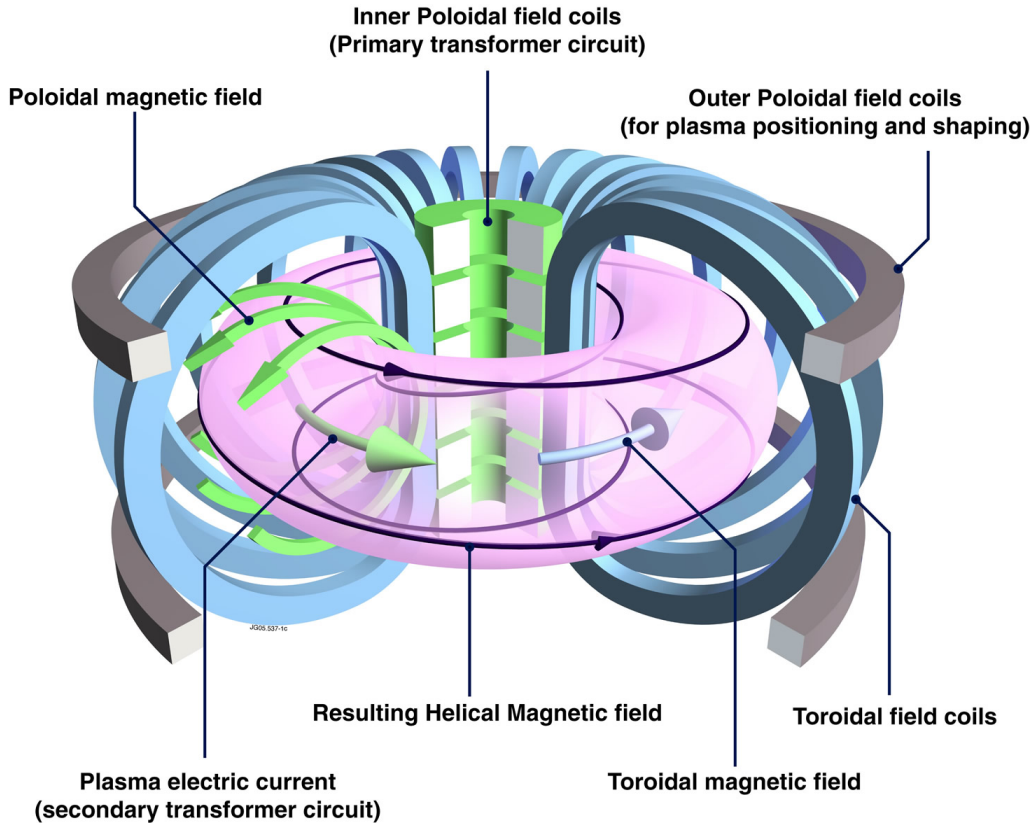


Figure 1: Sketch of the tokamak device. The toroidal magnetic field is produced by external toroidal field coils. A plasma current, induced by the inner poloidal field coils, produces the poloidal magnetic field and the twist of the field lines required for good plasma confinement. (Figure from [4])

today is the tokamak, whose basic principles are illustrated in Fig. 1. The first intuitive idea of a simple closing of the magnetic field lines on themselves does not provide particle confinement nor a stable configuration. A helical shape of the field lines, as indicated in Fig. 1, is required. This is achieved by a combination of an externally applied toroidal field and a poloidal field created by a current flowing inside the plasma. This current is induced by a varying magnetic flux created by the inner poloidal field coils. Additional sets of coils are used to stabilize and shape the plasma. A vacuum vessel (not shown) surrounds the plasma volume and isolates it from the external environment.

The magnetic structure consists of nested toroidal magnetic surfaces, called closed flux surfaces. Magnetic field lines that wind around the plasma volume (see the example in Fig. 1) lie on such surfaces. The outermost surfaces intercept parts of the vacuum vessel. This leads to localized heat loads caused by the free streaming of hot plasma particles along field lines. In order to control this interaction between charged particles and the wall, modern high performance tokamaks use the magnetic divertor configuration. This is illustrated in Fig. 2. External magnets (not shown in the figure) are used to modify the magnetic field lines in the peripheral region of the plasma. While field lines in the confined region of the plasma, the red region

in Fig. 2, still form closed magnetic surfaces, field lines outside the Last Closed Flux Surface (LCFS) are directed towards regions where they intercept the divertor plates. This region of open magnetic field lines is called the Scrape-Off Layer (SOL). Plasma particles that cross the LCFS and travel into the SOL are (ideally) transported along the magnetic field towards the divertor. This configuration has several advantages over the limiter configuration, where physical objects (limiters) are inserted into the peripheral region of the plasma to define the separation between confined plasma and SOL. Indeed, in the divertor configuration, plasma-facing components are not in direct contact with the main (confined) plasma. This facilitates the pumping out of both helium "ash" produced in the fusion reactions and impurities that are released when plasma particles hit the divertor. Different strategies can further be employed in the divertor region to cool or disperse the hot plasma that crosses the LCFS before it reaches the divertor.

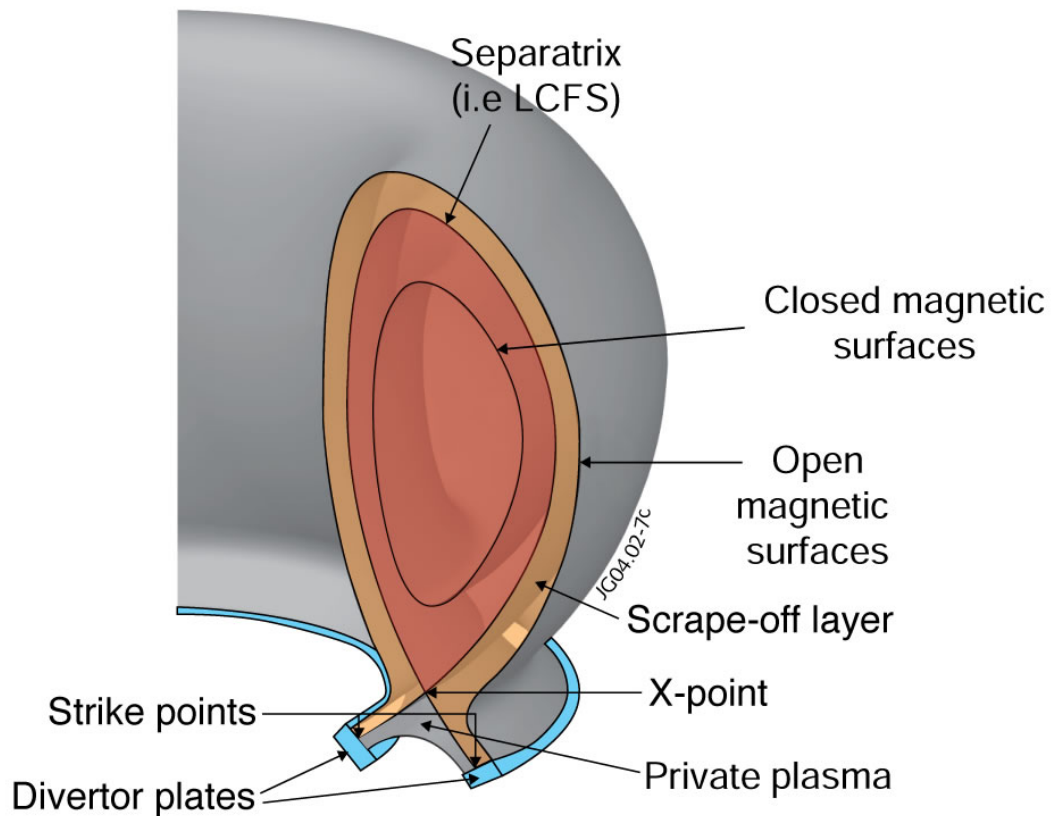


Figure 2: Sketch of the tokamak divertor configuration. In the confined or core plasma, magnetic field lines form closed magnetic surfaces. To control the location where plasma is in contact with material parts, field lines in the peripheral region are directed downwards to the divertor plates with the help of externally applied magnetic fields. Due to the free streaming of particles along the magnetic field, plasma that leaves the confined region is essentially scraped-off from the core plasma. (Source: EFDA-JET)

To reach the extreme temperatures required for fusion, the plasma needs to be heated. Part of the heat is produced through resistive dissipation (Joule effect) of the current that circulates in the plasma. This effect is, however, not sufficient and additional heating schemes, such as injection of high energetic neutral particles or microwaves are used. Due to plasma turbulence, this injected energy is lost much faster from the plasma than expected from collisional processes [5–8]. This obstacle has forced fusion scientists to develop, from originally small scale experiments, large facilities. The worlds largest tokamak is the Joint European Torus (JET). In Fig. 3, we show the interior of its vacuum vessel. It has a height of ≈ 4 m. In 1997, JET has reached a fusion gain of $Q \approx 65\%$, where Q is the ratio of the energy produced in the fusion reactions to the external heating power. A net energy gain, including transformation of the fusion power into electricity via a heat engine, requires values of $Q = 10$ and higher. Reaching $Q = 10$ is among the goals of the next step fusion experiment ITER (International Thermonuclear Fusion Reactor [9]), which is now under construction in France. Like JET, ITER is based on the tokamak concept, with a plasma volume approximately 10 times larger. The important mission of ITER is "to demonstrate the scientific and technological feasibility of fusion power for peaceful purposes" [10].

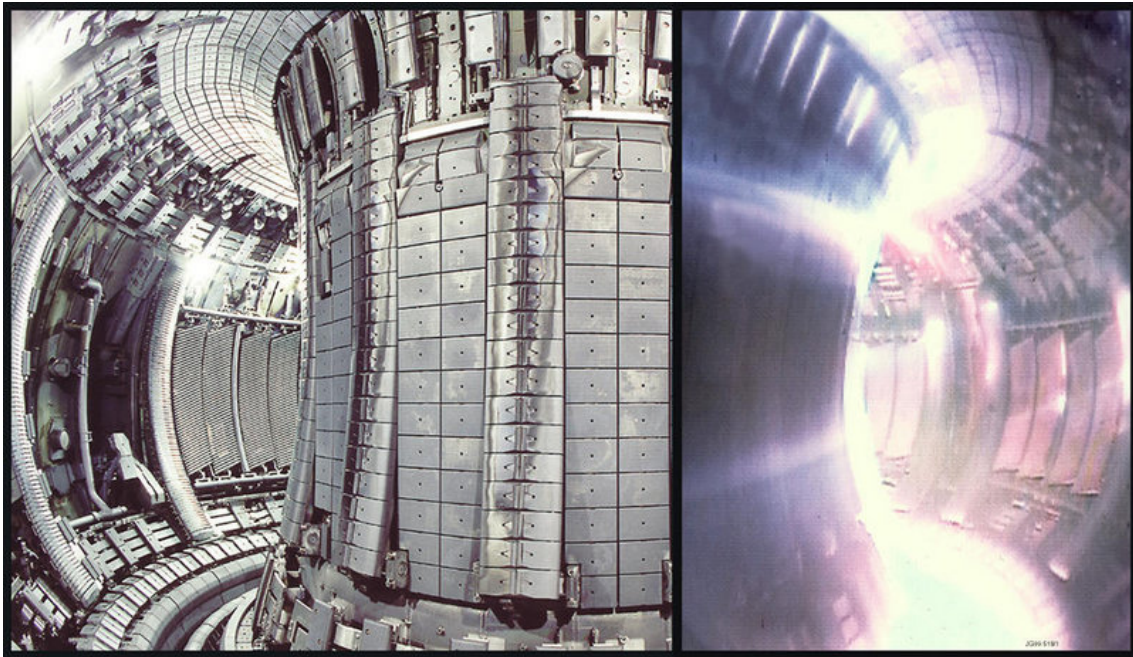


Figure 3: Interior of the vacuum vessel of JET (Joint European Tokamak). At the left, we see the carbon tiles that protect the first wall, antennas and other diagnostics and, at the bottom, the divertor plates. At the right, we see a picture taken during a plasma discharge. Visible light is emitted only in the relatively cool plasma near the walls, where recombination and excitation processes occur. (Source: EFDA-JET)

One of the most critical challenges for the success of ITER and future fusion reactors is a good understanding and handling of turbulence in the plasma edge/SOL. Indeed,

as a boundary condition for the core plasma, the dynamics in the edge controls, to a large extent, the overall plasma confinement. It also determines the strength of steady-state and transient heat fluxes to the divertor and the first wall that can limit the life time of plasma facing components. Further, it affects processes like impurity production and influx, main chamber recycling, tritium retention, and He ash removal [11–17].

The tokamak SOL can often be divided in two distinct regions [11]. The first region, adjacent to the core plasma and dubbed near-SOL, is characterized by strong gradients and fluctuations of near-Gaussian statistics. Turbulence in this region determines the steady-state parallel heat flux profile. At the divertor, heat fluxes perpendicular to the surface must not exceed values of $\approx 10 \text{ MWm}^{-2}$ for actively cooled structures. Besides transient heat fluxes during edge-localized modes (ELMs) and disruptions, this is the main concern for divertor life time [11,12,18]. The second region, the far-SOL, exhibits usually flat density profiles and strongly non-Gaussian statistics. Turbulent transport in this region is convective and bursty and can lead to significant plasma-wall interactions (e.g. [14–16]). Often, turbulence in the far-SOL is dominated by the intermittent ejection and subsequent propagation of blobs. These are structures of enhanced plasma pressure compared to the background that are elongated along magnetic field lines but localized in the perpendicular plane. They can propagate across the confining field as individual entities over a distance of several times their size and thus account for the bursty transport properties. Blobs are observed in low-confinement (L-mode) plasmas and in between ELMs in high-confinement (H-mode) and show similarities with filaments generated during ELMs. They are observed in the edge of many laboratory plasmas and seem to be a universal phenomenon observed irrespectively of the details of the magnetic geometry and driving instabilities [19,20].

Due to its importance for magnetic fusion, a large research effort is ongoing to improve the understanding of edge turbulence in fusion experiments and develop methods and tools to handle it. This effort includes the development of scaling laws to predict the heat flux width for ITER and beyond [11,12], and an exploration of strategies to reduce the peak divertor heat flux, e.g. by inclination of divertor tiles, magnetic flux expansion, detachment [13], induced convective flows [21], or different magnetic geometries [22–25]. Edge physics research includes the development of ways to control or mitigate ELMs [26–30], investigation of the L-H transition [17], exploration of new, advantageous regimes [30–32], numerical simulations of edge turbulence [33,34] and blobs [20], and comparison with experiments [35].

In a wider context, turbulence is considered to be the most important unsolved problem of classical physics. It often shows universal properties in different physical systems [36–38] and is of great scientific and practical interest. In neutral fluids, turbulence is omnipresent. It is observed when smoke is rising from a chimney, it determines the mixing of coffee and milk as well as fuel and oxidizer in the combustion chambers of engines, it controls the drag on cars and airplanes, and its

influence on large-scale atmospheric and oceanic flows determines the weather. Due to the interplay between charged particles and electromagnetic fields, including resonant interactions, and the presence of very large thermodynamic potentials driving them, turbulent phenomena in plasmas are particularly rich. Turbulence governs the dynamics in the solar wind [39], it plays an important role in the accretion of matter around black holes and young stars [40], and generates phenomena such as large scale magnetic fields (dynamo effect), zonal-flows [41, 42], transport barriers, or particle pinches [43, 44]. Studies motivated by magnetic fusion research may also lead to important progress in understanding turbulent dynamics in solar and distant astrophysical plasmas.

1.1 Motivation and outline

Physical insights from studies in fusion edge plasmas can be hindered by the difficulty of diagnosing such plasmas with adequate spatial and temporal resolution and the variety of effects that occur simultaneously. This motivates the study of basic physics effects of edge turbulence in plasma devices with qualitatively similar yet much simpler plasma configurations. Such an environment is achieved in TORPEX [45, 46], which features important ingredients of SOL physics such as pressure gradients, " ∇B " and curvature, and open magnetic field lines. At the same time, its magnetic geometry is simple and the relatively low densities and temperatures allow full access with internal probes. Furthermore, a well-defined set of external controls allows for scans of important physics parameters. This makes it possible to isolate and study instabilities and turbulence effects that take place in more complicated forms in fusion and astrophysical plasmas. Being a relatively small and flexible device facilitates testing ideas of turbulence control. Finally, TORPEX provides an ideal testbed for turbulence code validation, in order to quantify the maturity of turbulence simulations.

In this thesis, we present progress in the understanding of blob formation and propagation and develop several tools to influence the cross-field velocity of these turbulent structures. On the way towards the almost utopian goal of a full, first-principle modeling of turbulent magnetized plasmas, we present the work for the TORPEX code validation project performed in collaboration with members of the theory group. This is accompanied by electrostatic probe development, in particular the construction of a compensated triple probe, which incorporates practical solutions to difficulties often encountered with such probes.

In **chapter 2**, we give an overview of the TORPEX experiment. We present the device, its magnetic field configuration, the plasma production scheme, the main diagnostics, typical plasma parameters, and the nature of the dominant instabilities. This thesis focuses on the regime characterized by ideal interchange waves. These waves develop in a region of strong pressure gradients and, similarly to the edge

of fusion devices, intermittently eject bunches of plasma radially outwards. The general properties of these plasmas are presented at the end of this chapter.

Chapter 3 presents the experimental techniques used in this thesis. It discusses operation and interpretation of electrostatic (Langmuir) probes, and describes conditional average sampling techniques, which are a useful tool to reconstruct the ensemble-averaged, spatio-temporal evolution of waves and turbulent structures. We further describe the construction and testing of a 'compensated' triple probe that provides local, time-dependent measurements of density n , electron temperature T_e and electrostatic potential V_{pl} . We discuss the solutions incorporated in the design of this probe, which avoid common experimental pitfalls. Finally, detailed measurements with the new probe in the ideal interchange mode regime are presented, providing new insights on fluctuations of n , T_e and V_{pl} and their mutual phase relations.

Chapter 4 describes the identification of a blob generation mechanism from ideal interchange waves. Blobs form from radially extending positive wave structures that are sheared apart by the $\mathbf{E} \times \mathbf{B}$ flow. Studies of blob formation in different scenarios provide evidence that a decrease of the radial density scale length is driving the radial elongation of the wave.

In **chapter 5**, we perform theoretical and experimental studies to identify the physical mechanisms that determine blob cross-field velocities. We review previously published velocity scaling laws for the case where blob motion is damped by parallel sheath currents, cross-field ion-polarization currents, or currents due to ion-neutral collisions. We then derive a generalized formula that simultaneously takes into account these effects and find good agreement with numerical blob simulations. Next, we investigate blob motion experimentally on TORPEX in a configuration with an internal limiter. Using different gases, we span a wide range of normalized blob sizes, which allows for a meaningful comparison with the derived blob velocity formula. Good quantitative agreement is found between theory and experimental measurements, indicating that blobs in hydrogen are close to the regime where blob motion is damped by parallel currents, while for heavier atomic species, ion-polarization currents are the dominant damping mechanism. Predicted changes of blob velocity when a second limiter is installed or the neutral gas pressure is varied follow the predicted trends and already provide tools for blob control. Some open questions related with the interpretation of blob motion and possible future measurements to resolve them are discussed at the end of this chapter.

In **chapter 6**, we investigate the parallel dynamics associated with blobs. We present first two-dimensional measurements of parallel currents associated with blobs and confirm the importance of these currents in damping blob motion in hydrogen plasmas. We further demonstrate the link between blobs and toroidal flows. Two-dimensional measurements show that blobs inherit a flow pattern from the interchange wave and convect it radially outwards. This chapter is concluded with a proposal on how to measure the variation of blob density along the magnetic field.

In **chapter 7**, we investigate methods for active blob and turbulence control. A

dedicated limiter setup is installed to explore the possibility of blob control by continuously varying the incidence angle between magnetic field and limiter. In contradiction to theoretical predictions, no significant effect on the blobs is observed. Possible issues intrinsic to our setup and ways to overcome them are discussed. Next, an insulating (glass) limiter is installed in the blob region. This is found to charge up strongly negatively and create background flows that significantly influence blob trajectories. The possibilities of modifying blob motion with induced electric fields is pursued more systematically with active biasing of an array of 3×8 electrodes that is installed on a steel limiter. Using different biasing patterns, blob radial and vertical velocities are significantly changed. We investigate the time-averaged effects of biasing both along and across the magnetic field and explore the source of cross-field currents that impose limits on the achievable cross-field flows.

Chapter 8 discusses a methodology for plasma turbulence code validation, focusing on the quantities for the simulation-experiment comparison and the quantitative assessment of the agreement. As an example, this methodology is applied to a 2D and a global 3D two-fluid code that has recently been developed to simulate TORPEX plasmas. As assessed quantitatively, the 3D model describes well many aspects of turbulent dynamics on TORPEX and in particular performs considerably better than the 2D model in the regime dominated by resistive interchange waves. Next steps, both for the experimental and theoretical side, to further improve agreement between simulation and experiments are discussed. Finally, **chapter 9** summarizes the achievements of this thesis and offers an outlook of possible future developments.

Experimental setup

In this chapter, TORPEX is presented. The device, its magnetic geometry and main control parameters are described, and an overview of TORPEX diagnostic systems is given. Plasma production and basic properties of TORPEX plasmas, such as the dominant instabilities and properties of the turbulence are also discussed.

2.1 TORPEX device

The TORoidal Plasma EXperiment TORPEX [45] is located at the CRPP at EPFL and is operating since 2003. A picture of the device is shown in Fig. 2.1.1, together with the visible light emitted from the plasma seen through a window (inset). The main element is the stainless steel vacuum vessel with major and minor radius of $R_0 = 1$ m and $a_0 = 0.2$ m, respectively. Copper coils around the vessel are used to externally apply magnetic fields. The twelve sectors of the vessel have ports where remotely controlled diagnostics, antennas or other devices can be installed [47]. Access to the vessel is further facilitated by the four movable sectors, which can conveniently be pulled out on an ad hoc designed rail system. Although different magnetic geometries are possible, including Ohmic discharges [48, 49], TORPEX is usually operated in the so called Simple Magnetized Torus (SMT) configuration. This configuration is or has been used in several other experiments [50–55] to study basic aspects of instabilities, turbulence and transport. It consists of a relatively

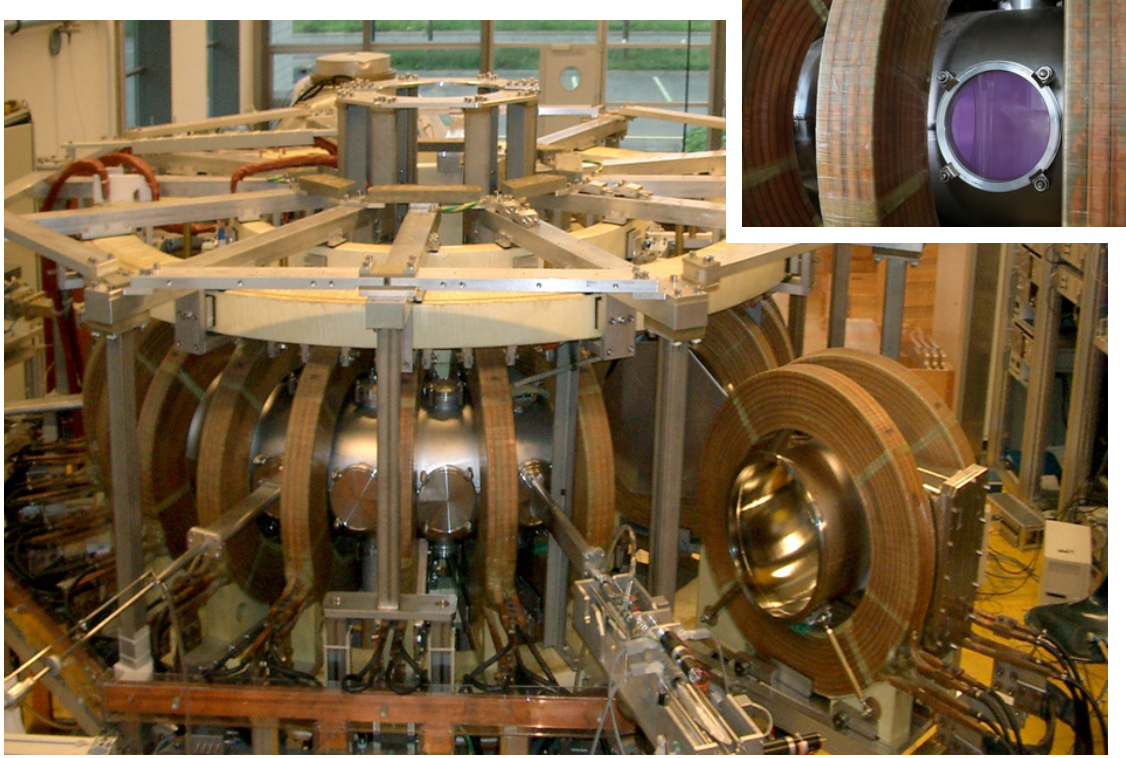


Figure 2.1.1: Photograph of the TORPEX experiment [45]. One of the four movable sectors is pulled out to install a new diagnostics. The inset shows light emission from the plasma during a discharge.

weak vertical magnetic field component B_z added to a dominant toroidal magnetic field B_ϕ . This leads to helical magnetic field lines that wind around the torus and intercept the vacuum vessel at the bottom and the top, as visualized in the sketch of Fig. 2.1.2. The TORPEX vessel is pumped to a base pressure $\lesssim 10^{-6}$ mbar and flow-meters allow adjusting the injection rate of different gases to reach a neutral pressure of typically $p_n \approx 2 \cdot 10^{-4}$ mbar during operation. A magnetron is installed for the production and sustainment of the plasma [56]. It injects microwaves at 2.45 GHz, which corresponds to the electron cyclotron range of frequencies. The power can be adjusted between $P_{rf} = 0.2$ kW and 20 kW and can be modulated with sinusoidal, squared and triangular waveforms. Lower values of P_{rf} can be achieved with a second magnetron, which is used for continuous operation only [57].

TORPEX operation is performed remotely from a control room. Two physicists are required for operation. Plasmas of typically 1 – 2 s can be produced at a repetition rate of ≈ 3 min and data is stored automatically in a MDSplus database [48]. Highly reproducible plasmas are generated with electron density $n \approx 10^{16} \text{ m}^{-3}$, electron temperature $T_e \approx 5$ eV, ion temperature $T_i \ll T_e$, and $\beta \ll 1$, where β is the ratio of thermal to magnetic pressure. An overview of device and typical plasma parameters as well as the coordinate system used on TORPEX are given in Fig. 2.1.2.

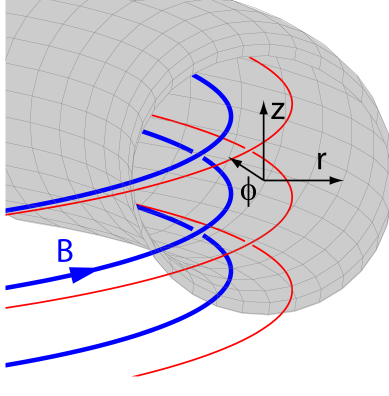
$R_0 = 1 \text{ m}$	$n_e \approx 10^{16} \text{ m}^{-3}$	
$a_0 = 0.2 \text{ m}$	$T_e \approx 5 \text{ eV}$	
$B_\phi \approx 76 \text{ mT}$	$T_i < 1 \text{ eV}$	
$B_z < 5 \text{ mT}$	$n_n \approx 5 \cdot 10^{18} \text{ m}^{-3}$	
$p_n \approx 2 \cdot 10^{-4} \text{ mbar}$	$L_p \approx 4 \text{ cm}$	
$P_{rf} \approx 200 \text{ W}$	$\lambda_D \approx 0.17 \text{ mm}$	
$v_{the} \approx 9.4 \times 10^5 \text{ m/s}$	$\omega_{pe} \approx 5.6 \text{ GHz}$	
$v_{thi} < 9.8 \times 10^3 \text{ m/s}$	$\omega_{pi} \approx 0.13 \text{ GHz}$	
$c_s \approx 2.2 \cdot 10^4 \text{ m/s}$	$\omega_{ce} = 13 \text{ GHz}$	
$\rho_e \approx 0.007 \text{ cm}$	$\omega_{ci} = 7.3 \text{ MHz}$	
$\rho_i < 0.13 \text{ cm}$	$\nu_{iH} \approx 3 \cdot 10^4 \text{ s}^{-1}$	
$\rho_s \approx 0.3 \text{ cm}$	$\nu_{eH} \approx 10^6 \text{ s}^{-1}$	

Figure 2.1.2: Left: Typical device and plasma parameters for hydrogen. Quantities are defined in App. A.1. Estimates of the dominant momentum exchange collision processes, ν_{eH} and ν_{iH} , are discussed in App. B. Right: Sketch of the TORPEX magnetic geometry and the definition of the coordinate system used in this thesis.

Besides a number of well defined control parameters (B_ϕ , B_z , p_n , P_{rf}), relatively simple geometry, flexible handling and easy operation, TORPEX benefits from the relatively low values of plasma density and temperature that allow full access with probes over the entire plasma cross-section.

2.2 Overview of the main diagnostics

Besides important discharge parameters that are automatically measured during each discharge such as B_ϕ , B_z , $p_n^{(*)}$, or P_{rf} , most plasma measurements are obtained on TORPEX with electrostatic diagnostics, a fast framing camera, and magnetic probes. Examples of diagnostics with their acronyms are shown in Fig. 2.2.1. The fast imaging system consists of a Photron Ultima APX-RS fast framing camera combined with a Hamamatsu C10880-03 image intensifier. Applying a tomographic inversion, this allows non-perturbative measurements of plasma emissivity with high spatial and temporal resolution (up to 200'000 frames per second) [58, 59]. Fig. 2.2.1 shows a photograph of a magnetic pickup coil, referred to as Bdot. It has been constructed in collaboration with colleagues from the Reversed-Field eXperiment (RFX) in Padova, Italy and is used to measure parallel currents on TORPEX [60]. The other photographs in Fig. 2.2.1 show a selection of electrostatic probes. There is the almost indispensable 2D probe array HEX TIP [61], that consists of 86 Langmuir probes (LPs) and covers the whole plasma cross-section. There is SLP [47], a 1D array of 8 LPs, that can be moved radially and tilted toroidally. Further, there are the five-tip triple probe, FRIPLE [62], a Mach probe [63], a set of wall electrodes, used both to apply plasma biasing and to measure plasma parameters near the

(*) Neutral pressure measurements are performed with a PFEIFFER Compact Capacitance Gauge (CMR 275).

wall (see Chapter 7.3). Finally, there are the TWIN probes, two identical, simple LPs. Construction and use of electrostatic probes constitute an important part of my thesis work and are discussed in some detail in Chapter 3. In the following paragraphs, I am merely giving an introductory overview on their working principle. The simplest electrostatic diagnostics is the single Langmuir probe (LP) [64]. An LP consists usually of a wire that is isolated up to a short tip at the end and that is immersed into the plasma (see for example the TWIN probes in Fig. 2.2.1). As long as the probe is held at a potential V_{pr} below the electrostatic plasma potential V_{pl} , a sheath with thickness of a few Debye lengths, $\lambda_D = \sqrt{\frac{\epsilon_0 T_e}{n e^2}}$, forms around the probe surface. Inside this sheath, the plasma is no longer quasi-neutral and strong electric fields exist. While ions are accelerated towards the probe surface, electrons are partly repelled inside the sheath, more efficiently the lower the probe potential. Within the simplest theoretical treatment, one finds that the current I_{pr} collected by the probe depends on probe potential and plasma parameters as follows (see e.g. [13, 64])

$$I_{pr} = \frac{1}{2} n e c_s A \left[1 - \exp \left(\frac{e(V_{pr} - V_{fl})}{T_e} \right) \right]. \quad (2.2.1)$$

Here, $c_s = \sqrt{T_e/m_i}$ is the ion sound speed for cold ions, A is the probe surface, and V_{fl} is the floating potential. The latter is defined as the potential for which the probe draws no current. Eq. (2.2.1) is called the $I - V$ characteristics or $I - V$ curve of an LP. The first and second term on the right hand side represent the current carried by the ions and electrons, respectively. We see that the electron current increases exponentially with V_{pr} . This is true as long as $V_{pr} \lesssim V_{pl} \approx V_{fl} + \mu \cdot T_e/e$, where μ is a constant (≈ 3 in hydrogen) [64]. Above V_{pl} , I_{pr} saturates and Eq. (2.2.1) is no longer valid.

LPs can be operated in different modes. If the probe is biased to a strongly negative potential, $V_{pr} - V_{fl} \ll -T_e/e$, only ions are collected. The current measured this way is called ion saturation current, I_{sat} , and, from Eq. (2.2.1), we find $I_{sat} = \frac{1}{2} n e c_s A \propto n \sqrt{T_e}$. Time traces of I_{sat} are probably the most common measurements with LPs. They are used to measure fluctuation properties such as power spectra or fluctuation levels. I_{sat} signals from two probes allow wave number measurements with the two-point correlation technique [65, 66]. In TORPEX, we use for example SLP to measure the vertical wave number k_z , or the TWIN probes, well separated toroidally from each other, to measure the toroidal wave number k_ϕ in this way. Further, I_{sat} is often used to deduce density, neglecting the square root dependence on electron temperature.

Another time-dependent quantity that is relatively easily obtained is the floating potential. For this, $I_{pr} = 0$ is imposed and the probe potential is measured. As already mentioned, V_{fl} and V_{pl} are linked by $V_{pl} \approx V_{fl} + \mu \cdot T_e/e$. In some cases, the T_e term is neglected and fluctuations of plasmas potential and electric fields (from the difference of two nearby probes) are deduced from V_{fl} . As we will see in Chapter 3, this is in general not a good approximation in TORPEX.



Figure 2.2.1: Photographs of the main diagnostics used on TORPEX.

In order to deduce density, electron temperature, and plasma potential, one point of the I-V curve is not sufficient. To measure the full I-V curve, one applies a voltage sweep to the probe. Fitting the result with Eq. (2.2.1) provides n , T_e , V_{fl} , and, from the relation $V_{pl} \approx V_{fl} + \mu \cdot T_e/e$ (or from the point where the electron current starts to saturate), the plasma potential. It can be quite difficult to perform the voltage sweep over a time where plasma parameters stay approximately constant. Therefore, one often evaluates the mean I-V curve, averaged over many sweeping cycles. Obviously, this way, one is limited to time averaged values of n , T_e , V_{fl} , and V_{pl} . To measure 2D profiles of these quantities, SLP is operated in sweep mode and displaced radially shot-by-shot. Time-dependent, conditionally averaged measurements of n , T_e , and V_{pl} can be obtained with the BOX-CAS technique, as discussed in Chapter 3.4. Actual time traces can be obtained with the triple probe technique [67]. On TORPEX, we operate FRIPLE as a five tip triple probe. Working principle, common issues and measurements obtained with this diagnostics are discussed extensively in Chapter 3.

2.3 Plasma production

In TORPEX, plasmas are produced and sustained by microwaves injected perpendicularly to the magnetic field from the low field side (LFS) [56]. The waves are injected in O-mode, i.e., with the polarization of the electric field along the TORPEX magnetic field. This avoids the low density cutoff of the X-mode (see e.g. [68]). Prior to plasma formation, naturally existing free electrons are accelerated at the electron cyclotron (EC) layer, where the microwave frequency f_{rf} equals the electron cyclotron frequency $f_{ec} = \frac{eB}{2\pi m_e}$ (note that $B_z \ll B_\phi$ such that $B \approx B_\phi \propto 1/R$ and the EC layer is located at a region of limited radial extent). When the energy of the accelerated electrons exceeds the ionization potential of the neutral gas, electron impact ionization occurs and a plasma forms.

Once the plasma is created, some ionization still occurs at the EC layer. However, only a fraction of the wave power is absorbed there. The remaining fraction is reflected from the vessel wall on the high field side (HFS). This leads to a loss of the original polarization and both O-mode and X-mode waves propagate back into the plasma. It is found that most of the microwave power is in fact absorbed at the upper hybrid (UH) layer, where the X-mode encounters a fluid plasma resonance [56]. The resonance condition is given by $f_{rf}^2 \approx f_{ec}^2 + f_{pe}^2$, where $f_{pe} = \sqrt{\frac{ne^2}{4\pi^2 m_e \epsilon_0}}$ is the electron plasma frequency. The location of the UH resonance depends thus on the electron density profile. Expressed differently, the resonance occurs at positions where the local density equals the density n_{uh} given by

$$n_{uh}(R)[10^{16} \text{ m}^{-3}] \approx 1.24 \cdot f_{rf}^2[\text{GHz}] \left[1 - \left(\frac{R_{ec}}{R} \right)^2 \right], \quad (2.3.1)$$

where R_{ec} is the radial position of the EC layer. The UH layer lies further to the

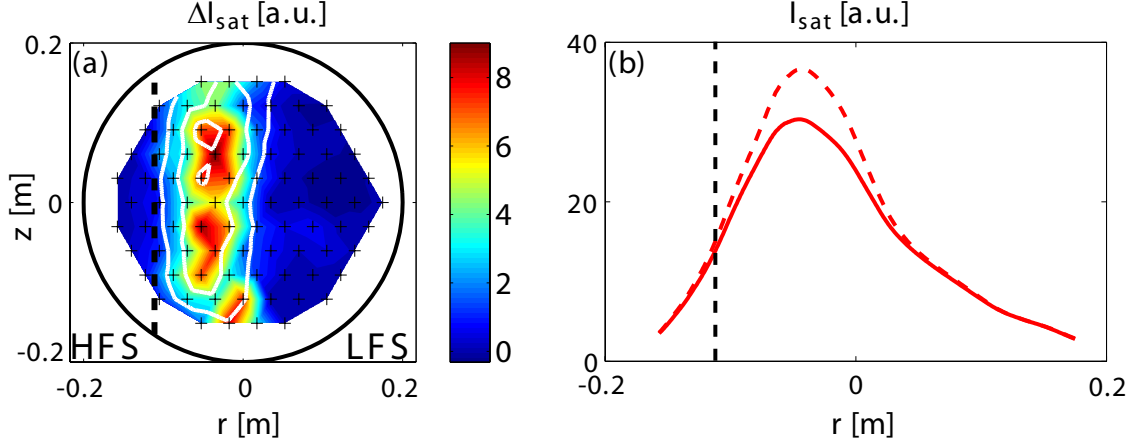


Figure 2.3.1: (a): Average change in the I_{sat} profile due to a modulation in microwave power, indicating the location of the plasma source. The unperturbed I_{sat} profile is shown by the white contour lines. The vertical, dashed line indicates the position of the EC resonance. (b): Vertically averaged I_{sat} profile in the absence (solid line) and shortly after (dashed line) the start of the microwave pulses.

LFS than the EC layer and the two coincide as $n \searrow 0$.

Fig. 2.3.1 shows the experimentally determined location of the particle source for a plasma with $N = 2$, i.e., where each magnetic field line does two toroidal turns before intercepting the vacuum vessel. The method introduced in [56] is applied: short pulses of additional power are superimposed on the stationary level of magnetron power. Then, the I_{sat} ^(†) profile measured with the HEX TIP probe array shortly after the start of a pulse and averaged over many (here 368) such pulses is evaluated. The average effect of the pulses and thus the average position of the particle source is then inferred by subtracting the average I_{sat} profile measured during periods well separated from any pulse. Fig. 2.3.1 (a) shows the average effect ΔI_{sat} of the microwave pulses. The average I_{sat} profile at times well separated from any pulse is indicated by the white contour lines and the position of the EC resonance layer is indicated by the dashed, black line. The same information is displayed differently in Fig. 2.3.1 (b), where the vertically averaged I_{sat} profile before (solid line) and right after (dashed line) the start of the pulse is shown. We see that for the plasma investigated here, the source location coincides roughly with the region where the I_{sat} profile peaks and no significant contribution from the EC layer is observed. Although multiple UH resonance layers are in principle possible, a single UH layer is usually observed in TORPEX. This layer moves radially outwards when the injected microwave power and thus peak density is increased [56], as dictated by Eq. (2.3.1). The dependence of the EC and UH resonance layer on magnetic field strength provides a convenient way for plasma positioning. This is shown in Fig. 2.3.2. The strength of the toroidal field at $r = 0$, B_0 , is increased from ≈ 76 mT to ≈ 87 mT, resulting in a strong outward shift of the plasma.

^(†) Throughout this thesis, I_{sat} is given in arbitrary units. Current densities, which are independent from probe size, are given in physical units.

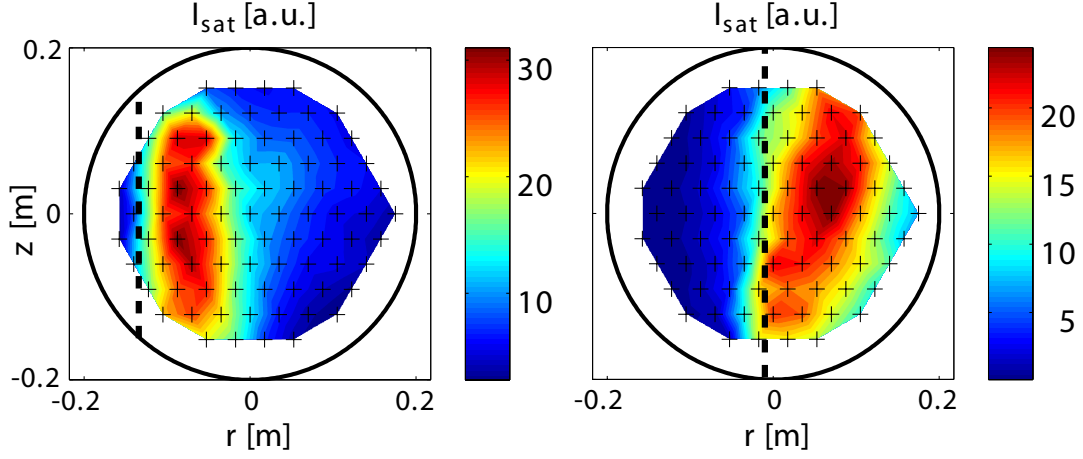


Figure 2.3.2: An example showing the dependence of the radial location of the EC layer and the plasma profile on the magnetic field strength. The plasma moves radially outwards as B_0 is increased from ≈ 76 mT to ≈ 87 mT.

While plasma density and position can thus be controlled by the magnitude of P_{rf} and B_0 , the achievable plasma densities and the possibilities of varying the magnetic field strength is limited in microwave produced plasmas. To avoid squeezing the plasma towards the LFS-wall, the electron density is limited to a few 10^{16} m^{-3} and variations of B_0 are limited by the requirement that the EC layer lies inside the vacuum vessel. To overcome these limitations, a helicon wave source [69] is currently under development on TORPEX.

2.4 The dominant instabilities on TORPEX

During the past four years, research on TORPEX has been supported by an important and still ongoing simulation effort [70–75]. The tools developed include the GBS code [73] that provided the first global, 3D fluid simulation of the simple magnetized torus (SMT) configuration. Linear stability analysis and GBS simulations reveal three regimes of turbulence in the SMT, each driven by a distinct plasma instability: an ideal interchange mode regime, a previously undiscovered resistive interchange mode regime, and a drift-wave regime [73] (an introduction to drift and interchange waves can be found for instance in [76]). For large values of B_z or, equivalently, low values of N , where N is the number of toroidal turns of a field line inside the SMT, the ideal interchange mode is the dominant instability. This is characterized by a wave number along the magnetic field $k_{\parallel} = 0$. As long as sheath effects are negligible, this mode is most unstable for the largest perpendicular scale compatible with $k_{\parallel} = 0$. This gives a vertical wave length of $\lambda_z = \Delta$, where Δ is the vertical field line displacement after one toroidal turn. A mode with a vertical wave length larger than Δ is possible only for $k_{\parallel} \neq 0$. For finite parallel resistivity, interchange modes with sufficiently small but finite k_{\parallel} are still linearly unstable [73]. Due to the role played by parallel resistivity, these modes are called resistive interchange

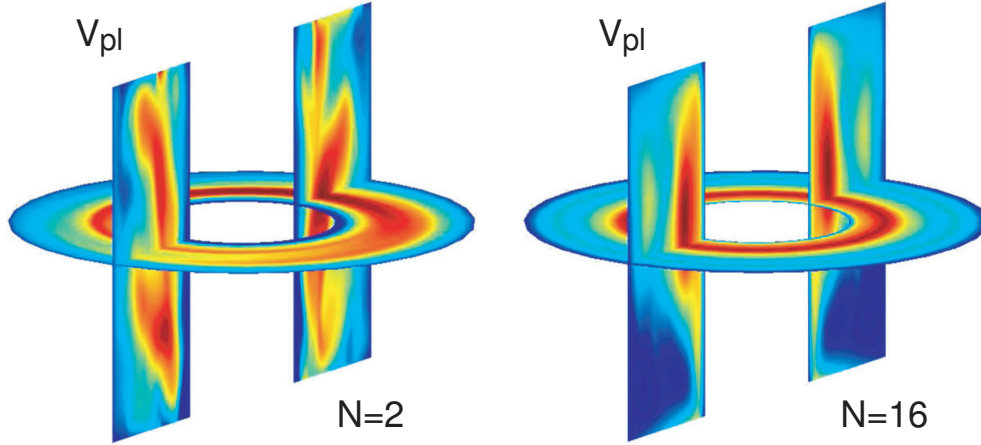


Figure 2.4.1: Snapshots of V_{pl} from [73] for a simulation with $N = 2$ and $N = 16$.

modes. Their linear growth rate increases as k_{\parallel} goes to zero. For a vertical wave length equal to the full height L_v of the SMT, the smallest possible k_{\parallel} is achieved for a toroidally symmetric mode. This results in $k_{\parallel} \approx 1/(RN)$ [73]. Now, as N increases, the perpendicular wave number $\lambda_z = \Delta$ of the ideal interchange mode is reduced. This leads also to a reduction of its linear growth rate. At the same time, the parallel wave number of the resistive interchange wave gets smaller and the mode is getting more unstable. Therefore, for large enough N , a transition from ideal to resistive interchange dominated turbulence occurs. This is shown in Fig. 2.4.1, which shows a snapshot of plasma potential from a GBS simulation with $N = 2$ and $N = 16$, respectively. In the $N = 2$ case, fluctuations are constant along B and the observed mode is an ideal interchange mode. For $N = 16$, a resistive interchange mode with largest possible vertical scale and toroidal symmetry is observed. Pure drift waves, long believed to dominate turbulence in the SMT at large N , are found to be unimportant for realistic values of parallel resistivity and density gradients [73].

In TORPEX experiments, two-point correlation measurements [65] indeed show this transition from the ideal interchange mode regime, where $k_z \approx 2\pi/\Delta$ and $k_{\parallel} \approx 0$, to a regime with $k_z \approx 2\pi/L_v$ and toroidal wave number $k_{\phi} \approx 0$ [75, 77, 78]. As shown in Fig. 2.4.2 (a), $k_z \approx 2\pi/\Delta$ is measured up to $N \lesssim 7$. Then, the transition occurs and $k_z \approx 2\pi/L_v$. In Fig. 2.4.2 (b) and (c), we show a snapshot of the conditionally averaged^(‡) evolution of the dominant mode obtained with HEX TIP. (b) shows the case $N = 2$, where the $\lambda_z = \Delta$ mode growing on the vertically elongated profile is clearly visible (the time averaged profile is indicated by white contours). The $N = 8$ case is shown in (c). The observed vertical elongation of the wave structures is consistent with $\lambda_z = \Delta$. One can also identify a relatively large radial wave number. The full time evolution shows that the observed mode structures are moving in the radial direction. It is possible that dynamics of the UH resonance layer also play a role here, something that might be interesting to investigate further in the future.

^(‡) See Chapter 3.4 for an explanation of this technique.

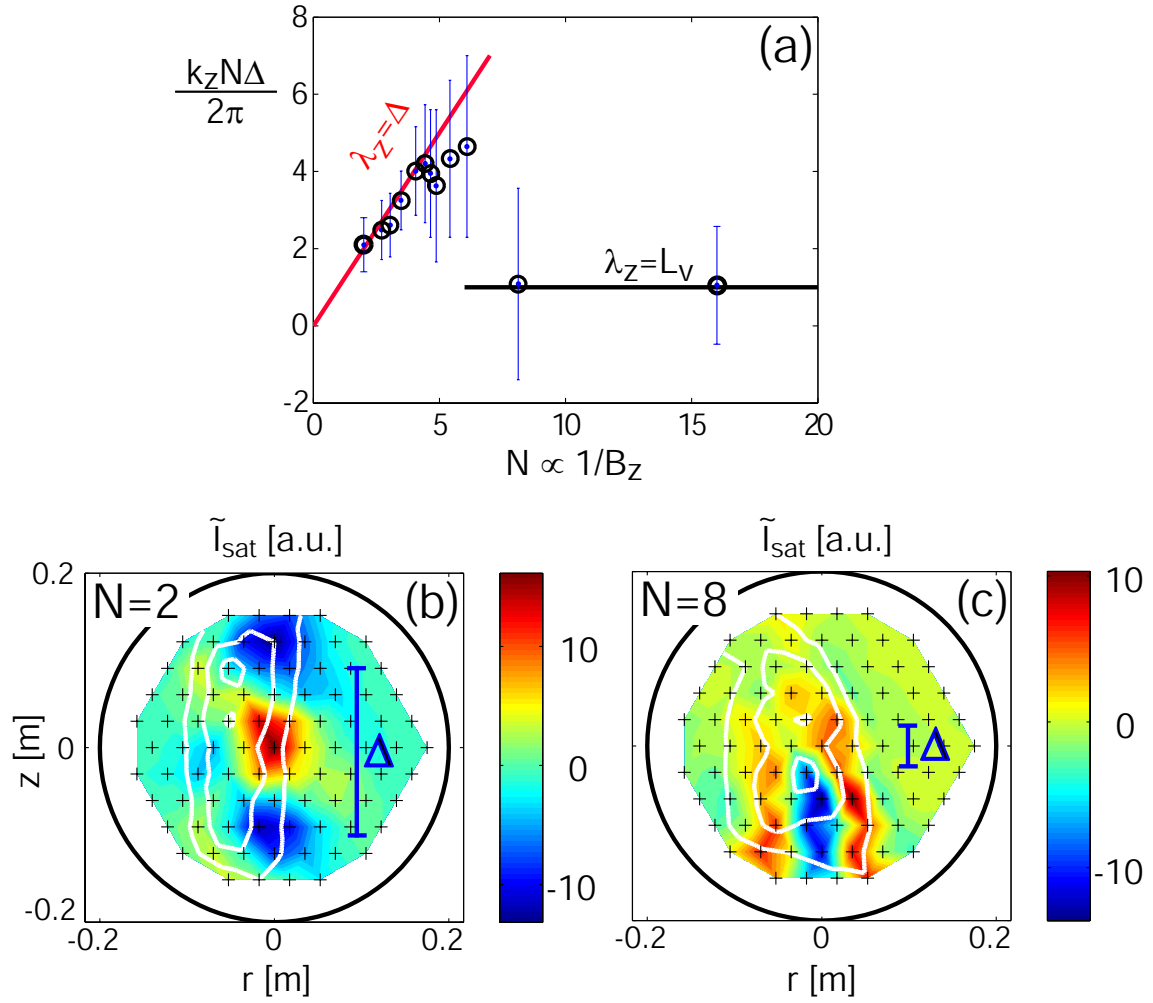


Figure 2.4.2: (a): Measured vertical mode number as a function of the field lines turns N inside TORPEX. Drawn are also the values expected for the ideal interchange mode, red line, and for the resistive interchange mode, black line. (b), (c): Snapshot of the conditionally averaged mode for a case with $N = 2$ and $N = 8$. White contours represent the time averaged I_{sat} profile.

2.5 Plasmas in the ideal interchange mode regime

This thesis deals mainly with plasmas in the ideal interchange mode regime. Therefore, some general properties of these plasmas are presented here. Fig. 2.5.1 shows time-averaged profiles of n , T_e , and V_{pl} for a case with $N \approx 3$. The plasma is positioned sufficiently to the HFS to allow investigating wave properties and turbulent transport towards the LFS. The profiles are vertically elongated and the ideal interchange mode is destabilized in the region between $r \approx -3$ cm and $r \approx 1$ cm, where strong gradients in n and T_e , collinear with magnetic field gradients, exist. This region, referred to as the mode region, is characterized by quasi-coherent fluctuations. An example of an I_{sat} time trace from this region is shown in Fig. 2.5.1 (a). The frequency of the mode (≈ 8 kHz in this case) is mainly determined by an upwards $\mathbf{E} \times \mathbf{B}$ convection, indicated by the calculated $\mathbf{E} \times \mathbf{B}$ velocity field that is superimposed on the plasma potential plot, Fig. 2.5.1 (f). The gross structure of the plasma potential and the resulting background convection is determined by sheath physics. To avoid large net currents flowing along the magnetic field to the wall, a potential drop of $\approx \mu T_e / e$ is required in the thin sheath between plasma and wall [13]. Therefore, the plasma potential follows approximately the temperature profile and gradients in T_e cause steady-state perpendicular plasma flows.

Moving further to the LFS, fluctuations become less coherent and I_{sat} time traces are dominated by intermittently occurring bursts, see Fig. 2.5.1 (g). This is a clear signature of the regime characterized by intermittent convective particle transport observed in the edge of many magnetically confined plasmas. These bursts are caused by bunches of plasma that are ejected from the main plasma and move radially outwards. An example of such a plasma *blob* and its radial movement can be identified in the two I_{sat} profiles measured with HEX TIP, Fig. 2.5.1 (h).

Reminiscent of dynamics in the edge of tokamaks and other fusion devices are also the high relative fluctuation level of I_{sat} (b) and the skewness profile (c), which is close to zero or negative at the HFS and becomes strongly positive as we move outwards. Additional universal features of edge turbulence are suggested by similar parabolic relations that link skewness and kurtosis of I_{sat} signals both on TORPEX and on tokamaks [79–81].

While we have focused here on dynamical properties in a given cross section of the plasma, some information on parallel dynamics is contained in Fig. 2.5.1 (g). Two time traces are shown here. The red one is measured with a HEX TIP tip, while the other one with the MACH probe, on the same field line but toroidally separated by 205° . This demonstrates the excellent uniformity of fluctuations along the magnetic field in these plasmas.

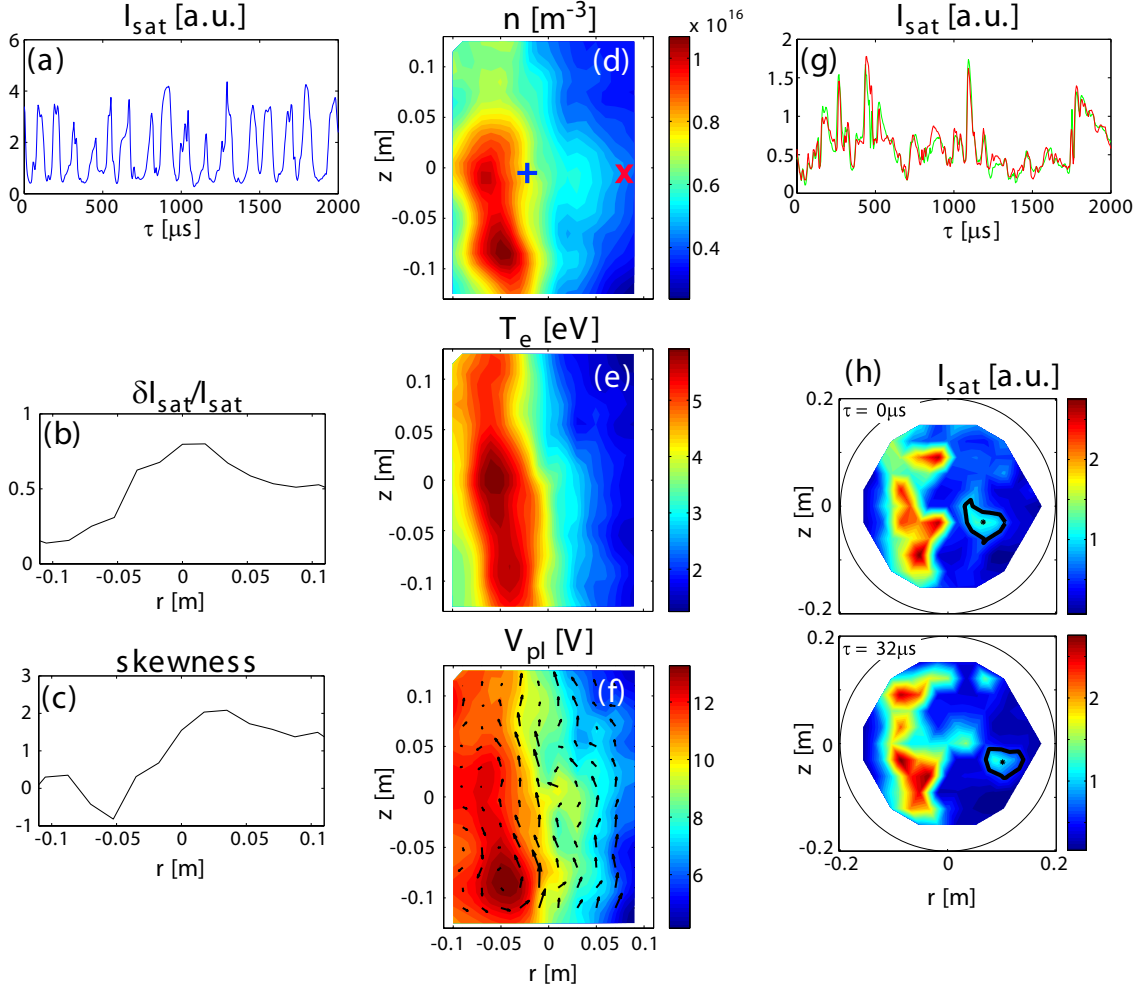


Figure 2.5.1: Overview of plasma properties in the ideal interchange mode regime (here $N \approx 3$). The middle column, (d) - (f), shows time averaged profiles of n , T_e , and V_{pl} . Typical I_{sat} time traces in the mode and blob region are plotted in (a) and (g). They are measured at the location indicated by a blue cross and a red 'x' in figure (d), respectively. The green time trace in (g) is measured on the same field line as the red one, but toroidally displaced by 205° . Finally, (b) and (c) show radial profiles of relative fluctuation level and skewness of I_{sat} at $z = 0$ and (h) shows an example of a blob.

Experimental techniques

Most measurements on TORPEX are obtained with the help of Langmuir probes (LPs). As already seen in Sec. 2.2 and Fig. 2.2.1, an LP can be a simple piece of wire that is held into the plasma and connected to some electrical circuitry. The current drawn from the plasma as a function of the applied probe voltage is used to deduce local plasma parameters such as density, electron temperature, and plasma potential. The use of LPs goes back to the work by Irving Langmuir and collaborators in the 1920s [82] and is common in interplanetary, magnetospheric and ionospheric plasmas, as well as in laboratory plasmas, provided the probe is able to withstand the heat loads from the plasma. The relative simplicity of LPs is in contrast to the difficulty in the interpretation of the measurements. Indeed, the modeling of current collection by an LP is a difficult problem, especially in the presence of magnetic fields. It involves many complicated and partly not well understood problems of plasma physics such as plasma-wall transition, effective cross-field electrical conductivity, and anomalous transport. Thousands of papers have been written on this subject and different probe theories exist, depending on plasma and probe parameters such as probe dimensions and shape, Debye length, particle mean free paths, or gyroradii of ions and electrons. An overview of probe theories for unmagnetized plasmas can be found in Francis Chen’s lecture notes [83] that are available online and the full complexity of LPs becomes apparent from the review article, Ref. [84]. Introductions to probe theories and practical considerations can be found in text-

books [13, 64, 85, 86].

This chapter presents the probe theory used on TORPEX and how I-V curves are obtained and fitted to extract the time averaged quantities n , T_e , V_{fl} , and V_{pl} (*). This is followed by a discussion on the applicability of the present probe theory on TORPEX, the influence of different undesired effects, and some practical issues. This part is not a final proof of the accuracy of LPs, but a starting point to assess the reliability of LP measurements on TORPEX. Next, the conditional average sampling technique (CAS) is described, which is commonly used to obtain the average evolution, e.g. of ion saturation current or floating potential, for coherent events in the plasma. A discussion of a modified CAS method, referred to as BOX-CAS, is also included. This provides the conditionally averaged dynamics of density, plasma temperature, and potential. The last part of this chapter deals with the design, testing and results of the FRIPLE probe [62], which is operated as a triple Langmuir probe to directly measure time traces of n , T_e , and V_{pl} .

3.1 Probe theory used on TORPEX

In TORPEX, Langmuir probe measurements are interpreted using the following formula relating the current I_{pr} collected by the probe and the probe potential V_{pr} :

$$I_{pr}(V_{pr}) = I_{sat}^0 \left[1 - \alpha(V_{pr} - V_{fl}) - \exp\left(\frac{V_{pr} - V_{fl}}{T_e/e}\right) \right]. \quad (3.1.1)$$

The first two terms on the right hand side represent the ion current to the probe. The surface of the Debye sheath that forms around the probe depends on the probe potential. This gives rise to an imperfect saturation of the ion current at low V_{pr} that we approximate by a linear term with parameter α . The third term on the right hand side is the contribution of the electrons to the probe current. The factor I_{sat}^0 is the value of the ion current extrapolated to the floating potential V_{fl} . It is taken as the Bohm value [13, 64]

$$I_{sat}^0 = \frac{n}{2} c_s e A_{eff}^0, \quad (3.1.2)$$

with n the plasma density in the unperturbed plasma and A_{eff}^0 the sheath surface at the floating potential.

The electron current in Eq. (3.1.1) does not grow indefinitely with an exponential dependence. Ideally, it saturates at the electron saturation current $I_{sat}^e = n\sqrt{T_e/(2\pi m_e)} e A_{eff}^e$ when the probe potential reaches the plasma potential. Here, A_{eff}^e is the effective collection surface for the electrons, which can differ from that for the ions, A_{eff}^0 . From the condition that the electron current in Eq. (3.1.1) reaches

(*) The discussion on the other operational modes of LPs to measure time traces of I_{sat} or V_{fl} can be found in Sec. 2.2 and will not be repeated here.

I_{sat}^e when $V_{pr} = V_{pl}$, we find the following relation between V_{pl} and V_{fl} :

$$V_{pl} = V_{fl} + \mu \cdot T_e/e, \quad \mu = \log \left(\frac{A_{eff}^e}{A_{eff}^0} \sqrt{\frac{2m_i}{\pi m_e}} \right). \quad (3.1.3)$$

While this expression is used on TORPEX to evaluate the plasma potential from V_{fl} and T_e , the factor μ is evaluated experimentally rather than from the above relation, as discussed in the next section.

3.2 Analysis of swept LPS

In order to evaluate time averaged values of n , T_e , and V_{pl} with Langmuir probes, a sawtooth sweep is applied to the probe tip while the applied voltage and the probe current are measured. Typically, we use a voltage sweep with a period of 3 ms, which is slow compared to the fluctuations in the plasma. The voltage range needs to be sufficiently large to cover the ion saturation current regime and the exponentially growing part of the I-V characteristics. Usually, a voltage sweep between -40 V and 20 V is appropriate. Based on previous analysis routines described in [47], I have developed an analysis package for automatic downloading, fitting and plotting of the measurements. The routines are available on the TORPEX SVN server. The individual steps of the analysis are described in the following.

Fig. 3.2.1 (a) shows an example of a sawtooth voltage sweep applied to an LP. The corresponding probe current is shown by the blue line in (b). The time window covered by the plot was chosen here such that we can see the time $t \approx 1.216$ s when the magnetron power is turned off and the discharge terminates. The measurement was performed in the blob region, where fluctuations in density are of order unity. Plasma parameters change strongly during one sweep cycle and it is therefore not surprising that the current signal in Fig. 3.2.1 (b) shows strong fluctuations instead of monotonic I-V curves. As is common practice for slowly swept LPS, the I-V characteristics is therefore evaluated by averaging over many sweeping cycles.

As we can see from the zoomed view in Fig. 3.2.1 (b), a non-zero probe current is measured even after the end of the discharge. This is due to impedance to ground in the circuit, here mainly due to stray capacitance in the coaxial cables connecting the probe tip to the Langmuir amplifier. For fast-sweep LPS, an additional reference or dummy probe is often used to avoid this problem. The dummy probe is identical to the first probe and operated in the same way, except that it is kept outside of the plasma. The current measured by this probe is then subtracted from the one on the first probe. This cancels stray capacitance effects and common noise that influence the two probes [87, 88]. In our case, we evaluate the I-V characteristics in the absence of plasma by performing an average over several sweep cycles after the discharge. This gives the red curve in Fig. 3.2.1 (b) that is then subtracted from the current measured during the discharge.

Fig. 3.2.2 (a) shows the average I-V characteristics for the present example,

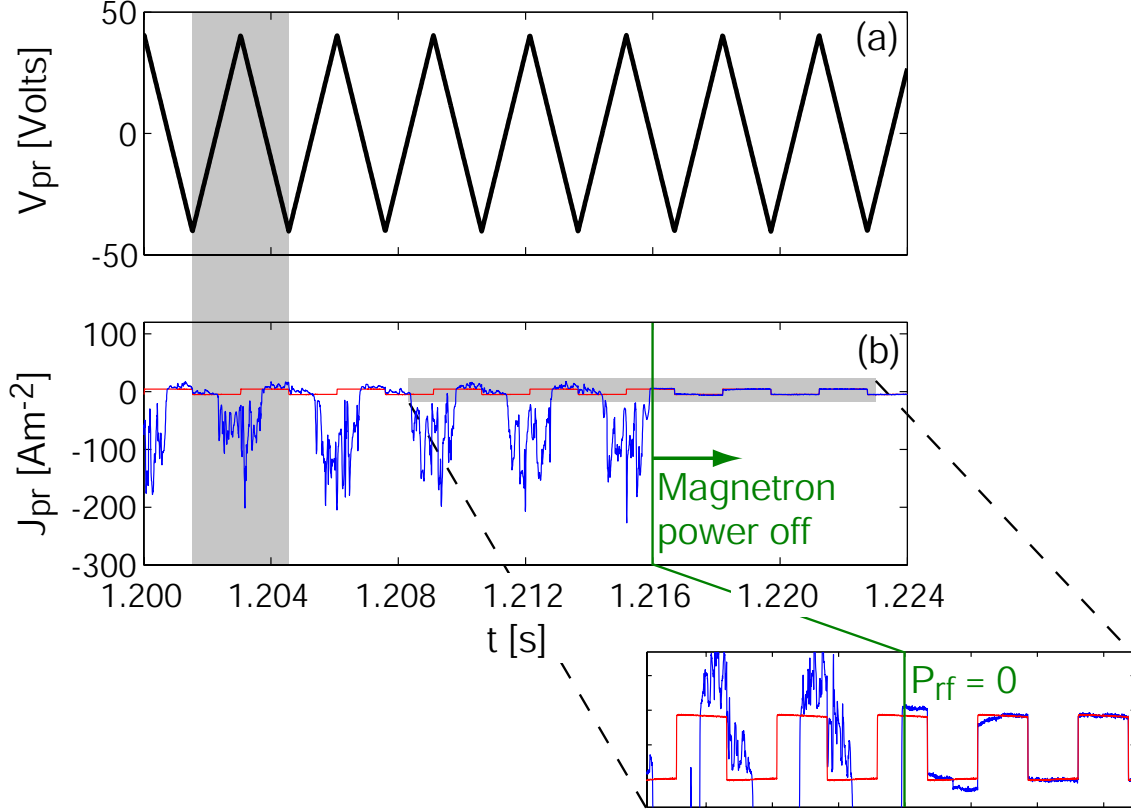


Figure 3.2.1: (a): Voltage sweep applied to an LP. (b): Corresponding current collected by the probe (blue curve). The red curve shows the current caused by an impedance to ground in the circuitry. It is estimated from the signal during several sweeping cycles after the magnetron power is turned off. What is shown here is actually the current density, i.e., the probe current is already divided by the ion collection surface A_{eff}^0 .

obtained here by averaging over 132 voltage ramps. It shows a rather typical LP characteristics: a relatively weak positive current appears at low bias voltage, the ion saturation current, then an exponential growth of the negative electron current around $V_{pr} \approx 0$ V, which shows an imperfect saturation at large positive voltage. The red data points in the figure show the raw data for 10 voltage ramps. This illustrates again the large fluctuations in this region of the plasma. The curve in Fig. 3.2.2 (a) is now fitted to Eq. (3.1.1) with the four fitting parameters I_{sat}^0 , T_e , V_{fl} , and α . Eq. (3.1.1) is valid at most up to the plasma potential and an appropriate voltage range needs to be determined for the fit. Especially the right voltage cutoff used for the fit is rather crucial. In a first step, we use the *minimum temperature approach* described in [89]. The right voltage cutoff is varied step by step between the floating potential and the maximum voltage value. The minimum temperature value obtained this way, T_e° , and the corresponding floating potential value, V_{fl}° , are then evaluated. Next, data is again fitted, now over the interval $[V_{fl}^\circ - \varpi_0 \cdot T_e^\circ/e, V_{fl}^\circ + \varpi \cdot T_e^\circ/e]$. While a single, sufficiently large value is chosen for ϖ_0 , $\varpi_0 = 25$ for instance, a range of values is usually chosen for the input parameter ϖ , e.g. $\varpi \in [0.5, 2.5]$. This gives different values for the fitted parameters that display the uncertainty related to the

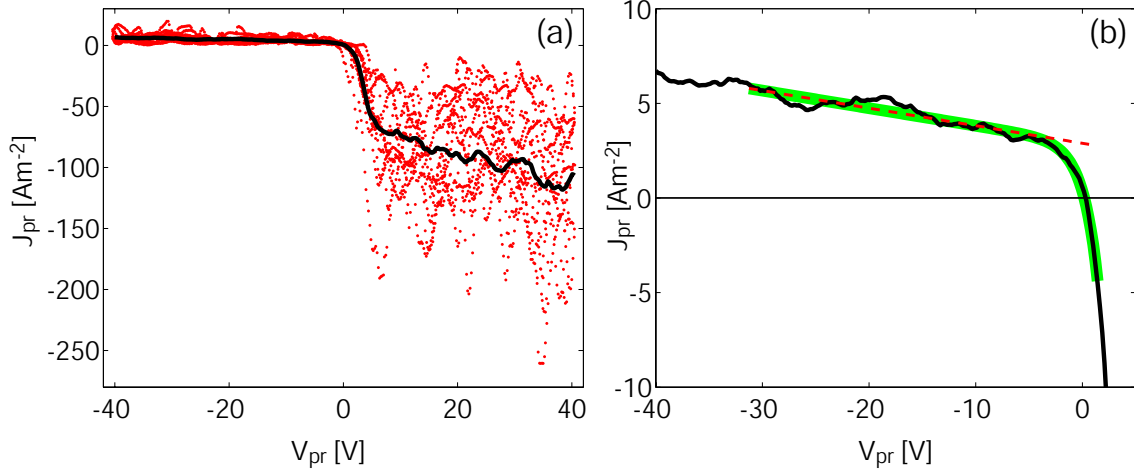


Figure 3.2.2: (a): I-V characteristics, averaged over 132 voltage ramps. The red dots are the raw data points for ten of these voltage ramps. (b): Zoomed in view of the I-V characteristics. The green curve is the fit of Eq. (3.1.1) to the data and the red dashed line the linear fit to the ion current.

choice of the voltage range used for the fit. The result of this procedure for $\varpi = 1$ is shown in the zoomed in view in Fig. 3.2.2 (b) by the green line. The red dashed line shows the linear fit to the ion saturation current. The values extracted from the fit are $I_{sat}^0/A_{eff}^0 = 2.85 \pm 0.04 \text{ Am}^{-2}$, $T_e = 1.4 \pm 0.1 \text{ eV}$, $V_{fl} = 0.20 \pm 0.03 \text{ V}$, and $\alpha = 0.033 \pm 0.001 \text{ V}^{-1}$. The indicated uncertainty here is merely that due to different values of ϖ . It should be noted that if Eq. (3.1.1) is directly fitted to an I-V curve, it can happen, especially for low values of ϖ , that the linear part of the fit does not well represent the ion current. Therefore, it is preferable to perform first the linear fit to the ion saturation current and in a second step fit the exponential part.

After the fitting has been performed, density is evaluated from Eq. (3.1.2). This requires an estimate of A_{eff}^0 . For a cylindrical probe of radius r_p that does not satisfy $r_p \gg \lambda_D$ and $r_p \gg \rho_i$, with λ_D the Debye length and ρ_i the ion Larmor radius, this estimate is subject to uncertainty [64]. It can be estimated experimentally by adjusting A_{eff}^0 such that the measured radial density profile intercepts the upper-hybrid density calculated from Eq. (2.3.1) at the experimentally determined position of the upper-hybrid resonance, Fig. 2.3.1. For more accurate measurements of the absolute value of plasma density, comparisons with independent measurements, e.g. a microwave interferometer, would be necessary.

Finally, the plasma potential is determined from $V_{pl} = V_{fl} + \mu T_e/e$. The value μ is measured experimentally for a given probe. For SLP operated in a hydrogen plasma, for instance, $\mu \approx 3.1 \pm 0.6$ [56]. This method avoids sweeping the probe each time up to electron saturation and V_{pl} being evaluated from the knee of the electron current.

3.3 Considerations on the validity of the simple probe theory on TORPEX

Eqs. (3.1.1) and (3.1.2) (with $\alpha = 0$) are derived from a 1-D collisionless sheath model, assuming Maxwellian electrons, $T_i \ll T_e$, and a perfectly absorbing probe surface, i.e., no reflection or secondary emission of charged particles [13, 64]. This 1-D model directly applies to a Langmuir probe in an unmagnetized plasma, provided that the probe radius satisfies $r_p \gg \lambda_D$ and the electron and ion mean-free paths l_e, l_i are much smaller than the diffusion length d [64, 84]. The model also assumes that the fluctuations in the plasma (and the sweep frequency of the probe voltage) are slow enough such that the sheath is in equilibrium at all times. In the remainder of this section, the validity of Eqs. (3.1.1) and (3.1.2) for TORPEX plasmas is discussed.

The conditions $T_i \ll T_e$ and $l_e, l_i \gg d$ are always satisfied in the electron heated TORPEX plasmas for typical neutral and plasma densities. The ion mean-free path l_i for collisions with unlike species is determined by charge-exchange collisions with neutrals. With a momentum transfer cross section $\approx 1 \times 10^{-18} \text{ m}^2$ for H-H⁺ collisions [90, 91] and a typical neutral density of $5 \times 10^{18} \text{ m}^{-3}$, we find $l_i \approx 0.2 \text{ m}$. For electrons, the cross section for collisions with neutrals is $\approx 1 \times 10^{-19} \text{ m}^2$ for $T_e = 5 \text{ eV}$ [91] and we find $l_e \approx 2 \text{ m}$. For a cylindrical probe, the diffusion length [84] is given by $d \approx r_p \ln(\pi l_p / 4 / r_p)$ with l_p the probe length. d measures thus a few times the probe radius and $l_e, l_i \gg d$ is well satisfied.

The extension of Eqs. (3.1.1) and (3.1.2) to cylindrical probes in magnetized plasmas with $\rho_i, \lambda_D \ll r_p$ can be justified by a quasi-collisionless model [64]. This model assumes that the probe causes a depleted, quasi-neutral region along the magnetic field that needs to be refilled by an ionization source, cross-field diffusion or convection. If the length L of this region along the field is shorter than the ion mean-free path l_i , Eqs. (3.1.1) and (3.1.2) are still found to be valid when A_{eff}^0 is taken as the projection of the probe surface along the magnetic field. An estimate of L is given in Hutchinson's book [64], $L \approx r_p^2 c_s / D_\perp$, with D_\perp the cross-field diffusion coefficient. Assuming Bohm diffusion, $D_{Bohm} = T_e [\text{eV}] / (16B)$, we find that $L < 5 \text{ cm} < l_i$ for all probe sizes used in TORPEX.

Typically, we have $\lambda_D \sim 0.1 - 0.2 \text{ mm}$ and $\rho_i \lesssim 1.3 \text{ mm}$ for $T_i \lesssim 1 \text{ eV}$ (hydrogen) in TORPEX. For a probe with $r_p = 0.35 \text{ mm}$ as in the case of FRIPLE [62], we are thus not in the limit $\rho_i, \lambda_D \ll r_p$. Therefore, tests have been performed to compare measurements with probes of radius $r_p = 0.3 \text{ mm}$ and $r_p = 3 \text{ mm}$, respectively. In either case, the I-V curves are well represented by Eq. (3.1.1) and yield consistent values of T_e and V_{fl} . The main difference is the reduction of the normalized slope α of the ion saturation current of approximately a factor of 1/2 to 1/3 for the larger probe. The deduction of the plasma density requires an estimate of A_{eff}^0 which is subject to uncertainty (full or projection area). Further, we expect A_{eff}^0 to depend on λ_D and thus on position. However, for a wide range of plasmas in TORPEX, λ_D

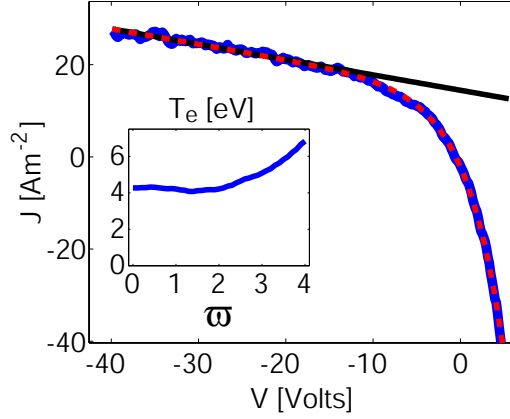


Figure 3.3.1: Example of a fit of Eq. (3.1.1) to an I-V curve obtained in the mode region. The blue solid curve is the average I-V characteristics, the red dashed curve the fit with Eq. (3.1.1), and the black solid line the fit to the ion current. Inset: Dependence of the evaluated electron temperature on ϖ , which defines the right voltage cutoff used for the fit.

is fairly constant over the cross-section and one would expect to find similar density profiles with different probes, up to a constant factor of order unity. This is in fact observed with the two different probe radii.

The assumption of a perfectly absorbing probe surface can be violated when a significant fraction of impinging electrons are reflected or give rise to secondary electron emission. For Maxwellian electrons, this results in floating potential values closer to the plasma potential, while the evaluation of T_e remains unaffected [13, 85]. The reflection of non-neutralized ions and ion-induced electron emission could also occur. This would alter the apparent ion current and add, besides the uncertainty in A_{eff}^0 , additional uncertainty to the determination of density.

Departures from a Maxwellian electron distribution have been observed with an electrostatic energy-analyzer in TORPEX. A suprathermal population representing a few percent of the total density was measured around the upper-hybrid resonance [92]. Such a suprathermal population can strongly affect the determination of the bulk electron temperature in plasmas where the I-V curve can only be fitted up to the floating potential [93]. Fig. 3.3.1 shows the fitted I-V curve for a measurement in the mode region. The inset shows the obtained electron temperature for different values of the cutoff voltage, $V_{fl}^0 + \varpi \cdot T_e^0/e$, used for the fit. This shows that T_e is almost constant for $0 \leq \varpi \leq 2.5$ and increases for higher values, where the electron current starts to saturate. This suggests that the evaluated temperature is not strongly influenced by a suprathermal population and that fitting the I-V curves over voltage ranges well above the floating potential is justified in TORPEX.

The application of a d.c. sheath theory requires that fluctuations are slow enough such that the ions have time to respond. The frequency limit for this is usually assumed to be of the order of the ion plasma frequency [86]. In TORPEX, the ion plasma frequency lies in the range $\approx 10 - 20$ MHz, which is well above the observed fluctuation spectra. Modifications to Eqs. (3.1.1) and (3.1.2) can still arise due to

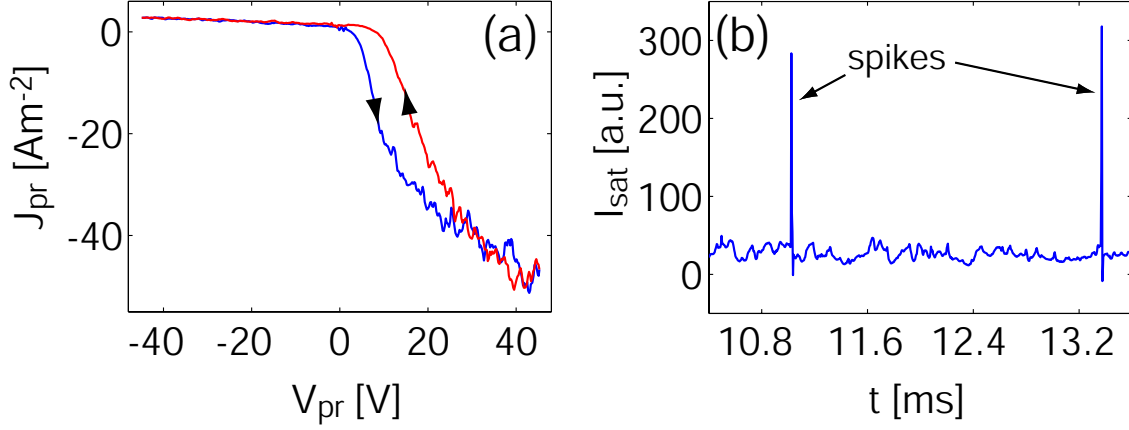


Figure 3.3.2: (a): Strong hysteresis observed on a dirty probe. The average I-V curve during the upward sweep phase (blue curve) differs strongly from the one measured during the downward sweep phase (red curve). (b): I_{sat} time trace with two spikes.

sheath capacitance or ion-polarization currents [87]. However, these effects should not contribute to the time averaged I-V curves.

The presence of parallel and cross-field flows can also give corrections to the ion current [94–96]. We have typically parallel and cross-field flows $\lesssim 40\%$ and $\lesssim 5\%$ of c_s over most of the cross section in hydrogen plasmas [97]. From the cited references, we expect small corrections to the ion current for such values of the flows. One should note, however, that these works do not quite apply to our parameter regime.

A problem that can arise from the averaging of I-V curves is that, due to the nonlinear nature, a time averaged I-V curve is not identical to the I-V curve of the time averaged plasma parameters. This adds additional uncertainty to this kind of measurements [86, 98]. The good agreement in Sec. 3.5.5 between time averaged profiles obtained with swept probes and with the triple probe method indicate however that this is not an important issue here.

A practical issue that can occur is that of impurity layers on the probe surface. It is well known that dirty probe surfaces can distort the I-V curve and give false plasma parameters [85, 99]. A sign of dirty probes can be a hysteresis, i.e., a different I-V curve for the upwards and downwards sweeps [100, 101]. Indeed, hysteresis has been observed on some probes on TORPEX. An example is shown in Fig. 3.3.2 (a). Cleaning the probe with alcohol, possibly baking it in an oven prior to installation and then operating it in ion saturation current during plasma discharges of several minutes to sputter clean it usually allows to avoid this hysteresis. In certain plasmas, impurity layers can reform quickly. Therefore, tests have been performed in TORPEX where, instead of the usual continuous sawtooth sweep, the probe was held on a strong negative potential (-40 V or -80 V) during 20 ms prior to each sweep cycle. This procedure has not shown any significant change in the I-V curve. Another issue is that of large positive spikes that are sometimes observed in ion saturation current signals, see Fig. 3.3.2 (b) for an example. The origin of these

spikes is not known. It is possible that they are caused by arcing, i.e., that electrons are emitted from the probe surface due to large local electric fields. Usually, for clean probes and not too low negative bias voltages, these spikes can be avoided.

3.4 Conditional average sampling techniques

Conditional average sampling (CAS) is a widely used method to investigate coherent structures in turbulent plasmas and neutral fluids [102–104]. This technique allows evaluating the average spatio-temporal evolution of these structures with high spatial resolution. It is described in the following for probe measurements, although it can be applied to any kind of signals. CAS requires only two probes, one reference probe and one that is moved during the experiment. This makes it very interesting for plasma physics, where obtaining high resolution measurements can be very challenging.

Let us assume a fluctuating equilibrium, i.e., a turbulent state with stationary mean values. We consider a quantity $f(\mathbf{x}, t)$, ion saturation current for instance, that consists of a randomly fluctuating part together with intermittently occurring coherent structures. The average spatio-temporal evolution of these structures, denoted by $\langle f \rangle_{ca}$, can be found using CAS. A reference signal f_{ref} , e.g. from a probe at a fixed position, is used to detect the occurrence of the structures. This is done by defining an appropriate trigger condition. Then, the average dynamics of the detected events at a position \mathbf{x}_j in the plasma is obtained as follows

$$\langle f \rangle_{ca}(\mathbf{x}_j, \tau) \approx \frac{1}{N} \sum_{i=1}^N f(\mathbf{x}_j, t_i + \tau), \quad (3.4.1)$$

where t_i is a time when the trigger condition on f_{ref} is satisfied and N the total number of triggered events. This procedure is illustrated graphically in Fig. 3.4.1 (b). Here, f_{ref} is an I_{sat} time trace in the blob region. This signal is sampled for local maxima exceeding a threshold value. The second signal stems from a probe at a position \mathbf{x}_j approximately on the same field line but toroidally displaced. Time intervals around the detected events are selected and averaging is performed. This yields the conditional average at that position. Using probes at different positions or moving the second probe in between reproducible discharges then provides $\langle f \rangle_{ca}(\mathbf{x}, \tau)$ with in principle arbitrarily high spatial resolution. This standard conditional average sampling technique is limited to observables that are directly measured. For LP measurements, these are usually I_{sat} and V_{fl} . A generalization of CAS, dubbed BOX-CAS [105], allows evaluating also conditionally averaged dynamics of density, electron temperature and plasma potential from slowly swept LPs, that otherwise provide only the time averaged quantities. While the reference signal can still be the same as for CAS, a voltage sweep is applied to the movable probe in the BOX-CAS method and both probe potential V_{pr} and current I_{pr} are acquired. For a given time lag τ with respect to the detected events. this gives the

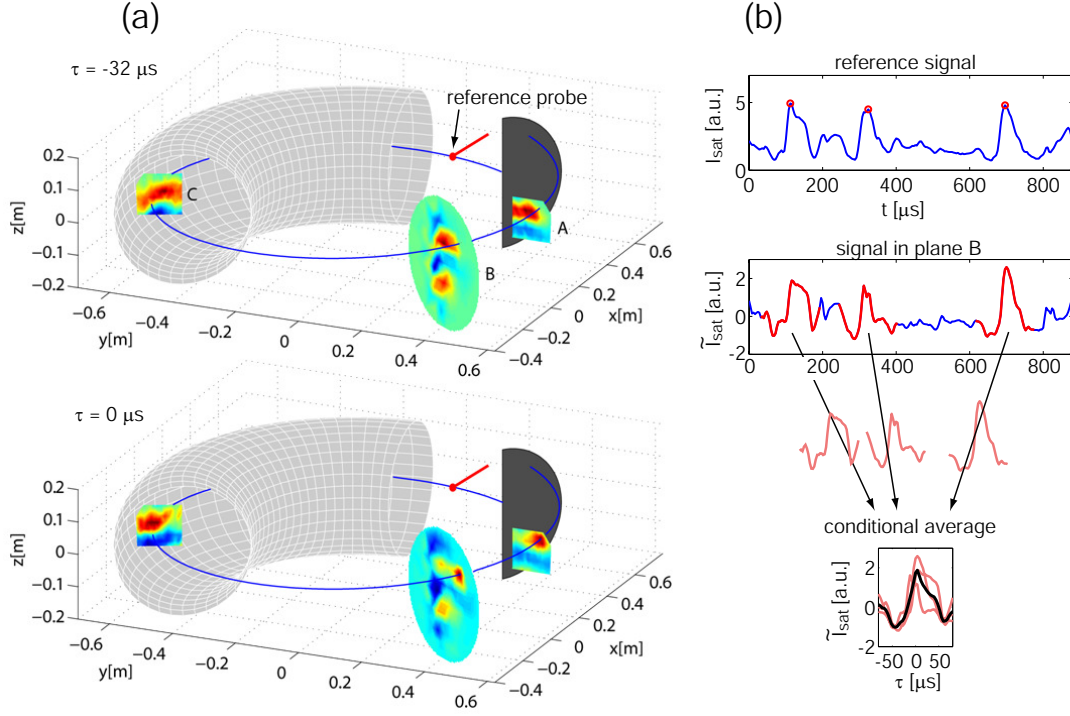


Figure 3.4.1: (a): 3D dynamics of a plasma blob, reconstructed in different toroidal planes using CAS and BOX-CAS. Profiles are shown for $\tau = -32 \mu\text{s}$ and $\tau = 0 \mu\text{s}$ with respect to the time blobs are detected on the reference probe. Planes A, B, and C show $\langle \tilde{n} \rangle_{ca}$, $\langle \tilde{I}_{sat} \rangle_{ca}$, and $\langle \tilde{V}_{fl} \rangle_{ca}$, where \sim denotes fluctuations around mean values. In these experiments, a limiter was installed in TORPEX, as indicated in grey. (b): Illustration of CAS. Local maxima, interpreted to be due to a blob passing in front of the probe, are selected in the reference signal. Time intervals synchronous with the detected events are selected in the reference signal and an averaging is performed.

pairs $(V_{pr}^i(\tau), I_{pr}^i(\tau)), i = 1, \dots, N$. For a sufficiently large number of detected events N , these values give conditionally averaged I-V curves that can be fitted to obtain the conditionally averaged dynamics of n , T_e , and V_{pl} . This BOX-CAS technique is successfully benchmarked with measurements from a triple probe in [62], see Sec. 3.5.5, and the routines for BOX-CAS are included in my LP analysis package. It should be mentioned that BOX-CAS requires considerably more detected events and therefore longer time traces for good convergence (usually several seconds) than standard CAS.

Fig. 3.4.1 (a) illustrates how CAS and BOX-CAS can be applied to reconstruct the 3D dynamics of a plasma blob. Blobs are detected on a fixed reference probe. Data in plane B is obtained from HEXTIP operated in I_{sat} . CAS is applied simultaneously to all 86 HEXTIP signals. To reconstruct conditionally averaged density fluctuations in plane A, BOX-CAS is applied to SLP. SLP is an array of 8 vertically aligned LPs and it was moved radially between reproducible discharges to reconstruct the 2D profile. Floating potential fluctuations in plane C are also obtained with SLP in an experimental session where SLP was installed on another port.

3.5 The triple probe on TORPEX

As we have seen earlier in this chapter, measurements with slowly swept Langmuir probes are usually limited to time averaged values of plasma density, electron temperature and plasma potential. An exception is the BOX-CAS technique [105] presented above, which provides time dependent, conditionally averaged measurements of these parameters. Nevertheless, direct time traces can not be obtained in this way. Although rapidly swept LPs can be used [87, 88, 106], probably the most common method to obtain local, time-dependent measurements of n , T_e , and V_{pl} is the triple probe technique [67]. In its simplest configuration, it consists of three nearby Langmuir probe tips, which instantaneously measure three points of the I-V characteristics. This allows a direct evaluation of the above quantities, provided that all probes see the same plasma conditions. To come close to this ideal situation, the probe tips are usually aligned perpendicular to background plasma gradients. In order to avoid shadowing effects between tips, they need to be sufficiently spaced and, in the presence of a magnetic field, positioned on separate field lines. However, other effects such as phase delay errors, ion-sheath expansion and stray capacitance can affect the measurements [67, 84, 107].

Expecting rather straight-forward measurements of fluctuation-induced particle transport and blob temperature with the triple probe technique, I went through a phase of trial and error, encountering essentially all of the above mentioned difficulties. After several initial probe designs, this effort was completed successfully with the construction of FRIPLE [62] during a semester project in spring 2010 [108]. The reminder of this chapter discusses the basic principle of the triple probe and sources of errors. An electric circuitry is presented that allows reducing significantly stray capacitance. Then, the design of FRIPLE, cross checks with swept LPs and measurements of fluctuations and particle transport are presented.

3.5.1 Triple probe principle

The standard triple probe consists of three probe tips as shows in the scheme in Fig. 3.5.1 (a). Probe 1 measures the floating potential V_{fl} while the other two tips form a double probe circuit [109]. A constant potential difference ΔV is applied between the two tips and the potentials V^+ and V^- adjust to satisfy current continuity in the double probe circuit. In an ideal situation and for sufficiently large values of ΔV ($\Delta V \gg T_e/e$), the time evolution of electron temperature T_e , density n and plasma potential V_{pl} can be obtained from

$$T_e = \frac{e(V^+ - V_{fl})}{\ln(2)}, \quad n = \frac{2I}{ec_s A}, \quad V_{pl} = V_{fl} + \mu T_e/e, \quad (3.5.1)$$

where A is the surface of the probe, I the current flowing in the double probe circuit, and V_{fl} and V^+ the potentials of probe tip 1 and 3 in in Fig. 3.5.1 (a). However, even if the three probe tips are aligned perpendicularly to the background plasma

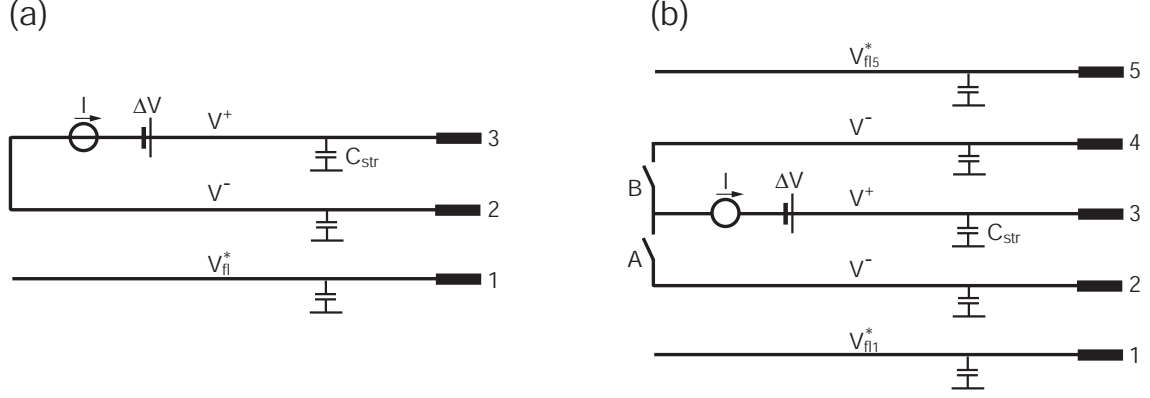


Figure 3.5.1: (a): Standard, three tip scheme of the triple probe [67]. Probe tips 1 to 3 are indicated together with the quantities they measure. The capacitances C_{str} indicate undesired stray capacitances in the circuit. (b): Modified five-tip scheme [107] used for FRIPLE. The switches A and B allow changing between the standard triple probe method and the modified five-tip method.

gradients and they measure the same time-averaged parameters, the instantaneous parameters can vary from tip to tip. A wave propagating along the direction of the tip alignment for example leads to phase delay errors and erroneous measurements. This problem can be addressed by the modified triple probe method [107], which uses a symmetric arrangement with five probe tips. This corresponds to the configuration shown in Fig. 3.5.1(b) when the two switches A and B are closed. The two additional tips (4 and 5) provide conjugate phase information to reduce phase delay errors in the standard three tip configuration to second order in kd , with k the perpendicular wave number and d the tip spacing [107].

Tip 1 and 5 measure the floating potential. These measurements are combined to evaluate the floating potential at the center (tip 3). The two signals are acquired independently. This allows us to evaluate gradients in the floating potential, to estimate the vertical wave number $k_z(f)$ as a function of frequency from two-point correlation [65] and the amplitude reduction of floating potential fluctuations due to the averaging of the two signals and the error caused by this (see the particle transport analysis in Sec. 3.5.6).

Tips 2-4 form the double probe circuit. Besides V^+ and $V^- = V^+ - \Delta V$, the current I flowing through the circuit is also measured. Assuming that phase delay errors have been reduced sufficiently and that all tips are identical, Eqs. (3.5.1) then take the following form [107]:

$$T_e = \frac{e(V^+ - V_{fl})}{\ln(3)}, \quad n = \frac{I}{ec_s A}, \quad V_{pl} = V_{fl} + \mu T_e / e. \quad (3.5.2)$$

In the following, the relations (3.5.2) are derived including two effects that can lead to important corrections. One is due to stray capacitance to ground in the circuit, for instance capacitance in the coaxial cables connecting the pins. The other is due to an imperfect saturation of the ion current.

We begin with the measurement of the floating potential. Ideally, no current is drawn from the plasma. However, a finite leakage current exists due to stray capacitance as indicated in Fig. 3.5.1. The potential of the probe, V_{fl}^* , can thus deviate from the floating potential V_{fl} . Using expression (3.1.1), the current collected by the floating probe is given by

$$I = I_{sat}^0 \left[1 - \alpha(V_{fl}^* - V_{fl}) - \exp\left(\frac{V_{fl}^* - V_{fl}}{T_e/e}\right) \right] + C_{sh}(\dot{V}_{pl} - \dot{V}_{fl}^*). \quad (3.5.3)$$

The parameter α accounts for the imperfect saturation of the ion current and I_{sat}^0 is the ion current extrapolated to the floating potential and given in Eq. (3.1.2). Here, a term due to the capacitance C_{sh} of the sheath has been added. This can be estimated as $C_{sh} \approx \epsilon_0 A / \lambda_D$ and is usually very small [87]. For $T_e = 5$ eV, $n = 10^{16} \text{ m}^{-3}$ and a probe surface A of 10^{-5} m^2 for example, one finds that $C_{sh} \approx 0.5 \text{ pF}$. A contribution of ion-polarization currents to Eq. (3.5.3) could also occur [87]. For the present case where the scale length of electric fields around a probe tip are comparable or smaller than the ion Larmor radius, the estimate of such a contribution possibly requires kinetic studies and is not considered here.

The current in Eq. (3.5.3) equals the current flowing through the stray capacitance

$$I = C_{str} \dot{V}_{fl}^*. \quad (3.5.4)$$

We assume $C_{str} \gg C_{sh}$. Therefore, when we equate Eq. (3.5.3) and (3.5.4), we neglect the sheath capacitance term in Eqs. (3.5.3) with respect to the term in Eq. (3.5.4). If we further linearise the exponential term in (3.5.3) around V_{fl} , neglect α with respect to e/T_e and arrange terms, we find

$$V_{fl} = V_{fl}^* + \frac{T_e}{e I_{sat}^0} C_{str} \dot{V}_{fl}^*. \quad (3.5.5)$$

One can define $R_{sh} = T_e / e I_{sat}^0$, the sheath resistance for a probe potential close to the floating potential. In cases where fluctuations of R_{sh} can be neglected, Eq. (3.5.5) is equivalent to an RC-circuit. In this case, the spectral components of V_{fl} and V_{fl}^* satisfy

$$\hat{V}_{fl}^*(f) = \frac{\hat{V}_{fl}(f)}{1 + 2\pi i f R_{sh} C_{str}}. \quad (3.5.6)$$

One can see that $\hat{V}_{fl}^*(f)$ is reduced in amplitude and delayed with respect to $\hat{V}_{fl}(f)$. Important phase errors occur already for fluctuations well below the cutoff frequency $f_c = 1/(2\pi R_{sh} C_{str})$. As an example, we assume typical parameters for TORPEX, $T_e = 5$ eV, $n = 10^{16} \text{ m}^{-3}$ and $A = 10^{-5} \text{ m}^2$. In this case, using Eq. (3.1.2) to express

I_{sat}^0 , we find that $R_{sh} \approx 28 \text{ k}\Omega$. If we assume $C_{str} = 300 \text{ pF}$, typical for 1.5 m of a heat and vacuum resistant coaxial cable, we find $f_c \approx 19 \text{ kHz}$. For fluctuations at 4 kHz, the phase error would already attain 0.2 rad. Further, since $R_{sh} \propto \sqrt{T_e}/n$, the sheath resistance can be significantly higher for lower values of plasma density. In a similar way as for the floating potential measurement, we apply current continuity to the double probe circuit (pins 2-4 in Fig. 3.5.1 (b)), neglect again sheath capacitance and assume $2 \cdot \exp(-e\Delta V/T_e) \ll 1$. We find

$$T_e = \frac{e(V^+ - V_{fl})}{\ln(3 + \delta_0 + \delta_1)}, \quad (3.5.7)$$

where we have defined δ_0 and δ_1 by

$$\delta_0 = \bar{\alpha} [2\Delta V - 3(V^+ - V_{fl})] \quad (3.5.8)$$

$$\delta_1 = \tilde{\alpha} [2\Delta V - 3(V^+ - V_{fl})] - \frac{3C_{str}}{I_{sat}^0} \dot{V}^+. \quad (3.5.9)$$

The overbar indicates time averages and the tilde fluctuating quantities such that $\tilde{\alpha} = \alpha - \bar{\alpha}$. Combining Eqs. (3.5.5) and (3.5.7) and expanding the logarithm, we find

$$T_e = \frac{e \left(V^+ - V_{fl}^* - \frac{T_e}{eI_{sat}^0} C_{str} \dot{V}_{fl}^* \right)}{\ln(3 + \delta_0)} \cdot \left[1 - \frac{\delta_1}{(3 + \delta_0) \ln(3 + \delta_0)} \right]. \quad (3.5.10)$$

With the same approximations, we finally find the expression for the current flowing in the circuit:

$$I = 2I_{sat}^0 [1 + \alpha\Delta V - \alpha(V^+ - V_{fl})] - 2C_{str} \dot{V}^+. \quad (3.5.11)$$

The density is then given by

$$n = \frac{I + 2C_{str} \dot{V}^+}{ec_s A_{eff}^0 (1 + \epsilon_0 + \epsilon_1)} \quad (3.5.12)$$

with

$$\epsilon_0 = \bar{\alpha} [\Delta V - (V^+ - V_{fl})] \quad (3.5.13)$$

$$\epsilon_1 = \tilde{\alpha} [\Delta V - (V^+ - V_{fl})] \quad (3.5.14)$$

and A_{eff}^0 the ion sheath surface at floating potential (see discussion in Sec. (3.3)). Eqs. (3.5.10) and (3.5.12) are the expressions of the modified triple probe method for T_e and n with effects of stray capacitance and ion sheath expansion included. Eq. (3.5.5) gives further the expression for V_{fl} needed for the evaluation of the plasma potential through $V_{pl} = V_{fl} + \mu T_e/e$. In the limit of C_{str} and $\alpha \rightarrow 0$, these expressions retrieve those in Eq. (3.5.2). When using FRIPLE, we take into account corrections due to $\bar{\alpha}$ and neglect terms proportional to $\tilde{\alpha}$, as discussed in Sec. 3.5.5. As far as stray capacitance effects are concerned, one might want to correct numerically these

effects in Eqs. (3.5.5), (3.5.10), and (3.5.12). However, these depend on plasma parameters and involve nonlinear terms and time derivatives. It seems therefore better to keep C_{str} sufficiently low. Often, coaxial cables of 1 m or more are required between probe and electronics. In the next section, it is shown how the related stray capacitance can effectively be reduced.

3.5.2 Novel guarding circuit to reduce stray capacitance

In this section, a novel guarding circuit that allows a strong reduction of the stray capacitance is presented. An idealized scheme of this circuit is shown in Fig. 3.5.2. The basic idea is to drive the shield of the coaxial cable to follow potential fluctuations in the inner conductor. This is done by the unity gain voltage follower in Fig. 3.5.2. It allows reducing the current needed to charge the capacitance C_{str} and thus reduces the effective capacitance in the circuit, while still keeping the shielding properties of the coaxial cable with respect to external noise. Relatively large d.c. potential values can arise in the circuit (e.g. for tips on V^-). These can exceed the voltage limits of the voltage follower in the circuit. Therefore, the system is a.c. coupled through the potential divider including C_1 , C_2 and R . This circuit thus reduces stray currents at relatively high frequencies where they are important. At low frequencies, stray currents are even increased due to the additional capacitance C_1 . Although the new circuit is not purely capacitive anymore, we still represent it by an effective, frequency dependent capacitance $C_{eff}(f)$. We find

$$C_{eff}(f) = (C_{str} + C_1) \frac{1 + 2\pi i f R C_2}{1 + 2\pi i f R (C_1 + C_2)}, \quad (3.5.15)$$

such that the leakage currents I_{leak} that were simply given by terms of the form $C_{str} \dot{V}$ in the previous section now become

$$I_{leak} = FT^{-1} \left[2\pi i f C_{eff}(f) \hat{V}(f) \right]. \quad (3.5.16)$$

Here FT^{-1} is the inverse Fourier transform. The module $|C_{eff}|$ is a decreasing function of f , with the following properties

$$C_{eff}(f \rightarrow 0) = C_{str} + C_1, \quad (3.5.17)$$

$$C_{eff}(f \rightarrow \infty) = (C_{str} + C_1) \frac{C_2}{C_1 + C_2}, \quad (3.5.18)$$

$$\frac{|C_{eff}(f)|}{C_{str}} < \frac{1}{2} \quad \text{for } f > f_{1/2} \approx \frac{C_1 + C_{str}}{\pi R C_1 C_{str}}. \quad (3.5.19)$$

For the estimate of $f_{1/2}$, we have assumed $C_2 \ll C_{str}$, C_1 . The reduction of $|C_{eff}(f)|$ with respect to C_{str} becomes thus effective only for frequencies $\gtrsim f_{1/2}$. $f_{1/2}$ should

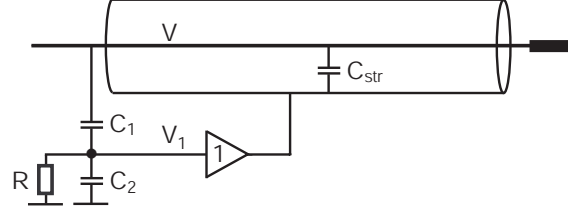


Figure 3.5.2: Guarding circuit to reduce the capacitance between the inner conductor and the shield of a coaxial cable. "1" represents a unity gain voltage follower.

therefore be smaller than the frequencies that give rise to important stray currents. As $f_{1/2} \propto 1/R$ (Eq. (3.5.19)), this can be controlled by the value of the resistance R in the circuit. However, the value of R should not be chosen too large, otherwise the d.c. decoupling of the circuit becomes less effective. As the plasma is turned on, the d.c. part of the potential V of the inner conductor can change strongly. The potential V_1 of the shield follows this change and can thus exceed the potential limits of the amplifier. The d.c. part of V_1 relaxes to 0 at a characteristic time of $\tau = R(C_1 + C_2) \approx RC_1$. This characteristic time should be kept short compared to the length of the plasma discharge.

3.5.3 Triple probe and guarding circuitry construction

Fig. 3.5.3 shows a photograph and a scheme of the probe head of FRIPLE. The five tips are made of stainless steel wires of 0.7 mm diameter. The wires protrude by 6 mm from the ceramic tubes of 6 cm in length that separate the tips from the Boron Nitride (BN) casing. A replaceable piece made out of Vespel® allows for a good alignment of the tips as well as for a variable spacing between adjacent tips in the range of 2.5 – 6 mm. Until now, we have only used a tip spacing of 4 mm. For $T_e = 5$ eV and $n = 10^{16} \text{ m}^{-3}$, this corresponds to a gap between tips of ≈ 20 Debye lengths.

The probe is installed on a 1D movable system that allows moving the probe over the whole radial range of the TORPEX vacuum vessel. The probe tips are aligned perpendicular to the magnetic field and in the vertical direction. At least for the ideal interchange regime in TORPEX [73, 78], where plasma profiles are slab-like, this corresponds to the direction perpendicular to the gradients in the plasma profiles.

Inside the BN casing, the stainless steel wires are connected to coaxial cables that transport the signals to the electronics right behind the vacuum-feedthrough. Coaxial cables with an outer diameter of 1.4 mm and a low capacitance of 50 pFm^{-1} are used. They have a length of approximately 1.2 m resulting in a stray capacitance to ground for each individual channel of $\approx 70 \text{ pF}$. To further reduce this capacitance, the circuit described in Sec. 3.5.2 is applied to each channel. The values $C_1 = 1200 \text{ pF}$, $C_2 = 8 \text{ pF}$ and $R = 10 \text{ M}\Omega$ are chosen. For stability reasons, a resistance of $15 \text{ k}\Omega$ is added in series to C_1 , with very little effect on $|C_{eff}|$ for

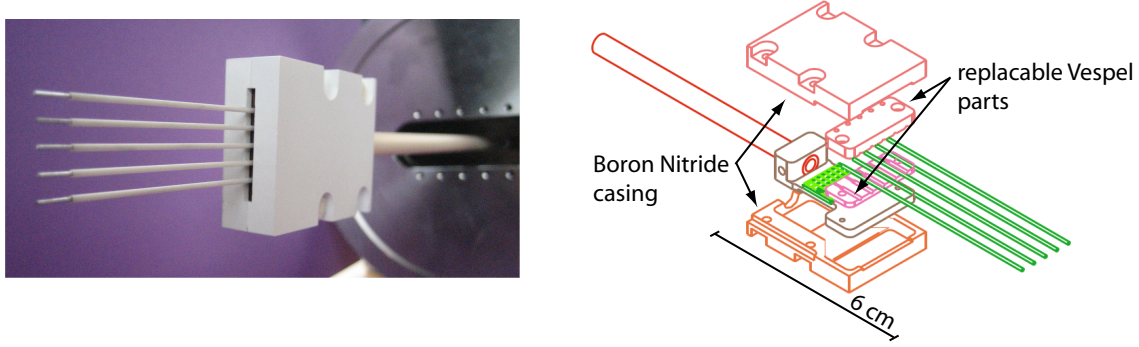


Figure 3.5.3: Top: Photograph of the probe head showing the five probe tips, the BN casing, and (in the background) a stainless steel flange. Bottom: Scheme showing the interior of the probe. A central part made out of Vespel® is holding the probe head. Replaceable Vespel® parts allow controlling alignment and spacing of the five probe tips. The interior is protected by a BN casing.

the frequency range of interest. This allows reducing the stray capacitance of each channel to approximately 20 pF, including compensated potential dividers for the potential measurements. Finally, the current signal in the double probe circuit is measured over a 10 Ω resistance and numerically corrected for instrumental transfer function.

3.5.4 Consistency tests

After installation, the probe tips have been biased to -40 V with respect to device ground during plasma phases of ~ 1 min to sputter clean them. This has allowed us to remove hysteresis effects observed on the I-V characteristics due to surface impurity contamination. In the following, a series of tests and detailed measurements with the FRIPLE probe are presented. The target is a hydrogen plasma with 300 W of injected microwave power and $N \approx 2$. The plasma is dominated by an ideal interchange wave with a frequency of $\approx 3 - 4$ kHz. FRIPLE is operated both in sweep mode and in triple probe set-up. Except for the tests in Fig. 3.5.8, it is always the 5-tip triple probe scheme that is used.

A necessary condition for reliable measurements with the triple probe is that all probe tips show similar plasma response. In particular, they should provide similar measurements of time averaged plasma parameters when operated in swept mode. To test this, all five probe tips were operated in swept mode and the radial profiles of n , T_e , V_{fl} , and the parameter α obtained this way are shown in Fig. 3.5.4. Tips 1 and 5 measure densities about $\approx 15\%$ higher than the tips in between. This could be due to a slight overlap of the probe sheaths and could be further investigated in the future by using a different probe spacing. Some differences are also observed in the floating potential measurements. Nevertheless, the profiles of the different probe tips show rather good agreement.

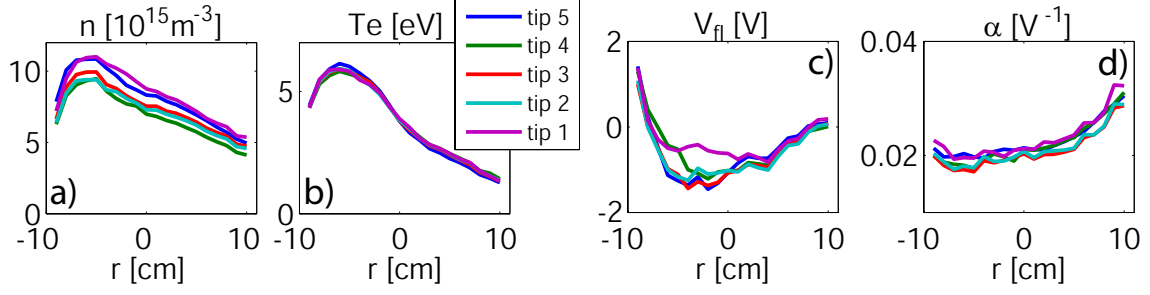


Figure 3.5.4: Radial profiles of time average a) density, b) electron temperature, c) floating potential, and d) the parameter α for the five probe tips obtained by slowly sweeping the probe voltages.

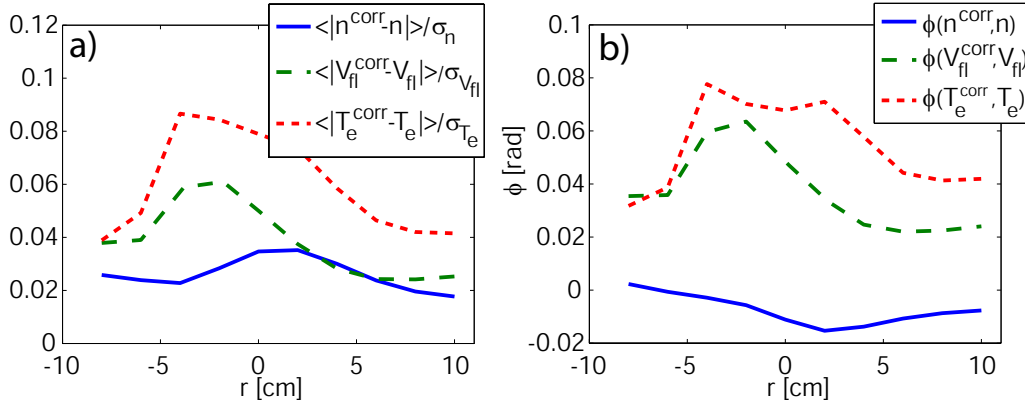


Figure 3.5.5: Study of the effects of the residual stray capacitances on the measurements. n^{corr} , T_e^{corr} , and V_{fl}^{corr} are obtained from Eqs. (3.5.5), (3.5.10), and (3.5.12) including realistic stray capacitances while n , T_e , and V_{fl} are obtained with $C_{str} = 0$. In a), we compare the average difference between corrected and non-corrected signals with the signals standard deviations. In b), we deduce the mutual phase shifts, evaluated by weighting the frequency dependent phase shift with the power spectral density of the non-corrected signals.

Next, we have tested that stray capacitance has been reduced sufficiently for the present plasma configuration to have only negligible effects on the measurements. The probe was operated in the (five tip) triple probe configuration and we have determined the parameters T_e , n , and V_{fl} from Eqs. (3.5.5), (3.5.10), and (3.5.12), with and without realistic estimates of the C_{str} -terms. The time traces of the evaluated quantities with and without these corrections, labeled e.g. as n^{corr} and n , look very similar. To quantify this for the whole radial range, we plot in Fig. 3.5.5 the average difference between corrected and non-corrected quantities, normalized to the standard deviation of the signals, as well as the mutual phase differences. We find indeed that corrections due to stray capacitances are weak. The average absolute difference is smaller than 10 % of the signals standard deviation and phase errors are below 0.08 rad. These tests should be repeated for different plasmas, especially for plasmas with higher fluctuation frequencies or lower densities.

In the next two sections, we present cross-checks of triple probe measurements with other LP-techniques and measurements achieved only with the new probe.

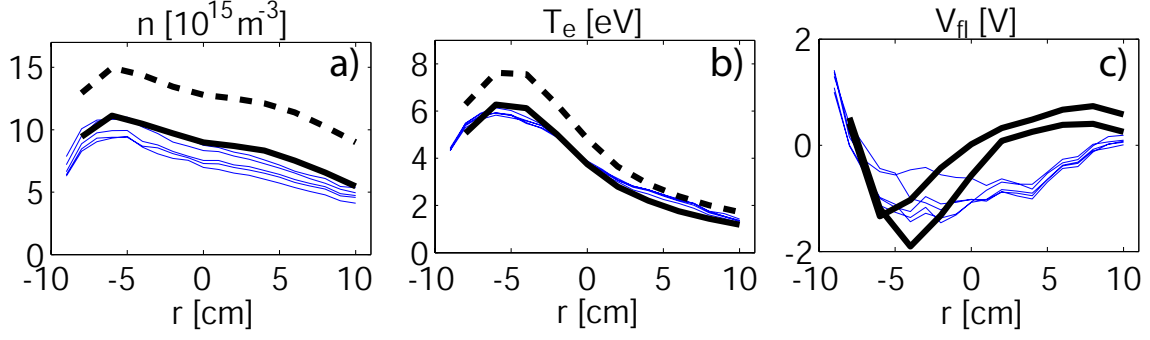


Figure 3.5.6: Time-averaged profiles of a) density, b) electron temperature, and c) floating potential. Thin blue lines show the profiles obtained from sweeping the probes. Thick dashed lines in a) and b) show the profiles obtained with the triple probe assuming $\bar{\alpha} = 0$, solid lines the ones including $\bar{\alpha}$ -corrections. The two thick lines in c) are the time-averages for the outer two probe tips (tips 1 and 5) that are operated in floating potential.

3.5.5 Cross-checks with other LP-based techniques

In this section, measurements obtained with the triple probe are compared with results from other LP-based techniques. We start with time-averaged profiles. In Fig. 3.5.6, the time-averages of n , T_e , and V_{fl} obtained with the triple probe technique as well as from FRIPLE in sweep mode are plotted. We neglect C_{str} and $\tilde{\alpha}$ in Eqs. (3.5.5), (3.5.10), and (3.5.12). If we further set $\bar{\alpha} = 0$, we obtain the thick dashed profiles in Fig. 3.5.6, which deviate significantly from the profiles obtained from sweeping the five probe tips (thin lines). Including the values for $\bar{\alpha}$ of Fig. 3.5.4 (d), however, leads to a satisfactory agreement for n and T_e (thick solid profiles). There are some differences in the profiles of V_{fl} for the two techniques, Fig. 3.5.6 (c). These are not entirely understood. We note, however, that these differences are relatively small and the two techniques result in very similar profiles of plasma potential $V_{pl} = V_{fl} + \mu T_e / e$.

In a next step, we want to check the reliability of time dependent measurements obtained with the triple probe. We do not have another technique at hand that provides direct time dependent measurements of n , T_e , and V_{fl} . We can, however, apply the modified conditional sampling or BOX-CAS technique described in Sec. 3.4 and compare the results to standard CAS applied to triple probe measurements. We have done this, choosing a reference probe in mode region, toroidally separated by $\approx 35^\circ$ from FRIPLE. The I_{sat} probe signal is conditionally sampled to detect the passage of positive wave crests. FRIPLE was positioned in the center of the mode region at $r = -1$ cm to evaluate the conditional average of the mode dynamics. First, a voltage sweep was applied to the five probe tips to perform the BOX-CAS technique. The result for the central tip for n , T_e , V_{fl} , and α is shown in Fig. 3.5.7, blue solid lines. We see that the amplitude of the fluctuations decreases as we move away from $\tau = 0$, which is a common feature of conditional sampling. Then, we repeated the measurements with the same reference signal, using FRIPLE in the

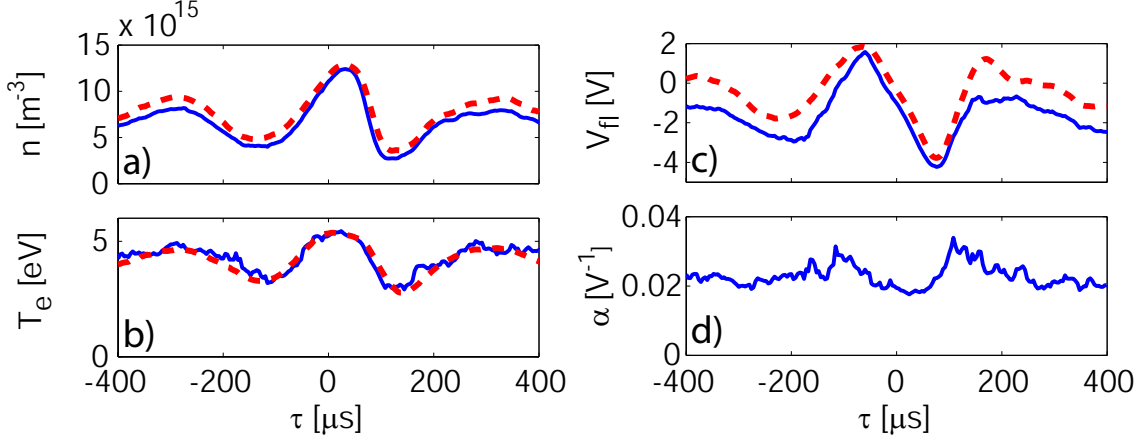


Figure 3.5.7: Conditionally averaged time traces of a) density, b) electron temperature c) floating potential, and d) parameter α in the mode region at $r = -1$ cm. Blue solid lines are obtained with the BOX-CAS method [105]. Red dashed lines are obtained with standard conditional sampling applied to triple probe data.

triple probe scheme. Applying standard conditional sampling, we obtain the red dashed curves in Fig. 3.5.7. We find very satisfactory agreement between the two techniques in terms of fluctuation amplitudes, phase shifts and absolute values. An offset in the floating potential is observed, similarly as in the time-average profiles in Fig. 3.5.6 (c). A similarly good agreement is found at the other radial locations where this analysis was performed, i.e. for FRIPLE at $r = -6$ cm, $r = -3$ cm, and $r = 3$ cm.

In Fig. 3.5.7 (d), we also see the conditionally sampled time trace of α . α fluctuates and has a phase shift of $\approx \pi$ with respect to density and temperature. To include α -fluctuations in the analysis of triple probe data (see Eqs. (3.5.10) and (3.5.12)), the dependence of α on plasma parameters would need to be determined. This is beyond the scope of this study. Another possibility is to use different values of ΔV for the triple probe and thus change the influence of the α -terms in Eqs. (3.5.10) and (3.5.12). We have done this for $\Delta V = 24$, 36, and 48 V, but no significant differences were found as long as corrections due to $\bar{\alpha}$ were included. We therefore neglect the $\tilde{\alpha}$ -terms in Eqs. (3.5.10) and (3.5.12).

Finally, to evaluate the effect of phase delay errors, we have repeated the conditional sampling analysis for the configurations of the standard, 3-tip triple probe scheme that are possible by opening or closing the switches A and B (see Fig. 3.5.1). This allows for the following combinations: (V_{fl}, V^+, V^-) , (V^+, V^-, V_{fl}) , (V^-, V^+, V_{fl}) , and (V_{fl}, V^-, V^+) . The results of this for T_e are shown in Fig. 3.5.8 and compared with the result from the swept probe (thick solid blue line). We observe similar time-average values, but considerable differences in both phase and amplitude of fluctuations in all four cases. This clearly motivates the use of the modified, five-tip method.

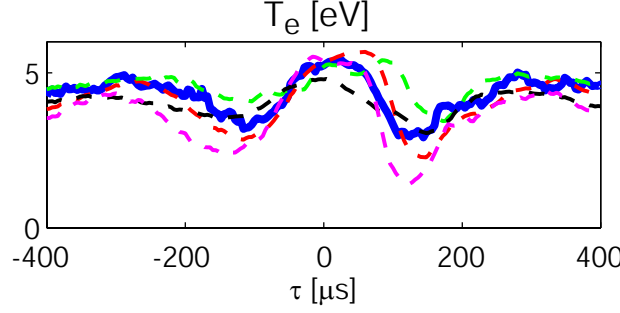


Figure 3.5.8: Comparison of the conditionally averaged time traces of T_e obtained from the swept probe (thick blue line) with results from the standard, three-tip triple probe. Different colors correspond to the following tip order (from bottom to top): red: (V_{fl}, V^+, V^-) , green: (V^+, V^-, V_{fl}) , black: (V^-, V^+, V_{fl}) , magenta: (V_{fl}, V^-, V^+) .

3.5.6 Measurements of fluctuations and transport with the triple probe

After the successful cross-check of the triple probe measurements with other LP techniques, we present now the main results obtained with this probe in the plasma under investigation. The main properties of the fluctuations of n , I_{sat} , T_e , V_{fl} , and V_{pl} are summarized in Fig. 3.5.9. In (a), we show raw-data time traces at a radial position of $r = -2$ cm for approximately three periods of the interchange wave. In (b), we compare the relative fluctuation levels for the positive-definite quantities I_{sat} , n , and T_e . The fluctuation level is defined as the signal standard deviation over its mean value. We find the commonly observed large fluctuation levels, with $\delta T_e/T_e$ roughly two thirds of $\delta n/n$. In (c), we compare fluctuations in T_e , V_{fl} , and V_{pl} by plotting the signal standard deviations. We find that $\sigma_{V_{fl}} \approx 3 \cdot \sigma_{T_e}/e$. This shows clearly that temperature fluctuations should be taken into account when evaluating V_{pl} from $V_{fl} + \mu T_e/e$. In Fig. 3.5.9 (d), we plot the power spectral density of \tilde{n} . The main instability at a frequency of 3.4 ± 0.5 kHz and its radial extension are apparent. A much weaker mode at a frequency of 15.5 ± 1.5 kHz is also present. It can be identified as the first harmonic of the dominant mode.

Focusing on fluctuations related with the dominant instability, we show in Fig. 3.5.9 (e) radial profiles of the phase-shift between T_e , V_{fl} , and V_{pl} with respect to density, averaged over the frequency range 3.4 ± 1 kHz. We find that the phase shift between temperature and density is close to zero for $r \geq -2$ cm. It increases for smaller values of r and is close to π at $r = -6$ cm. This feature is consistent with the conditionally averaged time traces for $r = -3$ cm and $r = -6$ cm mentioned in the previous section. We further observe a phase shift between plasma potential and density that is significantly smaller than that between floating potential and density. The sign of the phase shift between V_{pl} and n is consistent with that expected for an interchange wave. However, as noted in [105], the phase shift is in the range $0.5 - 0.9$ rad ($30^\circ - 50^\circ$) in the mode region, clearly below the 90° phase shift expected from linear theory.

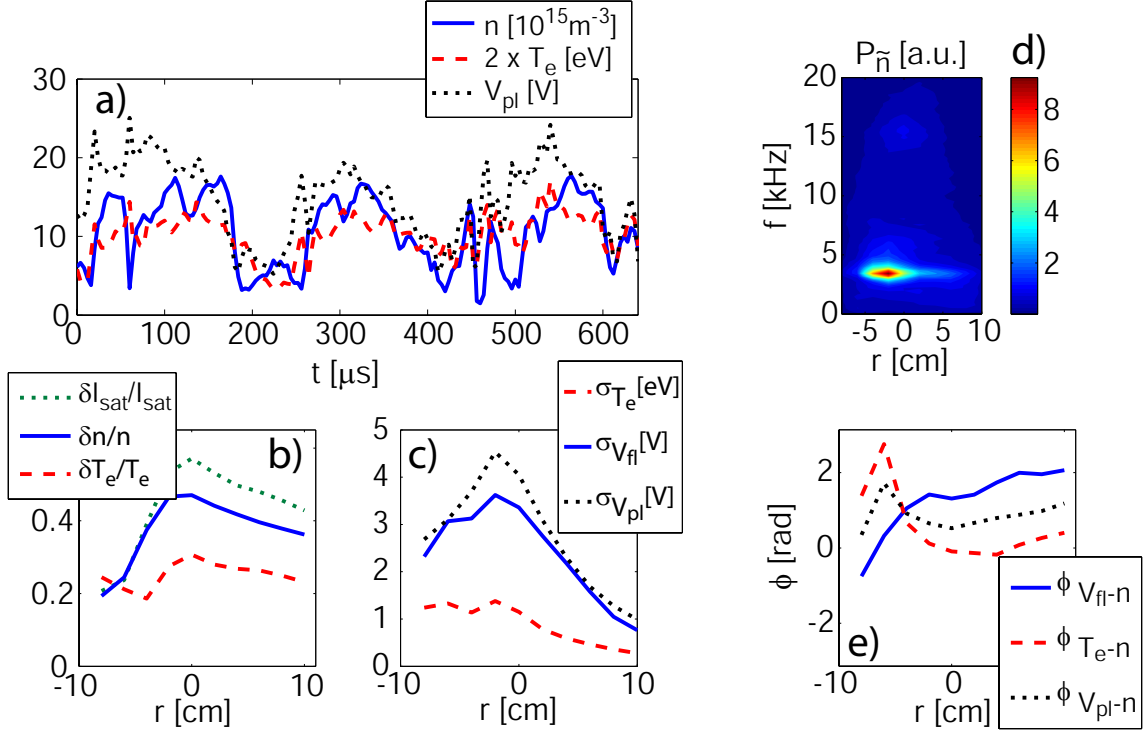


Figure 3.5.9: Fluctuation measurements with the modified, 5-tip triple probe FRIPLE. a): time traces of n , T_e , and V_{pl} . b): relative fluctuation levels of I_{sat} , n , and T_e . c): standard deviation of T_e , V_{fl} , and V_{pl} . d): Power spectral density of \tilde{n} as a function of r . e): phase shifts between V_{fl} , T_e , V_{pl} and n in the frequency range $[2.4, 4.4]$ kHz of the dominant mode.

We turn now to the evaluation of particle transport with triple probe measurements. More specifically, we focus on the time-averaged radial particle flux $\langle \Gamma_r \rangle$. In the present case where magnetic fluctuations can be neglected, we can write $\langle \Gamma_r \rangle = \langle n v_r \rangle$ with $v_r = -E_z/B$ the radial $\mathbf{E} \times \mathbf{B}$ velocity. The negative sign in the expression for v_r stems from the direction of the magnetic field. In the present experiments, \mathbf{B} is directed in the counter-clockwise direction when TORPEX is seen from the top, such that a positive radial particle flux corresponds to a negative vertical electric field E_z . Setting $n = \bar{n} + \tilde{n}$ and $v_r = \bar{v}_r + \tilde{v}_r$, we can decompose the flux in a steady state component and a contribution due to the fluctuations in the plasma

$$\langle \Gamma_r \rangle = \bar{n} \bar{v}_r + \langle \tilde{n} \tilde{v}_r \rangle. \quad (3.5.20)$$

We discuss the first term on the right hand side quickly at the end of this section and focus now on the term caused by fluctuations of n and v_r . A difficulty arises in the estimation of \tilde{v}_r as it requires the determination of vertical electric field fluctuations, while the triple probe provides only one local measurement of the plasma potential. This difficulty can be overcome in cases where fluctuations satisfy a dispersion relation, $k_z = k_z(f)$. In this case, one finds [110]

$$\langle \tilde{n} \tilde{v}_r \rangle = \frac{2}{B} \int_0^\infty df k_z \sqrt{P_{V_{pl}} P_{\tilde{n}}} \gamma \sin(\phi) \quad (3.5.21)$$

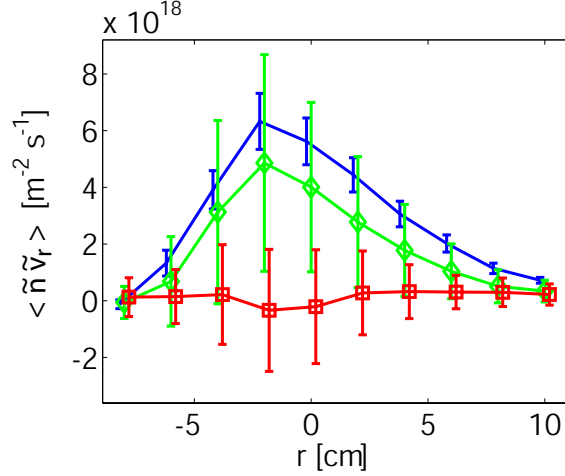


Figure 3.5.10: Radial particle flux associated with fluctuations in V_{fl} (diamonds) and T_e (squares) calculated assuming a dispersion relation, Eq. (3.5.21). The blue profile is the radial fluctuation induced flux obtained from Eq. (3.5.22). For clarity, the three profiles have been slightly displaced radially such that error bars do not lie on top of each other.

with $\gamma = \gamma(f)$ and $\phi = \phi(f)$ being the coherence and phase angle between \tilde{V}_{pl} and \tilde{n} and $P_{\tilde{V}_{pl}}$, $P_{\tilde{n}}$ their power spectral densities. The wave number $k_z(f)$ can be estimated experimentally from two-point correlation [65] of the V_{fl} -signals acquired at tip 1 and 5 of the probe (see Fig. 3.5.1 (b)) and one local measurement of V_{pl} is now sufficient to determine $\langle \tilde{n} \tilde{v}_r \rangle$.

The flux $\langle \tilde{n} \tilde{v}_r \rangle$ is linear in \tilde{V}_{pl} and we can thus separate Eq. (3.5.21) in a contribution from \tilde{V}_{fl} and a contribution from $\mu \tilde{T}_e / e$. These two contributions are shown in Fig. 3.5.10 respectively as green diamonds and red squares. As expected from the positive phase shift between \tilde{V}_{fl} and \tilde{n} in Fig. 3.5.9, floating potential fluctuations drive a positive radial flux, while the time-average contribution from electron temperature fluctuations is weak. The error bars for these curves take into account uncertainties in the phase of the V_{fl} measurements (Fig. 3.5.5), in μ , and in $k_z(f)$, as well as a reduction of the fluctuation amplitude of $V_{fl} = (V_{fl1} + V_{fl5})/2$ introduced by averaging the signals from tips 1 and 5. The latter two dominate the error bars for transport due to temperature fluctuations. The error bars of the floating potential driven transport are dominated by $\delta k_z(f)$ alone, which we take as the standard deviation of the wavenumber-frequency-(statistical) spectrum. We note that we have included all fluctuations with $f \leq 50$ kHz in the transport calculation. Significantly smaller error bars than in the present case are obtained when calculating the contribution from a coherent part of the spectrum only (here the 3.4 kHz mode).

As temperature fluctuations are found to contribute weakly to the radial particle transport, it seems more direct to evaluate $\langle \tilde{n} \tilde{v}_r \rangle$ from electric field fluctuations

deduced from gradients in the floating potential. We thus set

$$\langle \tilde{n}\tilde{v}_r \rangle = \langle \tilde{n} \frac{\tilde{V}_{fl5} - \tilde{V}_{fl1}}{d_{tip}B} \rangle \quad (3.5.22)$$

with $d_{tip} = 1.6$ cm the spacing between tip 1 and 5. Results are shown as a blue solid line in Fig. 3.5.10. Error bars are deduced from uncertainties in the tip spacing and the phase of the floating potential signals as well as differences in the fluctuation level of \tilde{V}_{fl1} and \tilde{V}_{fl5} . In the mode region, we find reasonable agreement between transport driven by \tilde{V}_{fl} evaluated in this way and that through Eq. (3.5.21). A relative difference of ≈ 20 % between the two is found in the central region of the mode at $r = -2$ cm. The relative difference between the two increases monotonically up to ≈ 55 % at $r = 10$ cm. In that region, cross-field transport is dominated by the propagation of turbulent structures (blobs) that do not satisfy a dispersion relation and Eq. (3.5.21) can not properly account for their transport [111, 112].

For the present case where the phase between electron temperature and density is small, the calculation of $\langle \tilde{n}\tilde{v}_r \rangle$ with the simple formula (3.5.22) seems more accurate than that with Eq. (3.5.21), which relies on the existence of a dispersion relation. We note, however, that the interpretation of the two terms on the right hand side of Eq. (3.5.20) as the transport due to the background and due to turbulence, respectively, is not necessarily meaningful if velocity perturbations due to turbulence are not zero on average, as can be the case if turbulence is vertically asymmetric. In such a case, other definitions of the turbulent flux, such as that associated with blobs as defined in [111, 112] for example, are more appropriate. Further, to calculate the total radial particle transport $\langle \Gamma_r \rangle$, the measurement of $\bar{n}\bar{v}_r$ is required as well. We note, however, that evaluating the time averaged potential difference between tip 1 and tip 5 of FRIPLE to estimate $\bar{v}_r = (\bar{V}_{pl5} - \bar{V}_{pl1})/(d_{tip}B)$ is rather delicate. Sometimes, we see differences in the time averaged floating potential between the probe tips that do not seem physical, see e.g. Fig. 3.5.4 (c). An explanation for this could be residual impurity layers on the probe surfaces. A difference of only 1 V between the time-average plasma potential at tip 1 and 5, which at $r = -2$ cm is less than 10 % of V_{pl} , results, however, already in $|\bar{n}\bar{v}_r| \sim |\langle \tilde{n}\tilde{v}_r \rangle|$. Additional studies are therefore needed to have satisfactory measurements of the total radial particle transport.

3.6 Conclusions

Most measurements on TORPEX are obtained with Langmuir probes (LPs). They are operated in ion saturation current or floating potential to obtain local, time resolved measurements of these quantities. However, these are combinations of basic plasma parameters. Direct measurements of plasma density, electron temperature, and plasma potential are more challenging. Applying a slow voltage sweep to an LP and subsequent fitting of the current-voltage characteristics provides time averaged

profiles of n , T_e , and V_{pl} . The BOX-CAS technique [105], a modification of standard conditional average sampling, allows extending these measurements to the average evolution of coherent structure, such as blobs or mode structures. In order to obtain direct, time dependent measurements of these quantities, a triple probe [62] has been developed. Different solutions were incorporated to reduce sources of errors associated with this diagnostics. This probe has been tested in hydrogen plasmas that are dominated by an ideal interchange wave, and provided new, quantitative insights on fluctuation level and phase relations of plasma parameters. It is fully operational and can be used, e.g. to extend the set of observables for the TORPEX code validation project [74, 75] in the future.

Blob formation

As already discussed in the course of this thesis, blobs are structures of enhanced plasma density relative to the background plasma. They are localized in the plane perpendicular to the magnetic field and elongated along its direction, therefore also referred to as *filaments*. Direct observations of blobs go back to the 1980s, when they were observed at the edge of tokamaks using optical imaging [113] and 2D Langmuir probe arrays [114]. There have been indications for blobs even earlier than that. Probe measurements in the edge of ZETA for example showed that “..., the probe current traces give the impression of isolated plasma bunches moving over the probe” [115]. With improved diagnostics systems such as gas puff imaging [116, 117], more detailed measurements of their structure and dynamics have been achieved, see e.g. [118–122]. It rapidly became clear that blobs are present in the edge of virtually all magnetized laboratory plasmas, including tokamaks [118–120], stellarators [123], reversed field pinches [124], simple magnetized tori [111, 125] and linear devices [126, 127].

As suggested in [128, 129], blob-induced transport can account for many aspects of SOL turbulence, such as the intermittency of density fluctuations, the convective rather than diffusive nature of particle transport, the two-scale structure of the SOL, and high levels of wall recycling [130]. Measurements indeed show that a large fraction of cross-field particle transport in the tokamak SOL can be attributed to blobs [119].

These observations triggered a large theoretical effort over the past years to elucidate the mechanisms behind blob formation and subsequent propagation in different regimes and geometries (see the review articles [20] and [131] and references therein). In this chapter, we discuss the mechanism of blob formation from ideal interchange waves identified on TORPEX. Detailed investigations on the subsequent blob propagation follow in Ch. 5.

4.1 Blob formation from ideal interchange waves

As we have seen e.g. in Sec. 2.5, the dynamics regime investigated in this work is dominated by quasi-coherent fluctuations associated with an ideal interchange mode in the region of strong pressure gradients. Further towards the LFS, fluctuations become bursty, attributed to the intermittent ejection of blobs.

Blobs form from the intermittent radial elongation of positive wave crests [111]. Detailed insights of this process are obtained using the BOX-CAS technique (see Sec. 3.4 and [105]), which provides the conditionally averaged, 2D evolution of density, electron temperature and plasma potential. As described in the following, this shows that a radially sheared, vertical $\mathbf{E} \times \mathbf{B}$ flow breaks apart radially elongated wave structures, generating blobs. A local steepening of the pressure profile is observed to precede the radial elongation of the wave [105, 125].

We study here a hydrogen plasmas with a number of field line turns $N \approx 2$ and an injected microwave power of 400 W. Profiles of plasma pressure and potential are shown in Fig. 4.1.1. The vertically elongated profiles are typical of the ideal interchange regime in TORPEX. Fig. 4.1.1 (c) clearly shows the upwards $\mathbf{E} \times \mathbf{B}$ flow and its radial shear.

The ideal interchange wave develops in the region of minimum radial pressure scale

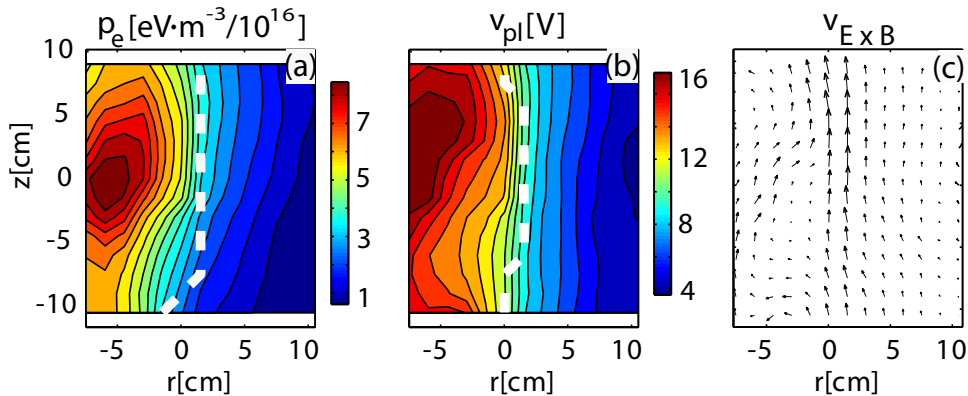


Figure 4.1.1: 2D poloidal profiles of the time-averaged plasma pressure, plasma potential, and $\mathbf{E} \times \mathbf{B}$ velocity [125]. Dashed lines indicate the position of (a) minimum radial pressure scale length and (b) maximum of the radial electric field.

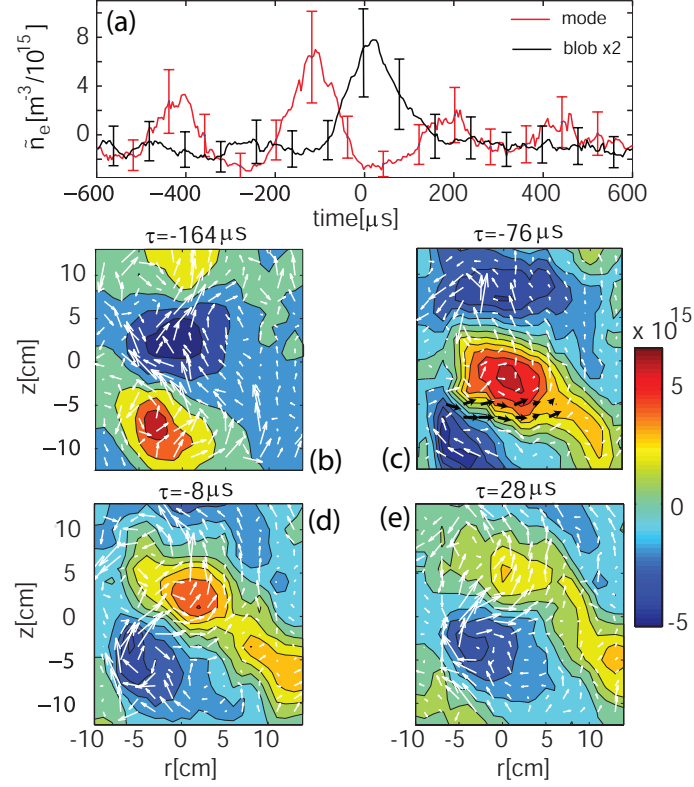


Figure 4.1.2: Time evolution of the 2D, conditionally averaged density fluctuations, showing the mechanism of blob formation from ideal interchange waves [125]. The arrows in (b)-(e) show the instantaneous pattern of the total $\mathbf{E} \times \mathbf{B}$ flow. The mode is convected upwards, radially elongates in (c), and gets sheared apart, leading to the formation of a blob, (d)-(e). In (a), time traces of \tilde{n} at a position in the mode region (red) and in the blob region (black) are also shown.

length, indicated by the dashed line in Fig. 4.1.1 (a). The wave is convected upwards by the $\mathbf{E} \times \mathbf{B}$ flow shown in Fig. 4.1.1 (c).

The dynamics of blob formation and ejection from the wave, obtained using the BOX-CAS technique, is captured in Fig. 4.1.2 (b)-(e). A radially elongated density structure forms from the positive cell of the wave, Fig. 4.1.2 (c). This structure forms from the convection of plasma by the $\mathbf{E} \times \mathbf{B}$ flow in a corridor, i.e., a radially extended region in which the $\mathbf{E} \times \mathbf{B}$ flow is mainly in the radial direction. This is highlighted in Fig. 4.1.2 (c) by black arrows. This corridor extends radially over several ion sound radii ($\rho_s \approx 0.3$ cm). In Fig. 4.1.2 (d), the elongated density structure is convected upwards in a sheared velocity field that moves HFS and LFS parts of the density structure with different vertical velocities. A relative displacement between them results and, eventually, the original density structure breaks into two parts, Fig. 4.1.2 (e). The new structure on the LFS forms a plasma blob.

To quantify the role of the $\mathbf{E} \times \mathbf{B}$ flow in shearing off the density structure, we compute the shearing time $1/\tau_{sh} = (k_z L_r / 2\pi) \partial v_{z,E \times B} / \partial r$ [132], where L_r is the radial width of the shear layer, k_z the wave number in the z direction and $v_{z,E \times B}$ the vertical component of the $\mathbf{E} \times \mathbf{B}$ velocity. Both L_r and $v_{z,E \times B}$ are estimated by

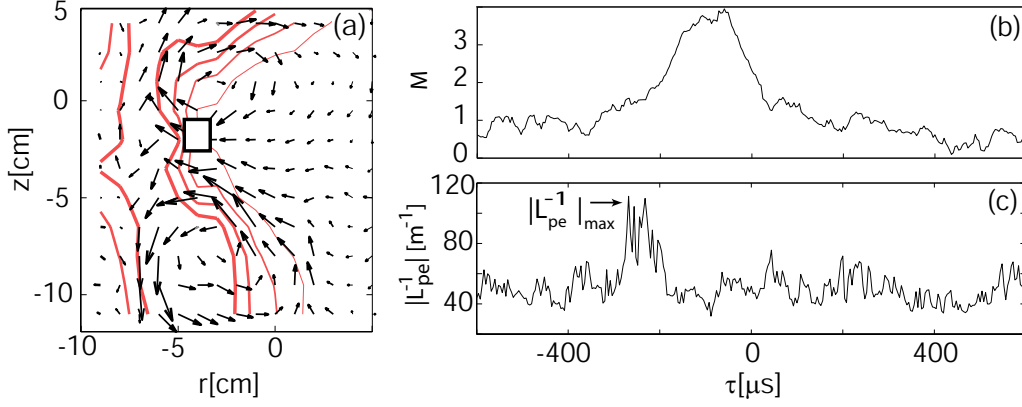


Figure 4.1.3: (a): A zoomed view of the instantaneous fluctuating $\mathbf{E} \times \mathbf{B}$ velocity at $-184 \mu\text{s}$ shows the convective cells interchanging zones of high and low plasma pressure. Solid red lines represent equispaced pressure contours with $\Delta p_e = 10^{16} \text{ m}^{-3} \text{ eV}$. Time evolution of (b) mode amplitude and (c) inverse pressure gradient length $|L_{pe}^{-1}|$ at the point of maximum observed intensity, indicated by the square in (a).

averaging the instantaneous values over the trajectory of the positive cells. For the data set considered here, using $L_r \approx 0.03 \text{ m}$, $k_z \approx 30.6 \text{ m}^{-1}$ and $(\partial v_{z,E \times B})/\partial r \approx 3 \times 10^4 \text{ s}^{-1}$, we find $\tau_{sh} \approx 200 \mu\text{s}$. The shearing time τ_{sh} is of the same order of the transit time $\tau_{tr} = 2\pi/(k_z v_{z,E \times B}) \approx 200 \mu\text{s}$, during which a density structure moves upwards by $2\pi/k_z$. These estimates confirm that the radially elongated density structure, which forms from the ideal interchange wave, can be sheared off by the $\mathbf{E} \times \mathbf{B}$ flow. The observed behavior is reminiscent of numerical simulations of edge/SOL turbulence in tokamaks, which show the generation of plasma blobs via shearing off density streamers by the plasma flow [133].

Next, we investigate the evolution of the local inverse radial pressure scale length $|L_{pe}^{-1}|$ as a possible drive for the radial elongation of the wave. Fig. 4.1.3 (a) shows a zoomed view of the instantaneous pattern of the fluctuating $\tilde{\mathbf{v}}_{E \times B}$ together with contours of the total electron pressure. The interchange mechanism that exchanges zones of high plasma pressure with zones of low plasma pressure is clearly at play. $|L_{pe}^{-1}|$ is maximum in the region where the pressure negative wave crest is localized, indicated by the square in Fig. 4.1.3 (a). The time evolution of $|L_{pe}^{-1}|$ at the position of maximum intensity is shown in Fig. 4.1.3 (c). At each time, we compute the 2D spatial Fourier transform $\tilde{n}_e(k_r, k_z)$ of the fluctuating density and, from this, a mode amplitude

$$M = \sqrt{\sum_{k_r} |\tilde{n}_e(k_r, k_{z0})|^2} \quad , \quad (4.1.1)$$

where $k_{z0} \approx 30 \text{ m}^{-1}$ is the vertical wave number of the dominant mode and the summation is performed over all the computed radial wave numbers k_r . The time evolution of the mode amplitude is shown in Fig. 4.1.3 (b).

During a first period, $-600 \mu\text{s} < \tau < -350 \mu\text{s}$, both the mode amplitude and $|L_{pe}^{-1}|$ remain approximately constant. $|L_{pe}^{-1}|$ is observed to increase at $\tau \approx -350 \mu\text{s}$ from

$|L_{pe}^{-1}| \approx 40 \text{ m}^{-1}$ to a maximum value $|L_{pe}^{-1}|_{max} \approx 110 \text{ m}^{-1}$ at $\tau \approx -260 \text{ } \mu\text{s}$. This is followed by an increase of the mode amplitude and the radial elongation of the positive wave crest.

Performing the BOX-CAS analysis for blobs of different amplitudes further shows that the maximum value of $|L_{pe}^{-1}|$ preceding the growth of the mode increases with increasing blob amplitude [105, 125]. These results indicate that the local steepening of the pressure profile is the cause for the radial elongation of the wave.

4.2 Gradient steepening in the blob formation process

In the following, we present a complementary study to gain insights on blob formation and gradient steepening [134]. Measurements are performed with HEXTIP operated in I_{sat} . Contrary to the BOX-CAS technique in the previous section, measurements of plasma potential and $\mathbf{E} \times \mathbf{B}$ flow profiles are therefore not available. On the other hand, simultaneous measurements over the plasma cross section allow also the analysis of individual events, and the use of nonlocal trigger conditions for conditional sampling. We find that isolated peaks detected at a single probe on the LFS can be caused by detached structures (blobs) as well as by radially elongated structures. Therefore, the more general term *intermittent cross-field particle transport events* (ITEs) is used in this context.

In a first step, conditional average sampling is applied to two vertically separated reference probes on the LFS. This gives different average dynamics of ITEs at the two positions. ITEs detected at the lower of the two reference probes originate predominantly from a steep density^(*) profile. A novel analysis technique reveals a monotonic dependence between the vertically averaged inverse radial density scale length and the probability for a subsequent ITE. The conditionally averaged dynamics leading to ITEs at the upper reference probe, on the contrary, reveal a different picture. The mode is already observed before the start of the ITE. It does not grow radially in a first stage, but at a later time. It is shown that this sudden radial elongation of the positive wave crest is preceded by a steepening of the density profile as well. This is done by comparing the dynamics leading to ITEs with the average evolution of the mode.

4.2.1 Spatio-temporal ITE dynamics from CAS

The target plasma is similar to the one in the previous section [105, 125], i.e., a hydrogen plasma with the number of field line turns is $N \approx 2$ and the injected microwave power is 400 W. Basic characteristics of these plasmas measured with HEXTIP are highlighted in Fig. 4.2.1, i.e., the slab like density profile (a), the

(*) In this chapter, I_{sat} measurements are identified with density measurements.

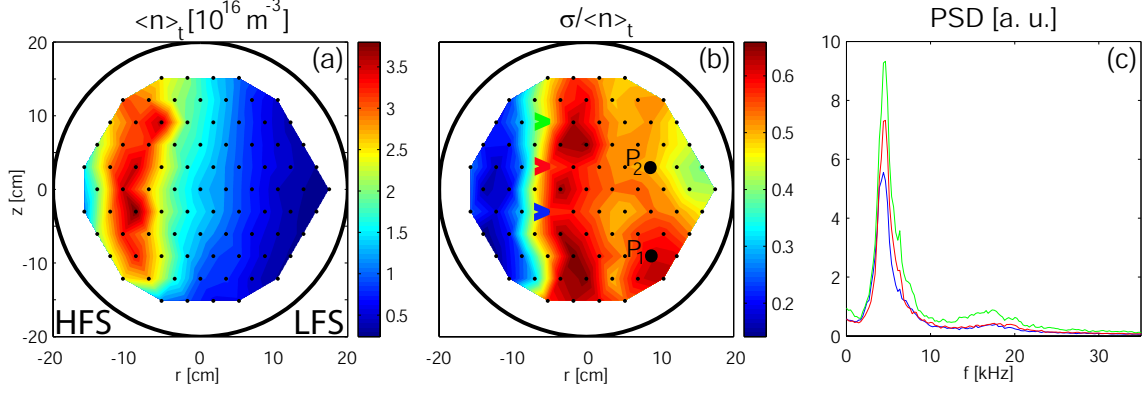


Figure 4.2.1: (a): Time averaged profile of density (I_{sat}) over the poloidal 2D cross-section, obtained with HEX TIP. The black dots indicate the location of the probes, covering most of the cross-section at a resolution of 3.5 cm. (b): Profile of relative density fluctuations, i.e., the standard deviation of density divided by its mean value (c): Power spectral density of \tilde{n} for tips indicated in (b) by angles of corresponding color.

high relative fluctuation level at the LFS (b), and the coherent features of density fluctuations in the mode region (c).

The 2D, spatio-temporal dynamics of ITEs is investigated using conditional average sampling [103]. HEX TIP tips P_1 and P_2 , indicated in Fig. 4.2.1 (b), are separately used as reference probes. The two tips lie well outside the source region on the LFS at $r = 8.8$ cm, $z = -9.1$ cm and $z = 3.0$ cm, respectively. We note that P_1 and P_2 represent points characterized by different distances to the vacuum vessel. The shortest paths from P_1 and P_2 to the vessel wall along the magnetic field lines have a length of approximately 2.5 m and 4.3 m, respectively. The connection length L_c of the field lines is the same at both points ($L_c \approx 10.3$ m at $r=8.8$ cm).

We assume that every local maxima in the reference signal $\tilde{n}_{P_{1,2}}$ that exceeds a certain threshold value corresponds to an ITE. The conditional average $\langle \tilde{n} \rangle_{ca}(\mathbf{x}, \tau)$ of \tilde{n} is evaluated as

$$\langle \tilde{n} \rangle_{ca}(\mathbf{x}, \tau) = \frac{1}{N} \sum_{i=1}^N \tilde{n}(\mathbf{x}, t_i + \tau), \quad (4.2.1)$$

where t_i is a time at which the trigger condition at the reference position (P_1 or P_2) is satisfied and N is the total number of triggered events. We use a threshold value of 3.5σ as trigger condition, where σ is the standard deviation of the reference signal. This corresponds to a threshold of $\approx 1.1 \times 10^{16} \text{ m}^{-3}$ for \tilde{n}_{P_1} and $\approx 1.2 \times 10^{16} \text{ m}^{-3}$ for \tilde{n}_{P_2} .

In addition to the conditional average, we also evaluate the reproducibility C_{rep} , which measures the deviation of individual events from the average. Following Ref. [104], this is defined as:

$$C_{rep}(\mathbf{x}, \tau) \equiv 1 - \frac{\sigma_{ca}^2(\mathbf{x}, \tau)}{\langle \tilde{n}^2 \rangle_{ca}(\mathbf{x}, \tau)} = \frac{\langle \tilde{n} \rangle_{ca}^2(\mathbf{x}, \tau)}{\langle \tilde{n} \rangle_{ca}^2(\mathbf{x}, \tau) + \sigma_{ca}^2(\mathbf{x}, \tau)},$$

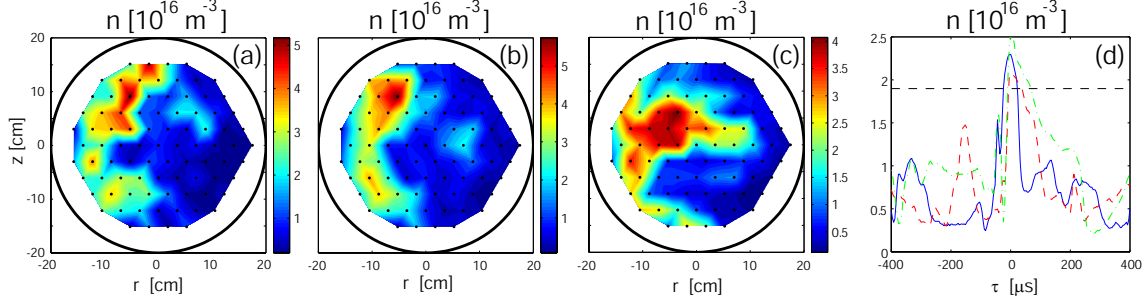


Figure 4.2.2: (a)-(c) Three examples of the instantaneous density (I_{sat}) profile at a time when the reference signal at P_2 satisfies the trigger condition. (d) Time traces of the total density n at P_2 that correspond to the event in (a) (blue), to the one in (b) (dashed red) and to the one shown in (c) (dash-dotted green). The dashed horizontal line indicates the threshold value for n_{P_2} .

with $\sigma_{ca}^2(\mathbf{x}, \tau) \equiv \langle (\tilde{n} - \langle \tilde{n} \rangle_{ca})^2 \rangle_{ca}(\mathbf{x}, \tau)$. C_{rep} lies between 0 and 1, being high for a good reproducibility of the selected events.

Before turning to the conditional average of ITEs, we give in Fig. 4.2.2 (a)-(c) three snapshots of individual events at times when the trigger condition at P_2 is satisfied. The corresponding time traces of density at P_2 are shown in Fig. 4.2.2 (d). This shows that a peak in the density time history detected at a single probe tip on the LFS is not always associated with a detached structure (blob), as in frame (a) and (b), but it can also be caused by a radially elongated structure, frame (c). The same behavior can be observed for ITEs detected at P_1 . We conclude that the radially elongating positive structure of the mode, which is at the origin of ITEs, can break apart and form a blob, as observed in Ref. [125]. However, this is not required for the plasma to be convected to tip P_1 or P_2 . We can interpret this behavior in the frame of semi-analytical blob models (see Ref. [20] and references therein, as well as chapter 5). The polarization mechanism of blobs, which causes their propagation, depends on the vertical shape of the density (pressure) profile and applies therefore also to streamer-like structures. We remark that there is no strong difference between single point measurements of blobs and streamers. It is not true in general that streamers lead to wider peaks, as Fig. 4.2.2 (d) could suggest.

The conditionally averaged dynamics leading to ITEs at P_1 and P_2 as well as the reproducibility C_{rep} are shown in Fig. 4.2.3, for five different values of time τ , where $\tau = 0$ corresponds to the time when the ITE is detected at P_1 or P_2 .

The conditional average $\langle \tilde{n} \rangle_{ca}$ for ITEs at P_1 (frames 1-5) shows a steep profile at $\tau = -160 \mu\text{s}$, where the mode has a small amplitude. In the next two frames, a radial elongation of the mode is seen, which gives rise to the peak at P_1 in frame 5 imposed by the trigger condition. We should note that the reproducibility of the triggered events is poor in this case.

In column 3 of Fig. 4.2.3, we show $\langle \tilde{n} \rangle_{ca}$ for ITEs detected at P_2 . It clearly differs from the previous case by the fact that the mode can already be clearly distinguished

at $\tau = -204 \mu\text{s}$, frame 11, while there is no coherent signal for ITEs at P_1 at that time. At first, the mode does not grow radially. It rather seems to slightly 'pull back' radially in frame 12, in the sense that the positive wave structure moves inwards and the negative one outwards. It is only in frames 14 and 15 that the positive structure of the mode elongates radially, leading to the ITE. This is accompanied by an inward motion of the negative wave crests. Compared to ITEs detected at P_1 , an improved reproducibility is observed for the positive and negative wave crests, as shown in column 4.

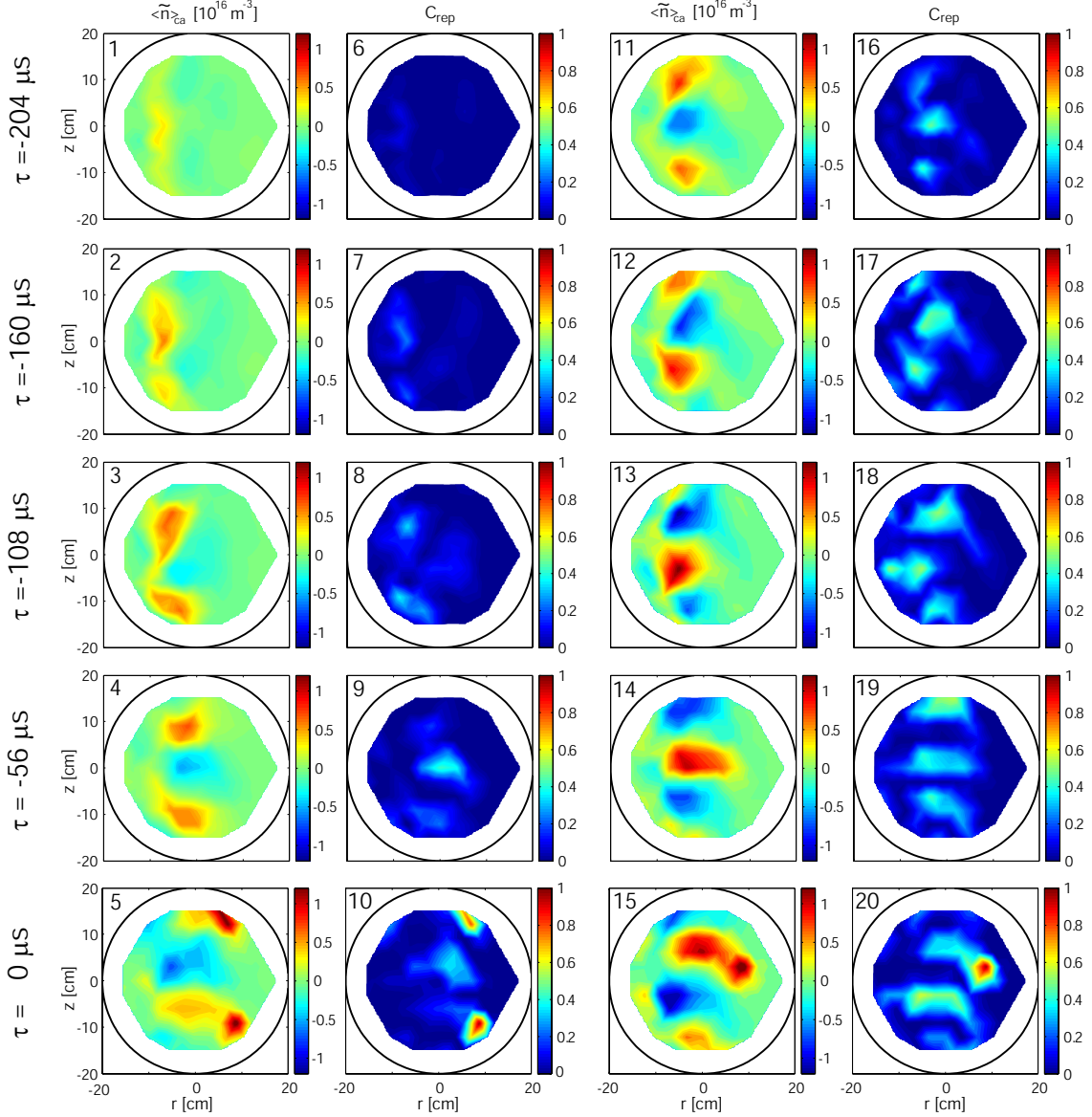


Figure 4.2.3: Column 1: Conditional average of \tilde{n} obtained by triggering on ITEs at tip P_1 for five values of τ . All local maxima exceeding 3.5 times the standard deviation of the signal were selected. Column 2: Reproducibility C_{rep} of the conditional average in column 1. Column 3 and 4: The same for ITEs at probe tip P_2 .

4.2.2 Link between the inverse radial density scale length and ITEs at P_1

The CAS results in the previous section suggest that ITEs detected at position P_1 are preceded by a steepening of the density profile. However, the low reproducibility found for the conditional average does not allow to obtain more information from it. Motivated by numerical simulations of interchange turbulence in Ref. [33], we investigate the relation between the vertically averaged inverse radial density scale length $\langle L_n^{-1} \rangle_z(r, t) \equiv \langle 1/n \times \partial n / \partial r \rangle_z(r, t)$ and the occurrence of ITEs. Note that $\langle L_n^{-1} \rangle_z(r, t)$ is defined in such a way that it is typically negative in the region of interest and strongly negative values correspond to steep profiles.

In the following, we introduce and apply a technique that, contrary to the conditional average, is not based on an averaging process. This analysis technique can be used quite generally to investigate the relation between a certain condition on the plasma profile and the probability for an ITE. In a first step, the signal $\langle L_n^{-1} \rangle_z(r, t)$ is searched for local minima that fall in a desired interval $[L_l^{-1}, L_h^{-1}]$. For every such event and different values of the time τ after these events, a signal \tilde{n} on the LFS is searched for the maximum value in a window of length $\Delta\tau$ around τ , and this value is stored. All maxima exceeding a certain threshold value are interpreted as an ITE. In this way, for the local minima of $\langle L_n^{-1} \rangle_z(r, t)$ that fall in the interval $[L_l^{-1}, L_h^{-1}]$, we obtain the number of ITEs at a certain position on the LFS as a function of τ and the threshold value. By taking the maximum value of \tilde{n} in the interval $[\tau - \Delta\tau/2, \tau + \Delta\tau/2]$, we allow for a spread in the evolution time of ITEs. In the following, $\Delta\tau = 80 \mu\text{s}$ is used. The results depend only weakly on the choice of this parameter.

In order to establish the significance of the results obtained with this technique, the whole procedure is repeated for a ‘random’ trigger, i.e., a trigger that arbitrarily selects events in the time series of $\langle L_n^{-1} \rangle_z(r, t)$. Finally, the results are assessed in a *probability comparison chart* (PCC) as follows. The number of ITEs after a value of $\langle L_n^{-1} \rangle_z(r, t)$ in $[L_l^{-1}, L_h^{-1}]$ divided by the number of ITEs found by the random trigger (for the same number of initially triggered events) is plotted as a function of τ and the threshold value for ITEs. These representations allow us to quantitatively evaluate how more likely it is to have an ITE after times when our condition on the plasma profile is fulfilled, than at arbitrary times, and this as a function of time τ and of the threshold value defining ITEs.

The inverse radial density scale length is evaluated between two neighboring HEXTIP-tips by

$$L_n^{-1} = n^{-1} \frac{\partial n}{\partial r} \approx \left(\frac{n_R + n_L}{2} \right)^{-1} \times \frac{n_R - n_L}{\Delta r}, \quad (4.2.2)$$

where n_L and n_R are the instantaneous densities measured at the left and at the right tip and $\Delta r = 3.5 \text{ cm}$ is the tip separation. The choice of the radial position where we evaluate the vertical average of $L_n^{-1}(r, z, t)$ is motivated by the conditional

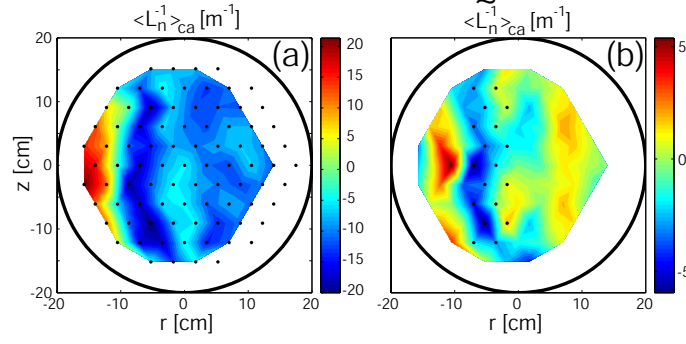


Figure 4.2.4: Conditionally averaged value of L_n^{-1} (a) and its deviation $\langle \tilde{L}_n^{-1} \rangle_{ca} \equiv \langle L_n^{-1} \rangle_{ca} - \langle L_n^{-1} \rangle_t$ from the mean value (b) at $\tau = -160 \mu s$ before the ITEs are detected at P_1 . The value of $\langle L_n^{-1} \rangle_{ca}$ and $\langle \tilde{L}_n^{-1} \rangle_{ca}$ evaluated between two neighboring tips is plotted at the position of the left tip. In (b) the pairs of tips used to evaluate $\langle L_n^{-1} \rangle_{z,0}$ are indicated.

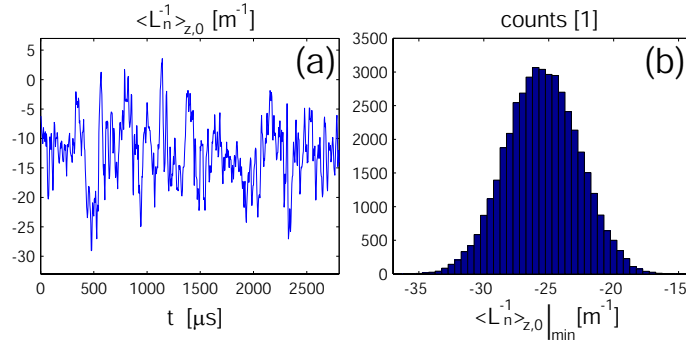


Figure 4.2.5: (a) Time trace of $\langle L_n^{-1} \rangle_{z,0}$. (b) Histogram of local minima of $\langle L_n^{-1} \rangle_{z,0}$.

average results shown in the previous section. In Fig. 4.2.4 we show the conditionally averaged value of L_n^{-1} , as well as its deviation $\langle \tilde{L}_n^{-1} \rangle_{ca} \equiv \langle L_n^{-1} \rangle_{ca} - \langle L_n^{-1} \rangle_t$ from the mean value at $\tau = -160 \mu s$, i.e., at the same time as frame 2 in Fig. 4.2.3. Negative values of $\langle \tilde{L}_n^{-1} \rangle_{ca}$ are found in the region $r_0 \approx -7$ cm. Guided by this, we estimate $\langle L_n^{-1} \rangle_z(r, t)$ around r_0 by averaging L_n^{-1} over the values evaluated between the pairs of tips indicated in Fig. 4.2.4 (b). We denote the result as $\langle L_n^{-1} \rangle_{z,0}(t)$ and we keep in mind that it is a function of time.

The analysis described above is then applied to the plasma scenario of interest. In Fig. 4.2.5 (a), a subsample of the time trace of $\langle L_n^{-1} \rangle_{z,0}$ is shown. We see that it fluctuates strongly and even assumes positive values. In Fig. 4.2.5 (b), the histogram of local minima of $\langle L_n^{-1} \rangle_{z,0}$ is shown. We only consider local minima of $\langle L_n^{-1} \rangle_{z,0}$ that are a minimum in a time interval of $400 \mu s$ centered around each of them. This implies that the selected local minima are spaced by at least $200 \mu s$, which is the typical evolution time of ITEs.

As a first step, we look at very strong minima in $\langle L_n^{-1} \rangle_{z,0}$, i.e., at minima in the interval $[-33.5 \text{ m}^{-1}, -29.5 \text{ m}^{-1}]$. More than 3000 such events are found. In Fig. 4.2.6 (a) and (b), we show the conditional average $\langle \tilde{n} \rangle_{ca}$ for these events at $\tau = 0 \mu s$ and at $\tau = 52 \mu s$ ($\tau = 0$ corresponds to the time of the local minima of $\langle L_n^{-1} \rangle_{z,0}$).

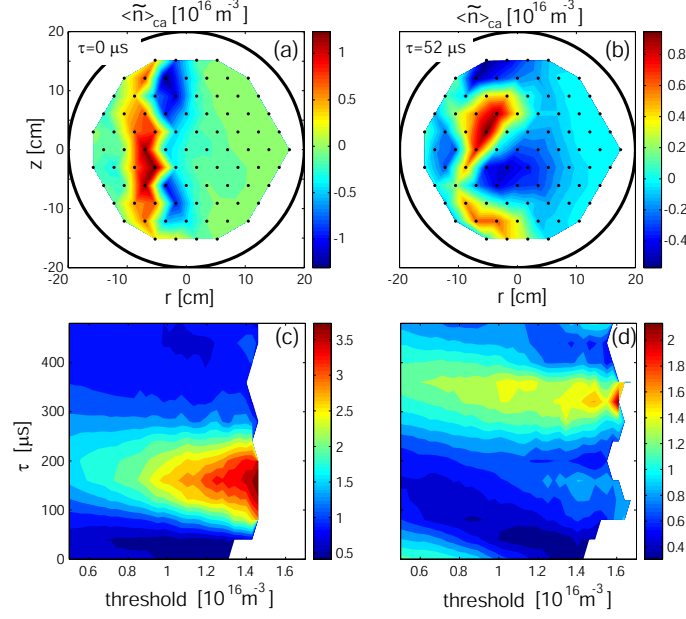


Figure 4.2.6: Results obtained by searching $\langle L_n^{-1} \rangle_{z,0}$ for local minima in the lowest considered interval $[-33.5 \text{ m}^{-1}, -29.5 \text{ m}^{-1}]$. (a), (b) Conditional average of these events at $\tau = 0$ and $\tau = 52 \mu\text{s}$, respectively. (c), (d) Probability comparison chart for tip P_1 and P_2 , respectively. The ratio of the number of ITEs after a strong negative value of $\langle L_n^{-1} \rangle_{z,0}$ and the number after arbitrary chosen times is plotted as long as both values exceed 10 counts.

As anticipated, we find a steep profile at $\tau = 0 \mu\text{s}$. At $\tau = 52 \mu\text{s}$, the positive and negative wave crests are located at roughly the same vertical position as in frame 3 of Fig. 4.2.3.

The corresponding PCCs for probe tips P_1 and P_2 are shown in Fig. 4.2.6 (c) and (d), respectively. The PCC for P_1 clearly shows an enhanced probability for ITEs for a time $\tau \approx 160 \mu\text{s}$, which corresponds to the time expected from the conditional average as shown in the preceding section.

The PCC for P_2 shows an increased probability for ITEs at τ around $360 \mu\text{s}$, however at a lower level than for P_1 . We have evaluated the conditional average of \tilde{n} for the events with a strong minimum of $\langle L_n^{-1} \rangle_{z,0}$ that are followed by an ITE at P_2 (peak above $0.9 \times 10^{16} \text{ m}^{-3}$ for $\tau \in [320 \mu\text{s}, 400 \mu\text{s}]$). The result showed that in these cases the mode grows radially in a first step. It then stops extending further and gets convected upwards. It further elongates at a much later time, in a similar way as observed in the conditional average in Sec. 4.2.1. From this, we conclude that the quantity $\langle L_n^{-1} \rangle_{z,0}$ is not the one that governs the occurrence of ITEs at P_2 . The reason why a weak pattern can still be identified in the PCC is due to the fact that the mode grows from a steep profile with a preferred phase.

We repeat now the analysis for subsequent intervals $[L_l^{-1}, L_h^{-1}]$. For each such interval, the PCC for P_1 looks similar to the one in Fig. 4.2.6 (c), with a maximum number of ITEs for τ between $160 \mu\text{s}$ and $200 \mu\text{s}$. In Fig. 4.2.7, this maximum divided by the number of triggered events in the corresponding interval is plotted,

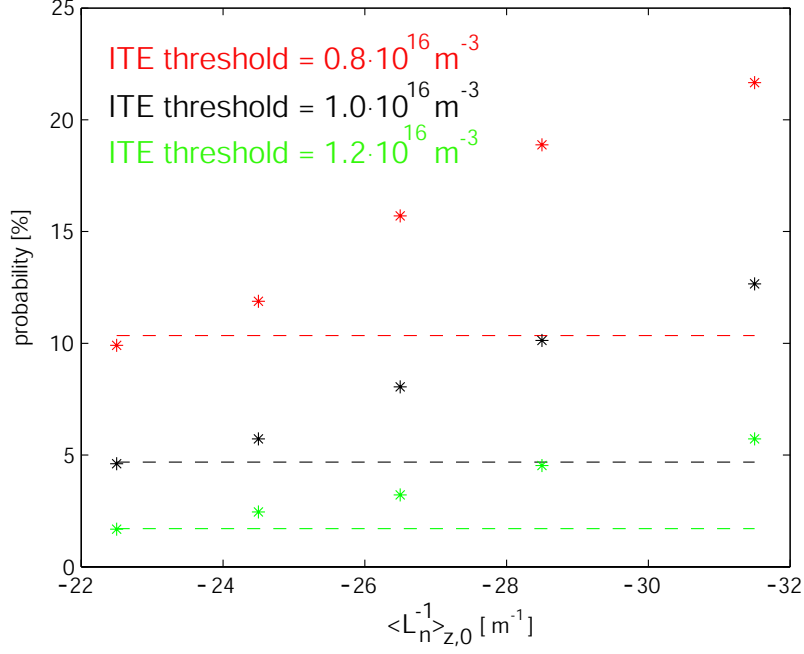


Figure 4.2.7: Probability for an ITE at P_1 as a function of the preceding minimal value of $\langle L_n^{-1} \rangle_{z,0}$ for three different values above which a peak is interpreted as an ITE. The dashed lines show the corresponding probabilities for ITEs for arbitrarily chosen triggers in the time series.

for three different threshold values defining ITEs. This gives an estimate of the probability for an ITE as a function of the preceding minimal value of $\langle L_n^{-1} \rangle_{z,0}$. The result shows a monotonic dependence between $\langle L_n^{-1} \rangle_{z,0}$ and the probability for an ITE. As a reference, we also show the ITE-probability obtained for the randomly chosen times in the discharges (dashed lines).

4.2.3 ITEs at probe tip P_2

We have seen in the previous section that the "steeper" the density profile, i.e., the smaller the (negative) quantity $\langle L_n^{-1} \rangle_{z,0}$, the higher the probability for a subsequent ITE at P_1 . In the CAS results for P_2 in Sec. 4.2.1, the mode seems to slightly pull back radially before the start of the ITE, which would result in a steepening of the density profile. This indicates that profile steepening could be the drive for ITEs at P_2 as well. However, since there is already a strong mode before the ITE, a radial gradient might not be needed for an increase in cross-field transport. It is possible that the positive structures of the mode behave rather like independent structures (blobs) and it is for example a change in the vertical shape of the positive crests that triggers the ITE. We try to clarify this by the approach described below.

We select times $\{t_k\}_{k=1}^N$ in the discharges at which the mode has a given phase along the z-direction, i.e., at which the positive and negative wave structures are at a given vertical position. Among these N events, we select a subseries of N' triggers at $\{t_{k_i}\}_{i=1}^{N'}$ which are followed by an ITE at P_2 . Then we compare the 2D evolution

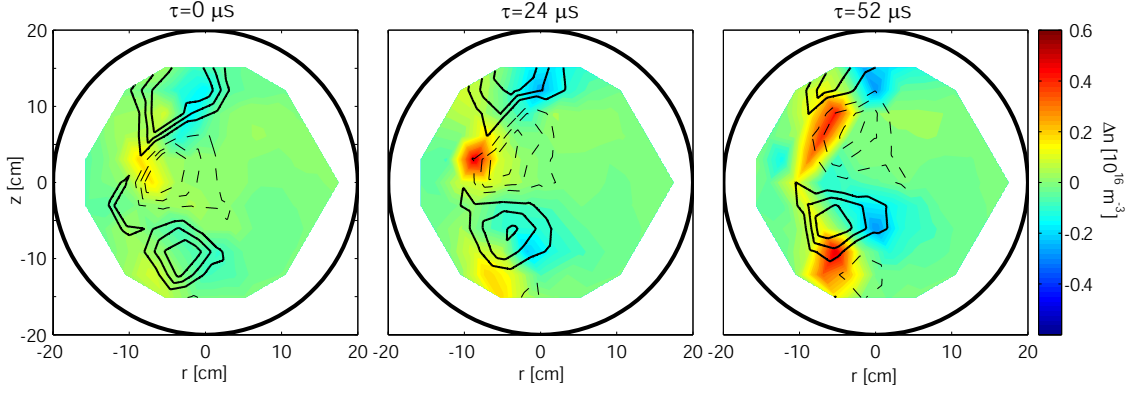


Figure 4.2.8: Difference $\langle \tilde{n} \rangle_{ca}^{ITE} - \langle \tilde{n} \rangle_{ca}^{mode}$ between ITEs detected at P_2 and the average evolution of the mode at three different times τ . Here, $\tau = 0$ indicates the time of the CAS evolution at which the imposed condition on the phase of the mode is satisfied. In $\langle \tilde{n} \rangle_{ca}^{ITE}$, the ITE reaches P_2 at $\tau \approx 200 \mu\text{s}$. Also shown are the positive (solid lines) and the negative (dashed lines) contours of $\langle \tilde{n} \rangle_{ca}^{ITE}$.

of \tilde{n} averaged over the N and N' events, respectively, to study how their dynamics, starting from similar initial profiles, differs as we proceed in time.

As a starting point, we select the mode at a phase as in frame 11 of Fig. 4.2.3, i.e., we take the corresponding conditional average $\langle \tilde{n} \rangle_{ca}(\mathbf{x}, \tau_0)$ at $\tau_0 = -204 \mu\text{s}$. The result of the following analysis does not change significantly if we choose a different time τ_0 before the radial elongation of the mode in $\langle \tilde{n} \rangle_{ca}$. For each time sample, we evaluate the spatial correlation $corr(t, \tau_0)$ between the raw signal $\tilde{n}(\mathbf{x}, t)$ and $\langle \tilde{n} \rangle_{ca}(\mathbf{x}, \tau_0)$:

$$corr(t, \tau_0) \equiv \frac{\sum_{i=1}^{\#tips} \tilde{n}(\mathbf{x}_i, t) \times \langle \tilde{n} \rangle_{ca}(\mathbf{x}_i, \tau_0)}{\sqrt{(\sum_{i=1}^{\#tips} \tilde{n}(\mathbf{x}_i, t)^2) (\sum_{i=1}^{\#tips} \langle \tilde{n} \rangle_{ca}(\mathbf{x}_i, \tau_0)^2)}} \quad (4.2.3)$$

where the sums are performed over all probe tips of HEXTIP. The quantity $corr(t, \tau_0)$ is a scalar function bounded between -1 and 1. It is dominated by fluctuations in the frequency range of the mode and it assumes high values if the phase of the mode at time t coincides with the one in $\langle \tilde{n} \rangle_{ca}(\mathbf{x}, \tau_0)$. The times $\{t_k\}_{k=1}^N$ are selected by the additional requirement that $corr(t_k, \tau_0)$ is a local maximum exceeding 0.5 for each k .

The subseries $\{t_{k_i}\}_{i=1}^{N'}$ of times which correspond to ITEs are selected by the requirement that the signal \tilde{n}_{P_2} at probe tip P_2 assumes a maximum value of at least $1.3 \times 10^{16} \text{ m}^{-3}$ for $t \in [t_k + 160 \mu\text{s}, t_k + 240 \mu\text{s}]$. This additional constraint reduces the number of detected events from ≈ 47000 to ≈ 1700 .

Now the conditional averages of the events triggered at $\{t_k\}_{k=1}^N$ and $\{t_{k_i}\}_{i=1}^{N'}$ are evaluated. We denote them as $\langle \tilde{n} \rangle_{ca}^{mode}(\mathbf{x}, \tau)$ and $\langle \tilde{n} \rangle_{ca}^{ITE}(\mathbf{x}, \tau)$, respectively. Here, $\tau = 0$ indicates the time of the CAS evolution at which the imposed condition on the phase of the mode is satisfied. While $\langle \tilde{n} \rangle_{ca}^{mode}$ shows a mode that is being convected upwards, $\langle \tilde{n} \rangle_{ca}^{ITE}$ is very similar to the CAS result from Sec. 4.2.1. The two conditional averages are compared in Fig. 4.2.8, where $\langle \tilde{n} \rangle_{ca}^{ITE} - \langle \tilde{n} \rangle_{ca}^{mode}$ as well as

the contours of $\langle \tilde{n} \rangle_{ca}^{ITE}$ are plotted, for three different values of τ . At $\tau = 0$, the difference between $\langle \tilde{n} \rangle_{ca}^{mode}$ and $\langle \tilde{n} \rangle_{ca}^{ITE}$ is small. Later in time, but still before the start of the ITE, a clear difference builds up. Negative values of $\langle \tilde{n} \rangle_{ca}^{ITE} - \langle \tilde{n} \rangle_{ca}^{mode}$ build up on the LFS of positive wave crests of $\langle \tilde{n} \rangle_{ca}^{ITE}$ and positive values on the HFS of its negative wave crests. Therefore, with respect to its average evolution, the mode shifts to the HFS before an ITE at P2. There is no indication that the vertical shape of the positive wave structure drastically changes. No vertical narrowing can be seen, for example. This strongly suggests that the pulling back of the mode that could already be guessed from the CAS result of Sec. 4.2.1 and the profile steepening that goes along with it are at the origin of ITEs at P_2 .

4.3 Conclusions

We have discussed the experimental identification of the blob generation mechanism from ideal interchange waves. Individual time frames from HEX TIP [111] and the 2D, conditionally averaged evolution of n , T_e , and V_{pl} associated with blobs [105, 125] show that blobs form from radially extending positive wave crests. A local steepening of the conditionally averaged pressure profile is observed prior to an increase in mode amplitude and its subsequent radial elongation. This indicates that local profile steepening is driving the blob formation process. The $\mathbf{E} \times \mathbf{B}$ flow is shown to be responsible for breaking apart the radially elongated wave structures that eventually form the blobs [105, 125]. Similar dynamics of blob formation have also been observed in the drift-interchange regime in TORPEX [135].

A complementary study was conducted to further investigate details of the process of profile steepening at the origin of blob ejection, using ion saturation current measurements from HEX TIP [134]. It is found that intermittent bursts detected in probe measurements on the LFS can be caused both by detached structures (blobs) and by radially elongated structures. We refer to them as intermittent cross-field particle transport events (ITEs).

We have studied ITEs detected at two vertically separated probe tips. Conditionally averaged data shows ITEs at the lower probe being preceded by a steep density profile. Another scenario is observed for ITEs at the upper probe. The mode pattern is observed in the conditionally averaged evolution long before the start of the ITE. The mode does not elongate radially at first. It rather seems to move radially inwards (towards the HFS) before it elongates radially at a later time. Despite their difference, both conditionally averaged ITE dynamics suggest that a steepening of the density profile is at the origin of ITEs. Results from CAS need to be interpreted with care, however. It may happen that the averaging process is performed over different kinds of coherent structures, which can confuse the result. As discussed in Sec. V of [134], this is indeed the case for ITEs detected at the lower reference probe. Also, differences in the evolution time of coherent events lead

to a smearing out of the conditional average and unphysical amplitude reductions. This effect becomes important especially for times far from the detection time of the ITE on the reference probe. To avoid these shortcomings of CAS, we have introduced and applied an alternative analysis technique. This reveals a monotonic dependence between the vertically averaged inverse radial density scale length and the probability for a subsequent ITE at the lower probe. The inward movement of the mode prior to an ITE at the upper probe could be confirmed by comparing ITEs to the average evolution of the mode.

These results provide a confirmation that profile steepening is at the origin of ITEs on TORPEX. Evidence for both local [105,125] and global [134] steepening has been obtained.

Blob motion

After identifying the blob generation mechanism from ideal interchange waves in the preceding chapter, we focus in the following on the properties of blobs once they are formed.

The basic mechanism governing blob propagation has first been described in [128] and can be understood as follows. An effective gravity force, due to ∇B and curvature for instance, gives rise to particle drifts that are directed in opposite direction for electrons and ions. Due to the vertical density gradient of the blob, this leads to charge accumulation at the top and at the bottom of the blob, as sketched in Fig. 5.1.1. The resulting vertical electric field gives rise to a radial $\mathbf{E} \times \mathbf{B}$ convection. The magnitude of this cross-field drift depends on the available current paths to damp charge separation. It is a crucial quantity, as it governs the fraction of particles and heat that is transported to the wall.

In the first part of this chapter, we discuss blob motion in the framework of the 2D, sheath limited model [128, 129]. This assumes that parallel currents are determined by sheath boundary conditions. After introducing simplified model equations, we discuss previously published scaling laws for the blob velocity in the three limits where charge separation is damped by parallel currents [128], inertia [136, 137], and ion-neutral collisions [138]. We then generalize these results and derive an analytical expression for the blob velocity that incorporates all these effects [139]. This scaling law is then compared with numerical simulations from [140] and results from recent

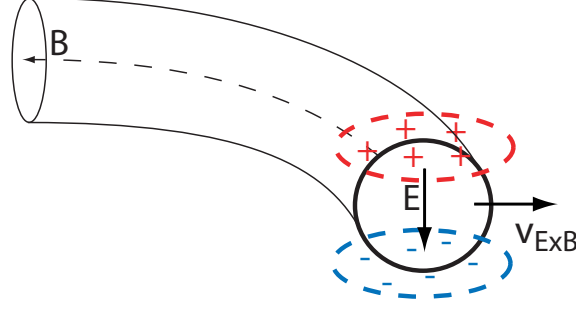


Figure 5.1.1: Sketch illustrating the basic mechanism of blob propagation proposed in [128]. The blob is a field aligned structure of enhanced density compared to the surrounding plasma. It gets polarized due to charge dependent drifts such as those generated by ∇B and curvature. The resulting electric field gives rise to a radial $\mathbf{E} \times \mathbf{B}$ convection.

simulations performed in our group [141, 142].

In the second part, blob motion is studied experimentally on TORPEX and measured blob velocities are compared with theory predictions. By using different ion gases, we cover for the first time in an experiment two different regimes, with blob propagation damped either by parallel currents or by ion-polarization currents, respectively. Good agreement with the above mentioned scaling law suggests that parallel currents significantly damp blob motion in hydrogen, while it provides a negligible contribution in heavy gases. This interpretation is confirmed in experiments where the connection length, thus the importance of parallel currents, is varied by inserting a second limiter. Performing a neutral pressure scan further shows the damping of blob motion due to neutral friction. Finally, open questions and possible further studies are discussed.

5.1 Simple 2D models for blob motion

In this section, we discuss the simplified model equations that describe sheath limited, 2D blobs. Integrating $\nabla \cdot \mathbf{J} = 0$ (quasi-neutrality condition) along the magnetic field under the assumption of constant electron temperature, cold ions ($T_i \ll T_e$), a curved magnetic field that is intercepted perpendicularly at both ends by conducting walls, and 2D dynamics, yields the following vorticity equation [20]

$$\frac{2c_s^2 m_i}{RB} \frac{\partial n}{\partial z} = \frac{m_i}{B^2} \nabla_{\perp} \cdot \left(n \frac{D \nabla_{\perp} V_{pl}}{Dt} + n \nu_{in} \nabla_{\perp} V_{pl} \right) - \frac{n e^2 c_s}{T_e L_c} V_{fl}. \quad (5.1.1)$$

Here, $c_s \approx \sqrt{T_e/m_i}$ is the ion sound speed, m_i the ion mass, n the electron density, B the magnetic field (oriented as in Fig. 5.2.1 (b)), L_c the connection length (wall-to-wall), R the major radius, V_{pl} the electrostatic plasma potential and $V_{fl} = V_{pl} - \mu T_e/e$ the floating potential. ν_{in} is the ion-neutral collision frequency and $D/Dt = \partial/\partial t + \mathbf{v}_{E \times B} \cdot \nabla$. The left hand side (l.h.s.) term is the divergence of the electron diamagnetic current, the drive for blob motion. The current loop is closed by ion

polarization currents, ion currents caused by a neutral friction force, and sheath currents. These effects are taken into account by the three terms on the right hand side (r.h.s) of Eq. (5.1.1). The sheath current term is a factor of two smaller compared to some simulations, owing to the assumption of a density at the sheath edge which is half the upstream density in the bulk plasma.

The sheath current term is the linearized expression of $-j_{\parallel\text{tot}}/L_c$, where $j_{\parallel\text{tot}}$ is the total parallel current density (at both ends of a field line) given by

$$j_{\parallel\text{tot}} = 2 \cdot \frac{nc_s e}{2} (1 - \exp^{-eV_{fl}/T_e}). \quad (5.1.2)$$

Eq. (5.1.1) has two unknowns, n and V_{pl} (V_{fl} and V_{pl} differ here merely by a constant). To close the system, we take the first order continuity equation

$$\frac{D}{Dt} n = (\partial/\partial t + \mathbf{v}_{E \times B} \cdot \nabla) n = 0. \quad (5.1.3)$$

In the following, we use Eqs. (5.1.1) and (5.1.3) to derive blob velocities in different limits and finally, in Sec. 5.1.4, a blob velocity formula that takes into account all different damping mechanism.

5.1.1 Blob motion damped by parallel currents

Here, we consider blob motion for the case where the sheath parallel current, the third term on the r.h.s of Eq. (5.1.1), dominates over the two other damping mechanisms. As shown in [128], Eqs. (5.1.1) and (5.1.3) then allow for an analytical solution for a density blob of the form

$$n_b = n_b^{(r)}(r, t) \cdot n_b^{(z)}(z) = n_b^{(r)}(r - v_b t) \cdot \exp(-z^2/\delta^2), \quad (5.1.4)$$

which describes a blob moving radially with constant velocity v_b and with a fixed Gaussian shape of width δ in the vertical direction. $n_b^{(r)}$ is an arbitrary function. Inserting this expression in the continuity equation (5.1.3), and using the coordinate system as in Fig. 5.2.1 (b) (except that the toroidal coordinate has been integrated out), one finds

$$\begin{aligned} \left(\frac{\partial}{\partial t} + \mathbf{v}_{E \times B} \cdot \nabla \right) n_b &= \frac{\partial n_b}{\partial t} + \frac{1}{B} \left(\frac{\partial V_{pl}}{\partial z} \frac{\partial n_b}{\partial r} - \frac{\partial V_{pl}}{\partial r} \frac{\partial n_b}{\partial z} \right) = 0 \\ \iff \frac{n_b}{n_b^{(r)}} \frac{\partial n_b^{(r)}}{\partial r} \left(\frac{1}{B} \frac{\partial V_{pl}}{\partial z} - v_b \right) &= \frac{1}{B} \frac{\partial V_{pl}}{\partial r} \frac{\partial n_b}{\partial z}. \end{aligned} \quad (5.1.5)$$

If $\partial V_{pl}/\partial r = 0$, this reduces to $v_b = 1/B \cdot \partial V_{pl}/\partial z$. Next, we insert expression (5.1.4) in Eq. (5.1.1), where we retain only the third term on the r.h.s. From this, we obtain the following expression for V_{fl}

$$V_{fl} = 4 \frac{L_c}{R} \frac{\rho_s^2}{\delta^2} c_s B \cdot z, \quad (5.1.6)$$

where $\rho_s = \sqrt{T_e m_i / (eB)}$ is the ion sound Larmor radius. Inserting this expression for V_{fl} in Eq. (5.1.5) and noting that V_{fl} and V_{pl} differ only by a constant yields

$$v_b = 4 \frac{L_c \rho_s^2}{R \delta^2} c_s. \quad (5.1.7)$$

This is the expression for the blob velocity from [128]. Among other dependencies, it states that the blob velocity increases with decreasing blob size.

5.1.2 Blob motion damped by neutrals

Here, we examine blob motion damped by neutral friction. We consider a density blob n_b as defined in Eq. (5.1.4) and look for solutions where V_{fl} is a linear function of z . From Eq. (5.1.5), we find that V_{fl} is given by $V_{fl} = Bv_b z + \text{const.}$ Inserting n_b in Eq. (5.1.1), where we retain only the second term on the r.h.s, we find

$$\begin{aligned} \frac{2c_s^2 m_i}{RB} \frac{\partial n_b}{\partial z} &= \frac{m_i \nu_{in}}{B^2} \nabla_{\perp} \cdot (n_b \nabla_{\perp} V_{pl}) \\ &\iff \\ \frac{2c_s^2 m_i}{RB} \frac{(-2z)}{\delta^2} n_b &= \frac{m_i \nu_{in}}{B^2} (\nabla_{\perp} n_b \cdot \nabla_{\perp} V_{pl} + n_b \Delta_{\perp} V_{pl}) \\ &= \frac{m_i \nu_{in}}{B^2} \left(\frac{(-2z)}{\delta^2} n_b B v_b + 0 \right) \\ &\iff \\ v_b &= \frac{2c_s^2}{R \nu_{in}}. \end{aligned} \quad (5.1.8)$$

This is the scaling law that was derived and experimentally verified in [138].

It is interesting to note that a blob of the form (5.1.4) and a floating potential given by $V_{fl} = Bv_b z$ allows for a solution of the complete system of equations (5.1.1) and (5.1.3). The first term on the r.h.s of Eq. (5.1.1) vanishes in that case and v_b can be written as

$$v_b = \frac{\sqrt{\frac{2\delta}{R}} c_s}{\frac{1}{\rho_s^2 L_c} \sqrt{\frac{R}{2}} \frac{\delta^{5/2}}{2} + \frac{\nu_{in} \sqrt{R\delta}}{\sqrt{2} c_s}}. \quad (5.1.9)$$

This solution retrieves expressions (5.1.7) and (5.1.8) in the limit $\nu_{in} \rightarrow 0$ and $L_c \rightarrow \infty$, respectively.

5.1.3 Blob motion damped by ion-polarization currents

Eqs. (5.1.1) and (5.1.3) allow for solutions describing blobs that move as rigid structures at constant radial velocity. In this case, V_{pl} and V_{fl} are linear functions of z . However, this can not be a solution when inertia, the first term on the r.h.s of Eq. (5.1.1), is the only damping term (i.e., when parallel currents and neutral friction are absent). Indeed, the inertia term vanishes in that case and one would find $\partial n_b / \partial z = 0$. A simple analytical blob solution for the case where inertia is

the main damping mechanism does therefore not exist. Refs. [137, 143] propose a blob velocity that scales as $v_b \propto \sqrt{\delta/R} \cdot c_s$. We use here an argument similar to that in [143] to derive this expression. We consider Eqs. (5.1.1) and (5.1.3) in the limit $L_c \rightarrow \infty$ and $\nu_{in} \rightarrow 0$. We normalize spatial scales to the blob vertical size δ , temporal scales to $\gamma_{int}^{-1} = \sqrt{R\delta}/(\sqrt{2}c_s)$, electrostatic potential to $\gamma_{int}B\delta^2$, and n to an arbitrary reference density. We can then express Eqs. (5.1.1) and (5.1.3) in the following normalized form

$$\begin{aligned} \frac{\partial \tilde{n}}{\partial \tilde{z}} &= \tilde{\nabla} \cdot \left(\tilde{n} \frac{D \tilde{\nabla}_\perp \tilde{\phi}}{D \tilde{t}} \right) \\ \frac{D \tilde{n}}{D \tilde{t}} &= 0. \end{aligned} \quad (5.1.10)$$

Here, the tilde symbol indicates dimensionless quantities. By solving this system of equations, one can obtain the blob velocity $\tilde{v}_{peak}(\tilde{t})$, e.g. the velocity of the density peak. Using physical units, we obtain the family of solutions

$$v_{peak}(t) = \sqrt{\frac{2\delta}{R}} c_s \tilde{v}_{peak} \left(\sqrt{\frac{2}{R\delta}} c_s t \right). \quad (5.1.11)$$

Therefore, provided that $\tilde{v}_{peak}(\tilde{t})$ reaches a quasi stationary phase, this velocity scales as $v_{peak} \propto \sqrt{\frac{2\delta}{R}} c_s$. This motivates the *inertial scaling* [137, 143]

$$v_b \propto \sqrt{\frac{2\delta}{R}} c_s. \quad (5.1.12)$$

5.1.4 Generalized expression for blob velocity

In the previous sections, we have discussed scaling laws for blob velocity considering different damping mechanisms individually. We have also derived a blob formula, Eq. (5.1.9), that includes the combined damping by sheath parallel currents and by neutral friction. Here, we perform an estimate of the different terms in Eq. (5.1.1) to derive a blob velocity formula that takes into account the combined effect of all three damping mechanisms [139]. We assume that the density blob is a monopole structure. In the blob solutions in Secs. 5.1.1 and 5.1.2, the plasma potential was found to be a linear function of the vertical coordinate z . At least for the potential far away from the center of the blob, this is unphysical. In agreement with numerical simulations (see e.g. Fig. 5.1.2) and measurements shown in Fig. 5.2.6, we assume instead a dipolar potential structure with a positive and negative pole at the top and at the bottom of the density blob, respectively. We define now the blob size a_b as the vertical half width at half maximum of the density profile of the blob. Note that this slightly differs from the blob size δ used above and we have $a_b = \sqrt{\log 2} \cdot \delta$. We further allow for a finite background density and define δn and n as the blob density

above background and the total blob density, respectively. This is illustrated in Fig. 5.2.3 (b). We estimate the terms of Eq. (5.1.1) at the position of the maximum positive potential as follows: $\partial n/\partial z \sim -\delta n/a_b$, $\nabla_\perp V_{pl} = 0$, $\nabla^2 V_{pl} \sim -V_{pl}/a_b^2$, and $V_{fl} \sim Bv_b a_b$. Further, we assume that the blob is subject to secondary instabilities with a growth rate γ_{inst} that can limit its motion [144, 145]. Setting $D/Dt \sim \gamma_{inst}$, we obtain

$$v_b = \frac{\sqrt{\frac{2a_b}{R}} c_s}{\frac{\gamma_{inst}}{\gamma_{int}} + \frac{1}{\rho_s^2 L} \sqrt{\frac{R}{2}} a_b^{5/2} + \frac{\nu_{in} \sqrt{R a_b}}{\sqrt{2} c_s}} \frac{\delta n}{n}, \quad (5.1.13)$$

with $\gamma_{int} = \sqrt{2} c_s / \sqrt{R a_b}$ the ideal interchange growth rate and $\rho_s \approx \sqrt{T_e m_i} / (eB)$ the ion sound Larmor radius.

The terms in the denominator represent the damping of blob velocity due to inertia, parallel currents to the sheath, and ion-neutral collisions, respectively. The factor $\delta n/n$ describes the slowing down by a finite background density [146]. Eq. (5.1.13) is very similar to Eq. (5.1.9) except for the additional damping term due to secondary instabilities on the blob. We set $\gamma_{inst} = \gamma_{int}$. Then, Eq. (5.1.13) retrieves the formulas (5.1.7), (5.1.8), and (5.1.12) in the limits where either of the different damping terms dominates over the others.

In [147], we have also considered the case where secondary instabilities are driven by shear flows. We have set $\gamma_{inst} = v_b/a_b$, and found a very similar result as with $\gamma_{inst} = \gamma_{int}$.

It is useful to define dimensionless quantities $\tilde{a}_b = a_b/a^*$ and $\tilde{v}_b = v_b/v^*$, where a^* and v^* , similarly to [20] and references therein, are defined as

$$a^* = \left(\frac{4L_c^2}{\rho_s R} \right)^{1/5} \rho_s, \quad v^* = \left(\frac{2L_c \rho_s^2}{R^3} \right)^{1/5} c_s. \quad (5.1.14)$$

Using this normalisation, Eq. (5.1.13) takes the following form

$$\tilde{v}_b = \frac{\sqrt{2\tilde{a}_b} \cdot \delta n/n}{1 + \sqrt{2\tilde{a}_b^{5/2}} + \tilde{\eta} \sqrt{\tilde{a}_b}}, \quad \tilde{\eta} = \frac{\nu_{in} \rho_s}{c_s} \left(\frac{L_c R^2}{\sqrt{8} \rho_s^3} \right)^{1/5}. \quad (5.1.15)$$

We see that the importance of the different damping mechanisms depends upon the two parameters \tilde{a}_b and $\tilde{\eta}$. The three limits discussed above correspond thus to $\tilde{a}_b^{5/2}, \tilde{\eta} \sqrt{\tilde{a}_b} \ll 1$, to $\tilde{a}_b^{5/2} \gg 1, \tilde{\eta} \sqrt{\tilde{a}_b}$, and to $\tilde{\eta} \gg 1/\sqrt{\tilde{a}_b}, \tilde{a}_b^2$.

5.1.5 Comparison with seeded blob simulations

Extensive theoretical and numerical studies have been performed to investigate the dynamics of 2D blobs in the sheath limited model [136, 140, 143–145, 148–151]. These works focus on the dynamics of a so-called seeded blob, i.e., the evolution of a (typically) Gaussian shaped initial density structure. This shows that blobs with $\tilde{a}_b \approx 1$ are the most structurally stable. Smaller blobs are subject to the Kelvin-Helmholtz instability and quickly deform in a mushroom-like structure. For blobs

with $\tilde{a}_b \gtrsim 1$, parallel currents are the dominant damping mechanism and blobs develop finger-like structures due to the interchange instability [144, 145, 148, 150]. Despite this rather complicated evolution, the blob velocity, at least if evaluated from the propagation of the density peak, reaches a quasi-stationary phase [140]. In Fig. 5.1.3 (a), we plot this blob velocity versus initial blob size from Ref. [140]. Blob size and velocity from [140] are multiplied by $(\alpha^2/2\beta)^{0.2} \cdot \sqrt{\ln 2}$ and $(4\alpha/\beta^3)^{0.2}$, respectively (α and β are parameters defined in [140]) for consistency with Eqs. (5.1.14) and (5.1.15). We also took into account a factor two in the parallel current term assumed in [140]. We compare these values in Fig. 5.1.3 (a) with the scaling law, Eq. (5.1.15). This shows good agreement with the simulation results for all blob sizes.

In all the above mentioned references and in our calculations above, a linearized expression for the parallel current, Eq. (5.1.2), is used. Recent measurements on TORPEX reveal an asymmetric dipolar structure of J_{\parallel} (see [60] and Sec. 6.1), which is attributed to the fact that $|eV_{fl}/T_e| \gtrsim 1$ and the linearization of the parallel current term thus questionable. To investigate the effect of this linearization on blob dynamics, we have performed 2D seeded blob simulations [141]. We used the 2D code of Refs. [70, 71] to solve the drift-reduced Braginskii equations

$$\frac{D\nabla^2 V_{pl}}{Dt} = \frac{2BT_e}{nm_i R} \frac{\partial n}{\partial z} + \nu \nabla^4 V_{pl} + \frac{c_s e B^2}{m_i L_c} \Theta \quad (5.1.16)$$

$$\frac{Dn}{Dt} = \frac{2}{eRB} \left(T_e \frac{\partial n}{\partial z} - en \frac{\partial V_{pl}}{\partial z} \right) + D \nabla^2 n - \frac{nc_s}{L_c} \exp(\mu - eV_{pl}/T_e) \quad (5.1.17)$$

Neutral friction is not taken into account and, contrary to the full code [70, 71], a constant electron temperature is assumed here. Compared to Eq. (5.1.1), there is a viscosity term in the vorticity equation (5.1.16) and the density inhomogeneity in the inertia term has been neglected. The latter is a common simplification known as the Boussinesq approximation [151]. Two expressions for Θ are used, namely $\Theta = \Theta_{sh} = [1 - \exp(\mu - eV_{pl}/T_e)] = [1 - \exp(-eV_{fl}/T_e)]$ and $\Theta = \Theta_{lin} = eV_{fl}/T_e$ for the full and the linearized expression of the parallel current, respectively. Higher order terms are added to the continuity equation (5.1.17) with respect to (5.1.3). These are a curvature term, a diffusion term, and parallel losses. As shown in [140], the curvature term has negligible effect on blob propagation, at least for the parameters considered in that work. The kinetic viscosity ν and the diffusion coefficient D , necessary for the stability of the code, are chosen such that their effect on the blob velocity is negligible [141].

Before discussing simulation results, we write the above set of equations using the normalized quantities of Eq. (5.1.15). We normalize spatial scales and temporal scales to a^* and a^*/v^* , respectively. Further, we define $\tilde{V}_{pl} = V_{pl}/(a^* B v^*)$, $\tilde{n} = n/n_0$, $\tilde{\nu} = \nu/(a^* v^*)$, and $\tilde{D} = D/(a^* v^*)$. The tilde indicates dimensionless quantities, n_0 is an arbitrary reference density and a^* , and v^* are defined in Eq. (5.1.14). For the case $\Theta = \Theta_{sh}$, we obtain

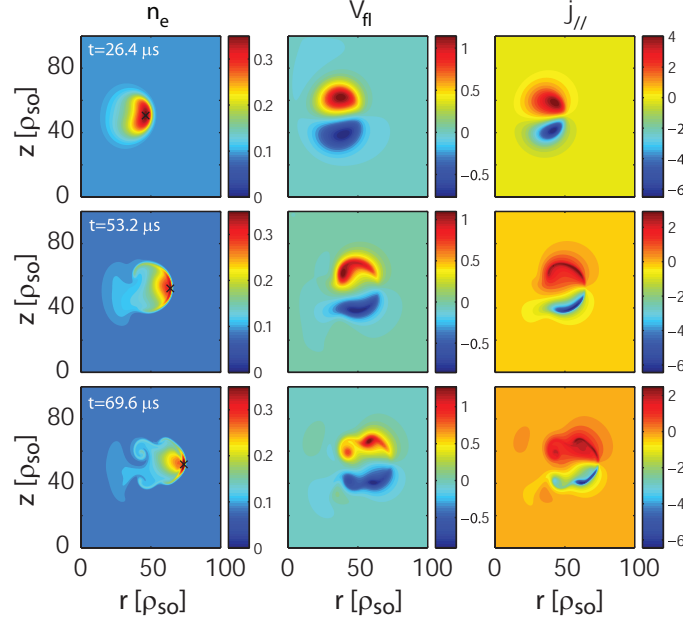


Figure 5.1.2: An example if a seeded blob simulation [141] using the 2D fluid code of Refs. [70,71]. The initial blob size for this simulation is $\tilde{a}_b \approx 0.9$ and the full form for the sheath current is used. At different times of the simulations, 2D profiles of the electron density, floating potential and parallel current density to the limiter are shown.

$$\frac{D\tilde{\nabla}^2\tilde{V}_{pl}}{D\tilde{t}} = \frac{2}{\tilde{n}}\frac{\partial\tilde{n}}{\partial\tilde{z}} + \tilde{\nu}\tilde{\nabla}^4\tilde{V}_{pl} + \frac{2}{\kappa_0}\left[1 - \exp(-\kappa_0\tilde{V}_{fl})\right] \quad (5.1.18)$$

$$\frac{D\tilde{n}}{D\tilde{t}} = \frac{2}{\kappa_1}\left(\frac{\partial\tilde{n}}{\partial\tilde{z}} - \kappa_0\tilde{n}\frac{\partial\tilde{V}_{pl}}{\partial\tilde{z}}\right) + \tilde{D}\tilde{\nabla}^2\tilde{n} - \frac{2}{\kappa_1\kappa_0}\tilde{n}\exp(-\kappa_0\tilde{V}_{fl}) \quad (5.1.19)$$

where κ_0 and κ_1 are defined as $\kappa_0 = (8L_c^3\rho_s/R^4)^{0.2}$ and $\kappa_1 = (2L_cR^2/\rho_s^3)^{0.2}$ and $\kappa_0\tilde{V}_{pl} = \kappa_0\tilde{V}_{fl} + \mu$. For $\tilde{\nu}, \tilde{D} \rightarrow 0$, linearization of the current term and neglecting the curvature and the parallel loss terms in the continuity equation, the evolution of Eqs. (5.1.18) and (5.1.19) depends indeed only on the initial conditions, i.e., on the normalized blob size \tilde{a}_b and $\delta n/n$, consistently with the scaling law given by Eq. (5.1.15).

We note that besides \tilde{a}_b and $\delta n/n$, blob dynamics and errors due to the linearization of the parallel current term depend at least on κ_0 as well.

For the simulations, we use a value of κ_0 evaluated for typical TORPEX parameters: $T_e = 2.5$ eV, $B = 0.8$ T, $R = 1$ m, $L_c = 2\pi$ m, and $m_i = 1$ a.m.u. This results in a value of $\kappa_0 \approx 1.3$. The blob is initialized with a Gaussian density profile $\tilde{n} = \tilde{n}_{bg} + \tilde{n}_b \exp\{-\log(2)[(\tilde{r} - \tilde{r}_0)^2 + (\tilde{z} - \tilde{z}_0)^2]/\tilde{a}_b^2\}$, where $(\tilde{r}_0, \tilde{z}_0)$ is the initial position of the blob. The background density \tilde{n}_{bg} and the peak blob density \tilde{n}_b are chosen such that $\tilde{n}_b/\tilde{n}_{bg} = 3$ and thus the factor $\delta n/n$ in Eq. (5.1.15) is equal to 0.75 (see definition of δn and n in Fig. 5.2.3 (b)).

Fig. 5.1.2 shows the simulated blob dynamics for a normalized blob size $\tilde{a}_b \approx 0.9$,

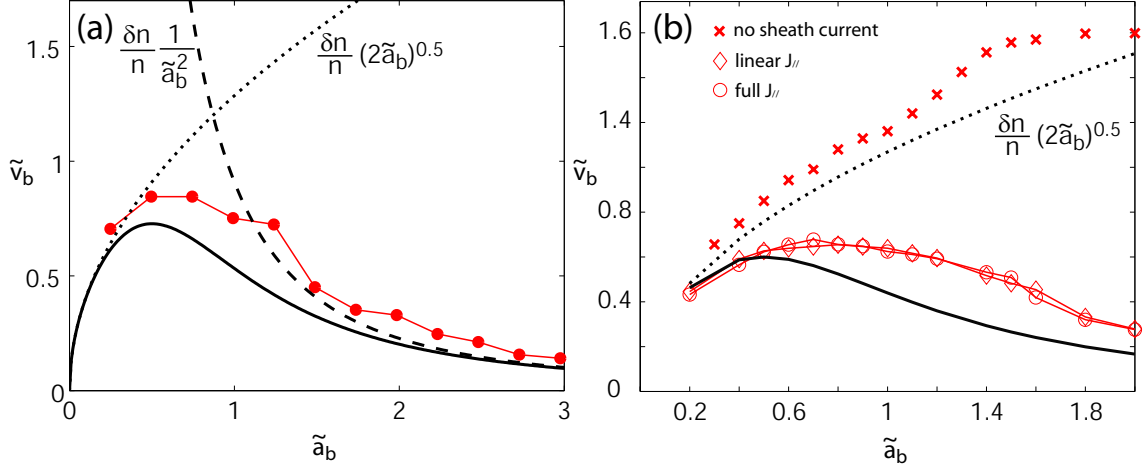


Figure 5.1.3: (a): Blob velocity vs. initial vertical size data from [140]. The scaling law, Eq. (5.1.15), is also plotted for $\nu_{in} = 0$ and $\delta n/n = 10/11$ (solid curve). The limits without parallel current (dotted) and without the effect of ion polarization currents (dashed) are also plotted. (b): Simulation results from [141]. Blob velocity vs. size is evaluated using the full parallel current term (circles), the linearized form (diamonds), and for the case without parallel currents (crosses). In these simulations, $\delta n/n = 0.75$.

using the full expression of the parallel current term. The left column shows the radial propagation of the density blob, the middle column the dipolar structure of V_{fl} , and the right column the parallel sheath current. Clear asymmetries in the dipolar structure of V_{fl} and more importantly of $j_{||}$ are apparent. This asymmetry, which does not occur if the sheath current is linearized, shows negligible effect on blob propagation [141, 142]. This is apparent from the almost identical radial velocity of the peak density in Fig. 5.1.3 (b), obtained using the linearized (diamonds) and the full (circles) current term and \tilde{a}_b in the range [0.2, 2]. In [141], runs were also performed with $R = 0.25$ m that result in a value of $\kappa_0 \approx 4$. Again, linearization of the parallel current term showed little effect on blob velocities.

The importance of the damping of blob velocity by parallel currents is highlighted by simulations where the sheath current term in the vorticity equation was removed (crosses in Fig. 5.1.3 (b)). Comparison with the scaling law, Eq. (5.1.15) (solid curve), and the expression when sheath damping is not included (dotted curve) show again satisfactory agreement with simulation results.

5.2 Blob motion in TORPEX and comparison with theory

In this section, we describe experiments performed to study the propagation of blobs in TORPEX and compare measurements with the blob theory discussed above. The main goal is to understand and quantify the physical effects that determine the blob radial velocity and to devise methods to actively influence blob motion.

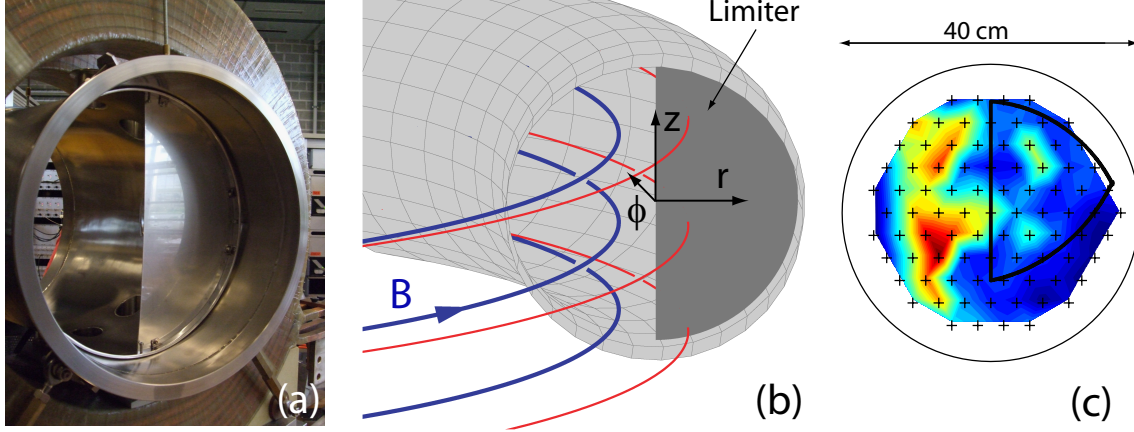


Figure 5.2.1: (a): Picture of the steel limiter installed on a movable sector of TORPEX. (b): Sketch of the experimental setup with two examples of helical magnetic field lines. The blue line lies in the main plasma region and does ~ 3 turns before intercepting the vacuum vessel. The red line lies in the blob region and intercepts the limiter plate after one turn. (c): Snapshot of the I_{sat} profiles obtained with HEXTIP. The arrangement of the LP tips (crosses) is also shown. The black contour indicates the region where both field line ends are connected to the limiter.

Discharges are performed in the ideal interchange mode regime with $N \approx 3$, where, as discussed in Ch. 4, blobs form from radially extending wave crests. In order to reproduce the situation modeled by Eq. (5.1.1), we insert a steel limiter in the blob region, i.e., the region where the plasma dynamics is characterized by radially propagating blobs. A picture of this limiter and a sketch of the setup are shown in Fig. 5.2.1 (a) and (b). Fig. 5.2.1 (c) shows a snapshot of I_{sat} measured with HEXTIP. Two blobs are visible in the limiter shadow region. This setup results in a region characterized by a nearly constant connection length $L_c \approx 2\pi R$ and a nearly perpendicular incidence of the magnetic field on the material surface. The latter avoids complicating effects such as the contribution of the electron diamagnetic current to the blob parallel current, expected for small incidence angles between the magnetic field lines and the wall [152]. This setup further features constant curvature along the magnetic field and good uniformity of fluctuations along magnetic field lines, which is apparent from Fig. 2.5.1 (g).

Theory predicts that the regime where blob motion is damped by parallel currents or ion polarization currents, respectively, depends on the normalized blob size $\tilde{a}_b = a_b/a^*$, where a^* is defined in Eq. (5.1.14). As $a^* \propto \rho_s^{4/5} \propto m_i^{2/5}$, we can expect to significantly vary the normalized blob size by varying the ion mass in the experiment. Therefore, blobs in different working gases (H_2 , He, Ne, Ar) will be studied. Due to the dependence $a^* \propto m_i^{2/5}$, we expect larger normalized blob sizes \tilde{a}_b and stronger damping of blob velocity by parallel currents the smaller the ion mass. The ion sound Larmor radius for the different gases is $\rho_s \approx 3$ mm (H_2), $\rho_s \approx 7$ mm (He), $\rho_s \approx 14$ mm (Ne), and $\rho_s \approx 16$ mm (Ar).

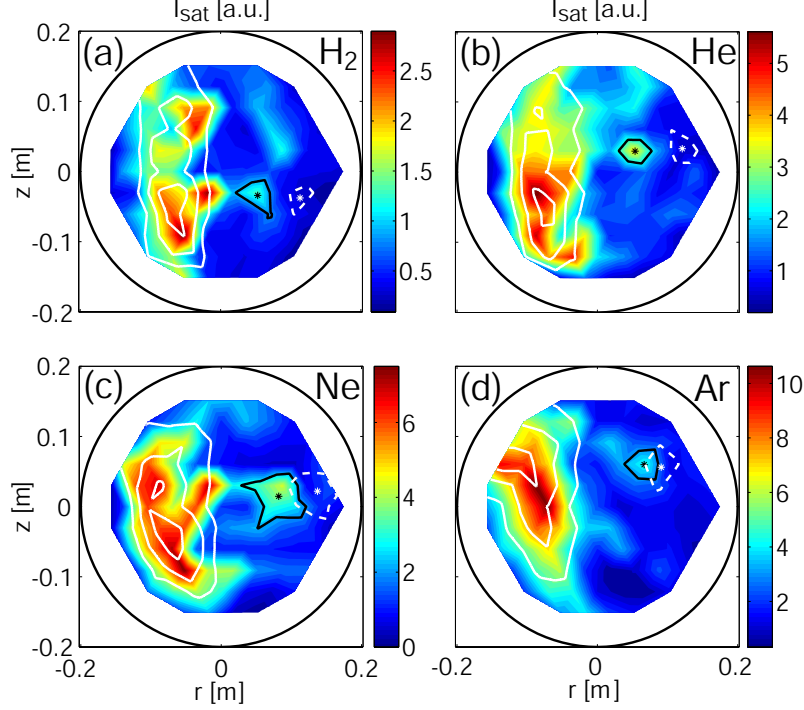


Figure 5.2.2: Snapshots of I_{sat} in the different plasmas. Time averaged profiles are indicated by white contours. A blob as well as its location 36 μs later (76 μs in the case of Ar) is shown on the low-field side.

5.2.1 Ion mass scan

Discharges have been performed in the four working gases hydrogen, helium, neon, and argon, using the setup shown in Fig. 5.2.1 [139]. Blob propagation is investigated using HEXTIP, toroidally displaced by 97° from the limiter. We recall here that this array comprises 86 LPs with 3.5 cm pin separation (see sketch in Fig. 5.2.1 (c)) and provides the evolution of I_{sat} with a temporal resolution of 4 μs . In Fig. 5.2.2 (a)-(d), we show snapshots of I_{sat} obtained in these plasmas. The time averaged profiles (white solid contours) peak on the HFS. Strong fluctuations around the average profiles and the radial movement of blobs are apparent.

Blobs are identified by pattern recognition [153]. This method defines structures as regions where ion saturation current fluctuations $\tilde{I}_{sat}(r, z, t) \equiv I_{sat}(r, z, t) - \langle I_{sat}(r, z) \rangle_t$ exceed a threshold value. It then tracks these structures frame by frame and determines structure-related quantities such as the radial velocity. For the blobs identified this way, we determine the vertical size a_b as follows. During the first four time frames, we evaluate the z -profile of I_{sat} over a vertical cut through the center of the blob. Examples are shown in Fig. 5.2.3 (a)-(b). We then subtract the background density, taken as the average of the nearest local minima located above and below the position of the maximum of I_{sat} . The vertical blob size a_b is defined as the average of the half width half maxima (HWHM) of these four I_{sat} z -profiles.

To assess the size resolution achieved by this procedure, we have applied the analysis to synthetic Gaussian shaped blobs mapped onto the LP grid. We find that

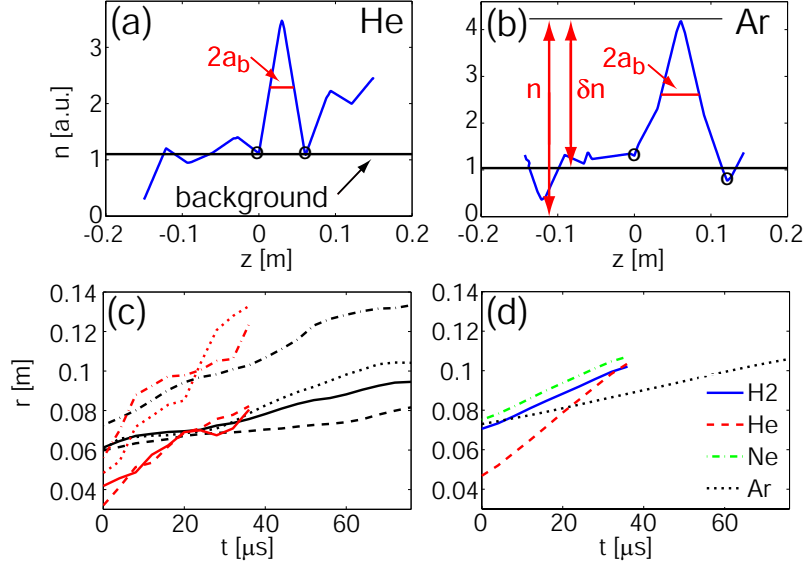


Figure 5.2.3: (a)-(b): Vertical cut through the He and the Ar blob in Fig. 5.2.2 (b) and (d), together with the evaluated quantities a_b , δn , and n (density has been deduced from I_{sat} measurements). (c)-(d): Radial position of the blob as a function of time (c) for examples in He (red) and Ar (black), as well as (d) averaged over all blobs in a given gas.

structure sizes are resolved with an average error $\lesssim 20\%$ as long as $a_b \gtrsim 1.5$ cm. Structures with $a_b \lesssim 1.5$ cm are not detected by pattern recognition, as long as they do not stay close to one LP tip during their lifetime. In the following, we consider structures that exist for at least 10 time frames ($36 \mu\text{s}$) for H₂, He and Ne and 20 time frames ($76 \mu\text{s}$) for the significantly slower blobs in Ar, respectively. The selected blobs typically move by at least one tip spacing during their trajectory, which avoids the detection of blobs with $a_b \lesssim 1.5$ cm. We additionally require that blobs do not undergo merging or splitting [153] during that time, that they travel radially at least to $r_{min} = 4$ cm, and that their trajectories lie mostly in the area defined by the black contours in Fig. 5.2.1 (c), which indicates the region where both ends of the field lines are connected to the limiter. Further, we focus on structures that propagate almost monotonically outwards, i.e. for which $\Delta r_i < 0$ is not allowed for two subsequent steps, where Δr_i is the radial displacement of the blob between frame i and frame $i + 1$. The latter condition excludes between $\sim 35\%$ (He) and $\sim 55\%$ (Ne) of the detected structures. These are mostly structures that, after detaching from the wave crest, do not propagate radially and do not contribute to perpendicular transport. Examples of blobs satisfying the selection criteria are indicated in Fig. 5.2.2 (a)-(d).

We have selected between 395 (Ar) and 1185 (H₂) blobs. In Fig. 5.2.3, we plot the radial position versus time for individual blobs (c) and on average (d). We note that the fluctuations of the instantaneous velocity during individual trajectories can be large (c). This can be explained by the finite spatial resolution of the grid. Trajectories in (d) where finite grid effects are averaged out show relatively small

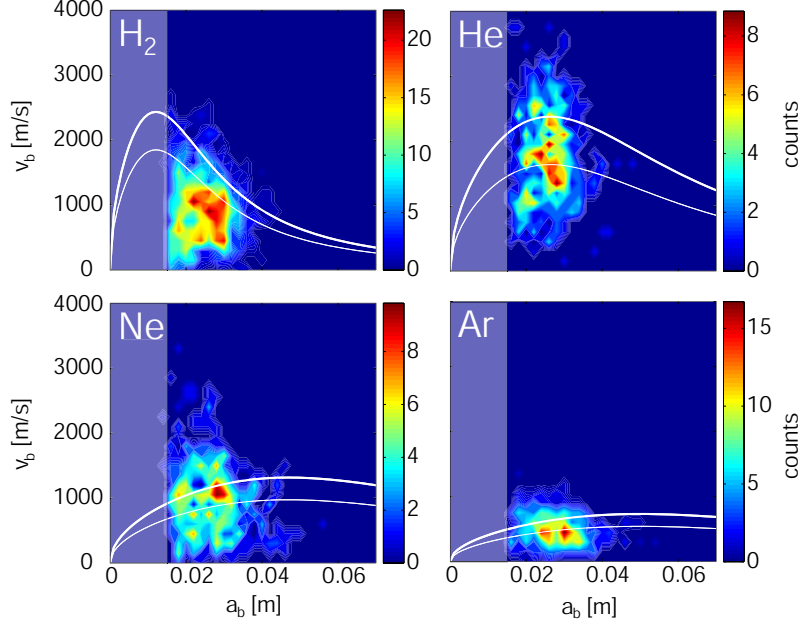


Figure 5.2.4: Joint probabilities of measured radial blob velocity versus vertical blob size in the 4 plasmas. The scaling law Eq. (5.1.13) for $\nu_{in} = 0$ is superimposed (thick solid) for $\delta n/n = 1$, and (thin solid) for $\delta n/n = 0.76, 0.69, 0.74, 0.74$ (H₂, He, Ne, Ar). Shaded areas show the range of blob sizes that are not accessible experimentally.

fluctuations ($\leq 30\%$). Therefore, we define the velocity of an individual blob as the mean velocity over its entire trajectory. In Fig. 5.2.4, we plot the joint probabilities of blob radial velocity versus vertical size, separately for the four gases. We find similar average vertical blob scales $\langle 2a_b \rangle \sim 5$ cm in all four plasmas, consistent with blobs forming from the wave crest of an interchange wave with same vertical wavelength ≈ 13 cm. The average of $\delta n/n$ (see Fig. 5.2.3 (b) for definition) is also similar in the four plasmas, lying between 0.69 (He) and 0.76 (H₂). Clear differences are found however for the typical blob velocities, ranging between $\langle v_b \rangle \sim 500$ m/s (Ar) and $\langle v_b \rangle \sim 1700$ m/s (He). We superimpose now the scaling law, Eq. (5.1.13), showing good agreement for the four gases. We assume a typical blob temperature of half the peak value of the temperature profiles measured with SLP in sweep mode, i.e. $T_e = 4, 7, 6$, and 3.5 eV for H₂, He, Ne, and Ar, respectively, and we neglect ion-neutral collisions by setting $\nu_{in} = 0$.

To investigate the parameter regime covered by the ion mass scan, we now turn to the dimensionless quantities \tilde{a}_b and \tilde{v}_b , for which the scaling law takes the form given in Eq. (5.1.15). Using this normalization, measurements in the different gases can be merged into the same plot, shown in Fig. 5.2.5. We have superimposed the scaling law in dimensionless units for $\tilde{\eta} = 0$ and $\delta n/n = 1$ (white) and $\delta n/n = 0.73$ (black). The dashed line is the expected blob velocity in the absence of parallel currents (see [137, 143] and Sec. 5.1.3) and the dash-dotted line the scaling where sheath currents determine blob velocity (see [128] and Sec. 5.1.1). We find \tilde{a}_b of the order of 1. By varying the ion mass, both regimes $\tilde{a}_b < 1$ and $\tilde{a}_b > 1$ are obtained. For $\tilde{a}_b < 1$, the parallel currents play a minor role and the dashed line approaches

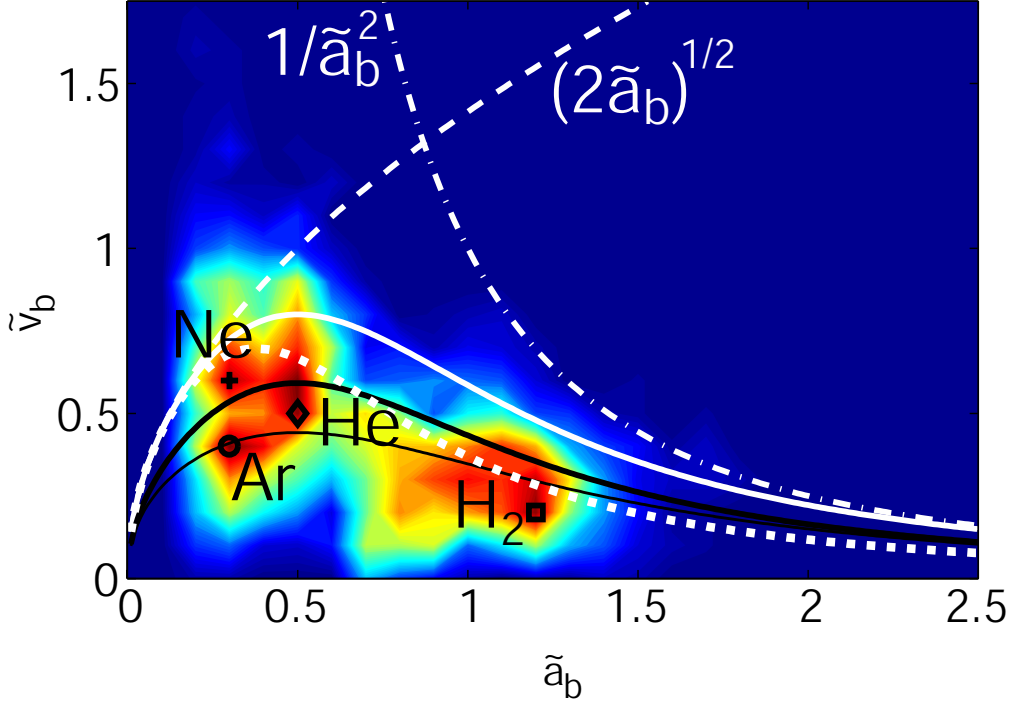


Figure 5.2.5: Joint probability of \tilde{v}_b versus \tilde{a}_b [139]. For better visibility, the distribution for H_2 (\square) and He (\diamond) are normalized to 1, the ones of Ne (+) and Ar (o) to 0.5. The symbols indicate the peak of each distribution. The scaling law Eq. (5.1.15) for $\tilde{\eta} = 0$, $\delta n/n = 1$ (white), $\tilde{\eta} = 0$, $\delta n/n = 0.73$ (black), and $\tilde{\eta} = 0.6$, $\delta n/n = 0.73$ (thin black) as well as the $1/\tilde{a}_b^2$ and $\sqrt{2\tilde{a}_b}$ limits are indicated. The white dotted curve shows the change in blob velocity with respect to the solid, white curve, that would follow from a doubling of the sheath damping.

the experimental results. However, we observe strong deviations from this scaling for $\tilde{a}_b > 1$, interpreted as due to the growing importance of parallel currents. Only in this range does the $1/\tilde{a}_b^2$ scaling show quantitative agreement with experimental results.

Thus far we have assumed $\nu_{in} = 0$. We provide now an estimate of an upper bound for $\tilde{\eta}$ in Eq. (5.1.15). With the measured neutral background pressures $p_n \approx 0.017$, 0.02, 0.014, and 0.0085 Pa for H_2 , He, Ne, and Ar, respectively, a momentum transfer cross section of $\sigma^{mt} \lesssim 2 \cdot 10^{-18} \text{ m}^2$ [90], an ambient temperature T_{amb} of 0.025 eV and an upper bound for the ion temperature $T_i \lesssim 1 \text{ eV}$, we obtain from $\nu_{in} = \frac{p_n}{T_{amb}} \sigma^{mt} v_{th,i}$ values of $\tilde{\eta} \approx 0.5 - 0.6$ for all four gases. By setting $\tilde{\eta} = 0.6$ in Eq. (5.1.15), a relatively small difference ($\leq 25\%$) is obtained compared to the case $\tilde{\eta} = 0$, as shown in Fig. 5.2.5. This indicates that blob velocity is only weakly reduced by ion-neutral collisions.

In the following two sections, we test two predictions that follow from the interpretation of blob motion developed in this section. First, reducing the connection length should influence blob motion for He and more importantly for H_2 blobs in TORPEX. Second, increasing the background gas pressure should reduce blob velocity.

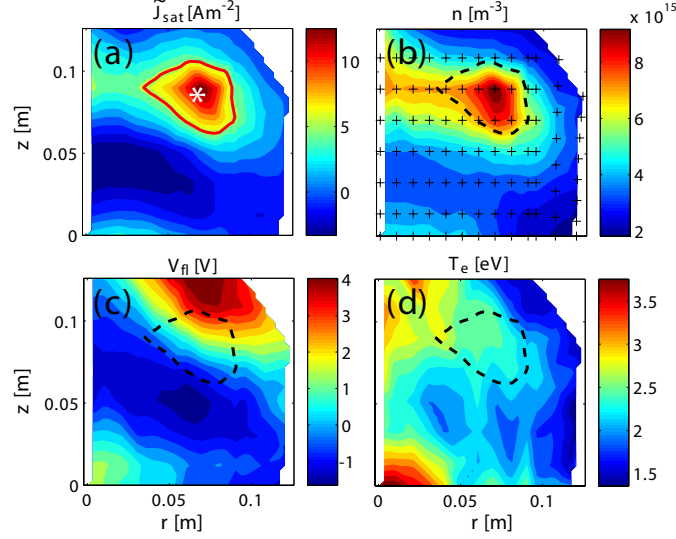


Figure 5.2.6: (a)-(d) Example of the 2D profile of \tilde{J}_{sat} , n , V_{fl} , and T_e for a H_2 blob obtained with the modified conditional sampling method, [105] and Sec. 3.4.

5.2.2 Effect of changes in the connection length

In order to study the dependence of blob velocity upon the connection length, we have installed a second limiter in TORPEX, identical to the first one and toroidally displaced by 180° . We compare blob motion with and without this second limiter. Along the magnetic field in the toroidal direction, HEXTIP is located at 83° and SLP at 118° from the second limiter.

The expected effect of halving the connection length on blob velocity in the different regimes, can be inferred from Fig. 5.2.5. The solid white curve shows the scaling law Eq. (5.1.15) for $\delta n/n = 1$ and $\nu_{in} = 0$ and the white dotted curve the predicted change when the connection length is divided by a factor of 2 (*). From this, we expect negligible changes of blob velocity for the heavy gases, but significant reductions in blob velocity for larger normalized blob sizes. These latter are closer to the regime where parallel currents are the dominant damping mechanism.

We use the same target plasmas as in the previous section, except for discharges in Ar. As argon is ionized very easily, it is difficult to produce profiles that are limited to the high field side with a level of ≈ 300 W of injected microwave power. Therefore, we use an even lower power source [57] to create the desired plasma configuration. We move SLP in between reproducible discharges and apply the BOX-CAS technique described in Sec. 3.4 to reconstruct the 2D propagation of blobs in the different working gases and limiter configurations. This allows us to measure also the blob temperature and its change as the second limiter is installed.

Fig. 5.2.6 shows one frame of the reconstructed 2D evolution of \tilde{J}_{sat} , n , V_{fl} , and T_e for a H_2 blob obtained this way. The reference signal is an I_{sat} signal of a HEXTIP

(*) We assume here that a variation in connection length enters in Eq. (5.1.15) and not in the definition of a^* and v^* . In reality, a variation of L_c changes \tilde{a}_b and \tilde{v}_b and the expected change in blob velocity is harder to access in normalized units.

probe tip at $r = 7$ cm. The measurement points of SLP are indicated by black crosses in (b). For $r \gtrsim 10$ cm, SLP has to be tilted slightly in the toroidal direction to avoid hitting the vessel wall. This is the reason for the non-uniformity of the measurement points in that region. In (a) and (b), we can clearly see a detached blob. Fig. (c) shows the dipolar structure in V_{fl} and (d) the perturbed temperature profile associated with the blob.

To analyze the radial movement of the blob, we identify the blob with a threshold condition on \tilde{J}_{sat} , determine its center of mass, and follow it on a frame by frame basis. We require that the blob be detached from the main plasma and that its contour do not intercept the boundary of our reconstruction domain. In Fig. 5.2.6 (a), we have indicated the blob contour and its center identified in this way by the red contour and the white star. We determine the blob center position as a function of time and evaluate an average radial blob velocity from a linear fit to this curve. Examples of such curves are shown in Fig. 5.2.7 for shots in H₂ and Ar, for different connection lengths and for analysis with different radial positions of the reference probe. To evaluate the blob temperature, we take the average temperature within the blob contour (see Fig. 5.2.6 (d)). For the evaluation of a_b and $\delta n/n$, we use a pin of SLP as a reference probe to determine the conditionally averaged vertical I_{sat} profile of the blob at a given radial position along the vertically aligned SLP probe tips. From this, we compute the half width at half maximum a_b and $\delta n/n$ of the blob. This technique provides more accurate evaluation of these parameters than if evaluated from the 2D profiles, such as the one shown in Fig. 5.2.6 (a). In this case, the blob peak value is underestimated when it falls between the SLP probe tips.

We perform the BOX-CAS analysis for blobs detected at three different radial positions on HEXTIP, $r = 5.25$, 7, and 8.75 cm, respectively. The obtained blob parameters are tabulated in Fig 5.2.10. In Fig. 5.2.8, we are plotting the measured blob radial velocity versus size. Open symbols correspond to blobs from one limiter shots, filled ones to blobs from two limiters shots. Overplotted is the scaling law Eq. (5.1.13) (for $\gamma_{inst} = \gamma_{int}$), including the measured blob T_e , $\delta n/n$, and an estimate of the ion-neutral collision frequency, as discussed in App. B.

These measurements confirm the predictions from Fig. 5.2.5 discussed above. The second limiter mainly affects blob velocities in H₂ and He, with little effect on blobs in Ne and Ar. From the tabulated values in Fig. 5.2.10, we see that inserting the second limiter also reduces the blob temperature, more importantly in H₂ ($\approx 20\%$ reduction) than in the heavier gases ($\approx 10\%$ reduction in Ar). The reduction of blob velocity and the trend across the different gases seem thus to result from both a reduction in blob temperature and an increased damping by parallel currents, which is more important for larger \tilde{a}_b . For example in the hydrogen case and for $a_b = 1.5$ cm, the scaling law in Eq. (5.1.13) predicts that $\approx 60\%$ and $\approx 40\%$ of the reduction of the blob velocity are due to the decrease of the connection length and the blob temperature, respectively. In absolute terms, Eq. (5.1.13) tends to underestimate blob velocity, but still provides a reasonably good estimate of it for the different plasmas.

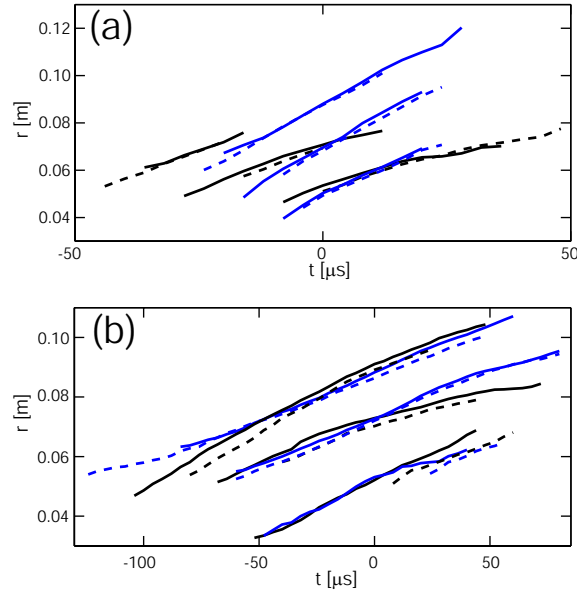


Figure 5.2.7: Radial blob position as a function of time determined from conditionally averaged blob propagation in H₂ (a) and Ar (b). Blue lines correspond to shots with a single limiter, black lines to shots with two limiters. Reference probes at three different radial positions are used. Solid and dashed curves are obtained with a different threshold value to trace the blob. For two-limiter shots in H₂, only data for $r < 10$ cm is available. This is the reason for the shorter trajectories in (a) compared to the one limiter results.

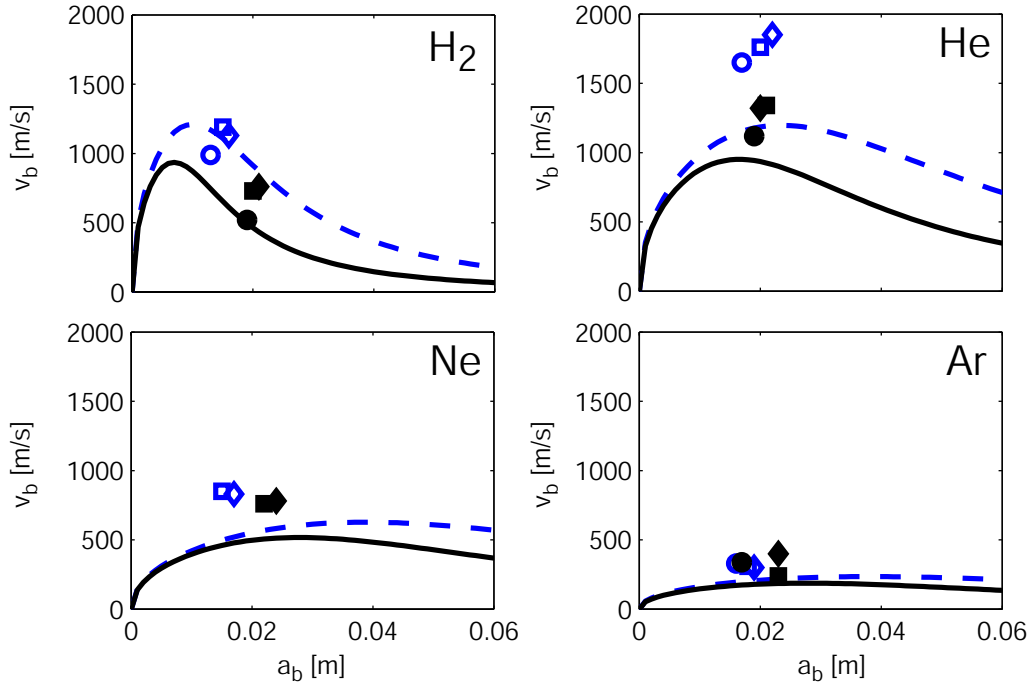


Figure 5.2.8: Blob velocity vs. size for shots with one limiter (blue) and two limiters (black). Eq. (5.1.13) is overplotted for the measured blob parameters. Measured blob parameters are also tabulated in Fig. 5.2.10.

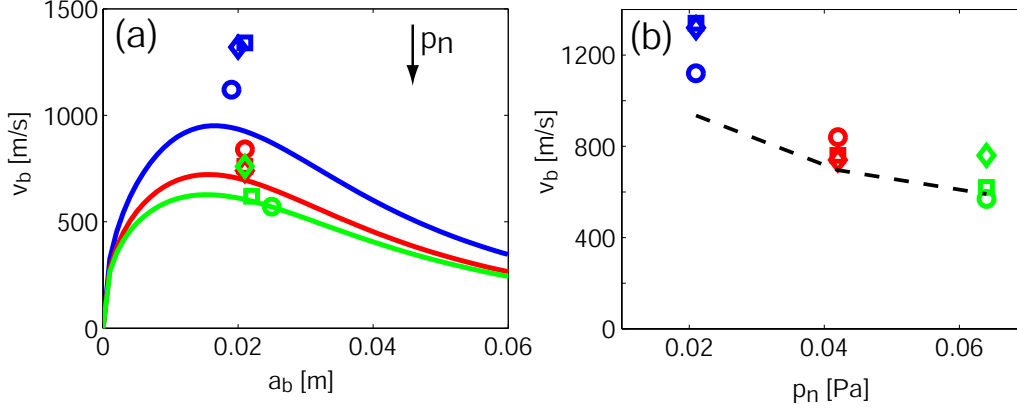


Figure 5.2.9: Results of blob velocity and size for a neutral gas pressure scan in helium. The gas pressure p_n is varied from ≈ 0.021 Pa (blue symbols) to ≈ 0.064 Pa (green symbols). The plotted curves show the predictions from Eq. (5.1.13). The values of blob parameters for the different pressure values are also tabulated in Fig. 5.2.10.

5.2.3 Effect of changes in the neutral gas pressure

Next, we investigate the dependence of blob velocity on the neutral gas pressure. The possibility of influencing the blob velocity by varying the neutral background pressure has already been demonstrated for seeded argon blobs in the VTF device [138]. Here, we investigate the neutral pressure dependence of blob velocity in helium. We have performed discharges for four different neutral pressure values, i.e., $p_n \approx 0.021, 0.042, 0.064$, and 0.085 Pa. We find that increasing the gas pressure affects not only the blobs, but also the mode properties. We observe a monotonic decrease in the mode frequency with increasing gas pressure from ≈ 14 kHz down to ≈ 6 kHz. As the wavelength of the interchange wave remains unchanged, this corresponds to a decrease in the vertical phase velocity of the mode.

Data for the BOX-CAS analysis is available for the three lower gas pressure values. Result of the analysis are tabulated in Fig. 5.2.10 and shown in the velocity vs. size plot in Fig. 5.2.9 (a) and the velocity versus gas pressure plot in Fig. 5.2.9 (b). As expected, we find that blob velocity reduces with increasing gas pressure. Comparison with the scaling law (5.1.13) shows good quantitative agreement, although the predicted trend with gas pressure is weaker than in the experiment.

TABLE I. Blob parameters.

Gas	L (m)	r (cm)	p_n (Pa)	v (m/s)	a (cm)	T_e (eV)	$\delta n/n$
H ₂	2π	5.25	0.014	990	1.3	2.6	0.79
H ₂	2π	7	0.014	1190	1.5	2.4	0.79
H ₂	2π	8.75	0.014	1130	1.6	2.5	0.75
H ₂	π	5.25	0.013	520	1.9	2.0	0.80
H ₂	π	7	0.013	730	2.0	1.9	0.81
H ₂	π	8.75	0.013	760	2.1	2.1	0.79
He	2π	5.25	0.019	1650	1.7	5.5	0.74
He	2π	7	0.019	1760	2.0	5.2	0.74
He	2π	8.75	0.019	1850	2.2	5.0	0.73
He	π	5.25	0.021	1120	1.9	4.6	0.76
He	π	7	0.021	1340	2.1	4.2	0.75
He	π	8.75	0.021	1320	2.0	4.3	0.75
He	π	5.25	0.042	840	2.1	4.1	0.73
He	π	7	0.042	760	2.1	3.6	0.73
He	π	8.75	0.042	740	2.0	3.7	0.74
He	π	5.25	0.064	570	2.5	3.8	0.77
He	π	7	0.064	620	2.2	3.5	0.75
He	π	8.75	0.064	760	2.1	3.6	0.73
Ne	2π	7	0.014	850	1.5	3.8	0.81
Ne	2π	8.75	0.014	830	1.7	3.6	0.80
Ne	π	7	0.013	760	2.2	3.2	0.84
Ne	π	8.75	0.013	780	2.4	3.2	0.82
Ar	2π	5.25	0.014	330	1.6	1.9	0.70
Ar	2π	7	0.014	310	1.8	1.7	0.65
Ar	2π	8.75	0.014	300	1.9	1.7	0.65
Ar	π	5.25	0.015	340	1.7	1.7	0.67
Ar	π	7	0.015	240	2.3	1.5	0.65
Ar	π	8.75	0.015	400	2.3	1.6	0.60

Figure 5.2.10: Summary of blob parameters determined with the BOX-CAS technique for two values of the connection length (Sec. 5.2.2) and three values of neutral gas pressure in He (5.2.3). The different columns indicate the working gas, the connection length in the blob region, the radial position of the reference probe for conditional sampling, the neutral pressure, and blob velocity, size, temperature and $\delta n/n$, i.e., the ratio of blob density above background and total blob density.

5.2.4 Some open questions and outlook for future experiments

In the previous sections, we have experimentally investigated dependencies of blob velocity on ion mass (and thus normalized blob size), connection length, and neutral gas pressure. We have found rather good qualitative and quantitative agreement with blob theories [20] and in particular with the scaling law derived in this thesis, Eq. (5.1.13). This gives us confidence that we have reached a good degree of theoretical understanding of the dynamics of these complicated turbulent structures.

More recently, in the course of biasing experiments that will be presented in Sec. 7.3, we have been investigating the details of floating potential profiles. This reveals time-averaged V_{fl} structures in the blob region even when the bias electrodes are grounded. An example is given in Fig. 7.3.5 (b). Such structures are also present in earlier experiments with one limiter. In Fig. 5.2.11, we plot the profiles of V_{fl} and V_{pl} in hydrogen plasmas, obtained with SLP in sweep mode in the case of one (left) and two (right) limiters. While the floating potential profiles in the blob region ($r \gtrsim 3$ cm) is fairly uniform along the vertical direction in the two-limiter case, significant vertical variations are observed for the one-limiter case. This could indicate that radial background flows are present in that region and they contribute to the blob velocity. Along the vertical, dashed line in Fig. 5.2.11 (a), we measure a potential variation of ≈ 4 V over a distance of 15 cm. A similar value is found for the plasma potential profile in (c). This would result in a quite significant radial velocity of ≈ 350 ms⁻¹ for the one-limiter case, while Fig. 5.2.11 (b) and (d) do not indicate such an effect for the case with two limiters. We presently do not know whether the floating potential structure observed in (a) acts on the blobs or is rather a consequence of them. For example, if blobs are predominantly ejected at midplane ($z \approx 0$), this could create a vertically asymmetric V_{fl} profile.

The observation of the time-averaged V_{fl} structure could motivate further experiments to verify the connection length dependence of blob velocity. A possibility could be to install again two limiters, toroidally separated by 180°. In this case, the V_{fl} profile is fairly uniform along z in the blob region and contributions from background radial flows can be excluded (Fig. 5.2.11 (b)). One could measure the effect on the blob velocity when a third limiter is introduced. It would be convenient if one could easily switch between the two- and the three-limiter configuration. A possibility could be to install the third limiter on a movable system, such that it can be moved in and out of the torus. In that case, it would have to be of reduced vertical size ≈ 15 cm to fit through the TORPEX ports.

There are additional points that should be further investigated and that could, besides contributing to the understanding of blobs, also be helpful for the TORPEX code validation project. The first one is the effect of neutrals on the parallel ion dynamics. For collisionless ions, the pre-sheath density drop is expected to be

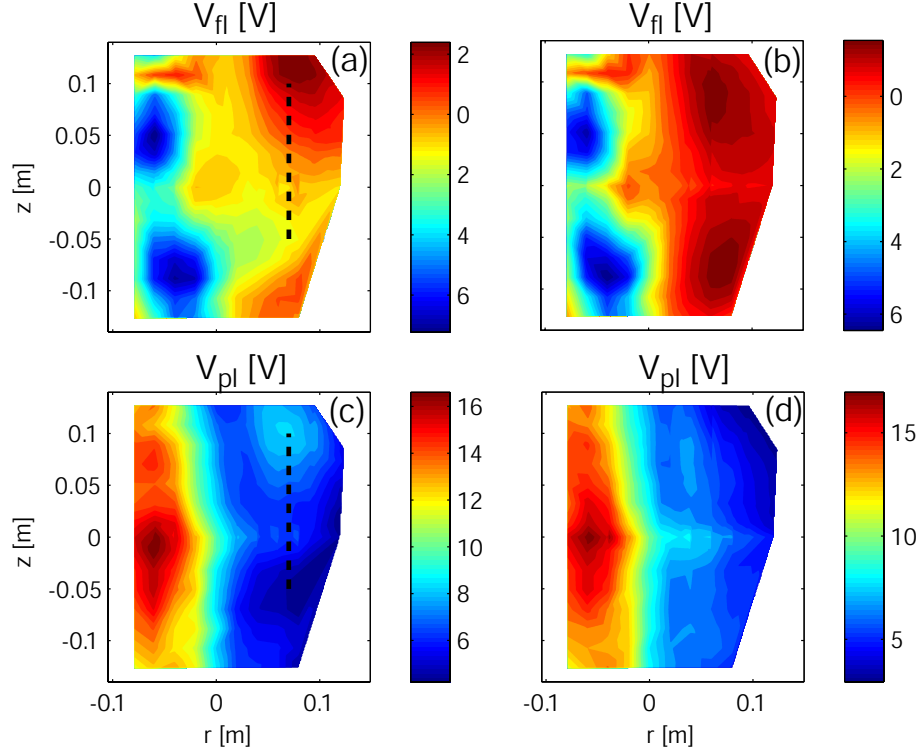


Figure 5.2.11: (a), (c): Profiles of V_{fl} and V_{pl} for one-limiter discharges in hydrogen. (b), (d): The same for two-limiter discharges.

$n_{se}/n_0 \approx 0.5$ [13]. This is the value assumed in Eq. (5.1.1). However, neutral friction can reduce this value. Estimates of this effect and preparations to perform measurements of n_{se}/n_0 in TORPEX are discussed in Sec. 6.3.

Another point is the effective ion mass. It would be useful to have an Omegatron [154] or another ion mass analyzer [155, 156] to measure impurity species and possible concentrations of H_2^+ and H_3^+ ions in hydrogen plasmas.

An open point is also the role of the vertical $\mathbf{E} \times \mathbf{B}$ flow in determining the blob velocity. In [157], it was suggested that energy is transferred from the mean flow to the blobs. It would be interesting to further investigate the importance of this effect for the blob radial velocity.

5.3 Conclusions

We have experimentally investigated cross-field blob velocities and sizes in the open magnetic field line configuration of TORPEX [139, 147]. This features constant curvature along the field lines, nearly constant connection length and almost perpendicular incidence of the magnetic field on a conducting limiter installed in the blob propagation region. Large blob statistics over a wide parameter range allowed a quantitative comparison with a blob velocity scaling derived in Sec. 5.1.4, which agrees remarkably well with the whole experimental data set. In the absence of ion-neutral collisions, it recovers the commonly used SOL-scalings $\tilde{v}_b = 1/\tilde{a}_b^2$ [128] and

$\tilde{v}_b = \sqrt{2\tilde{a}_b}$ [137, 143] for $\tilde{a}_b \gg 1$ and $\tilde{a}_b \ll 1$, respectively, where \tilde{a}_b is the normalized vertical blob size. Ion-neutral collisions provide the dominant damping term for blob velocity when the dimensionless parameter $\tilde{\eta}$ (see Eq. (5.1.15) for definition) satisfies $\tilde{\eta} \gg 1/\sqrt{\tilde{a}_b}$, \tilde{a}_b^2 . In this limit, we retrieve the scaling presented in [138]. We have realized two regimes for blob motion in the experiments. For $\tilde{a}_b < 1$, blob velocity is mainly damped by cross-field ion polarization currents, where for $\tilde{a}_b > 1$, it is limited by parallel currents to the sheath. The damping due to ion-neutral collisions is estimated to be weak ($\leq 25\%$) [139].

This study predicts that a reduction of connection length should allow reducing blob velocity in helium and, more importantly, in hydrogen, while little effect is expected for heavy gases, such as Ne and Ar. This has been tested by introducing a second limiter in TORPEX in order to halve the connection length, and results indeed follow the predicted trends. The scaling law also predicts that an increase in neutral pressure reduces blob radial velocity. This has been experimentally confirmed for blobs in helium plasmas [147].

Finally, some open questions, such as possible contributions of background radial flows to blob velocity, have been discussed and possibilities to address them have been proposed.

To confirm the role of parallel currents in damping blob velocity in the different regimes inferred from these studies, we have performed direct measurements of blob parallel currents [60, 142]. These measurements will be presented in the next chapter.

Blob parallel dynamics

In the previous chapter, we have elucidated the dynamics of blobs in the plane perpendicular to the magnetic field. In the SOL of tokamaks, it is the combination of parallel and cross-field dynamics that determines the distribution of particles and heat, divertor efficiency, transport of parallel momentum, or the distribution of parallel currents.

In this chapter, we investigate some basic aspects of parallel dynamics associated with blobs in TORPEX. We present the first experimental 2D measurements of the field-aligned current associated with blobs [60, 142]. Then, we demonstrate the link between toroidal flows and density blobs [97]. In the last part, we discuss experiments in preparation to measure the decrease of blob density along the magnetic field.

6.1 Measurements of blob parallel currents

Recent experiments on reversed field pinches show that blobs are associated with field-aligned current structures [158, 159]. In tokamaks, large parallel currents are observed during edge localized modes (ELMs) [160, 161] and measurements reveal current carrying filaments within ELMs in MAST [162], ASDEX Upgrade [163], DIII-D [164], and JET [165]. Although the field-aligned nature of current filaments is a common feature, measurements of their 2D structures in the plane perpendicular

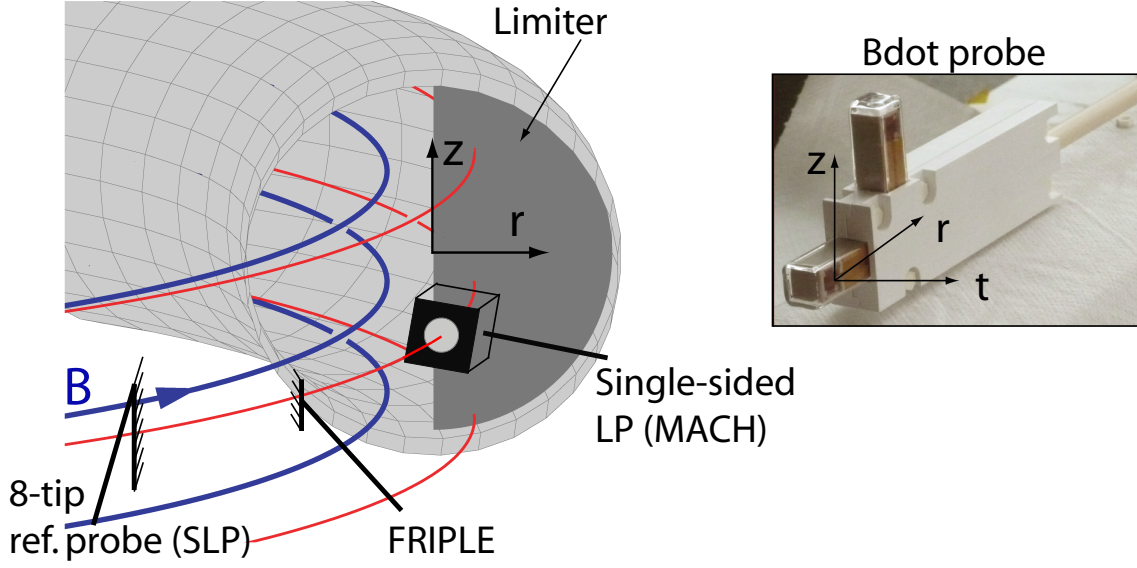


Figure 6.1.1: Schematics (not to scale) with a magnetic field line (in red) intercepting the limiter after one turn in the blob propagation region. Either the single-sided LP or the Bdot probe is placed in front of the limiter. FRIPLE is placed ≈ 1 m from the limiter. SLP, at ≈ 3 m from the limiter, is used as reference probe for CAS.

to the confining field are missing. These are of utmost importance for validating first-principle models of edge/SOL transport and for understanding the origin of the current itself.

In the following, we present the first 2D measurements of the parallel current density associated with blobs [60, 142]. From the study of blob motion on TORPEX, Ch. 5, we expect a dipolar structure of the blob parallel current that is determined by sheath boundary conditions. Further, we expect that these currents are significant in damping charge separation for blobs in hydrogen [139, 147].

6.1.1 Direct measurements of the parallel current density to the limiter

The target plasmas are similar to those in the previous chapter. The working gas is hydrogen and helium, $N \approx 3$, and a steel limiter is installed in the blob region, as sketched in Fig. 6.1.1. Time resolved 2D measurements of the parallel current density J_{\parallel} are obtained from conditionally sampled data of two different diagnostics: a single-sided LP (the MACH probe [63]), and a specially designed current probe, constructed in collaboration with colleagues from RFX [60].

A schematical view of the single sided LP (not to scale) together with the experimental setup is shown in Fig. 6.1.1. The electrode is circular, with a diameter of 8 mm and a collection area $A_{LP} \approx 50 \text{ mm}^2$. The probe is positioned ≈ 3 cm away

from the limiter and the plate is oriented perpendicularly to the magnetic field lines. The plate is kept at the limiter potential, such that the current, I_0 , flowing to the limiter is measured by the probe. The current density is simply $J_{\parallel} = I_0/A_{LP}$.

Time-resolved 2D current density profiles are obtained by performing conditional average sampling (CAS) of J_{\parallel} over many blob events in a time window centered around the blob detection. A description of CAS is given in Sec. 3.4. As schematically shown in Fig. 6.1.1, the eight-tip Langmuir probe array SLP (1.8 cm spacing between tips in the z direction) is located at $r = 7$ cm and toroidally displaced by ≈ 3 m from the limiter. Each SLP tip is biased to -40 V and measures the ion saturation current $I_{sat,i}$. These signals are alternately used as reference signals for CAS to detect blob events, defined by the condition $\tilde{I}_{ref,i} \geq 3\sigma$, where σ is the standard deviation over the whole discharge. The single-sided LP is moved radially in between discharges, thus allowing reconstructing 2D profiles of the parallel current density over a section of the $r - z$ poloidal plane.

The single-sided LP can also be operated in swept mode to apply the BOX-CAS method [105]. As discussed in Sec. 3.4, this provides additionally the conditionally averaged dynamics of electron density n , temperature T_e , floating potential V_{fl} , and plasma potential $V_{pl} = V_{fl} + \mu T_e/e$.

Figure 6.1.2 illustrates conditionally averaged data from the single-sided LP obtained from ≈ 3000 blobs over four identical, 1 s long plasma discharges in hydrogen. Shown are the time evolution of (a) the electron density n at the center of the blob, of (b) the floating potential V_{fl} and of (c) the parallel current density J_{\parallel} at $r = 7$ cm and above and below the center of the density blob. Figure 6.1.2 also shows 2D profiles of n in the left column, of V_{fl} in the central column, and of J_{\parallel} in the right column at three different times during the radial propagation of the blob. The blob detection time $\tau = 0$ corresponds to the central row. The electron temperature (not shown here) at the center of the blob is $T_e \approx 2.5$ eV.

The propagation of the blob with a radial speed ≈ 1100 m/s is clearly visible from the time evolution of the density profiles. Centered around the density blob, the floating potential exhibits an almost perfectly symmetric dipolar structure, with $|V_{fl}| \approx 3$ V at the positions of minimum and maximum values. A dipolar 2D structure of the parallel current density is convected with the density blob, as shown by Fig. 6.1.2 (k-m). Surprisingly, the current density dipolar structure is not symmetric, with a larger level ($J^- \approx -9$ A/m² at the minimum and at $\tau = 0$) of current flowing out of the limiter on the bottom of the blob than that ($J^+ \approx 2$ A/m² at the maximum and at $\tau = 0$) flowing into the limiter at the top of the blob. This asymmetry is discussed later in this section.

A further confirmation of the observed current density profile is provided by independent measurements obtained with a specially designed current probe. This consists of an L-shaped array of 3 miniaturized three-axial pick up coils ($\Delta = 3.5$ cm spaced, each with an effective area of 2.3×10^{-3} m²). This arrangement is a simplified version of that used in the Cluster satellite mission to measure magneto-

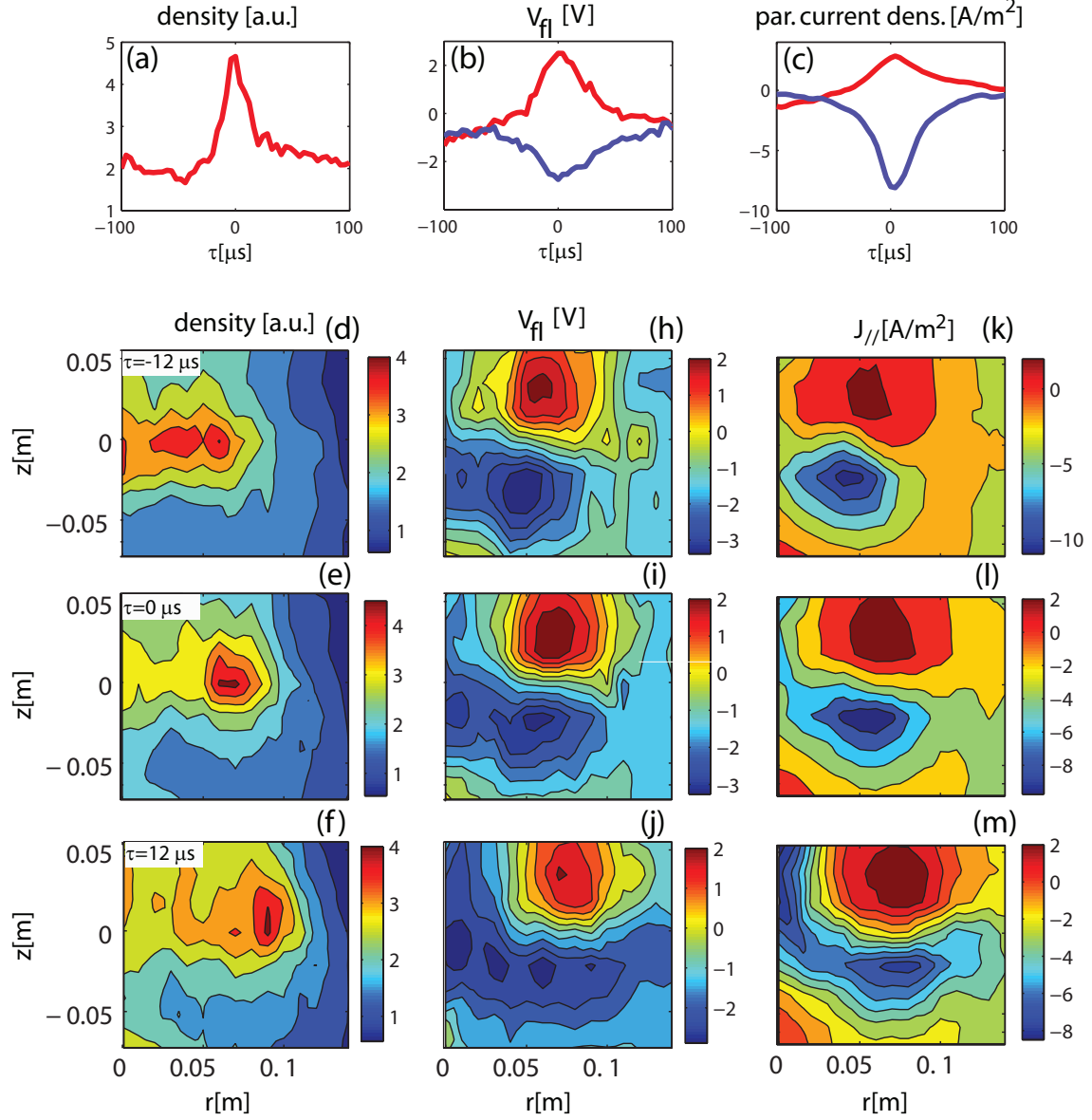


Figure 6.1.2: Conditionally sampled single-sided LP data measured ~ 3 cm in front of the limiter [60,142]. Shown are: time evolution of (a) electron density at the center of the blob, (b) floating potential and (c) parallel current density above (red) and below (blue) the center of the blob. 2D profiles of n , V_{fl} and $J_{||}$ are also shown at three different times during the blob radial propagation. In frames (k, l, m), positive/negative current densities correspond to excess of ions/electrons collected by the limiter.

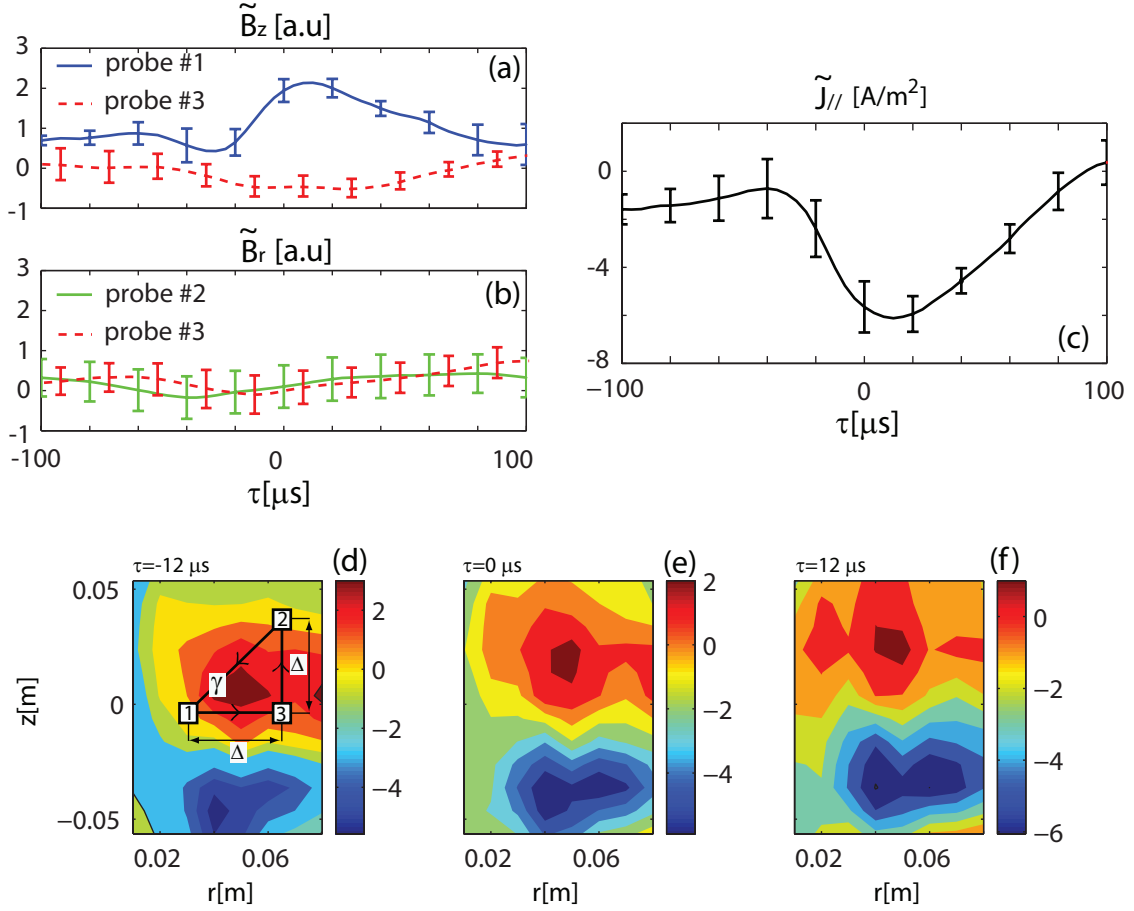


Figure 6.1.3: Conditionally sampled data from the current probe measured ~ 3 cm in front of the limiter [60, 142]. Frame (d) shows schematically the arrangement of the three triaxial pick up coils. Frames (a) and (b) show examples of time evolution of vertical magnetic field components $\tilde{B}_{z,1}$, $\tilde{B}_{z,3}$ and (b) radial magnetic field components $\tilde{B}_{r,2}$, $\tilde{B}_{r,3}$, respectively. These are used to compute the fluctuating parallel current density $\tilde{J}_{\parallel} = 2\tilde{I}_{\gamma}/\Delta^2$ at $r = 6$ cm and $z = -4$ cm in frame (c), where \tilde{I}_{γ} is the fluctuating parallel current enclosed by the contour γ in frame (d). Two-dimensional profiles of \tilde{J}_{\parallel} are shown at three different times during the blob radial propagation in frames (d-f).

spheric currents [166], and it has been recently used to directly estimate the parallel current density in thermonuclear oriented plasmas [163]. A picture of the probe, which is dubbed Bdot, is shown in Fig. 6.1.1 with the relevant coordinate system. This probe is installed 3 cm in front of the limiter and is oriented such that the fluctuating (r, z) components of the magnetic field are measured. To allow comparisons with the single-sided LP data, the time traces of $\tilde{B}_{z,i}$ and $\tilde{B}_{r,i}$, with $i = 1, 2, 3$ identifying each probe, are conditionally sampled using the different tips of SLP as reference probes. From these data the conditionally averaged fluctuating current \tilde{I}_γ enclosed by the contour γ , shown in Fig. 6.1.3 (d), is computed by integrating Ampere's law $\tilde{\mathbf{J}} = \mu_0^{-1} \nabla \times \tilde{\mathbf{B}}$ over the surface enclosed by the contour γ . This yields $\tilde{I}_\gamma = \frac{\Delta}{2\mu_0} [-\tilde{B}_{z,1} - \tilde{B}_{y,2} + \tilde{B}_{y,3} + \tilde{B}_{z,3}]$. The conditionally averaged fluctuating current density is computed as $\tilde{J}_\parallel = 2\tilde{I}_\gamma/\Delta^2$ and time-resolved 2D profiles are reconstructed by moving the Bdot probe in between discharges.

Fig. 6.1.3 (a,b) shows examples of conditionally sampled fluctuating magnetic fields, which yield the fluctuating current density at $r = 6$ cm and $z = -4$ cm, shown in Fig. 6.1.3 (c). Figure 6.1.3 (d-f) shows 2D profiles of \tilde{J}_\parallel at three times during the blob propagation. An asymmetric dipolar structure of the current density is revealed, which is in excellent agreement with the measurements in Fig. 6.1.2 from the single-sided LP (it should be mentioned here that single-sided LP measurements show a low level of time-averaged current densities, such that the difference between \tilde{J}_\parallel and J_\parallel is small, $|\tilde{J}_\parallel - J_\parallel| \approx 1 \text{ Am}^{-2}$).

6.1.2 Origin and importance of asymmetric parallel current structures

We use data from the single-sided LP to elucidate the origin of the asymmetry in the blob parallel current dipole observed in Fig. 6.1.2 (k)-(m) and Fig. 6.1.3 (d)-(f). We display in Fig. 6.1.4 the J_\parallel profile at the limiter as computed from (a) $J_\parallel = J_{sat} \{1 - \exp[-e(V_{pl} - \mu T_e)/T_e]\} \equiv J_{sat} [1 - \exp(-eV_{fl}/T_e)]$ (see [13] and Sec. 5.1), where $J_{sat} = 0.5 \cdot n_0 e c_s$ is the ion saturation current density, and (b) from the linearized expression $J_\parallel \approx J_{sat} (eV_{fl}/T_e)$. As discussed in Sec. 5.1.5, the latter is often used as a closure scheme in theory and numerical simulations of SOL dynamics under the assumption that $|eV_{fl}/T_e| \ll 1$. While the exact expression in Fig. 6.1.4 (a) is in excellent agreement with Fig. 6.1.2 (l), displaying an asymmetric dipolar structure, the linearized version in Fig. 6.1.4 (b) is almost perfectly symmetric. This is due to the assumption $|eV_{fl}/T_e| \ll 1$, which is not satisfied here ($|eV_{fl}/T_e| \approx 1$), such that the linearized expression leads to large errors in the J_\parallel estimate.

These measurements [60] have motivated the numerical simulations discussed in Sec. 5.1.5, where we have performed seeded blob simulations with and without linearizing the parallel current term [141, 142]. Simulations with the correct expression for the parallel current indeed result in asymmetric structures of the parallel current induced

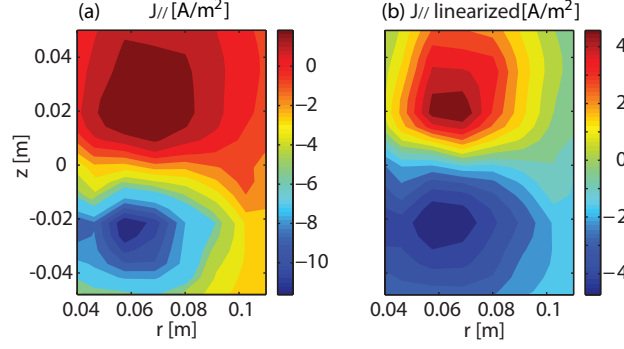


Figure 6.1.4: Parallel current density (a) from sheath boundary condition $J_{||} = J_{sat}[1 - \exp(-eV_{fl}/T_e)]$, and (b) from the linearized expression $J_{||} \approx J_{sat}(eV_{fl}/T_e)$.

by the blobs. At the same time, negligible effects of the current linearization on blob radial velocity are observed.

We can quantify the current asymmetry by the ratio $\alpha = |J^-/J^+| = |[1 - \exp(-eV_{fl}^{min}/T_e)]/[1 - \exp(-eV_{fl}^{max}/T_e)]|$, where J^+ and J^- are the peak current densities in the positive and negative lobes, respectively. For $|eV_{fl}/T_e| \approx 1$, we obtain a significant current asymmetry of $\alpha = |J^-/J^+| \approx 2.7$. Note that blobs commonly observed in fusion devices [131] have cross-field sizes $a_b \sim 1 - 3$ cm and radial speeds $v_b \sim 0.5 - 2$ km. An estimate of $V_{fl} \approx a_b v_b B$ ($B \sim 1 - 5$ T is the toroidal magnetic field of the device) indicates that $eV_{fl} \sim 5 - 300$ eV. This is in the range of SOL electron temperatures, thus suggesting that the current density asymmetry may be relevant also in these devices.

Recent measurements reveal parallel currents associated with filaments during ELMs [162–165]. Origin and detailed spatial structure of these currents are a matter of debate. Considering similarities between blobs and ELM filaments [131], it is interesting to discuss the importance of net parallel currents resulting from the asymmetric current structure caused by the polarization of the filament. An estimate of this net parallel current (assuming a circular filament of radius a_b) is $I \approx (\alpha - 1)J^+ \cdot \pi a_b^2$, where the absolute value of α (in our case ≈ 2.7) depends upon the ratio eV_{fl}/T_e . In the SOL of tokamaks, typical filament parameters are $c_s \sim 30 - 60$ km/s, $n \sim 1 - 3 \times 10^{19} \text{ m}^{-3}$, and $a_b \sim 1 - 3$ cm. Net currents in the range $\approx 50 - 500$ A can then be expected, which are of the order of measured filament currents [162, 165].

6.1.3 Importance of the parallel current in damping the charge separation

In Ch. 5, we presented a blob speed-versus-size scaling law, Eq. (5.1.13), which was successfully compared with experimentally measured blob velocities and sizes in different working gases [139, 147]. From this, it was inferred that damping of blob velocity by parallel currents is most important for hydrogen blobs. Here, we use the

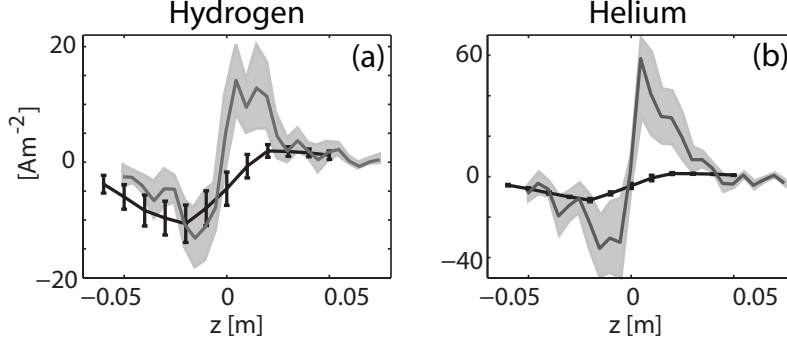


Figure 6.1.5: Comparison of the measured parallel current density to the sheath (thick black line) with the profile from Eq. (6.1.1) reveals that the former damps a significant part of charge separation in hydrogen (a) but not in helium (b) blobs [60, 142].

above direct measurements of blob parallel currents to confirm this interpretation.

We first compute the parallel current density $J_{\parallel}|_{sheath}$ that is required, in the absence of other closure paths for the current, to completely damp the blob charge separation induced by ∇B and magnetic field curvature. It follows from the vorticity equation (5.1.1), neglecting ion-polarization currents and ion-neutral collision and allowing for electron temperature variations:

$$J_{\parallel}|_{sheath} = -\frac{L_c}{RB} \frac{\partial(n_e T_e)}{\partial z} \Big|_{L_c/2}. \quad (6.1.1)$$

The r.h.s. of this equation represents the drive for blob motion and requires high spatial resolution measurements to be evaluated. These are obtained from FRIPLE [62]. As discussed in Sec. 3.5.3, FRIPLE is a 5-tip LP array with 4 mm spacing in the vertical direction between tips. It is located 1 m away from the limiter in the bulk plasma, as schematically shown in Fig. 6.1.1. This probe is operated in swept mode and profiles of electron density and temperature are obtained by using the BOX-CAS technique. Blobs are selected using, as a trigger condition, data from SLP.

In Fig. 6.1.5, we present results obtained in hydrogen and helium plasmas. The r.h.s. of Eq. (6.1.1) is evaluated on a vertical cut across the density blob center. These profiles are compared with the experimental profiles of the current density to the sheath. For hydrogen, Fig. 6.1.5 (a), the profiles agree within the error bars for $z < 0$, demonstrating that parallel currents efficiently damp the charge separation in this region. This is not the case for $z > 0$ in hydrogen and for helium over the entire profile, Fig. 6.1.5 (b). Other closure mechanisms, such as perpendicular ion polarization current and ion current due to neutral friction, must be effective to ensure $\nabla \cdot \mathbf{J} = 0$.

This supports the results of Ch. 5.2 that parallel currents to the sheath damp a significant fraction of the charge separation in hydrogen, but not in helium.

6.2 Blob induced transport of parallel momentum

In this section, we investigate the link between toroidal flows and density blobs [97]. For these experiments, no limiter is installed inside TORPEX and the target plasma is a hydrogen plasma with $N \approx 2$. We investigate two different magnetic configurations, one with $B_z \approx +2.4$ mT, referred to as 'case A', and one with $B_z \approx -2.4$ mT ('case B'). The toroidal field $B_\phi \approx 76$ mT is in the standard direction for both cases, namely in the counter-clockwise direction when the torus is seen from the top. Case A and case B are similar except for the direction of the magnetic field pitch. In both cases, the vertical $\mathbf{E} \times \mathbf{B}$ flow in the mode region is directed upwards and gives a Doppler-shifted frequency of the ideal interchange mode of ≈ 4 kHz [97].

To measure toroidal flows, the MACH probe described in [63] is used. It is installed on a 2D movable system such that it can scan a large fraction of the cross-section on a shot-to-shot basis. It is the same probe that we have used as single-sided LP in Sec. 6.1. A picture of the probe head is shown in Fig. 2.2.1. We recall that it consists of five identical circular electrodes (diameter: 8 mm) separated by an insulator. Two of the electrodes, on opposite sides and oriented perpendicular to the magnetic field, are operated in I_{sat} to measure the toroidal Mach number $M_\phi \equiv V_\phi/c_s$, where V_ϕ is the parallel ion velocity. In the presence of a flow, the ion saturation currents I_{up} and I_{down} on the two opposite electrodes differ. A commonly accepted formula to deduce the Mach number from the time resolved current measurements $I_{up}(t)$ and $I_{down}(t)$ is $M_\phi(t) = 0.4 \cdot \log [I_{up}(t)/I_{down}(t)]$ [64]. This expression is used in the following.

To obtain detailed insights on the relation between toroidal flows and density blobs, we perform conditional average sampling (see Sec. 3.4) over many blob events detected on a reference probe located in the blob region [97] (at $(r, z) = (13 \text{ cm}, 0 \text{ cm})$ and toroidally displaced by 90° from the MACH probe). This allows reconstructing the 2D conditionally averaged measurements of ion saturation current and toroidal Mach number during the ejection of a blob and its subsequent radial propagation. In Fig. 6.2.1, we show the fluctuations of ion saturation current and toroidal Mach number for case A at a time $\tau = -160 \mu\text{s}$ before detection of the blob on the reference probe and at $\tau = 0$. In the \tilde{I}_{sat} profile in (a), we can clearly identify positive and negative structures of the ideal interchange mode. Somewhat surprisingly, the mode structure is also visible in \tilde{M}_ϕ , Fig. 6.2.1 (b). Perturbations of the toroidal Mach number associated with the wave are radially elongated and lag behind the I_{sat} fluctuations, with a phase shift of $\approx \pi/2$.

Later in time at $\tau = 0$, the positive mode structure is radially elongated, (c). The blob can already be identified, although it is not yet fully detached from the wave crest. In the Mach number plot (d), we observe a negative ('hole-like') and a positive ('blob-like') perturbation at the top and the bottom of the I_{sat} blob, respectively. This corresponds to the same phase difference between \tilde{I}_{sat} and \tilde{M}_ϕ already observed in the mode region. The phase shift between Mach number and I_{sat} observed in the

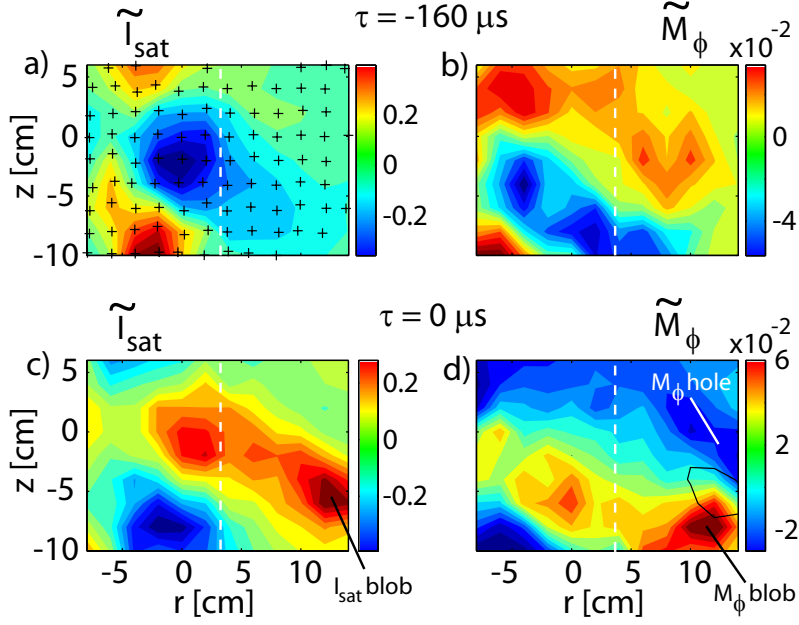


Figure 6.2.1: For case A, 2D snapshots of fluctuations of I_{sat} (left column) and toroidal Mach number (right column) reconstructed using CAS for two different values of τ [97]. The measurement points of the MACH probe are represented by crosses in (a). To guide the eyes, the density blob is added on plot (d) (black contour). The white vertical dashed line separates the source region on the left where the interchange wave propagates upwards from the source-free or blob region on the right.

interchange mode where the blob is born is conserved along the blob radial trajectory. Similar dynamics are observed for case B. In that case, the phase difference between \tilde{I}_{sat} and \tilde{M}_ϕ is $\approx \pi$ and blobs are associated with a monopolar negative perturbation of \tilde{M}_ϕ [97].

These measurements provide detailed insights on the spatiotemporal correlation between \tilde{I}_{sat} and \tilde{M}_ϕ . However, this does not necessarily imply a similar correlation between density and toroidal velocity V_ϕ . Indeed, fluctuations in Mach number $M_\phi = V_\phi/c_s \propto V_\phi/\sqrt{T_e}$ can also be due to electron temperature fluctuations.

To quantify this effect, we apply the BOX-CAS technique described in Sec. 3.4 to reconstruct the evolution of density, electron temperature, plasma potential, and toroidal Mach number correlated with a blob detected on the reference probe [63]. A vertical profile of these quantities is obtained for both cases A and B by performing a vertical scan with the MACH probe between $-7 \leq z \leq 6$ cm and at $r = 12.5$ cm. The spatial resolution along the direction z is 1 cm. As reference probes, we alternately use different tips of SLP, which is toroidally separated from the MACH probe by 90° . For case A, reference probes located at $(r_{ref}, z_{ref})^A = (12, +[3.5, 5.5, 8.5])$ cm are used. For case B, where the magnetic field pitch is reversed, the reference probe locations are changed to $(r_{ref}, z_{ref})^B = (12, -[3.5, 5.5, 8.5])$ cm. As sketched in Fig. 6.2.2 (a) and (b), this ensures that the field aligned blobs are detected in the vertical range covered by the MACH probe for both cases.

Fig. 6.2.2 shows the vertical profiles of electron density (Fig. 6.2.2 (c) and (d)) and the toroidal velocity (Fig. 6.2.2 (e) and (f)) for the three reference probe positions and cases A and B. Color profiles are averaged over $20 \mu\text{s}$ around τ_b , where $\tau_b \approx 20 \mu\text{s}$ is the time at which the density blob is detected on the MACH probe. A positive τ_b is consistent with the relative radial position of the MACH probe with respect to SLP. These profiles have to be compared with the time averaged profiles (thin black curves in Fig. 6.2.2 (c)-(f)), computed in the absence of blobs and independent of the trigger position.

Density blobs correspond to the maximum density in the vertical profiles in the MACH probe plane. Since blobs are field aligned structures, they should be detected at $z_b \approx z_{ref}^A - 5.5 \text{ cm}$ for case A and $z_b \approx z_{ref}^B + 5.5 \text{ cm}$ for case B, where 5.5 cm is a quarter of the vertical displacement of a magnetic field line after one complete toroidal turn. The observed locations of the maxima are in good agreement with this prediction for case A (Fig. 6.2.2 (c)), while the agreement is not as good for case B (Fig. 6.2.2 (d)). For case A, V_ϕ decreases by $\approx 20\%$ at $z = z_b$ and a phase shift reminiscent of the blob origin is evident: largest positive and negative fluctuations (up to 50% with respect to the unperturbed profile) are localized at $z = z_b \mp 4 \text{ cm}$, revealing again the dipolar structure (Fig. 6.2.2 (e)). The largest positive and negative structures are of the same order of magnitude. For case B, a density blob is associated with a hole of toroidal velocity (Fig. 6.2.2 (f)). The blob induces such a large perturbation that the toroidal flow is transiently reversed.

These results reveal the following picture [46,97]. The ideal interchange mode creates perturbations in toroidal velocity (whose origin still needs to be identified). This flow pattern is shifted with respect to the density perturbations. The blobs, which form from the wave crests, inherit this flow perturbation and convect it radially outwards. The phase shift between the toroidal flow and the density perturbations observed in the interchange mode where the blob is born is conserved along the blob radial trajectory. Depending on this phase shift, the blob-induced flow may have a dipolar or monopolar structure. In the latter case, the perturbations can be so large that the toroidal flow gets transiently reversed.

This strongly reminds on the mechanism proposed in [167,168] to explain intrinsic rotation in closed field line configurations. It is proposed that instabilities in the edge plasma transfer toroidal momentum to the blobs. The blobs then convect this momentum to the wall. Momentum is thus lost to the core plasmas, providing a recoil force that can induce a rotation in the core plasma.

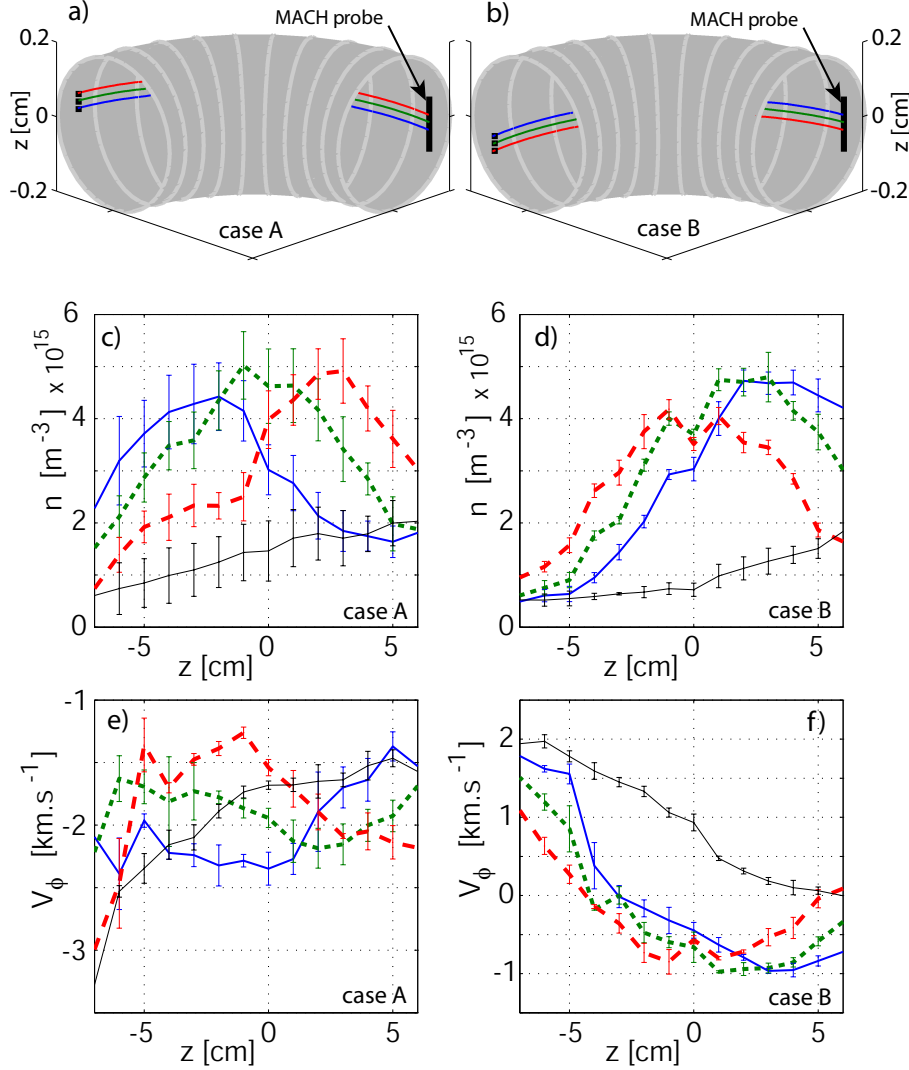


Figure 6.2.2: (a), (b): Sketch of the experimental setup to measure vertical profiles of density n and parallel velocity V_ϕ of blobs [97]. The vertical range across which the MACH probe is moved in between shots in the blob region is shown together with the positions of the reference probes, toroidally separated by 90° . Field lines intercepting the reference probes are also plotted. For clearness, the major radius of the torus is halved. (c), (e): Shown are vertical profiles of n and V_ϕ associated with blobs detected at the three different reference probes indicated in (a) for case A. Time averaged profiles are given by the thin, black curves. (d), (f): The same for case B. Error bars are given by the standard deviation of the plasma parameters estimated for three identical shots.

6.3 Proposal for measurements of the pre-sheath density drop inside blobs

In a quasi-neutral region called the pre-sheath, subsonic ions are accelerated to the ion sound speed at the entrance of the Debye sheath, which forms at the plasma-wall transition [13]. This acceleration goes along with a decrease in density from a value n_0 in the bulk plasma (far away from the sheath) to a value n_{se} at the sheath entrance. The pre-sheath density drop n_{se}/n_0 is an important quantity, as it determines the level of parallel particle and heat transport to the wall, and also determines the importance of parallel currents in damping blob velocity [128]. Before discussing an experimental campaign planned to directly measure n_{se}/n_0 on TORPEX, we study this problem using simplified model equations.

We consider a 1D situation where magnetic and electric fields are perpendicular to the wall. We indicate the spatial coordinate along B - and E -field with x and assume that the plasma is isothermal, quasi-neutral, is in steady-state, and that $T_i \ll T_e$. We assume a particle source S_p and no momentum input. The continuity equation and the sum of the ion and electron momentum equations take the form [13]

$$\frac{d}{dx}(nv) = S_p(x), \quad (6.3.1)$$

$$\frac{d}{dx}(m_i n v^2 + n T_e) = 0, \quad (6.3.2)$$

with v the ion fluid velocity. Assuming $v \approx 0$ in the bulk plasma and indicating the bulk density as n_0 , we find from Eq. (6.3.2) that

$$n(x) = \frac{n_0}{1 + (v/c_s)^2}. \quad (6.3.3)$$

This shows the decrease of plasma density when we approach the sheath and the parallel ion velocity increases (a finite particle source term S_p is necessary here to allow for a non-trivial solution of Eqs. (6.3.1) and (6.3.2)). At the sheath entrance, the ions reach the sound speed [169]. From Eq. (6.3.3), we see that the density n_{se} at that location is given by $n_{se} = 0.5 \cdot n_0$. This is the value we have assumed in the vorticity equation for sheath limited blobs, Eq. (5.1.1).

Following the steps in Ch. 10.4. of [13], we show now that the factor n_{se}/n_0 can be further reduced in the presence of neutrals. We assume that the wall (more precisely the sheath entrance), is located at $x = 0$, as indicated in Fig. 6.3.1 (a). We include a background of neutrals with zero mean velocity. This gives a term of the form $-m_i v n \nu_{in}$ on the r.h.s of Eq. (6.3.2), where ν_{in} is the ion-neutral collision frequency for momentum exchange. We further drop the particle source term in the continuity equation, neglecting any ionization or recombination processes. The continuity equation reduces then to $nv = \text{const.} = n(x=0) \cdot v(x=0) = n_{se} \cdot (-c_s)$, such that

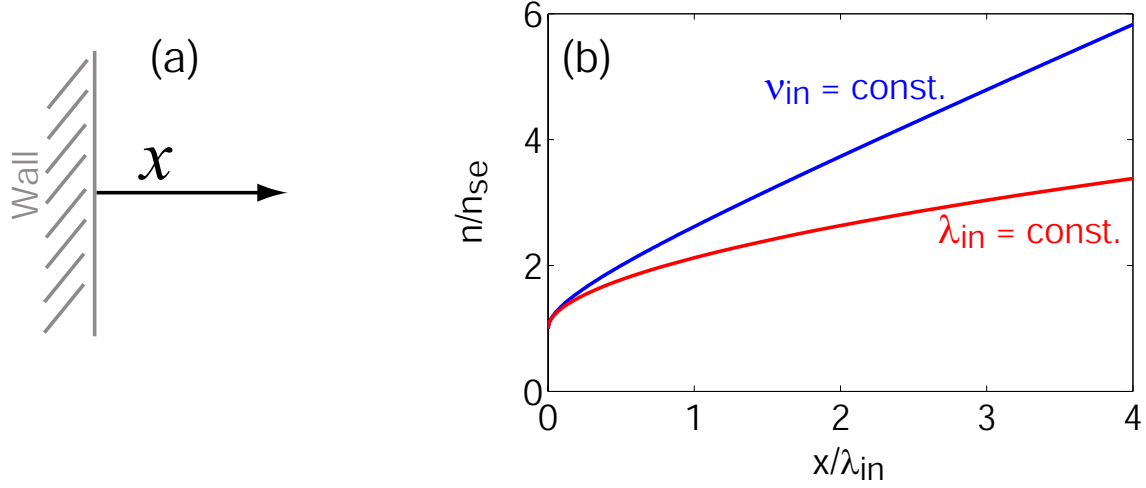


Figure 6.3.1: (a): Coordinate system used to solve the system of 1D equations (6.3.4) and (6.3.5). (b): Electron density normalized to its value at the sheath entrance as a function of the distance from the wall. Eqs. (6.3.4) and (6.3.5) are solved using different forms of the ion-neutral collision frequency ν_{in} .

$$nv = -n_{se}c_s, \quad (6.3.4)$$

$$\frac{d}{dx} (m_i n v^2 + n T_e) = -m_i v n \nu_{in}. \quad (6.3.5)$$

Replacing n in the momentum equation by $-n_{se}c_s/v$ (Eq. (6.3.4)) and defining the Mach number $M = v/c_s$, this system of equations can be written as

$$(M^2 - 1) \frac{dM}{dx} = -\frac{\nu_{in}}{c_s} M^2, \quad (6.3.6)$$

with the boundary condition $M(x=0) = -1$.

For illustration, we consider now two simplified forms for ν_{in} . In the first case, we assume a constant collision frequency, $\nu_{in}(v) = |v|/\lambda_{in}(v) = \text{const.} = c_s/\lambda_{in}(c_s)$. In the second case, we assume a constant ion-neutral mean-free path $\lambda_{in}(v) = \lambda_{in}(c_s)$, such that $\nu_{in}(v) = |v|/\lambda_{in}(c_s)$.

In the first case, Eq. (6.3.6) can be integrated. Using $n = -n_{se}/M$ (Eq. (6.3.4)), one finds

$$n(x) = \frac{n_{se}}{1 + \frac{1}{2} \frac{x}{\lambda_{in}} - \sqrt{\frac{x}{\lambda_{in}} + \frac{1}{4} \frac{x^2}{\lambda_{in}^2}}}. \quad (6.3.7)$$

This solution is represented in Fig. 6.3.1 (b) by the blue curve.

In the second case, where $\nu_{in}(v) = |v|/\lambda_{in}(c_s)$, integration of Eq. (6.3.6) gives (for $M < 0$ and satisfying the boundary condition $M(x=0) = -1$)

$$-\log(|M|) - \frac{1}{2M^2} + \frac{1}{2} = -\frac{x}{\lambda_{in}}. \quad (6.3.8)$$

Solving it numerically for M and using again $n = -n_{se}/M$ results in the red curve in Fig. 6.3.1 (b).

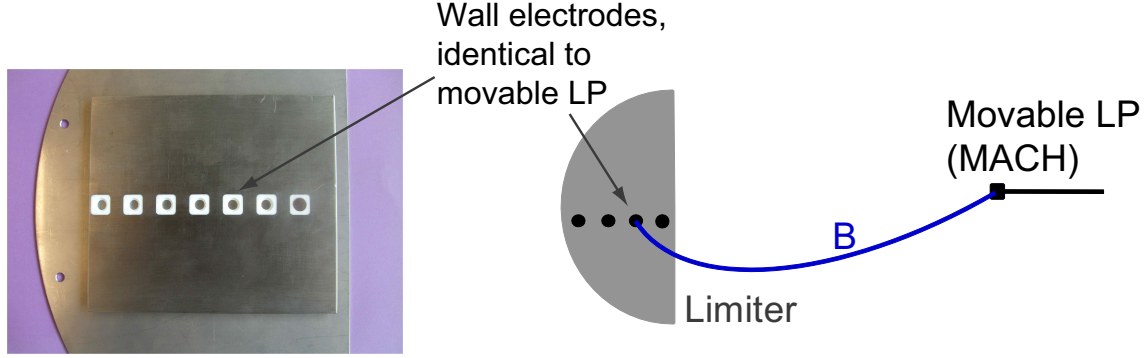


Figure 6.3.2: Left: Picture of a radial array of wall electrodes (Wall-Es) embedded into the limiter (under construction). They are identical to the faces of the MACH probe (see Fig. 2.2.1 for a picture of the latter). Right: Sketch illustrating measurements planned to determine the pre-sheath density drop inside blobs. The MACH probe, toroidally separated from the limiter by ideally $\approx 180^\circ$, will be aligned with one of the Wall-Es. A face of the MACH probe that is oriented perpendicular to the magnetic field will measure ion saturation current I_{bulk} . The pre-sheath density drop n_{se}/n_0 will be deduced from $I_{wall}/2I_{bulk}$, where I_{wall} is the ion saturation current measured simultaneously with the Wall-E that is aligned with the MACH probe.

From these examples, we see that density can significantly exceeds $2 \cdot n_{se}$ a few ion-neutral mean-free paths away from the wall. Estimating $\lambda_{in} = 1/(n_n \sigma_{in})$ with $n_n \approx 5 \cdot 10^{18} \text{ m}^{-3}$ and $\sigma_{in} \approx 10^{18} \text{ m}^2$ for typical TORPEX plasmas gives $\lambda_{in} \approx 20 \text{ cm}$. As this value is considerably smaller than the connection length L_c on TORPEX, values of n_{se}/n_0 below ≈ 0.5 can be expected. We note, however, that blobs propagating from the mode region into the limiter shadow, as is the case for the experiments in Sec. 6.1 and in the previous chapter, do not correspond to the steady-state situation modeled by Eqs. (6.3.4) and (6.3.5). When a blob enters the limiter shadow and is cut in half, we expect the Debye sheath to form almost instantaneously. On the other hand, for the formation of a pre-sheath as in Fig. 6.3.1 that extends over several λ_{in} 's, ions need to move long distances along the magnetic field. Intuitively, we expect this pre-sheath to form within a time $\propto L_c/c_s$, in which the blob could already have covered a considerable distance into the limiter shadow.

The above estimates of n_{se}/n_0 and the complexity of the limiter setup clearly motivate experimental measurements of the pre-sheath density drop.

Fig. 6.3.2 illustrates the experimental setup proposed for the measurement of n_{se}/n_0 during and in between blobs. A face of the MACH probe [63] (see Fig. 2.2.1) that is oriented perpendicular to the magnetic field is used to measure I_{sat} in the bulk plasma. We expect this measurement to provide an ion current of $I_{bulk} \approx n_0/2 \cdot c_s e A_{eff}$ [64]. Electrodes embedded in the limiter, with identical geometry as the MACH probe electrodes, measure I_{sat} in front of the wall. We expect this measurement to provide $I_{wall} \approx n_{se} c_s e A_{eff}$.

Aligning the MACH probe with one of the wall probes should thus allow the measurement of n_{se}/n_0 from $n_{se}/n_0 \approx I_{wall}/2I_{bulk}$, as a function of time in the blob

region and for different radial locations from the limiter edge.

Moving the plasma into the limiter shadow will then also provide measurements of the pre-sheath density drop in the source region or in other locations of the plasma profile.

6.4 Conclusions

In this chapter, we have investigated different aspects of parallel dynamics associated with blobs.

We have presented the first 2D measurements of the parallel current structure inside blobs [60, 142]. Measurements were performed in front of a limiter with two independent methods, a single sided LP and a specially designed current probe, based on an array of magnetic pickup coils. These reveal 2D dipolar structures of both floating potential and current density. While the floating potential is an almost perfectly symmetric dipole, this is not the case for the current density. The latter exhibits a stronger lobe on the side dominated by electron currents. This is due to the nonlinear dependence of the total current upon the floating potential. The relevance of the parallel current density asymmetry to ELM filaments was also discussed. Using internal measurements, we confirmed the existence of two regimes for blob propagation [139, 147], in which parallel currents to the sheath, respectively, do or do not efficiently damp ∇B and curvature induced polarization of the blob.

Toroidal rotation and velocity shear can have beneficial effects on plasma confinement and the suppression of instabilities in tokamaks [170]. The identification of mechanisms driving rotation in the absence of direct momentum input, which is of particular importance for burning plasmas like ITER, is an open issue. We have used a Mach probe to perform first 2D, time resolved measurements of parallel Mach number fluctuations associated with the formation and subsequent propagation of blobs [97]. Two configurations characterized by different vertical field components, $B_z > 0$ (case A) and $B_z < 0$ (case B), have been investigated. These measurements reveal a toroidal flow pattern that is associated with the ideal interchange mode. It is vertically shifted with respect to it. The origin of this flow perturbation and of the phase shift with respect to density fluctuations is not yet understood. The blobs, which form from the interchange wave crests, inherit this flow perturbation and convect it radially outwards. For case A, the flow perturbation caused by a blob shows a dipolar structure. For case B, the flow perturbation inside blobs is monopolar and so large that it gets transiently reversed.

These measurements provide the following picture: momentum is transferred from the ideal interchange mode to the blobs and convected radially outwards. Momentum is thus lost from the mode region. This mechanism provides a recoil force that can be a source of intrinsic rotation in systems with closed magnetic field lines [168].

Another important quantity related to blob parallel dynamics is the pre-sheath density drop, i.e., the drop in blob density along the magnetic field between positions far from the wall and at the sheath entrance, where the blob is in contact with a material wall. This density drop determines parallel transport of particles and heat and the importance of parallel currents to damp charge separation inside blobs. A simple model has been presented to compute the pre-sheath density drop, showing that the latter can be reduced below the standard value of $n_{se}/n_0 = 0.5$ due to neutral friction. An experimental method to directly measure this drop has been presented and will be tested in the near future.

C H A P T E R

7

Blob control

In Ch. 5, we have seen that blob motion can be influenced by changing connection length and neutral gas pressure [147]. In this chapter, we explore possibilities to actively controlling blob motion by changing the parallel boundary conditions. We discuss changes in blob dynamics when the incidence angle between magnetic field and limiter is varied and when the steel limiter is replaced by a limiter made of an electrically insulating material. We also present a detailed study of the possibilities of inducing convective cells and influencing blob motion using a set of biased electrodes installed on a steel limiter.

7.1 Variation of wall tilt

Up to now, we have studied blob motion in a setup where blobs intercept a steel limiter with nearly perpendicular incidence. It has been predicted that blob parallel currents and thus blob velocity can be changed by varying the incidence angle of the magnetic field onto the limiter [152, 171]. This could have direct applications in fusion devices, where magnetic field lines usually intercept the divertor plates at shallow angles. The choice of the angle between the normal to the divertor plate and the poloidal magnetic field should then affect blob velocity and possibly the SOL-width [171]. We have developed a dedicated setup to test this effect of wall tilt on blob velocities.

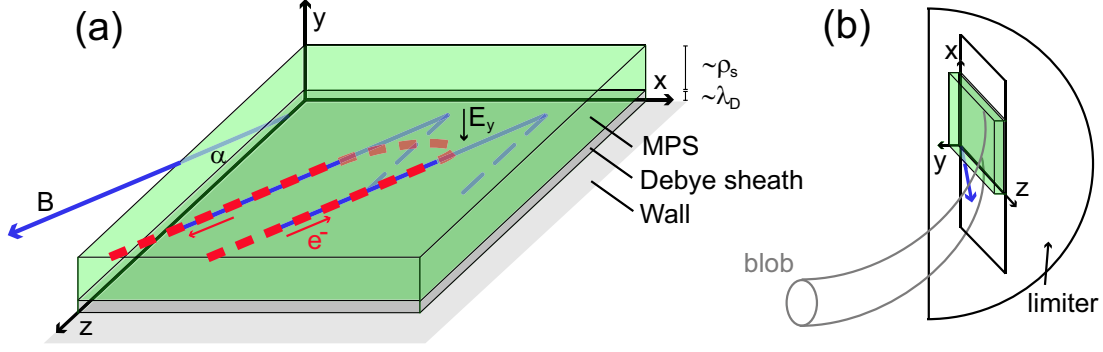


Figure 7.1.1: (a) Sketch of an electron trajectory (gyro-averaged) in the magnetic pre-sheath. (b) Sketch of a metal plate attached to the limiter in order to achieve grazing incidence of the magnetic field on the plate.

In the following, we discuss the origin of the dependence of the blob parallel currents upon the tilt angle and the setup to test it on TORPEX. Although our configuration is not entirely equivalent to the SOL of a diverted tokamaks, the same physics effect should be at play, namely the closure of the electron diamagnetic current approaching the wall by parallel currents flowing from the wall [152]. We present results that show the absence of the anticipated effect on blob motion and discuss possible explanations and further steps.

7.1.1 Predicted effects of wall tilt

We provide here a qualitative explanation of the dependence of blob parallel currents upon wall tilt based on a single particle picture and then discuss the expected effect on blob velocity. As illustrated in Fig. 7.1.1 (a), for small values of the angle α between magnetic field and wall, a magnetic pre-sheath (MPS) forms in addition to the usual Debye sheath [13, 172]. The MPS has a thickness of the order of ρ_s and is indicated by the green layer in Fig. 7.1.1 (a). Inside the MPS, an electric field component E_y exists. While all ions entering the MPS are ideally absorbed by the wall, a large fraction of electrons is reflected in the MPS due to the potential barrier. These reflected electrons undergo trajectories which are qualitatively illustrated by the red dashed curve in Fig. 7.1.1 (a): they enter the MPS along a magnetic field line, then $\mathbf{E} \times \mathbf{B}$ drift in the $-x$ -direction due to the electric field component E_y , and are finally reflected along a different field line. Provided that the electron pressure varies along x , this results in a change of the parallel electron current.

Ref. [152] estimates the contribution of these reflected electrons to the parallel current (directed towards the wall) to be

$$j_{\parallel e}^{refl} = -en_{se} \frac{v_{E,y}}{\alpha} + \text{sign}(B_z) \frac{1}{\alpha B} \frac{\partial p_e^{se}}{\partial x}. \quad (7.1.1)$$

n_{se} and p_e^{se} are the electron density and pressure at the plasma side of the MPS. Corrections in the case of an $\mathbf{E} \times \mathbf{B}$ drift $v_{E,y}$ along the y axis are also taken into account. Adding the contribution of the small fraction of electrons that overcome

the potential barrier and are absorbed by the wall, $j_{||e}^{abs} = -en_{se}c_s \exp^{-\frac{e(V_{pl}-\mu T_e/e)}{T_e}}$, as well as a parallel ion current of the form $j_{||i} = en_{se}(c_s + \frac{v_{E,y}}{\alpha})$ [13], we find for the parallel current at the entrance of the MPS

$$j_{||} = en_{se}c_s(1 - \exp^{-\frac{e(V_{pl}-\mu T_e/e)}{T_e}}) + \text{sign}(B_z) \frac{1}{\alpha B} \frac{\partial p_e^{se}}{\partial x}. \quad (7.1.2)$$

Small values of α can be achieved by installing a metal plate on the limiter as sketched in Fig. 7.1.1 (b). In this case, the derivative in the α -dependent part of $j_{||}$ in Eq. (7.1.2) is along the vertical direction (the z direction in the TORPEX coordinate system) and competes with the drive term of blob motion.

To evaluate the expected effect of wall tilt on the blob velocity, we include now the α -correction of the parallel current, Eq. (7.1.2), in the vorticity equation, Eq. (5.1.1). We assume $T_e = \text{const.}$, a pre-sheath density drop $n_{se}/n_0 = 0.5$, and take into account the parallel current at both ends of the blob. We then find that the drive term for blob motion, i.e., the term on the left hand side of the vorticity equation (5.1.1), changes by a factor r_{tilt} , where

$$r_{tilt} = 1 - \frac{R}{2L_c\alpha}. \quad (7.1.3)$$

We thus expect that wall tilt as sketched in Fig. 7.1.1 (b) reduces blob velocity by this factor. The same reasoning shows that blob velocity should increase when the plate attached to the limiter in Fig. 7.1.1 (b) is tilted inwards, such that the magnetic field intercepts the plate on its other surface. Eq. (7.1.3) remains valid if we define α to be negative in that case.

7.1.2 Experimental setup

To test the tilt angle dependence of blob velocity, a small incidence angle α between magnetic field and limiter is required in the blob region and across a radial range extending over several blob radii. Further, one would like to be able to switch easily between positive and negative values of α during one experimental session. This is rather challenging from the mechanical point of view. As an example, let us assume an angle of $\alpha = +0.2$ rad and $\alpha = -0.2$ rad, respectively, which results in $r_{tilt} \approx 0.6$ and $r_{tilt} \approx 1.4$. To reach these values of α in the radial range from $r = 0$ cm to $r = 20$ cm, limiters as sketched in Fig. 7.1.2 are required. They have a rather complicated shape and extend toroidally over almost one third of the torus. Additional complications arise when the possibility of switching between positive and negative values of α without opening TORPEX is needed.

Due to these difficulties, we have decided to take a different approach [173], mounting several plates perpendicularly to a halfmoon limiter. This is illustrated in Fig. 7.1.3 (a-b) by a picture and a sketch where the torus is seen from the top. Different values of α (including negative ones) are achieved in a region extending over several blob radii in the radial direction by pivoting the limiter around a vertical axis. The

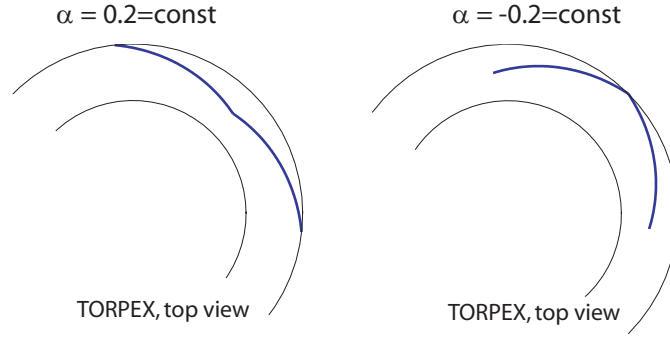


Figure 7.1.2: Sketch of the TORPEX vacuum vessel (top view) with limiters in blue that would be required to have (a) $\alpha = 0.2$ rad and (b) $\alpha = -0.2$ rad in the radial range between $r = 0$ cm and $r = 20$ cm.

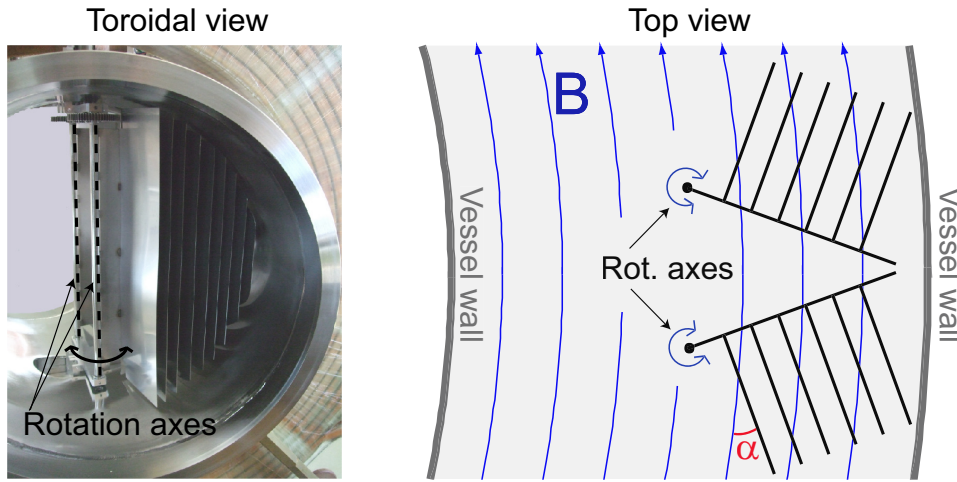


Figure 7.1.3: Setup adopted for TORPEX to change the angle α between magnetic field lines and limiter [147,173]. Left: Picture of the Limiter à Configuration Variable (LCV), installed inside a mobile sector of TORPEX. The view is along the toroidal direction. Right: Sketch of LCV (top view). Several stainless steel plates are mounted perpendicularly to two halfmoon limiters. The angle α between magnetic field lines and these plates can be varied by pivoting the two limiters around the vertical axes. α is defined positive if the plates are tilted as in the above sketch.

attached plates have a length in the toroidal direction of 10 cm and are radially separated by 1.7 cm ($\approx 8 \cdot \rho_s$ in H_2). This allows obtaining values of $|\alpha|$ as small as $\approx 1.7/10 = 0.17$ (smaller values would result in part of the field lines intercepting the limiter instead of the plates attached on it). Two such limiters have been constructed, for both ends of the blob. Values of r_{tilt} in the range 0.53 – 1.47 can thus be achieved with this setup.

This limiter, referred to as *Limiter à Configuration Variable* (LCV), has been installed in the same mobile sector as the second limiter for the experiments in Sec. 5.2.2. Rotation of the limiter around the two vertical axes in Fig. 7.1.3 can be performed remotely between shots and the position of the limiter can be verified through a quartz window.

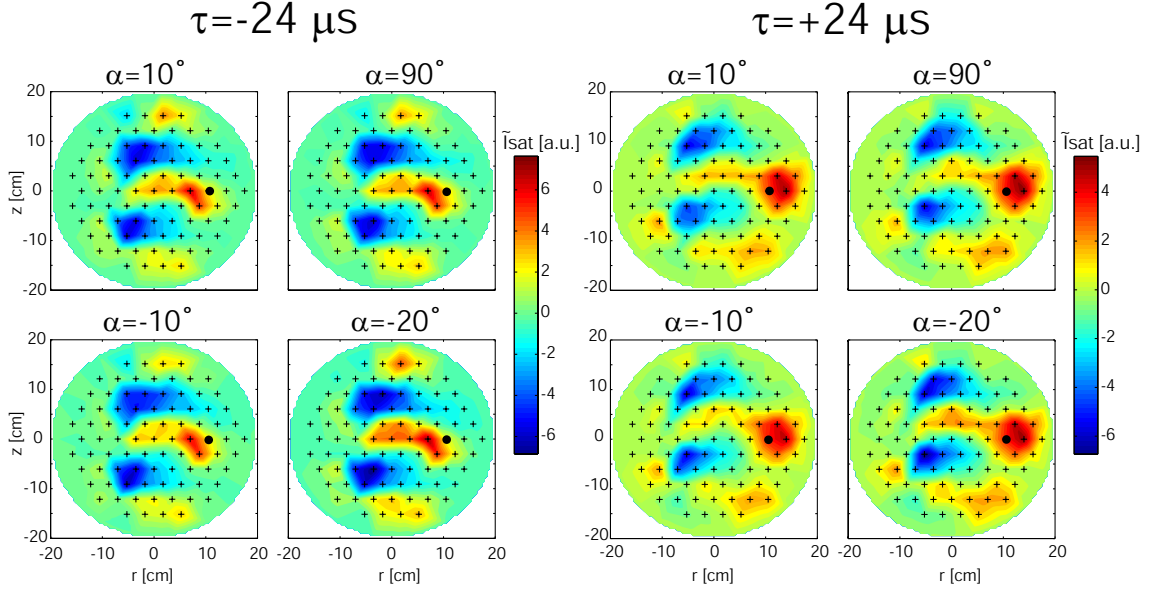


Figure 7.1.4: Frames of the conditionally averaged blob dynamics at $\tau = -24 \mu s$ (left) and $\tau = +24 \mu s$ (right) with respect to the detection time of the blobs on the reference probe. The position of the reference probe for CAS is indicated by a black dot in the plots. Results are shown for different values of α . For positive values of α , we expect from Eq. (7.1.3) a reduction of blob velocity, for $\alpha < 0$ an increase. $\alpha = 90^\circ$ corresponds to the case when the two halfmoon limiters of LCV are perpendicular to the magnetic field.

7.1.3 Results and discussion

In Fig. 7.1.4, we show two frames of the conditionally averaged blob dynamics for different values of α . The working gas is hydrogen and $(B_\phi, B_z) = (75, -1.5)$ mT, which corresponds to a case with $N \approx 3$. Measurements are performed with HEX-TIP and the tip indicated by a black dot in the subplots of Fig. 7.1.4 is used as reference probe for CAS. We observe almost identical results for all four values of α . In particular, there are no indications for any dependence of blob radial velocity upon the tilt angle. Similar results are obtained for different values of neutral gas pressure and vertical magnetic fields, as well as cases where the two wings of LCV are rotated in the same toroidal direction, such that the two halfmoon limiters are parallel to each other. The time averaged profiles of I_{sat} show some small but reproducible relative difference $\lesssim 10\%$ between the case $\alpha = 10^\circ$ and $\alpha = -10^\circ$. However, if an effect on blob velocity is present, this is certainly much weaker than expected from the above predictions.

We note that these results do not necessarily disprove the theoretical prediction. There are a number of issues related with our setup that could be responsible for the negative result. One issue is related to the edges of the limiter plates. In the vicinity of these edges, a proper MPS might not exist and perturbations around them possibly dominate all other effects. Another issue could be that blobs are not

always connected to the limiter plates. This is schematically illustrated for different cases in Fig. 7.1.5, where we schematically draw the blob in front of the limiter, seen from the top. Once the blob has lost contact to the limiter, it expands along the magnetic field until contact is reestablished. We expect this parallel expansion to take place with sound speed c_s . The competition between the blob parallel and radial velocity determines the contact of the blob with the limiter plates. In Fig. 7.1.5, we distinguish the two cases, $|\alpha| < \psi$ and $|\alpha| > \psi$, where we have defined the angle $\psi \equiv \arctan(v_b/c_s)$. In light, we highlight parts of the blob where contact with the limiter has been established. Dark areas indicate parts where the blob is expanding toroidally. In this case, we do not expect any parallel currents to occur such that the blob is electrically disconnected from the sheath.

For $\psi > |\alpha|$ (Fig. 7.1.5 (a-b)), the blob is completely disconnected from the limiter for $\alpha < 0$ (b) and partly for $\alpha > 0$ (a). If we assume an electron temperature of $T_e = 2.5$ eV, $m_i = 1$ a.m.u, and $v_b \approx 1000$ ms⁻¹, we find that $\psi \approx 0.065$. This is smaller than $|\alpha| \approx 0.17$ rad, such that we do not expect to be in this regime in our experiments.

The more relevant case $\psi < |\alpha|$ is illustrated in Fig. 7.1.5 (c-d). In this case, the blob is fully connected to the limiter plates for $\alpha < 0$ (d), while it is still partly disconnected for $\alpha > 0$ (c). Reduced contact of the blob with the limiter plates could thus be an issue for $\alpha > 0$. Parts of the blob are connected and we expect sheath damping to be increased compared to perpendicular incidence. For the disconnected part, on the other hand, sheath damping should be absent. This effect should reduce the difference in blob velocity between the case $\alpha < 0$ and $\alpha > 0$.

Yet another effect that would reduce the expected α -dependence of blob velocity is a pre-sheath density drop n_{se}/n_0 well below 0.5. In that case, r_{tilt} in Eq. (7.1.3) takes the form $r_{tilt} = 1 - \frac{n_{se}}{n_0} \frac{R}{L_c \alpha}$, which approaches unity as $n_{se}/n_0 \rightarrow 0$.

While the issue related with the pre-sheath density drop should soon be clarified on TORPEX (see discussion in Sec. 6.3), new limiter designs are probably needed to rule out effects related to edges of the plates and possible disconnection of the blobs. This favors limiters made of a single piece. A possible next step could be to install two limiters as indicated by the blue curves in Fig. 7.1.6. TORPEX would then be divided into two sections. Field lines in the blob region intercept the limiter with a positive angle (here $\alpha = +0.2$) in one toroidal section and with a negative angle (here $\alpha = -0.2$) in the other. Measurements of blob velocities in both toroidal sections can then be compared. To rule out effects due to toroidal asymmetries, the limiters could then be installed as indicated by the dotted curves in Fig. 7.1.6 and measurements be repeated. Such experiments will probably require ad hoc diagnostics developments to measure simultaneously blob velocities in both toroidal sections.

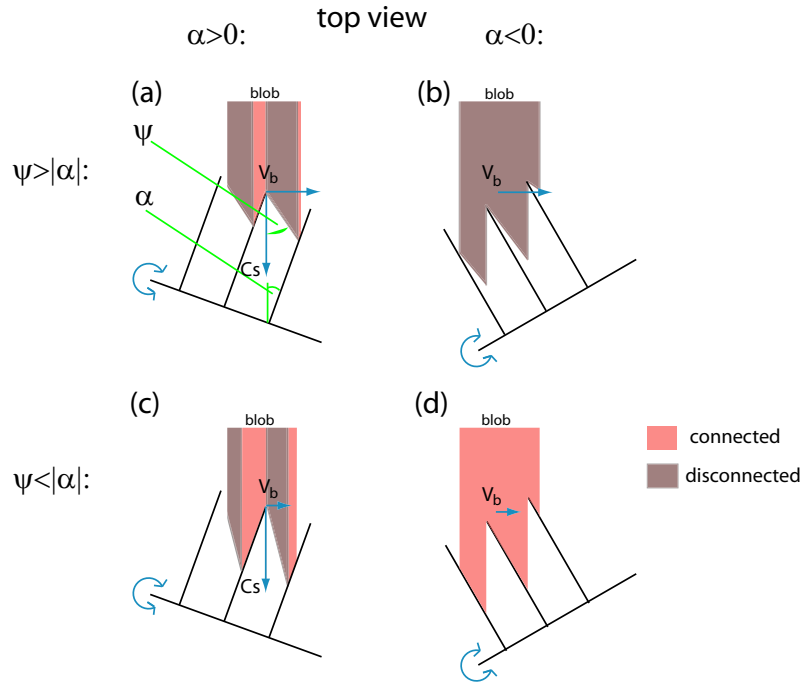


Figure 7.1.5: Sketch (top view) illustrating contact of the blob with the limiter plates for different signs of the tilt angle α and for the cases $\psi > |\alpha|$ and $\psi < |\alpha|$, where $\psi \equiv \arctan(v_b/c_s)$. Connected (light) and disconnected (dark) parts of the blob are indicated.

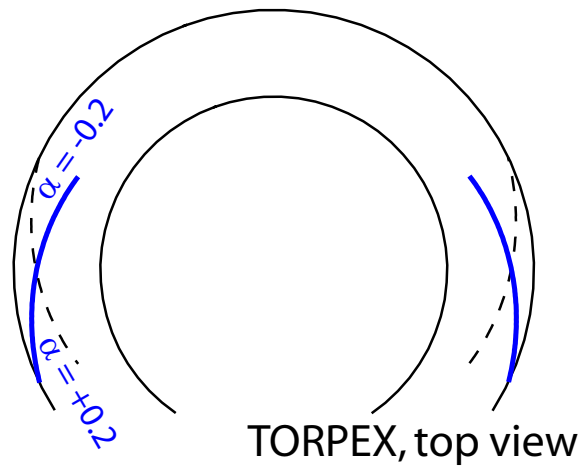


Figure 7.1.6: Possible next step to test the tilt angle dependence of blob radial velocity. The blue curves illustrate limiters viewed from the top which would generate a region with $\alpha = +0.2$ in the blob region for one section of the torus and with $\alpha = -0.2$ for the other one. To rule out effects due to a toroidal asymmetry, measurements could then be repeated with the limiters installed as indicated by the dotted curves.

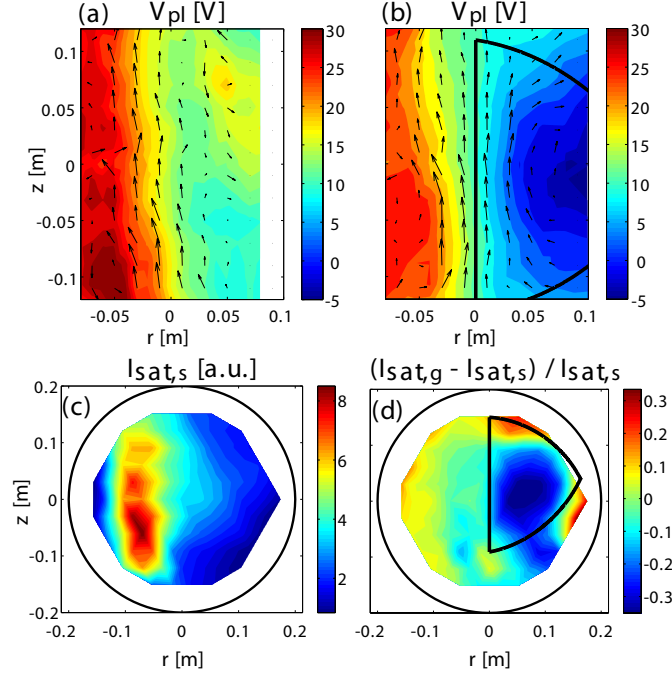


Figure 7.2.1: (a) Time averaged plasma potential profile in helium for discharges with a steel limiter installed. Arrows indicate the direction of $\mathbf{E} \times \mathbf{B}$ flows. (b) The same as in (a), but for discharges with a glass limiter. (c) Profile of the ion saturation current in the steel limiter case. (d) Relative difference in the I_{sat} profile between glass limiter and steel limiter discharges. The black contour in (b) and (d) indicates the region where both ends of the field lines intercept the glass limiter [147].

7.2 Experiments with a glass limiter

We have performed experiments where a glass limiter is used instead of a steel limiter [147]. Originally, the idea was to disconnect blobs from the limiter and avoid parallel currents to damp blob velocity. However, experiments in H_2 and He have shown that, in the region where both ends of the field lines end on the limiter, the plasma potential is strongly reduced by the presence of the glass limiter. This is shown in Fig. 7.2.1 for helium plasmas, where we plot the plasma potential profile at a toroidal angle of 210° from the limiter for discharges with the steel limiter (a) and with the glass limiter (b). In the glass limiter case, we even measure negative values of the plasma potential. The effect of this is that blobs are mainly convected around this region in the clockwise direction. This leads to a reduced radial cross-field particle transport in that region and in particular to a significant reduction of the ion saturation current, as shown in Fig. 7.2.1 (c) and (d) for HEX TIP data.

While we do not understand why the glass limiter is charging up negatively, these experiments show that biasing parts of the field lines on TORPEX can have significant effects on turbulence. Further, it shows that biasing can be achieved passively by inserting an insulating surface. In the remainder of this chapter, we will investigate systematically possibilities and limitations of active biasing of an array of 24 electrodes.

7.3 Biasing experiments: introduction and main results

It has been suggested that producing poloidal electric fields and convective cells in the tokamak SOL could serve as a tool to increase the SOL width and reduce heat loads on the divertor [21]. The most direct way to induce convective cells is by toroidally or poloidally asymmetric biasing. This is done by actively biasing different segments of the divertor or by biased electrodes immersed into the SOL.

Such ideas have already been tested in several tokamaks. In JFT-2M, biasing was applied to two out of 14 neighboring inboard divertor plates [174]. Strong changes in the poloidal electric field could be generated this way in the SOL. Further, significant modifications in the electron heat flux onto the divertor were observed. In MAST [175, 176], biasing was applied to every other rib of the outboard lower divertor in different experimental conditions. This led to a toroidally wavy wetted area on the divertor and modifications of the heat flux width and peak value. In CASTOR, an electrode was immersed in the SOL, leading to the formation of convective cells around the biased flux tube [177]. More recently, in NSTX, an array of four electrodes was installed in the SOL [178]. Experiments were performed in a wide range of regimes and strong local effects on the SOL profiles were measured.

In the following, we perform experiments with the goal of understanding the basic mechanisms of toroidally/poloidally asymmetric biasing, such as the properties of convective cells along and across the magnetic field, its effects on blob motion, and the effects that limit the achievable perturbations of cross-field flows.

We have installed an array of 3 x 8 electrodes on the surface of a metal limiter covering half of the cross-section (see Sec. 7.3.1). This provides considerable flexibility in applying different biasing patterns to one end of the field lines. Besides showing some clear effects on mode and blobs in specific cases, Sec. 7.3.2, we present in Sec. 7.3.3 a detailed analysis of the time averaged effect of biasing on potential and density profiles. This reveals characteristics of convective cells created by the biasing electrodes. A scan in applied bias potential shows, as expected, little effect for negative bias. For positive bias, significant changes in potential ($\delta V_{pl} \approx 2T_e/e$) and density are observed. The effect saturates as the biased electrodes reach the electron saturation current regime. It is shown that the achieved potential variations are proportional to the charge drawn from the plasma rather than to the applied bias voltage, as would be expected for a 1D problem at large bias voltages. Indeed, the biasing electrodes behave like a single Langmuir probe and cross-field currents strongly limit the effect of achievable potential variations in the plasma (Sec. 7.3.3.1). Measurements in two different toroidal locations in Sec. 7.3.3.2 indicate that biasing effects are fairly uniform along the magnetic field, in contrast to similar experiments in NSTX [178].

Two limitations for biasing experiments are further investigated. The first concerns

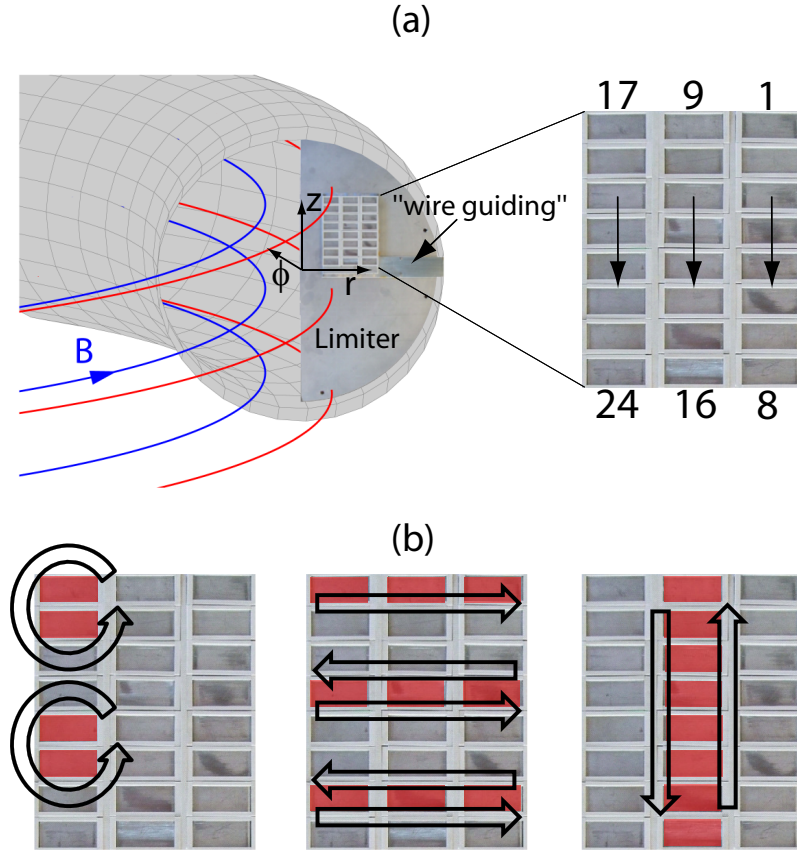


Figure 7.3.1: (a): Sketch of the TORPEX vacuum vessel and the electrodes installed on a conducting limiter. Examples of magnetic field lines and the coordinate system are also shown. The zoomed view of the electrodes indicates their numbering. (b): Different possible biasing schemes. Shaded areas indicate positively biased electrodes and arrows the expected flow pattern.

the observed shift of the induced potential variations with respect to the location of the biased flux tube. Biasing experiments in different regions in the plasma in Sec. 7.3.3.3 indicate that this is caused by the presence of propagating blobs and background flows. The other limitation, that on the magnitude of the achievable plasma potential variations, is investigated in Sec. 7.3.3.4. Based on simplified estimates, we can not identify a single mechanism for cross-field currents that explains these limitations.

7.3.1 Experimental setup

For the present experiments, a grounded stainless steel limiter is installed in the blob region and an array of 3×8 stainless steel electrodes is mounted on its surface. This is sketched in Fig. 7.3.1 (a). Each electrode has a rectangular surface of $2 \text{ cm} \times 0.9 \text{ cm}$ and an isolating support. A sketch of the array is shown in Fig. 7.3.1 (a) on the right. This setup protrudes from the limiter by $\approx 8 \text{ mm}$ and electrodes lie 1 mm behind the edge of the isolating parts. Wires are connected to the back side of each electrode and are guided between a stainless steel plate and the main limiter

towards a vacuum feedthrough at the LFS. This allows biasing individually the 24 electrodes and measuring their currents. This arrangement allows for some flexibility; for example, one can attempt to produce convective cells, radially elongated flows or vertical flows. The flow patterns that we would ideally expect for positively biasing the shaded, red electrodes are indicated by arrows in Fig. 7.3.1 (b). Electrodes that are not used for biasing can be used as Langmuir probes to measure plasma properties close to the limiter.

Measurements are also taken with HEXTIP. It is displaced toroidally by 90° from the limiter, in the clock-wise direction when the torus is seen from the top. Additionally, we use SLP. It is displaced by 55° from the limiter and lies thus between the limiter and HEXTIP. Besides measuring I_{sat} or V_{fl} , we operate SLP in swept mode to measure the time-averaged I-V characteristics.

For these tests, we use hydrogen as working gas and we set the number of field line turns N to $N \approx 3$, which falls in the ideal interchange regime.

7.3.2 Effect of biasing on mode and blobs

In this section, we present some examples that reveal clear effects of biasing on the plasma dynamics in TORPEX. The first example shows that time averaged profiles and properties of the ideal interchange mode can be significantly modified by biased electrodes on TORPEX. During the first 250 μs of the discharge, the 'bias on' phase, a positive potential of 40 V with respect to vessel ground is applied to electrode numbers 1, 3, 5, 9, 11, 13, 17, and 19 (see Fig. 7.3.1 (a)). These electrodes are represented by black rectangles at their field line-mapped position in the HEXTIP plane in Fig. 7.3.2 (a). In the same plot, we show the time averaged I_{sat} profile obtained with HEXTIP during the 'bias on' phase. In Fig. 7.3.2 (b), we show the I_{sat} profile during a second phase of 250 μs , the 'bias off' phase, where all electrodes are grounded. We can see a clear modification of the LFS profile caused by the electrodes. Moreover, the frequency of the dominant mode is significantly reduced from ≈ 7.1 kHz to ≈ 4.6 kHz, as shown by the power spectral density in (c). We have not further investigated the reason for the frequency reduction of the mode. A possibility is that the biasing changes the background $\mathbf{E} \times \mathbf{B}$ in the mode region and thus the Doppler shifted mode frequency.

Next, we show examples where blob propagation is substantially modified by using biased electrodes. SLP is operated in I_{sat} and moved in between reproducible discharges. Conditional average sampling (see Sec. 3.4) with a HEXTIP tip as reference probe is applied to obtain the average, 2D evolution of blob propagation. This is done for a 'bias on' phase and a 'bias off' phase. In the 'bias on' phase, a positive bias of 40 V is applied to the electrodes whose position in the SLP plane is indicated in Figs. 7.3.3 and 7.3.4. These figures also show contour plots of blob propagation obtained for successive time frames and the two different biasing patterns. Color plots represent the result for the 'bias on' phase and white contours indicate the

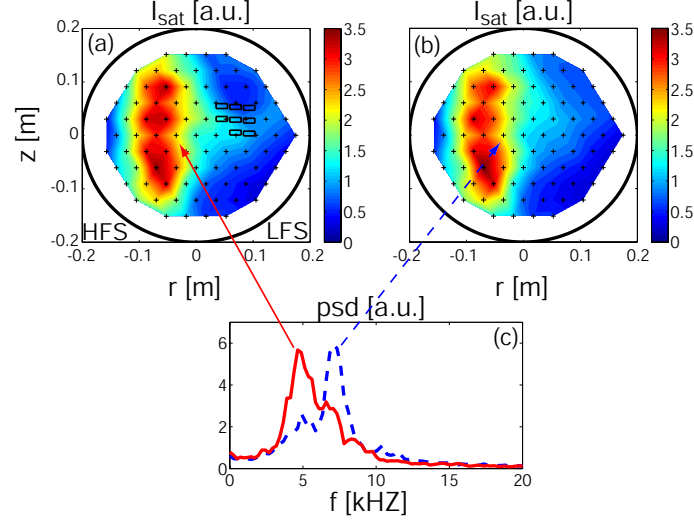


Figure 7.3.2: Profiles of I_{sat} during the 'bias on' (a) and the 'bias off' (b) phase. The electrodes that are biased to 40 V are indicated at their field line-mapped position in the HEXTIP plane in (a). (c): Power spectral densities of \tilde{I}_{sat} at the position indicated by the arrows.

position of the blob in the 'bias off' phase. $\tau = 0$ corresponds to the time when the blob is detected at the reference probe.

In Fig. 7.3.3, a vertical stripe of electrodes is used during the 'bias on' phase. Until $\tau = 0$, the average blob evolution is very similar between the two phases. After that, as expected, the blob is strongly swept downwards due to the applied bias. Nevertheless, in agreement with numerical simulations [144], the blob overcomes the bias "barrier". For the case shown in Fig. 7.3.4, a set of four electrodes is used to induce a counter-clockwise rotating cell. As expected, blobs passing below this set of electrodes are radially accelerated with respect to the unbiased case.

The above examples demonstrate that biasing influences blob motion, at least qualitatively in the expected manner. As shown in Fig. 7.3.5 for the latter biasing scheme, the effect of biasing is also clearly visible in the time averaged profiles. In (a) and (b), we plot time averaged I_{sat} and V_{fl} profiles in the 'bias off' phase, using HEXTIP. (c) shows the relative change in I_{sat} and (d) the change in V_{fl} due to the bias. We can observe characteristics of a convective cell, namely a positive structure in δV_{fl} and changes in I_{sat} up to 70% that are consistent with an outward convection at the bottom and an inward convection at the top of the δV_{fl} structure. What might have been less expected is the relatively large size of the δV_{fl} structure and its vertical and radial displacement with respect to the biased flux tube. Further, the peak value of δV_{fl} of ≈ 8 V, which corresponds to about three times the electron temperature in that region, is well below the applied bias of 40 V. In the following, we focus on time averaged measurements to investigate properties of the induced potential variations in more detail. The use of δV_{fl} to quantify the effect of the biasing will also be justified.

It should be mentioned that Fig. 7.3.5 (b) already reveals a structure in V_{fl} at the

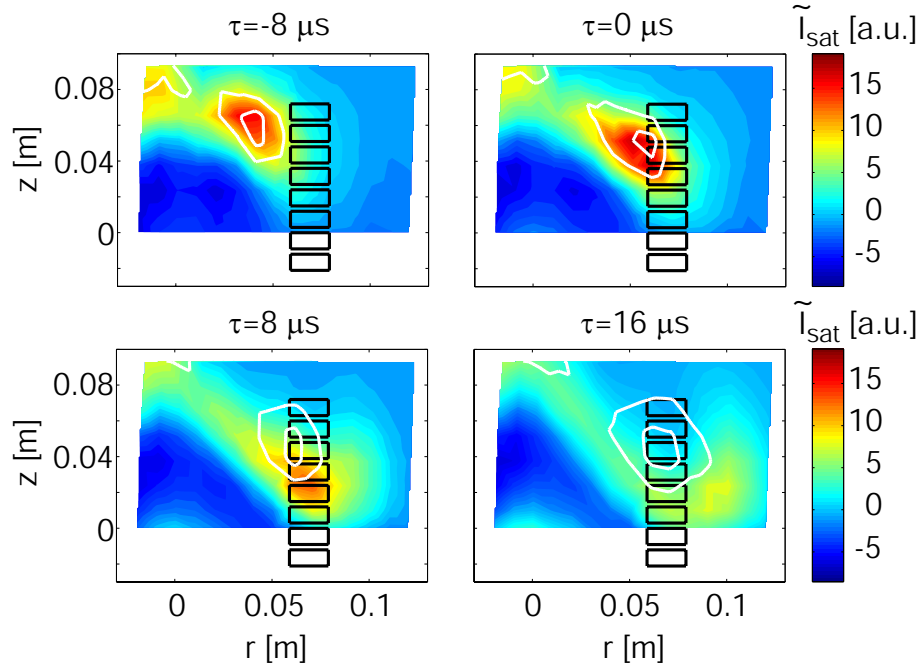


Figure 7.3.3: Conditionally averaged blob propagation (I_{sat} fluctuations) for the case where a vertical stripe of electrodes is biased to 40 V (color plots). For comparison, the white contours indicate the results of the same analysis when all electrodes are grounded.

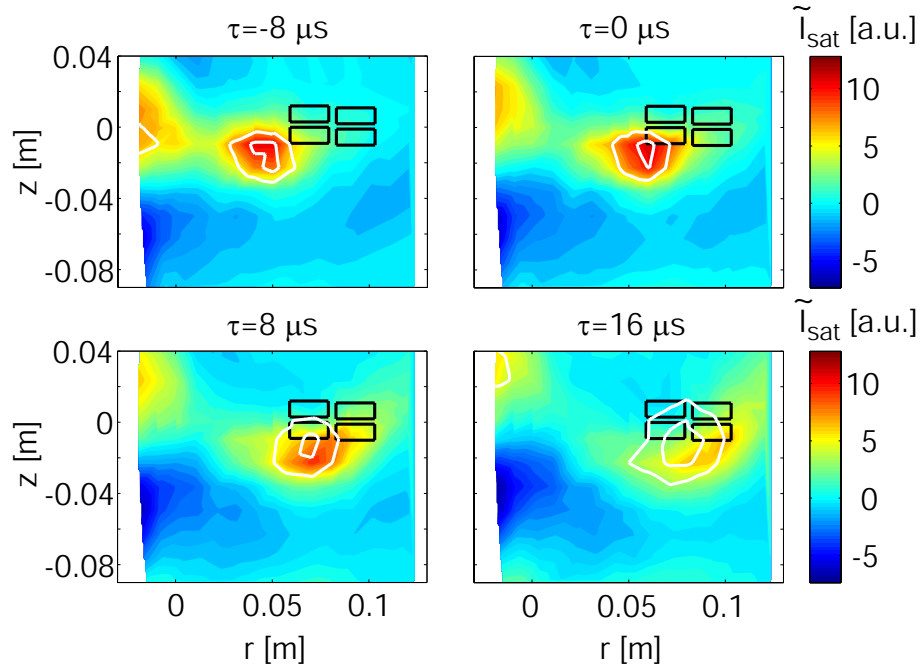


Figure 7.3.4: The same as in Fig. 7.3.3 for a different biasing pattern.

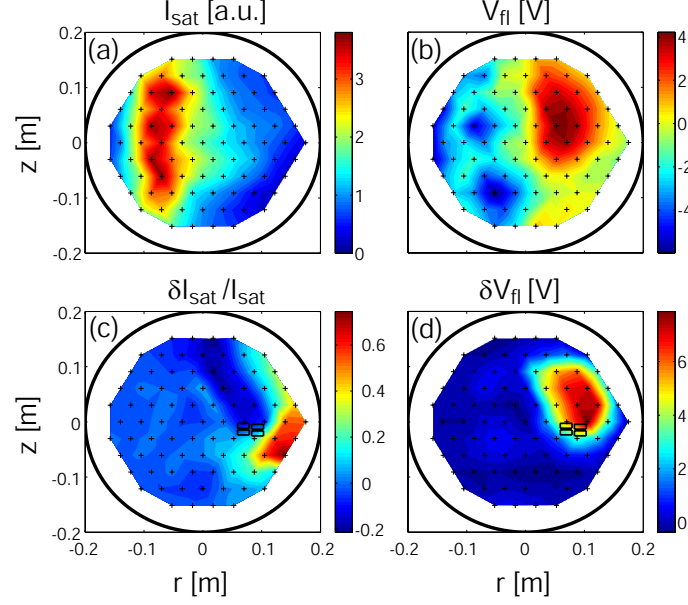


Figure 7.3.5: Profiles of (a) I_{sat} and (b) V_{fl} for experiments where all electrodes are grounded. (c) and (d) show the relative changes in I_{sat} and the absolute changes in V_{fl} induced by biasing positively the indicated set of electrodes. These are the same electrodes as in Fig. 7.3.4.

LFS for the unbiased case. This is an indication for steady state radial flows as reported also for tokamaks [179]. Origin and possible contributions of this to blob motion are not understood, as discussed in Sec. 5.2.4.

7.3.3 Time averaged effects of biasing

We will mainly use HEXTIP to investigate effects of the biasing on time averaged plasma quantities. As discussed in Sec. 3.2, the plasma potential measurements on TORPEX are obtained from $V_{pl} = V_{fl} + \mu T_e / e$, where $\mu \approx 3$ [56], and, due to the open field lines, plasma potential is mainly determined by the temperature profile. Despite this, we identify variations in plasma potential, δV_{pl} , due to the biased electrodes with variations in floating potential. To check the validity of this approach, we operate SLP in swept mode to reconstruct the quantities n , T_e , V_{fl} , and V_{pl} during a 'bias on' and a 'bias off' phase. During the 'bias on' phase, electrodes 15 and 16 are biased to +40 V. 2D profiles of plasma parameters are obtained by moving SLP discharge by discharge. In Fig. 7.3.6 (a) and (b), we compare the measured δV_{pl} and δV_{fl} obtained in this way. We observe a similar structure of potential variations in both cases. In particular, the non local effect on δV_{fl} that was already observed in Fig. 7.3.5 (d) is confirmed by the measurement of δV_{pl} . The two profiles also agree rather well quantitatively. This positive result can be explained by the fact that the biasing has a larger effect on the floating potential than on electron temperature, such that $\delta V_{pl} = \delta V_{fl} + \mu \delta T_e / e \approx \delta V_{fl}$. Fig. 7.3.6 (c) shows the measurement of δV_{fl} obtained with HEXTIP, showing satisfactory agreement with (a) and (b), despite a

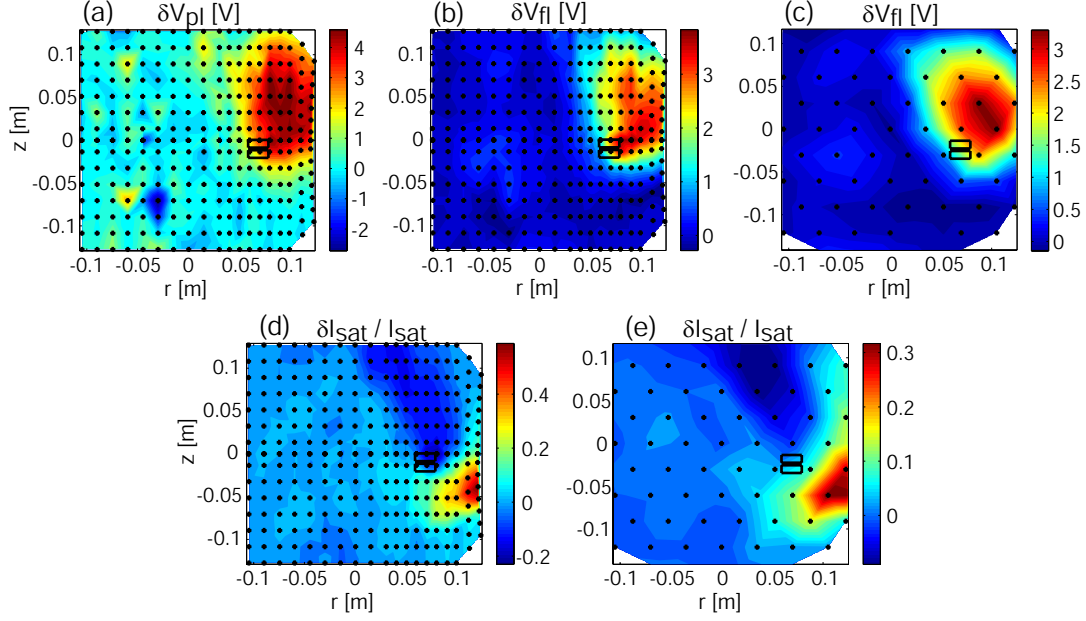


Figure 7.3.6: Tests performed to justify the use of the limited spatial resolution of the HEXTIP probe and δV_{fl} measurements to indicate plasma potential variations induced by the biasing. Plots (a), (b), and (d) are obtained from the SLP probe operated in swept mode and moved in between reproducible discharges. (c) and (e) are measurements with HEXTIP. Black dots indicate the measurement positions. The range of the z -axis is slightly different for HEXTIP and SLP profiles to take into account the pitch of the magnetic field.

lower spatial resolution, as indicated by the measurement points (black dots) in the figures. The measurements of $\delta I_{sat} / I_{sat}$ obtained with the two diagnostics also give a similar picture, as can be seen by comparing the plots in (d) and (e).

7.3.3.1 1D versus 2D

In a 1D situation, i.e., when cross-field currents are unimportant, the plasma potential in the biased flux tube always stays above the potential at both of its endplates. While negative biasing of one end-plate has little effect on plasma potential in this case, a positive bias strongly increases it. Indeed, if the bias potential exceeds several times T_e/e , the relative difference between potential increase and bias potential becomes small (more details on this and a generalization to finite cross-field currents can be found e.g. in [180, 181]). From the result in Fig. 7.3.5 (d), where the increase in potential of ≈ 8 V is significantly lower than the applied bias voltage of 40 V, it is clear that in our case this 1D picture does not apply. Another feature of the 1D case is that the current flowing to the biased electrodes can not exceed the ion saturation current. This is not the case here either, as we show in the next paragraph.

We investigate now in more detail the induced potential variations for different values of bias potential. Fig. 7.3.7 (a)-(c) show the measured potential variations for bias voltages of -40 V, $+3$ V, and $+40$ V, applied to the electrodes 15 and 16. For the strong negative bias, a small reduction in floating potential is observed around

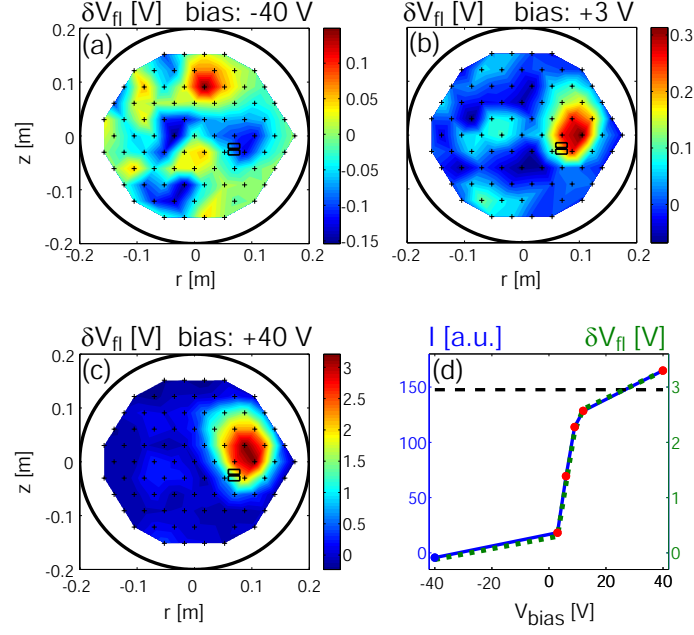


Figure 7.3.7: (a)-(c): Potential modifications induced by different values of bias potential. (d): Current emitted from the two biased electrodes (left axis, blue solid curve) and resulting potential modifications in the plasma (right axis, green dashed curve) for six different values of bias potential. The black dashed line indicated the expected level of the electron saturation current, obtained by multiplying the negative current emitted from the probes at -40 V by $-\sqrt{2m_i/(\pi m_e)}$.

the biased flux tube. For $+3$ V, we can already observe the familiar structure in δV_{fl} . It increases in amplitude while keeping a similar structure as the applied bias voltage is gradually increased. In Fig. 7.3.7 (d), we plot the current of the biased electrodes for the different bias voltages (here, the intermediate values $+6$ V, $+9$ V and $+12$ V are also included). This shows the strong asymmetry in the electrode current for positive and negative bias voltage. The horizontal, dashed line shows $I = \sqrt{2m_i/(\pi m_e)} \cdot |I_{sat}| \approx 34 \cdot |I_{sat}|$, evaluated for atomic hydrogen, which we expect for the electron saturation current [13]. The measured currents for strongly positive bias are close to this value. We are thus far from the 1D situation and the bias electrodes behave like single Langmuir probes. This is qualitatively similar to the results from NSTX, where the electron current at large positive bias exceeds the ion saturation current to the electrode by a factor ≈ 8 [178]. In the MAST experiments, on the contrary, this factor is ≈ 1 [176]. This was expected, however, as the surface ratio of grounded and biased parts was at most equal to 3 (taking into account grounded ribs of both the upper and the lower divertor) [180, 181]. In Fig. 7.3.7 (d), we also show the peak value of δV_{fl} for the different bias voltages (dashed green curve). It essentially falls on top of the current curve and is thus proportional to the electrode current. As this is limited by the electron saturation current, this sets a limit on the potential values that can be induced in these plasmas.

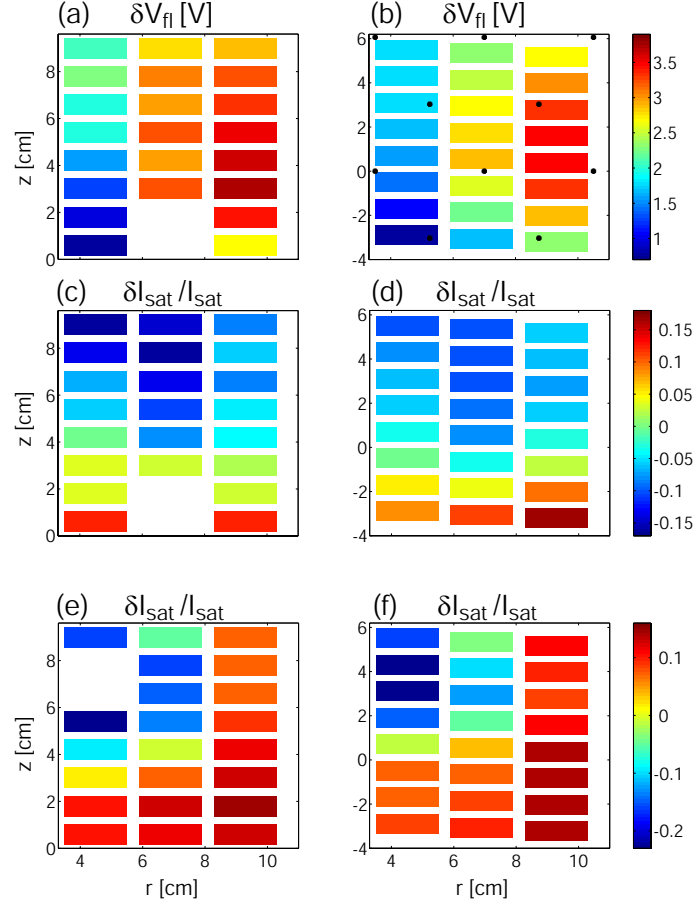


Figure 7.3.8: (a), (c), (e): Effects on V_{fl} and I_{sat} profiles due to the biasing, measured directly on the limiter. No measurements are available at the position of the electrodes that are used for the biasing. (b), (d), (f): The same measurements, but obtained with HEXTIP, at 90° from the limiter. Measurements at the positions indicated by black dots in (b) are linearly interpolated to obtain the values on the flux tubes connected to each electrode.

7.3.3.2 2D versus 3D

In this section, we investigate how changes in V_{fl} and I_{sat} induced by the biasing depend on the toroidal position. To this end, we compare measurements with HEXTIP at 90° from the limiter with measurements directly on the limiter. During the 'bias on' phase, we apply +40 V bias voltage to the electrodes 15 and 16 and ground them during the 'bias off' phase. The other electrodes are grounded except for one of them, which is used as a wall probe, operated in either I_{sat} or V_{fl} mode. During a series of reproducible discharges, each of the electrodes (except for number 15 and 16) is alternately used as wall probe. The 2D measurements of δV_{fl} and $\delta I_{sat}/I_{sat}$ in the limiter plane obtained this way are plotted in the left column of Fig. 7.3.8. In the right column, we plot the corresponding measurements in the HEXTIP plane. Such measurements are linearly interpolated from the probe data (black dots in Fig. 7.3.8 (b)), to obtain the values on the flux tubes connected to each electrode. Measurements of δV_{fl} , Fig. 7.3.8 (a) and (b), do not reveal strong differences in

structure and absolute values in the two toroidally separated planes. In both cases, the δV_{fl} structure is shifted radially and vertically with respect to electrodes 15 and 16. Further, we find $\delta V_{fl} \lesssim 4$ V in both planes. Good agreement is also found for relative changes in I_{sat} , Fig. 7.3.8 (c) and (d). These I_{sat} measurements are repeated with the bias applied to electrodes 18 and 19, Fig. 7.3.8 (e) and (f). In this case, a larger fraction of the region where I_{sat} increases due to the bias is captured. Again, we find good agreement between the two planes.

These measurements indicate that changes induced by the biased electrodes are not strongly dependent on the toroidal direction and that the problem can be treated to a good approximation as 2D. We note, however, that measurements directly in front of the biased electrodes are not available. High resolution measurements in this region are required to investigate the possibility of toroidally localized effects in front of the biased electrodes.

7.3.3.3 The effect of convective motion

As we have clearly seen e.g. in Fig. 7.3.6, the δV_{fl} structure is not centered around the flux tube where the bias is applied, but shifted both upwards and radially outwards. In this section, we investigate the reason for this non local effect of biasing. We have seen in Fig. 7.3.4 that in the LFS blobs move radially outwards. At the same time, a radial electric field exists at the LFS of the density profiles that leads to a vertical $\mathbf{E} \times \mathbf{B}$ drift (see e.g. Sec. 2.5). Conditionally averaged time series of blob motion for time intervals longer than that in Fig. 7.3.4 show that blobs indeed also move upwards. This becomes clear also from trajectory histograms of positive structures, such as those in Fig. 4 (a) of [111].

This is an indication that potential variations induced by the biased electrodes are shifted due to plasma flows. This hypothesis is strengthened here by a series of measurements where we have reversed the direction of the magnetic field, i.e., where we set $B_\phi \rightarrow -B_\phi$ and $B_z \rightarrow -B_z$. In this case, the steady-state vertical $\mathbf{E} \times \mathbf{B}$ flow is directed downwards at the LFS and upwards at the HFS of the density profile. Blobs of course still move radially outwards (they are polarized in the opposite way). Fig. 7.3.9 (a) shows δV_{fl} for a bias applied in the blob region. In agreement with the direction of blob trajectories, δV_{fl} is now shifted downwards and radially outwards. In Fig. 7.3.9 (b), the magnitude of B_ϕ is increased by $\approx 14\%$. This displaces the plasma radially outwards, as indicated by the white contour lines representing the I_{sat} profile. Now, biasing is applied to a region close to the peak of the density profile, where no large flows are present. In this case, the δV_{fl} structure is rather well centered around the biased flux tube. Finally, in Fig. 7.3.9 (c), B_ϕ is increased further by $\approx 5\%$ and bias is now applied to a region at the HFS of the density profile, where the $\mathbf{E} \times \mathbf{B}$ flow is directed upwards. In agreement with our hypothesis, the δV_{fl} cloud is now shifted upwards.

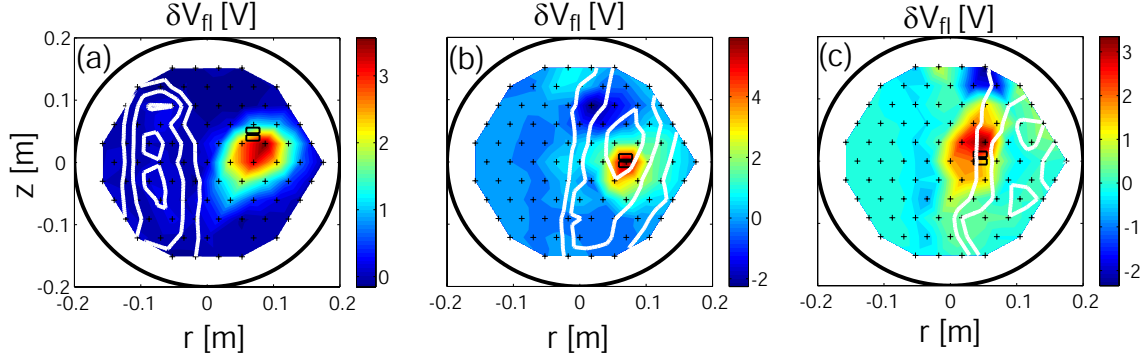


Figure 7.3.9: δV_{fl} for plasmas with reversed field ($B_\phi, B_z < 0$) and $B_\phi = -75.6$ mT (a), $B_\phi = -86.4$ mT (b), and $B_\phi = -91.0$ mT (c). I_{sat} profiles are indicated by white contours.

7.3.3.4 Estimates of cross-field currents

The experiments reported here demonstrate clear effects of biased electrodes on mode frequency, blob propagation, and time averaged profiles. At the same time, limitations on the magnitude of the achievable potential variations are observed. They are due to plasma cross-field currents, as discussed in Sec. 7.3.3.1. In the following, we investigate the origin of these currents.

As discussed in [182], cross-field currents in magnetized plasmas can be mainly attributed to collisions with neutrals, ion-polarization currents, and viscosity. The cross-field current \mathbf{j}_\perp can therefore be expressed as^(*)

$$\mathbf{j}_\perp = \frac{n_0 m_i}{B^2} \left(\nu_{in} \mathbf{E}_\perp + \frac{d}{dt} \mathbf{E}_\perp - \frac{\eta}{n_0 m_i} \Delta_\perp \mathbf{E}_\perp \right) \quad (7.3.1)$$

where ν_{in} is the ion-neutral collision frequency, $\frac{d}{dt} = \partial_t + \mathbf{v}_{E \times B} \cdot \nabla_\perp$ the convective derivative, $\mathbf{v}_{E \times B}$ the $\mathbf{E} \times \mathbf{B}$ drift velocity, and η the viscosity coefficient.

To estimate the importance of ion-neutral collisions in Eq. (7.3.1), we consider a situation in which we have a circular electrode with radius a installed on a conducting limiter, as sketched in Fig. 7.3.10 (a). We assume that the magnetic field lines intercept the limiter perpendicularly and end on another conducting plate located at a distance L_c . In the experiments, this second plate would correspond to the back-side of the limiter. Such scenarios have been investigated to model flush mounted Langmuir probes [182, 184]. Here, we adopt a similar but simplified approach. Motivated by the measurements discussed in Sec. 7.3.3.2, we assume a 2D problem, i.e., no variations along the magnetic field. We take into account a pre-sheath density drop n_{se}/n_0 in evaluating the boundary condition for parallel currents at the limiter, and assume uniform density otherwise. For the large bias potentials assumed in the following, this is a rather strong assumption [184]. Integrating current continuity,

^(*) We neglect here contributions due to collisional diffusion caused by ion-neutral and electron-neutral collisions (see e.g. [183]). The role of these terms will be investigated in future studies.

$\nabla \cdot \mathbf{J} = 0$, along the magnetic field gives

$$\nabla_{\perp} \cdot \mathbf{j}_{\perp} = -\frac{1}{L_c} j_{\parallel \text{tot}}, \quad (7.3.2)$$

where $j_{\parallel \text{tot}}$ is the total current density flowing out of the flux tube at both ends. We take the following expression for the parallel current density flowing to the electrode or the grounded limiter

$$j_{\parallel} = n_{se} c_s e \left(1 - \exp \frac{-e(V_{pl} - \mu T_e / e - V_{wall})}{T_e} \right), \quad (7.3.3)$$

as long as $j_{\parallel} > -\alpha_r n_{se} c_s e$ and

$$j_{\parallel} = -\alpha_r n_{se} c_s e \quad (7.3.4)$$

otherwise. $\mu T_e / e$ is the floating value of the plasma potential [13], V_{wall} is the voltage on the limiter (on, or around the electrodes), and $\alpha_r = \sqrt{2m_i / (\pi m_e)}$ the ratio of electron to ion saturation currents. We assume here a perfect saturation of these currents. Retaining only the contribution of ion-neutral collision in \mathbf{j}_{\perp} (the first term on the right-hand side of Eq. (7.3.1)), Eq. (7.3.2) becomes

$$\Delta_{\perp} V_{pl} = \frac{B^2}{n_0 m_i L_c \nu_{in}} j_{\parallel \text{tot}}. \quad (7.3.5)$$

We assume that the voltage applied to the electrode is strong enough that the electrode draws electron saturation current over its whole surface. In a first step, instead of Eqs. (7.3.3) and (7.3.4), we further assume a simplified structure of the parallel current. We assume that the current drawn by the electrode is balanced by ion saturation currents flowing to the grounded parts of the limiter at both ends of a flux tube of radius d . Outside of this flux tube, we set $j_{\parallel} = 0$. To assure charge conservation, the radius of this flux tube is given by $d = \sqrt{(\alpha_r + 1)/2} \cdot a$. A sketch of this current structure on and around the electrode is shown in Fig. 7.3.10 (a). Eq. (7.3.5) can now easily be solved analytically. The solution $\delta V_{pl}(\rho)$ has cylindrical symmetry and we define ρ as the radial coordinate. $\delta V_{pl}(\rho)$ is a monotonically decreasing function with its maximum value, $\delta V_{pl}(0)$, given by

$$\delta V_{pl}(0) = \left(\frac{\alpha_r + 1}{2} \right) \log \left(\frac{\alpha_r + 1}{2} \right) \cdot \frac{n_{se}}{n_0} \cdot \frac{c_s e B^2}{2 m_i L_c} \cdot \frac{a^2}{\nu_{in}} \quad (7.3.6)$$

This expression shows some interesting trends. When the plasma barely touches the wall, i.e., when n_{se}/n_0 goes to zero, the biasing effect vanishes. $\delta V_{pl}(0)$ also decreases with connection length, but increases with the ratio of electron to ion saturation currents, the magnetic field strength, and the surface of the electrode. Finally, the achieved bias potential is inversely proportional to the ion-neutral collision frequency ν_{in} .

In Fig. 7.3.10 (b), we plot the analytical solution $\delta V_{pl}(\rho)$ evaluated for realistic parameters (thick, blue line), as well as the numerical solution, obtained for j_{\parallel} given by

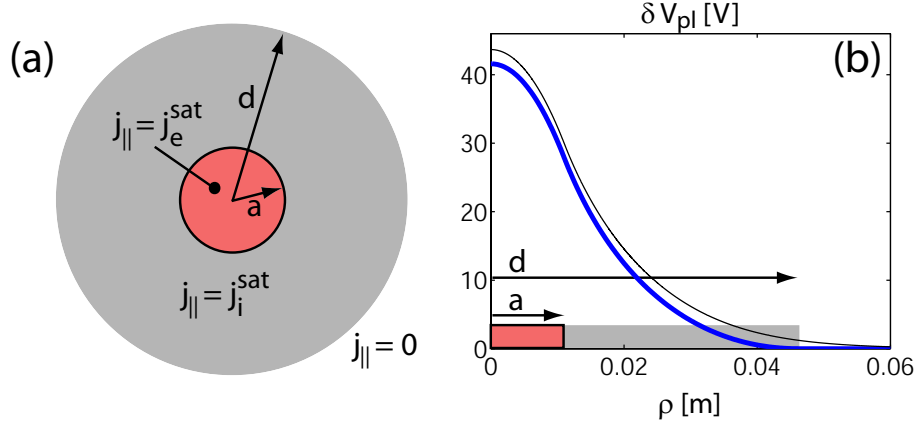


Figure 7.3.10: Estimate of the expected plasma potential variations induced by biased electrodes in the case where ion-neutral collisions are the only source of cross-field currents. The thick blue curve in (b) is obtained from Eq. (7.3.5), assuming the simplified structure of the parallel current density sketched in (a). For the thin black curve, Eqs. (7.3.3) and (7.3.4) are assumed instead for the parallel current density.

Eqs. (7.3.3) and (7.3.4) (thin black line). A bias potential $V_{bias} \gtrsim 53$ V is necessary to assure electron saturation current over the whole surface of the electrode. The values we have assumed here are $\alpha_r = \sqrt{2m_i/(\pi m_e)} \approx 34$, $n_{se}/n_0 = 0.5$, $B = 0.076$ T, $m_i = 1$ amu, $L_c = 2\pi$ m, $T_e = 2.5$ eV, and $a = 1.1$ cm, such that πa^2 corresponds approximately to the surface of two electrodes in the experiment. As in [147], we estimate ν_{in} as $\frac{p_n}{T_{amb}} \sigma^{mt} v_{th,i}$. With a neutral pressure of $p_n \approx 2 \cdot 10^{-4}$ mbar, an ambient temperature $T_{amb} = 0.025$ eV, a momentum transfer cross-section σ^{mt} for H-H⁺ charge exchange collisions of $\approx 10^{-18}$ m² and assuming an ion temperature of 1 eV in the evaluation of the thermal velocity $v_{th,i}$, we get $\nu_{in} \approx 5 \cdot 10^4$ s⁻¹.

Comparing the calculated values of δV_{pl} in Fig. 7.3.10 with measurements in Fig. 7.3.6 (a), (b), we find that the estimated potential variations exceed the experimentally measured ones by a factor ≈ 10 . Can this discrepancy be explained by uncertainties in the parameters used to calculate δV_{pl} in Fig. 7.3.10? To address this question, let us look at the expression for $\delta V_{pl}(0)$ in Eq. (7.3.6). The quantity α_r is evaluated experimentally (see Fig. 7.3.7 (d)), justifying the assumed value $\alpha_r \approx 34$. The pre-sheath density drop, on the contrary, could be reduced below the assumed value of 0.5 due to neutral friction, as discussed in Sec. 6.3. This would result in a better agreement with the experimental results. Direct measurements of n_{se}/n_0 will be necessary to determine the impact of this effect. Another uncertainty is related to the ion temperature, which is not measured in the experiment. As $\delta V_{pl}(0) \propto 1/\sqrt{T_i}$ and we do not expect ion temperature to exceed the assumed value of 1 eV, $\delta V_{pl}(0)$ should not be overestimated by this term. Finally, concentrations of impurities or molecular hydrogen ions (H₂⁺ and H₃⁺) are not known. This uncertainty enters as $1/(m_i \sigma^{mt})$ in Eq. (7.3.6) and would require an ion mass analyzer to be evaluated. We note here merely that the term $1/(m_i \sigma^{mt})$ does not necessarily

decrease significantly with respect to the value assumed above when other ions than H^+ are present. As an example, we assume that collisions between H_3^+ and H_2 are dominant. m_i equals 3 amu in that case. At the same time, the momentum transfer cross section reduces by a factor 2-3 compared to collisions between H^+ and H [91]. While we can not give here a definite answer on the level of uncertainty on the calculated value of δV_{pl} in Fig. 7.3.10, the strong discrepancy of about a factor 10 compared with experimental results indicates that currents due to ion-neutral collisions do not significantly contribute to cross-field currents.

To verify this experimentally, we perform discharges with four different values of neutral gas pressure, ranging from $p_n \approx 10^{-4}$ mbar to $p_n \approx 6 \cdot 10^{-4}$ mbar. In apparent contradiction to the above estimate, this does reveal a rather strong dependence of the magnitude of the induced potential variations on p_n . The measured structures of δV_{fl} are shown in Fig. 7.3.11 (a) and (b) for the two extreme cases. In (c), we show the maximum of δV_{fl} measured with HEXTIP as a function of gas pressure for two scans, where different pairs of electrodes (number 15, 16 and 19, 20, respectively) are used for the biasing. For comparison, the $1/p_n$ dependence is also plotted.

The trend in Fig. 7.3.11 (c) could be caused indirectly by a change in the pre-sheath density drop n_{se}/n_0 rather than by a significant increase of cross-field currents. We observe indeed that the current on the electrodes, which we assume $\propto n_{se}\sqrt{T_e}$, decreases by $\approx 30\%$ as we go from $p_n \approx 10^{-4}$ mbar to $p_n \approx 6 \cdot 10^{-4}$ mbar. This seems, however, consistent with a similar decrease in ion saturation current $\propto n_0\sqrt{T_e}$ measured with HEXTIP in the region of the biased electrodes, and n_{se}/n_0 does not seem to vary significantly with p_n . Another possibility could be that potential variations in front of the limiter are independent of p_n , but that an increase of parallel resistivity with p_n leads to a drop of δV_{fl} along the magnetic field and causes the observed trend in the HEXTIP plane. Performing the same measurements of δV_{fl} in the HEXTIP plane and right on the limiter as in Sec. 7.3.3.2 for the highest pressure value, however, still shows a fairly good toroidal symmetry of δV_{fl} . This suggests that the trend of δV_{fl} with gas pressure in Fig. 7.3.11 (c) is indeed due to an increase in cross-field currents.

A strong dependence of the induced bias potential on gas pressure despite low levels of estimated cross-field currents caused by ion-neutral collisions is reminiscent of results in [185, 186]. In this study, a similar problem was investigated. Plasmas in a purely toroidal magnetic field are generated by fast electrons emitted from a hot cathode inside the torus. This injected charge causes a negative potential well. Its magnitude could not be explained by ion-neutral collisions alone and simulations suggest a dominant role played by the fluctuating ion-polarization current. Nevertheless, similarly to the present experiments, the magnitude of the potential well was found to be roughly inversely proportional to the neutral gas pressure.

We now consider the other contributions to the cross-field current in Eq. (7.3.1), i.e., the ion-polarization current and the current caused by viscosity. Even without fluc-

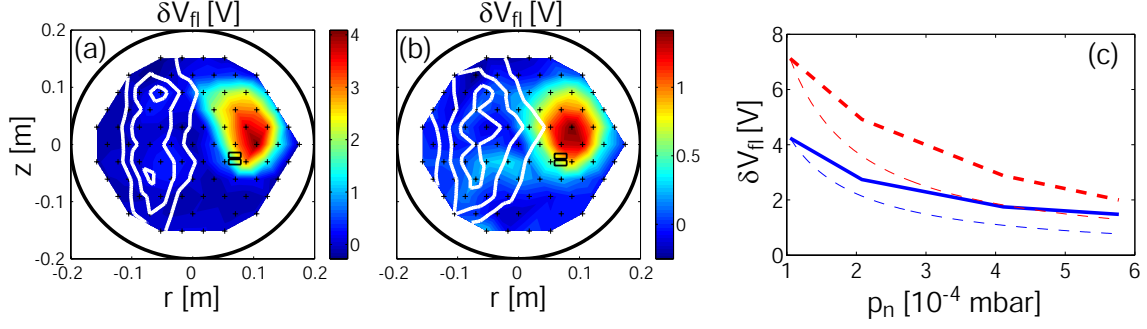


Figure 7.3.11: δV_{fl} for a discharge with neutral pressure $p_n \approx 10^{-4}$ mbar (a), and $p_n \approx 5.8 \cdot 10^{-4}$ mbar (b). The maximum of δV_{fl} for four different values of p_n is shown in (c) (thick, solid curve). The same is also plotted for a case where the bias is applied to a different pair of electrodes (thick, dashed curve). Thin, dashed curves show the $1/p_n$ dependence for comparison.

tuations, $\partial_t \mathbf{E}_\perp = 0$, the ion-polarization current can be important due to the term $(\mathbf{v}_{\mathbf{E} \times \mathbf{B}} \cdot \nabla_\perp) \mathbf{E}_\perp$. Assuming a vertically elongated wall electrode and a radial cross-field flow in the plasma would result in a potential variation induced by the electrode that is shifted in the direction of the flow [184], which would qualitatively agree with experimental observations (see Sec. 7.3.3.3). Here, we merely estimate the importance of the term $(\mathbf{v}_{\mathbf{E} \times \mathbf{B}} \cdot \nabla_\perp) \mathbf{E}_\perp$ with respect to $\nu_{in} \mathbf{E}_\perp$ in Eq. (7.3.1). Assuming a convective velocity $u_D \approx 1000 \text{ ms}^{-1}$ of the order of the blob velocity [139] and a scale length of the electric field of $l_\perp \approx 3 \text{ cm}$ gives $\mathbf{v}_{\mathbf{E} \times \mathbf{B}} \cdot \nabla_\perp \approx u_D / l_\perp = 3.3 \cdot 10^4 \text{ s}^{-1}$, which is of the same order as ν_{in} . The current due to viscosity on the other hand should be negligible, at least if a classical viscosity coefficient is assumed.

We conclude that the origin of cross-field currents that limit the achievable potential variation δV_{pl} in the biasing experiments reported here can not be unambiguously identified. Experiments reveal a strong dependence of δV_{pl} on the neutral gas pressure, indicating that currents due to ion-neutral collisions play an important role. At the same time, simplified theoretical estimates point towards a much smaller contribution of this current channel, although some uncertainties, related e.g. to the pre-sheath density drop, could not yet be quantified.

Different effects are certainly present at the same time and it is not clear at this point how they interplay. A clearer understanding of the effect of biasing in the presence of neutral friction, plasma convection and fluctuations of order unity most likely requires numerical studies.

7.4 Conclusions

We have explored experimentally several possibilities of blob and turbulence control. The first idea is based on a prediction that blob radial velocity can be controlled by varying the angle between magnetic field and limiter [152, 171]. We have designed

and constructed a special limiter to test this. Several plates have been mounted perpendicularly to two halfmoon limiters. Pivoting these limiters around a vertical axis allows varying the angle between magnetic field and limiter in the blob propagation region continuously down to $\approx 10^\circ$ [147, 173]. Following the theoretical prediction, this should allow increasing or reducing blob velocity by $\approx 50\%$, depending on the direction of the tilt. Such a dependence of blob velocity on tilt angle is clearly not observed in the experiment. We have discussed several reasons for this result, such as perturbations induced by the edges of the limiter plates. As pointed out, a different experimental setup is probably required to draw a conclusion on the validity of the theoretical prediction.

In another experiment, we have installed a glass limiter in the blob region. It was found that this charges up strongly negatively. The trajectory of blobs and time averaged profiles could be substantially modified by this 'passive' biasing scheme.

In view of controlling SOL width and peak heat fluxes on the divertor of fusion devices by toroidally (poloidally) asymmetric basing [21], we have conducted a detailed study of active biasing on TORPEX. An array of 3×8 electrodes was installed on a conducting limiter in a region where, as in the SOL, curvature driven turbulence and blobs cause a high level of particle and heat transport across the magnetic field. While negative biasing has negligible effects, it is clearly shown that the frequency of the dominant mode, the radial and vertical blob velocities as well as the time averaged profiles can be significantly modified by positively biasing the electrodes. The time averaged perturbation of plasma potential and density profiles induced by biasing a pair of electrodes shows characteristics of a convective cell. Measurements on the limiter and over a cross-section toroidally displaced by 90° were performed, showing that these perturbations are fairly uniform along the magnetic field.

Two limitations for biasing experiments are identified. The first one is on the locality of the induced potential variations. The strongest potential modifications are not observed along the biased flux tube, but at a position shifted in the direction of plasma flows. The second limitation concerns the magnitude of achievable potential variations, which is well below the potential applied to the electrodes. At the origin of this is a rather high level of cross-field currents, which is inferred from the strongly asymmetric current-voltage characteristics of the electrodes. Estimates have been performed to identify the origin of these cross-field currents. Assuming currents induced by neutral friction alone leads to predicting potential variations that are an order of magnitude higher than in the experiment, although some uncertainties in these estimates, e.g. on the value of the pre-sheath density drop could not be precisely quantified.

At the same time, scanning the neutral pressure in the experiment reveals strong effects of neutral pressure on the resulting potential variations. This suggests a complicate interplay of currents due to ion-neutral collisions and ion-polarization currents due to flows and high levels of turbulence. These findings are similar to results reported in [185, 186]. There, experiments and simulations were performed to understand the magnitude of the negative potential well and resulting cross-

field currents produced by injecting electrons from a hot negatively biased cathode. Simulations showed that the fluctuating ion-polarization current is the dominant source of cross-field current. Nevertheless, the magnitude of the potential well was found to be roughly inversely proportional to the neutral gas pressure.

The physics limiting the effect of biased electrodes and other findings reported here could be further investigated in the future with the help of two-dimensional [70] and global, three-dimensional [73] fluid codes. These have recently been developed for the simple magnetized torus configuration and are being validated with experiments on TORPEX (see [74, 75] and Ch. 8).

Most of the biasing experiments reported here have been conducted in a region where transport is dominated by plasma blobs. This is more characteristic for the far-SOL, where it might again be interesting to reduce radial transport and the contact of plasma with the first wall [187]. As we have seen in Fig. 7.3.3, a blob can overcome a vertically elongated potential barrier. Future studies could further investigate to what extent a reduction of transport in the blob region is possible.

Another possibility would be to investigate the feasibility of broadening plasma profiles in the region of strong gradients, where dynamics are dominated by interchange waves in TORPEX. This could be done by arranging the electrodes closer to the edge of the limiter and over the full height of the TORPEX vessel.

Code validation on TORPEX

Theoretical models have proven to be very useful to understand aspects of turbulence on TORPEX, such as the nature of the dominant instability or the propagation velocity of blobs. It is natural to ask to what extent these models reproduce the full turbulent properties on TORPEX. Answering this question requires detailed model validation. In a wider context, model validation is essential to assess predictive capabilities of plasma turbulence codes, e.g. for the design of future fusion reactors. TORPEX constitutes an ideal testbed for the validation of such codes, due to its relatively simple configuration, detailed diagnostics, and the possibility for controlled parameter scans.

The work described in this chapter was carried out in collaboration with members of the theory group at the CRPP and was published in [74, 75].

For a code validation project, it is essential to determine an appropriate comparison methodology. Based on ideas discussed in [188, 189], we divide this into four steps. First (i), the simulation model needs to be qualified; i.e., it is necessary to establish the applicability of the model hypotheses for the simulated physical phenomenon. Second (ii), verification of the code is necessary, in order to prove that the code solves correctly the model equations. Third (iii), simulation and experiment have to be compared considering a number of physical quantities, common to the experimental measurements and simulation results. These physical quantities, denoted as

validation observables, should be identified and organized into a primacy hierarchy that measures how stringent each observable is for comparison purposes. Fourth (iv), the overall degree of agreement between simulations and experiments needs to be quantified by using an appropriate composite metric, χ . This χ should combine the results of the comparison of all the observables, taking into account position in the hierarchy and precision. The metric χ should be complemented by a parameter Q that assesses the quality of the comparison. Practically, Q provides an indication of the number of observables that have been used for the validation and the strength of the constraints they impose.

While model qualification and code verification [point (i) and (ii) of the validation guidelines] are now routinely considered in plasma physics (see e.g. Ref. [190, 191]) and their methodology has been formulated in considerable detail, only recently has the plasma physics community approached a rigorous methodology for establishing the validation observables and the comparison metric.

In the first part of this chapter, we focus on the methodology for points (iii) and (iv) of the validation guidelines [74, 75]. In Sec. 8.1.1, we identify validation observables based on Langmuir probe (LP) measurements and discuss how to classify them according to the primacy hierarchy. Then, we propose a metric to quantify the agreement between experiment and simulation. This involves three steps. First, relative to each observable, we discuss how to quantify the agreement between experiment and simulation (Sec. 8.1.2). Second, we propose how to combine these individual levels of agreement to form the composite metric χ (Sec. 8.1.3). Third, we define the parameter Q , which qualifies the assessment of the agreement between experiment and simulation (Sec. 8.1.4). We remark that the validation procedure should remain simple. The goal is not mathematical rigor, but a useful tool that can easily be applied in order to compare models and assess their goodness and their limitations.

In the second part, we apply this methodology to the simulation of TORPEX plasmas [75] (Sec. 8.2), considering two recently developed models. One is a 3D two-fluid model [73], able to describe the global evolution of TORPEX plasmas. The other one is a reduced 2D two-fluid model [70], able to describe only the evolution of $k_{\parallel} = 0$ modes. In order to be meaningful, a comparison between experiment and simulation should be carried out across a parameter scan. As discussed in Sec. 2.4, the number of field lines turns N inside TORPEX is an important quantity, determining the nature of the dominant instability [73, 77, 78]. We therefore perform a scan of this parameter and consider the cases $N = 2, 4, 8$, and 16. Finally, results and possible future steps for the TORPEX code validation project are discussed.

8.1 Methodology of turbulence code validation

8.1.1 Validation observables and primacy hierarchy

For a validation project, an appropriate set of observables needs to be defined, common between the experiment and simulation, and analyzed using the same data analysis techniques. In principle, one should include as many observables as possible. If a code is specifically used to predict a particular set of quantities, these should be included as validation observables. On the other hand, an observable should be physically relevant, i.e., focus should be on quantities containing the most important theoretical predictions. For example, while skewness, the third standardized moment of the power distribution function (PDF) of a signal, can be a relevant quantity, highlighting different fluctuation characteristics in different regions of the plasma, this is most likely not the case for the 8th moment. Observables should be independent and not simply be a function of other observables. For example, if the time average of density, \bar{n} , and the time average of the temperature, \bar{T}_e , are observables, then the pressure, $\bar{p}_e = \bar{n}\bar{T}_e$ cannot be considered a new observable. However, if \bar{p}_e is evaluated using an independent measurement, such that it does not need to be written as a function of the other observables, then \bar{p}_e can be considered a new observable. Finally, the resolution of multi-dimensional observables should be sufficient to well describe their variation along all dimensions. For example, the spatial resolution of an observable such as the density profile should be sufficient to describe the typical density scale length.

It is important to note that not all validation observables are equally stringent for the comparison. I_{sat} for example is a directly measured quantity. On the other hand, the measurement of a quantity such as particle flux, if evaluated with a modified, five tip triple probe as in Sec. 3.5.6, is rather complicated. It requires a number of model assumptions and involves combinations of measurement from different probe tips that introduce additional uncertainties. These are related to possible differences in the response of the probes, mutual perturbations between tips, or that due to a finite spacing, the hypothesis that tips "see" exactly the same plasma parameters can be marginally satisfied. Evaluating rigorously all these uncertainties can be very challenging. Experiments and simulations could therefore fortuitously provide similar particle fluxes, simply because errors in the individual measurements or model assumptions cancel out. On the other hand, simulations could reproduce very well the experiment but still display very different levels of particle flux, for example due to a model assumption that is poorly satisfied. More directly obtained quantities such as I_{sat} are therefore more stringent for the comparison.

To account for this, we order the validation observables into a primacy hierarchy that tracks how the measurements are combined together and what assumptions are used to form the observables [74]. The higher the level of an observable in the hierarchy, the less stringent it is for the comparison. If simulations and experiments

are compared using an observable at a certain level in the primacy hierarchy, observables at the lower levels should also be considered, where the comparison is more stringent. This provides transparency on how measurements are obtained and what observables need to be included in a validation project. It should also assure that, when comparing the performance of two codes, one does not favor a code based on a good agreement of a quantity that involves a large number of hypothesis, while the comparison with directly measured quantities favors the other code.

To determine the hierarchy level h of an observable for the experiment-simulation comparison, we take into account the hypotheses used to obtain both the experimental and simulation observables. The quantity h is thus composed of the contribution from the individual experimental (h^{exp}) and simulation (h^{sim}) primacy hierarchy, such that

$$h = h^{exp} + h^{sim} - 1. \quad (8.1.1)$$

The primacy hierarchies h^{exp} and h^{sim} are evaluated by summing the number of model assumptions and hypotheses used to form an observable, respectively, from experimental measurements and simulation results. A directly obtained quantity (i.e., a code output or a directly measured value) is at level 1. As a combination of experimental measurements usually also involves a hypothesis (same plasma responses of the probes, no mutual disturbance, sufficient spatial resolution), the level of h^{exp} increases when combinations of measurements are involved. We note that these are not strict rules, but they provide a guideline to determine how stringent each observable is for the comparison. In some cases, there can of course be some arbitrariness in what one considers an additional hypothesis.

We consider now specifically LP based measurements and evaluate h^{exp} and h^{sim} for a number of possible observables. These are tabulated in Fig. 8.1.1.

The most directly measured quantities with LPs are I_{sat} and V_{fl} and they occupy the first level of the experimental primacy hierarchy. This is also true for quantities directly deduced from I_{sat} and V_{fl} , such as fluctuation levels, skewness, or the power spectral densities (PDFs). Simulations do not provide I_{sat} and V_{fl} directly since they typically evolve quantities such as n , T_e , and V_{pl} . A model for the LP has thus to be assumed in order to deduce I_{sat} and V_{fl} . Such a model can only approximately take into account how I_{sat} and V_{fl} depend on plasma parameters, how the geometrical properties of the probe influence the measurement, or how the frequency response of the LP is limited by plasma properties or electronics. Therefore, I_{sat} and V_{fl} are second level observables in the simulation primacy hierarchy. From Eq. (8.1.1), the hierarchy level for the experiment-simulation comparison is $h = 2$ for I_{sat} and V_{fl} . The time-averaged quantities \bar{n} , \bar{T}_e , and \bar{V}_{pl} are on the second level of the experimental primacy hierarchy, since a model is required to deduce these quantities from the measured $I - V$ characteristics of an LP. In the simulations, \bar{n} , \bar{T}_e , and \bar{V}_{pl} are direct outputs of the code and occupy thus the first level of the simulation hi-

	Experimental hierarchy h^{exp}	Simulation hierarchy h^{sim}	Comparison hierarchy h
I_{sat}, I_{sat} statistics	1	2	2
V_{fl}, V_{fl} statistics	1	2	2
$\bar{T}_e, \bar{n}, \bar{\phi}$	2	1	2
k_z, k_ϕ	2	1	2
n, T_e, V_{pl}	3	1	3
Γ_{fluct}	6	1	6

Figure 8.1.1: Primacy hierarchy levels for a set of observables, based on LP measurement [74]. We assumed that Γ_{fluct} is evaluated from Eq. (3.5.22).

erarchy. Also on the second level of the experimental primacy hierarchy are global quantities of turbulence that involve the combination of I_{sat} and/or V_{fl} measurements of multiple LPs. Examples are vertical and toroidal wave numbers, k_z and k_ϕ , obtained from spatial Fourier transform of probe arrays or the two-point correlation technique. On the other hand, global turbulence properties can directly be obtained from simulation data, involving no hypothesis. They thus occupy the first level in the simulation hierarchy.

As discussed in Sec. 3.5, time dependent measurements of n , T_e , and V_{pl} can be obtained with a triple probe. In that case, as this involves combination of measurements and an LP model, these quantities are at the third level of the experimental hierarchy. As direct outputs of the code, n , T_e , and V_{pl} are at the first level of the simulation hierarchy.

Even more indirect, as mentioned above, is the evaluation of the fluctuation-induced cross-field particle flux Γ_{fluct} . Let us assume that it is evaluated with a triple probe from $\Gamma_{fluct} = \langle \tilde{n} \tilde{v}_r \rangle$ with $\tilde{v}_r = (\tilde{V}_{fl5} - \tilde{V}_{fl1}) / (d_{tip} B)$ (see Sec. 3.5.6 for details). This involves a combination of measurements and relies on the hypothesis that electric fields can, for the purpose of evaluating the time averaged particle flux, accurately be deduced from the gradient in floating potential. Therefore, \tilde{v}_r can be identified as a third level quantity in the experiment. As Γ_{fluct} is deduced from the combination of two third level quantities (that together include four hypotheses), Γ_{fluct} is at the 6th level in the experimental hierarchy. In the simulation, where n and V_{pl} are direct outputs of the code, Γ_{fluct} is a first level observable.

8.1.2 Quantification of the agreement of each observable

As a first step in constructing a global metric for the experiment-simulation comparison, we quantify the agreement between experiment and simulation relative to each observable. We denote with x_j and y_j the values of the j -th observable obtained from the experimental measurement and the simulation results, respectively. Most of the observables depend on space and time, and the value of the observables is given on a discrete number of points. We denote with $x_{j,i}$ and $y_{j,i}$ the values of

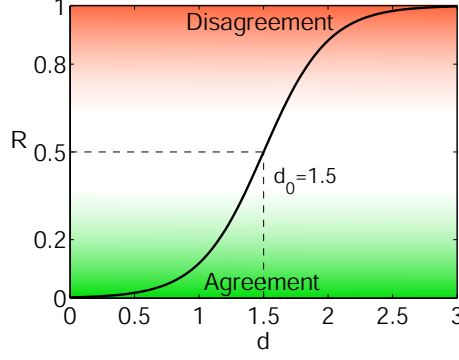


Figure 8.1.2: Functional dependence linking the normalized difference between experiment and simulation output d_j , Eq. (8.1.2) and the level of agreement R_j , Eq. (8.1.3).

the j -th observable at points $i = 1, 2, \dots, N_j$. For the j -th observable, we define the quantity d_j as the difference between experiment and simulation, normalized to the uncertainty related to these quantities:

$$d_j = \sqrt{\frac{1}{N_j} \sum_{i=1}^{N_j} \frac{(x_{j,i} - y_{j,i})^2}{\Delta x_{j,i}^2 + \Delta y_{j,i}^2}}. \quad (8.1.2)$$

Here, $\Delta x_{j,i}$ and $\Delta y_{j,i}$ are the uncertainties, i.e. the r.m.s., related to the evaluation of $x_{j,i}$ and $y_{j,i}$. Since it is possible to argue that the simulations and experiment agree if they fall within the error bars, we define the level of agreement between experiment and simulation for observable j as

$$R_j = \frac{\tanh[(d_j - d_0)/\lambda] + 1}{2} \quad (8.1.3)$$

with the meaning that $R_j \approx 0$ corresponds to perfect agreement (within the error bars), while $R_j \approx 1$ denotes complete disagreement between simulation and experiment. The functional dependence, Eq. (8.1.3), relating d_j and R_j is plotted in Fig. 8.1.2. We note that for $d_j = d_0$, we find $R_j = 0.5$. Therefore, d_0 identifies the transition from agreement to disagreement. The value of d_0 should then correspond to a discrepancy between experiment and simulation that is comparable to their uncertainties. In the case $\Delta x_{j,i} = \Delta y_{j,i}$, $d_0 \simeq 1.4$ is the distance corresponding to a discrepancy between experiment and simulation equal to the sum of the experimental and simulation uncertainties. The parameter λ instead denotes the sharpness of the transition from $R_j \approx 0$ to $R_j \approx 1$. As shown in [75], the conclusions of the validation exercise discussed in Sec. 8.2 are not affected by the choice of parameters in the range $1 \leq d_0 \leq 2$ and $0.1 \leq \lambda \leq 1$ and we believe that $d_0 = 1.5$ and $\lambda = 0.5$ are reasonable values.

Particular attention should be paid in evaluating the experimental and the simulation error bars. In the case of the experiments, we can identify four main uncertainty sources. First, the model of a measuring device provides predictions through

which one can infer the physical quantities of interest (e.g., from the I-V curve of a Langmuir probe one can infer plasma properties like n and T_e). Experimental measurements typically do not follow perfectly the model predictions: thus, a fit has to be made in order to evaluate the relevant physical parameters, introducing an uncertainty that we denote with $\Delta x_{j,i}^{fit}$. We emphasize that $\Delta x_{j,i}^{fit}$ is the uncertainty of data fitting and not of the model assumption. Second, a source of uncertainty is due to properties of the measuring device that are often difficult to evaluate accurately (e.g., geometry and surface condition of a Langmuir probe). Thus, measurements should be performed with different tools (e.g., Langmuir probes which differ in dimensions, surface conditions, and electronics). The quantity $\Delta x_{j,i}^{prb}$ denotes the uncertainty related to the probe properties. Third, the plasmas are not perfectly reproducible due to control parameters difficult to set or know precisely (e.g., the vacuum pressure). Experiments should be repeated in order to check the reproducibility of the plasma, while measurements are taken with different measurement devices. The quantity $\Delta x_{j,i}^{rep}$ is the uncertainty due to the plasma reproducibility, averaged over the different measuring devices. Finally, the use of a finite time data set constitutes a source of uncertainty, $\Delta x_{j,i}^{fin}$, which can be relevant particularly if high moments of the probability distribution functions are considered as observables, and which can be estimated through statistical techniques. One can show that the total experimental uncertainty is given by $\Delta x_{j,i}^2 = (\Delta x_{j,i}^{fit})^2 + (\Delta x_{j,i}^{prb})^2 + (\Delta x_{j,i}^{rep})^2 + (\Delta x_{j,i}^{fin})^2$.

Simulations are affected by uncertainties resulting from three sources: (i) errors due to the numerics (e.g., due to the limited accuracy of the numerical integration scheme or due to the finite grid resolution), (ii) errors due to unknown or imprecise input parameters, and (iii) statistical uncertainty due to a finite time series. While errors due to the numerics, $\Delta y_{j,i}^{num}$, can be estimated through convergence tests, the evaluation of the error related to imperfectly known input parameters, $\Delta y_{j,i}^{inp}$, requires a sensitivity study, i.e. an investigation of how the model results are affected by the input parameter variations. Usually, the number of input parameters of a turbulence simulation code is quite large and a complete study of the model response is prohibitive. However, the theory can indicate to which input parameters the results are particularly sensitive. The analysis must then focus on those. We remark that in the literature, a number of useful techniques have been proposed to predict the response of a model to variation of simulation parameters using the smallest possible number of simulations (see e.g. Ref. [192]). The uncertainty due to a finite set of data, $\Delta y_{j,i}^{fin}$, is typically more relevant for the simulation than for the experiment since, because of the computational cost, the time series obtained from the simulations is typically limited to a short time span. Also in this case, this uncertainty should be evaluated by using statistical techniques. As in the case of the experimental error bars, the three sources of error should be added, such that $\Delta y_{j,i}^2 = (\Delta y_{j,i}^{num})^2 + (\Delta y_{j,i}^{inp})^2 + (\Delta y_{j,i}^{fin})^2$.

We note that the error bars should not take into account the uncertainties related to model assumptions and/or to combinations of measurements, which are often needed to deduce the comparison observables from the simulation results and the

raw experimental data. Evaluating rigorously those uncertainties is usually very challenging. The idea is to take them into account approximately through the observables primacy hierarchy. More specifically, the higher the hierarchy level of an observable is the lower the importance of the observable in the comparison metric.

8.1.3 Metric

The overall level of agreement between simulation and experiment can be measured by considering a composite metric, which should take into account the level of agreement of each observable, R_j , and weight it according to how constraining each observable is for comparison purposes. This means that the hierarchy level of each observable as well as the level of confidence characterizing the measurement or the simulation of each observable have to be taken into account: the higher the level in the primacy hierarchy and the bigger the error affecting the observable measurement, the smaller the weight of the observable should be. We thus define the metric χ as

$$\chi = \frac{\sum_j R_j H_j S_j}{\sum_j H_j S_j}, \quad (8.1.4)$$

where H_j and S_j are functions defining the weight of each observable according to its hierarchy level and the precision of the measurement, respectively. The metric thus defined is normalized in such a way that perfect agreement is observed for $\chi = 0$ (within the considered observables), while simulation and experiment disagree completely for $\chi = 1$.

The definition of H_j and S_j is somewhat arbitrary. H_j should be a decreasing function of hierarchy levels. The definition we propose here is $H_j = 1/h_j$, where h_j is the combined experimental/simulation primacy hierarchy level (see Fig. 8.1.1 for a list of the hierarchy levels relative to LP measurements). This definition implies that if no assumptions or combinations of measurements are used for obtaining an observable, then $H_j = 1$. The quantity S_j should be a decreasing function of the experimental and simulation uncertainty. We introduce the following definition:

$$S_j = \exp \left(- \frac{\sum_i \Delta x_{j,i} + \sum_i \Delta y_{j,i}}{\sum_i |x_{j,i}| + \sum_i |y_{j,i}|} \right) \quad (8.1.5)$$

such that $S_j = 1$ in the case of zero uncertainty. We remark that, while the composite metric χ is a very useful tool to provide the overall assessment of the agreement, it is also very important to provide a table, which we will denote as "validation table," with a list of the observables used for the comparison, as well as the values of d_j , S_j , and H_j related to each observable. This is useful for two reasons. First, it can reveal if agreement between simulations has been evaluated by considering a relevant set of observables. Second, by studying the agreement of each observable one can infer physical effects missing from the simulations.

8.1.4 Quality

The validation metric should be complemented by a parameter, Q , that assesses the "quality" of the comparison. The idea is that a validation is more reliable with a larger number of independent observables, particularly if they occupy a low level in the primacy hierarchy and the measurement and simulation uncertainties are low. The quality of the comparison Q can thus be defined as

$$Q = \sum_j H_j S_j. \quad (8.1.6)$$

Particular attention should be paid to the interpretation of the parameter Q , since the quality of the comparison unavoidably depends on the choice of the observables used. Careful study of the validation table is therefore necessary to obtain a complete picture of the comparison quality.

A compromise between the single parameter Q and the analysis of the full validation table can be made by using a set of parameters to characterize the quality of the validation. In particular, we note that the quality of a comparison is higher if, e.g., a two-dimensional observable (a 2D profile) is used for the comparison instead of a one-dimensional observable. Therefore, a set of Q indexes, Q_n , can be introduced in order to take separately into account observables with different dimensionality: i.e., $Q_n = \sum_{j_n} H_j S_j$, where the sum is restricted to the n -dimensional observables.

8.2 Simulation-experiment comparison

The above described validation methodology is now applied to the simulation of TORPEX plasmas [75]. Two models are considered. The first one is a 2D two-fluid model [70], the second one is a global 3D two-fluid model [73]. These models are derived from the drift-reduced Braginskii equations in the electrostatic limit and assuming $T_i \ll T_e$. The 2D model evolves n , T_e , and V_{pl} , the 3D model additionally computes ion and electron velocities along the magnetic field. Particle and heat sources are implemented to mimic plasma production and power absorption at the upper hybrid and the electron cyclotron resonance on TORPEX (see [56] and Sec. 2.3). The source strengths are estimated using a global balance of TORPEX plasmas. More details on the model can be found e.g. in the appendix of [75] or directly in the references [70] and [73]. We emphasize that these codes simulate the full quantities.

For the validation, we consider four plasma scenarios, characterized by $N = 2, 4, 8$, and 16, respectively. The working gas is hydrogen and a microwave power of 300 W is used in the experiments. As validation observables, we use the equilibrium radial profiles at the vertical midplane of density, \bar{n} , electron temperature, \bar{T}_e , electric potential, \bar{V}_{pl} , ion saturation current, \bar{I}_{sat} , as well as the normalized I_{sat} fluctuations,

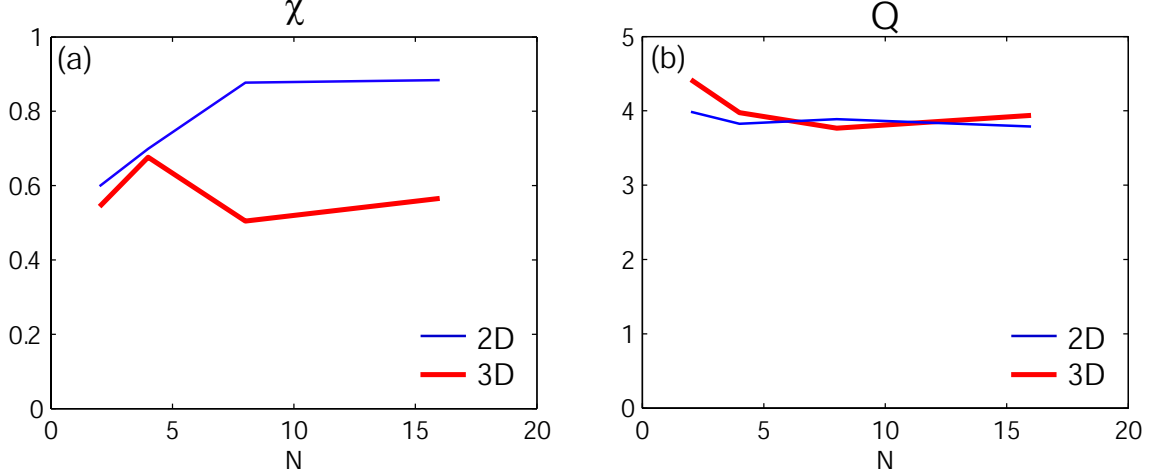


Figure 8.2.1: Global metric χ (a) and comparison quality Q (b) for the 2D and the 3D model and for different values of N [75]. For the evaluation of R_j from Eq. (8.1.3), the values $d_0 = 1.5$ and $\lambda = 0.5$ are used.

$\delta I_{sat}/\bar{I}_{sat}$, I_{sat} skewness and kurtosis, the value of the vertical and toroidal wavenumbers, k_z and k_ϕ , and PDF and PSD of I_{sat} at the vertical midplane, at the radial point where \bar{I}_{sat} is equal to 3/4 of its peak value (i.e., in correspondence of a point where we expect to identify more clearly the turbulence properties). We perform the comparison using the toroidal mode number only for the 3D simulations, since it is not calculated self-consistently by the 2D model, which assumes $k_\parallel = 0$. The validation observables and the results of the comparison are listed in the validation table, Fig. 8.3.1, at the end of this chapter.

We note that for this exercise, all measurements are performed with LPs, mainly SLP and HEX TIP. For the measurement of the toroidal wavenumber k_ϕ , we apply the two-point correlation technique [65] to the TWIN probes (see Fig. 2.2.1). These are toroidally separated by 180° . For each observable, the experimental error bar Δx is evaluated by performing the experiments at least twice and comparing the measurements of different probes. For the evaluation of \bar{n}_e , \bar{T}_e , and \bar{V}_{pl} from the I-V characteristics, we additionally consider uncertainties related with curve fitting as discussed in Sec. 3.2.

The simulation uncertainty, Δy , is evaluated by performing for each TORPEX scenario a number of simulations where the parameters that are expected to significantly affect the simulations and that are not well known are varied. For the 3D simulations, these are the plasma resistivity ν and the boundary conditions (see App. B in [75] for details). For the 2D simulations, instead, the sensitivity to the parallel losses is studied. We assume that the error due to the numerics is negligible with respect to the one due to the unknown input parameters.

8.2.1 Global agreement and quality of the comparison

We consider here the overall agreement between simulation and experiment as quantified by the global metric χ in Fig. 8.2.1 (a). It is deduced from Eq. (8.1.4) and the values listed in the validation table, Fig. 8.3.1, both for the 2D and the 3D model. We see that both models agree similarly well with the experiment at low N values. While χ remains approximately constant as N is increased for the 3D model, it strongly increases for the 2D model. This behavior is expected, due to the transition in TORPEX from waves with $k_{\parallel} = 0$ to waves with $k_{\parallel} \neq 0$ at $N \approx 7$. This transition is well captured by the global metric.

Overall, the 3D model is thus clearly preferable compared to the 2D model. It gives values of χ in the intermediate range between perfect agreement ($\chi \approx 0$) and disagreement ($\chi \approx 1$). We therefore expect that the model reproduces well some aspects of turbulence while others are less well reproduced in quantitative terms. We discuss the agreement for individual observables in the next section.

Fig. 8.2.1 (b) shows the quality Q of the comparison. Since the uncertainties for all the observables are relatively small and they are at the second level of the validation hierarchy, Q is about constant as a function of N , and in particular $Q \simeq 4$. The Q values reported in the present validation project can be compared with the Q that would be obtained in a validation carried out by comparing exclusively the agreement of the experimental and simulation particle fluxes, that is $Q \leq 1/6$.

8.2.2 Comparison of individual observables

In the following, we discuss the agreement of individual observables of the present comparison. We focus on the 3D model, for which the global metric χ shows values in the intermediate range for all N and which performs considerably better at high N than the 2D model.

Examples of the radial profiles of observables (\bar{n} and $\delta I_{sat}/\bar{I}_{sat}$) are shown in Fig. 8.2.2 and the agreement between experiment and simulation d relative to each observable is listed in the validation table, Fig. 8.3.1. The validation table shows that the observable that is best reproduced by the 3D model (the one with the lowest d) is the toroidal wave number. The 3D code reproduces well the transition from waves with $k_{\phi} \approx 1$ to toroidally symmetric modes with $k_{\phi} \approx 0$. Together with a good agreement for the vertical wave number k_z , this demonstrates the transition from ideal to resistive interchange waves predicted in [73] (see also the discussion in Sec. 2.4). Low values of d are also observed for the PDF and the PSD of I_{sat} in Fig. 8.3.1. However, error bars are large for these quantities, which is apparent from the low values of the precision parameter S . Comparison of the experimental and simulation PSDs reveals clearer coherent features related to the dominant mode in the experiment than in the simulations [74, 75]. An example is shown in Fig. 8.2.3, where we plot the PSD for the case $N = 2$.

Good agreement is found for the density profiles as shown in the left column of Fig. 8.2.2. Adjusting the particle source could significantly improve agreement in the case $N = 4$.

The largest disagreement between 3D simulations and experiments is found for the fluctuation level of I_{sat} , Fig. 8.2.2 right column, and for the temperature profiles. Fluctuation levels are a factor $\approx 2 - 3$ smaller in simulations than in the experiment, and simulated temperature profiles are considerably flatter than in the experiments [75].

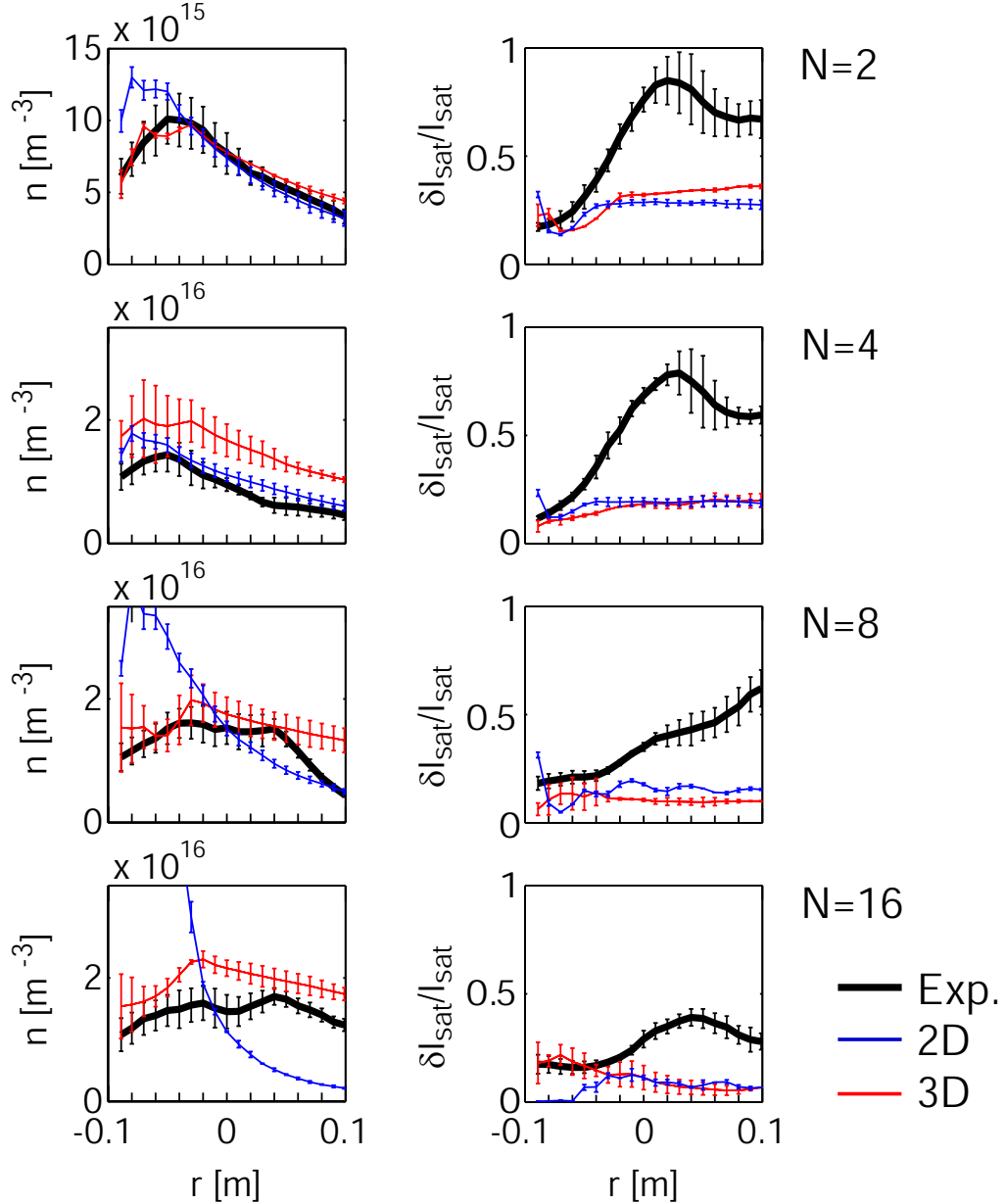


Figure 8.2.2: Examples of two observables used for the validation of the 2D and the global 3D code. The left column shows radial profiles of density, the right column the normalized fluctuation level of I_{sat} . Different rows correspond to different values of N .

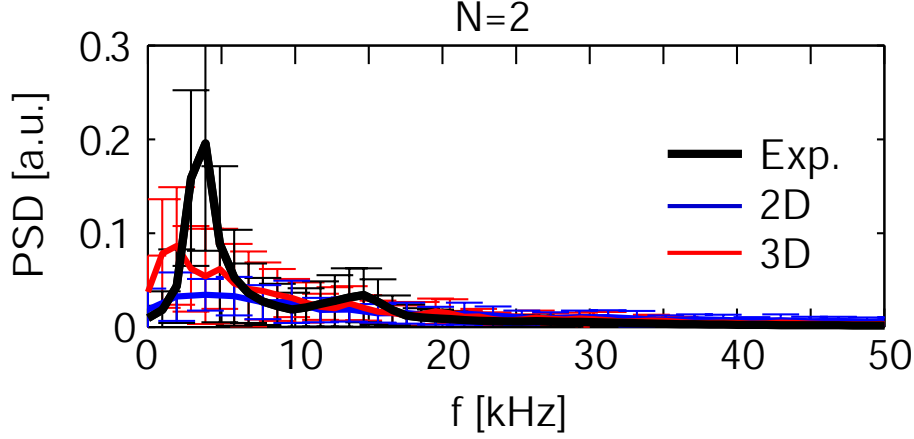


Figure 8.2.3: Example of the power spectral density of I_{sat} fluctuations in the mode region, for experiment and simulations and for $N = 2$.

8.3 Conclusions

We presented a methodology for code validation, with a particular focus on the classification of the observables used for the comparison [74] and on the assessment of the degree of agreement between simulation and experiment [75].

Depending on how directly observables are obtained from measurements or from simulation outputs, they are more or less stringent for the comparison. To account for this, we have ranked them into a primacy hierarchy. At a lower level in the hierarchy, we place observables that combine fewer measurements and require fewer model assumptions. Vice-versa, observables that require a higher number of model assumptions are at the highest levels of the primacy hierarchy. The assessment of the agreement between simulation and experiment starts at the level of each observable. We have pointed out that the distance between the experimental and simulation values should be evaluated and normalized to their uncertainties. Then, the agreement of each observable should be weighted into the global metric χ , and care should be taken to reduce the weight of observables higher in the comparison hierarchy and with higher levels of uncertainties. The metric χ has been normalized in order to be equal to 0 in the case of perfect agreement and 1 in the case of complete disagreement. To complete a validation, the quality of the comparison, Q , is also required. The parameter Q can be used to compare validations among them; it reveals how well a comparison has been performed, indicating the number of observables used for the comparison and how constraining they are. A validation table should also be provided in order to allow a complete picture of the comparison. This methodology has been applied to two simulation models for TORPEX. The first model is a 2D two-fluid model [70], the other one a global, 3D two-fluid model [73]. Eleven validation observables have been included into the comparison, nine of which are well resolved radial profiles. Moreover, the validation has been performed across a scan in the number of field line turns N inside TORPEX [75], considering the cases $N = 2, 4, 8$, and 16. The global metric χ clearly displays the fact that the 3D

model reproduces the transition from turbulence driven by ideal interchange modes for $N \lesssim 7$ to resistive interchange mode driven turbulence for $N \gtrsim 7$. Indeed, while 2D and 3D models perform similarly well for $N = 2$ and $N = 4$, the 3D model performs considerably better for larger N . Taking a look at individual observables reveals disagreements between the 3D model and simulations mainly for the fluctuation level of I_{sat} , the scale length of the electron temperature, and the coherency of the dominant mode.

The present work constitutes a solid basis for the TORPEX code validation project. It will allow an objective assessment of how the performance of the simulations can be further improved when additional physics effects will be included. Presently, work is ongoing to derive more accurate boundary conditions in presence of small angles between magnetic field and wall. Implemented into the 3D code, this could, in particular, provide more realistic parallel heat losses and probably lead to a more realistic electron temperature scale lengths. Additional improvement of the experiment-simulation agreement could possibly be achieved by including a background of neutrals into the code or taking into account the density dependence of the upper hybrid resonance layer.

On the experimental side, the number of observables used for the comparison should be extended, e.g. with measurements of the effective ion mass or with time dependent measurements of n , T_e , and V_{pl} from the new triple probe FRIPLE [62]. Confidence in existing measurements should also be improved. Measurements of the electron distribution function could, for example, allow estimating the contribution of fast electrons to the evaluated temperature profiles.

Observable	Dimensionality	H	N	d	R	S	d	R	S
				2D simulation			3D simulation		
\bar{n}	1	0.5	2	1.34	0.35	0.89	0.83	0.06	0.91
			4	1.33	0.33	0.88	3.21	1.00	0.84
			8	3.60	1.00	0.90	1.66	0.65	0.84
			16	7.81	1.00	0.91	2.00	0.88	0.89
\bar{V}_{pl}	1	0.5	2	1.19	0.22	0.89	3.12	1.00	0.89
			4	3.39	1.00	0.90	1.63	0.63	0.82
			8	6.91	1.00	0.91	0.82	0.06	0.73
			16	7.96	1.00	0.92	1.51	0.51	0.75
\bar{T}_e	1	0.5	2	2.30	0.96	0.91	3.59	1.00	0.92
			4	2.28	0.95	0.91	5.11	1.00	0.89
			8	6.05	1.00	0.92	6.42	1.00	0.93
			16	6.89	1.00	0.93	4.12	1.00	0.92
\bar{I}_{sat}	1	0.5	2	0.42	0.01	0.74	0.45	0.01	0.75
			4	0.66	0.03	0.69	2.56	1.00	0.73
			8	3.01	1.00	0.81	1.97	0.87	0.73
			16	4.55	1.00	0.84	1.61	0.61	0.77
$\delta I_{sat} \bar{I}_{sat}$	1	0.5	2	4.51	1.00	0.90	3.96	1.00	0.91
			4	7.77	1.00	0.90	7.47	1.00	0.90
			8	5.28	1.00	0.90	7.04	1.00	0.86
			16	5.56	1.00	0.88	4.00	1.00	0.82
I_{sat} skewness	1	0.5	2	3.10	1.00	0.85	3.72	1.00	0.81
			4	3.41	1.00	0.74	2.69	1.00	0.64
			8	4.02	1.00	0.83	2.27	0.96	0.62
			16	3.03	1.00	0.66	1.48	0.48	0.62
I_{sat} kurtosis	1	0.5	2	3.32	1.00	0.92	2.90	1.00	0.91
			4	2.94	1.00	0.85	2.93	1.00	0.83
			8	5.39	1.00	0.91	1.14	0.19	0.70
			16	2.77	0.99	0.83	1.32	0.32	0.86
I_{sat} PDF	1	0.5	2	1.08	0.15	0.72	0.88	0.08	0.68
			4	0.94	0.10	0.74	0.53	0.02	0.53
			8	0.46	0.02	0.67	0.25	0.01	0.40
			16	0.54	0.02	0.60	0.19	0.01	0.23
I_{sat} PSD	1	0.5	2	1.11	0.17	0.46	0.58	0.02	0.43
			4	1.16	0.20	0.44	0.41	0.01	0.31
			8	1.22	0.25	0.40	0.55	0.02	0.32
			16	1.28	0.29	0.40	2.13	0.93	0.49
k_z	1	0.5	2	1.79	0.76	0.42	1.32	0.33	0.69
			4	3.63	1.00	0.33	0.67	0.03	0.61
			8	7.24	1.00	0.36	0.71	0.04	0.53
			16	6.28	1.00	0.29	0.74	0.05	0.60
k_ϕ	0	0.5	2	-	-	-	0.25	0.01	0.92
			4	-	-	-	0.50	0.02	0.86
			8	-	-	-	0.64	0.03	0.86
			16	-	-	-	0.13	0.00	0.91

Figure 8.3.1: Validation table for the 2D and 3D TORPEX simulations [75]. The values R are evaluated assuming $\lambda = 0.5$ and $d_0 = 1.5$.

Conclusions

In the course of this thesis, a number of questions related to the open issues associated with turbulence and related structures in a toroidal plasma have been addressed. These issues are of interest both for fusion and the wide range of magnetized plasmas that exhibit similar turbulent phenomena. Below, the main results of this thesis are summarized and possible future experiments are proposed.

In TORPEX, blobs form from interchange waves that extend radially into a region of strong shear flows. This breaks apart the radially elongated wave structures, generating blobs. The conditionally averaged dynamics reveals a local steepening of the pressure profile prior to the radial elongation of the wave. This indicates that profile steepening is driving the blob formation process. To further investigate this point, blobs ejected at two different vertical positions in the same poloidal cross-section have been studied with time resolved measurements from a 2D Langmuir (LP) probe array. Conditional average sampling (CAS) revealed a slightly different dynamics for the two cases. For blobs detected at the first vertical position, the wave was observed to grow and radially extend from a steep, slab-like profile. The simultaneous measurements over the 2D cross section allowed us to evaluate the time evolution of the vertically averaged radial density scale length. We found that strong minima of this quantity ("steep" profiles) have an approximately three fold increased probability to be followed by a blob. For CAS applied to blobs at the

second vertical position, the wave was already observed long before its radial elongation, and profile steepening is less apparent. Comparing the average evolution of the mode to the subset of events that lead to a blob at the second position shows, however, that in the latter case, the mode moves radially inwards (towards the HFS) before it radially elongates (towards to LFS). This suggests a profile steepening at the origin of blob ejection in this scenario as well.

Next, we have focused on the properties of blobs once they are formed. An important parameter is the blob cross-field velocity, as it determines the distribution of quantities such as particles, heat, parallel currents and momentum in the SOL of tokamaks. Its magnitude depends on the available current paths to damp the charge separation induced by ∇B and curvature. We have reviewed previously published scaling laws for blob velocity where either parallel sheath-currents, ion-polarization currents or currents induced by ion-neutral collisions damp blob velocity. We have then derived a generalized formula that takes into account these effects simultaneously and found good agreement with numerical blob simulations. To investigate blob motion experimentally on TORPEX, we have installed a steel limiter in the blob propagation region. This avoids complicated boundary conditions due to grazing incidence of the magnetic field on the vacuum vessel and minimizes effects related to a radially varying connection length. We have used internal measurements combined with pattern recognition to determine blob radial velocities and sizes. Experiments in different gases (H_2 , He, Ne, Ar) have allowed us to cover a wide range of normalized blob sizes \tilde{a}_b and to perform a meaningful comparison with the derived blob velocity formula. Good quantitative agreement is found between theory and experimental measurements. This indicates that blobs in hydrogen, where $\tilde{a}_b \gtrsim 1$, are close to the regime where parallel currents are the dominant damping mechanism for blob motion. Blobs in helium and particularly in neon and argon fall in the regime $\tilde{a}_b \lesssim 1$, where blob velocity is damped mainly by ion-polarization currents. The damping effect due to ion-neutral collisions is estimated to be relatively weak for the neutral gas pressures used in these experiments.

Two predictions follow directly from this interpretation of blob motion. First, reducing the connection length should influence blob velocity in helium and, more importantly, in hydrogen, while little effect is expected for heavy gases such as neon and argon. This was tested by inserting a second limiter in TORPEX to halve the connection length. The results follow rather well the predicted trends. The second prediction is that increasing the neutral gas pressure should reduce blob velocity. This has been confirmed by varying the neutral gas pressure in helium.

To further study blob properties, we have investigated their parallel dynamics. We have presented first 2D measurements of blob parallel currents in front of the limiter, using both a single-sided LP and an array of magnetic pick-up coils. As expected, we observed a dipolar structure of the blob parallel current. Less expected was its asymmetric form with a stronger lobe on the side dominated by electron currents. This can be explained by floating potential values of the order of the electron temperature, such that the commonly used linearization of the expression for parallel

sheath currents is not a good approximation. This effect could possibly cause significant divertor currents in tokamaks. As shown by performing numerical simulations, it does, however, not significantly affect blob velocities. Using parallel current measurements and measured blob profiles in the bulk plasma, we have further confirmed that blob parallel currents are more important in damping blob velocity in hydrogen than in helium plasmas. First 2D Mach number measurements associated with blob formation and propagation revealed a toroidal flow pattern associated with the ideal interchange mode. This pattern is vertically shifted with respect to density perturbations. The blobs inherit this flow perturbation when they form from the positive wave crests and convect it radially outwards. These observations could shed light on the transport of parallel momentum in the edge of tokamaks and on the open question of the origin of spontaneous core rotation. Another important feature of blob parallel dynamics is the pre-sheath density drop n_{se}/n_0 . We have presented estimates showing that the value of n_{se}/n_0 could be significantly reduced below the assumed value of 0.5 due to neutral friction. A proposal to measure this quantity has been described as well as the ongoing wall probe development required for this study.

Besides varying the connection length and neutral gas pressure, we have explored additional ways of controlling blobs and turbulence by experimentally modifying the parallel boundary conditions. It has been predicted that blob velocity depends on the tilt angle between magnetic field and limiter, which could have direct application to divertor localized blobs in tokamaks. To test this on TORPEX, we have designed a special limiter where the tilt angle can be varied continuously over a relevant range. In contradiction to the theoretical prediction, no significant effect on blob velocity has been observed. Possible issues related with our experimental setup have been identified and a future limiter configuration to further explore this attractive way of blob control is proposed. Another method to affect blob motion, SOL width and peak heat loads is to induce toroidal/poloidal asymmetric potential variations. We have observed that potential variations can be achieved "passively" on TORPEX by inserting an insulating (glass) limiter into the blob region. This charges up strongly negatively, leading to significant changes of time averaged profiles and blob trajectories. Effects of toroidal/poloidal potential variations have been investigated more systematically with an array of 3×8 electrodes installed on a conducting limiter. Using different biasing patterns applied to these electrodes, we successfully modified blob radial and vertical velocities. Changes induced on time averaged density and potential profiles have features of convective cells, which are fairly uniform along the magnetic field. Two limitations for toroidal/poloidal asymmetric biasing experiments have been identified. The first one is on the locality of the induced potential variations. The strongest potential modifications are not observed along the biased flux tube, but at a position shifted in the direction of blob propagation and background flows. The second limitation concerns the magnitude of achievable potential variations, which is well below the potential applied to the electrodes. This is explained by high levels of cross-field currents. We have

performed simplified estimates to understand their origin. A single effect causing these currents could not be identified and a better understanding possibly requires fully non-linear simulations.

Most measurements reported in this thesis have been performed with Langmuir probes (LPs). We have investigated operation and interpretation of LPs and identified experimental difficulties such as hysteresis effects due to contaminated probe surfaces. We have extensively tested the triple Langmuir probe technique to obtain local, time-dependent measurements of density n , electron temperature T_e , plasma potential V_{pl} and the radial particle flux Γ_r . After several initial probe designs, we have developed a 'compensated' triple probe that overcomes difficulties such as phase-delay errors and effects caused by ion sheath expansion and finite bandwidth effects often encountered with this diagnostics. In particular, we have introduced a relatively simple electronic circuit to strongly reduce stray capacitance to ground. Measurements with the new probe showed good agreement with time-averaged profiles obtained from slowly-swept LPs and provided a benchmark for the BOX-CAS technique. This probe provides detailed measurements of fluctuations of n , T_e , and V_{pl} and their mutual phase relations. In particular, in the ideal interchange regime, it detects small phase shifts between density and temperature fluctuations over a large portion of the mode and blob region. For the purpose of evaluating the time-averaged particle flux, vertical electric fields can therefore be evaluated accurately from gradients in floating potential. Due to uncertainties with time-averaged floating potential values measured on nearby probes, further studies are, however, required for reliable measurements of the total radial particle flux with this probe.

Due to its relatively simple geometry, good diagnostics access and the possibility for controlled parameter scans, TORPEX is an ideal testbed for the validation of plasma turbulence codes. In collaboration with members of the theory group at the CRPP, we have proposed a methodology for code validation and applied it to 2D and global 3D two-fluid simulations of TORPEX plasmas. The comparison was performed using a relevant set of observables and across a scan in the number of field-lines turns N . As quantitatively assessed by a global metric, 2D and 3D codes perform equally well at small N , where ideal interchange waves with $k_{\parallel} = 0$ are the dominant instability. For large values of N , 3D effects become important and the 3D code performs considerably better than the 2D code. The 3D code reproduces most features of profiles and fluctuations and, in particular, captures the transition from ideal interchange waves to global 3D modes (resistive interchanges modes). A lower fluctuation level of the predicted ion saturation current (about a factor 2-3), flatter temperature profiles and less coherent features associated with the dominant instability were identified as the main discrepancies between 3D simulations and experiments.

A number of experiments could be conducted in the future to consolidate our interpretation of blob motion on TORPEX and further explore the presented tools for blob control. Most important is probably the measurement of the pre-sheath

density drop, which determines the electrical contact of blobs with the limiter. As discussed above, preparations for this experimental campaign are ongoing. Then, the connection length could be further varied to verify the observed effect on blob velocity. Measurements of the effective ion mass, especially in hydrogen, would also be important.

It would be interesting to pursue the toroidal/poloidal asymmetric biasing experiments. The measurements obtained so far reveal good toroidal symmetry of the effects of biased electrodes on time-averaged plasma profiles. Comparisons with 2D simulations, possibly including ion-neutral drag, could allow identifying the origin of the high level of cross-field currents inferred from the experiments. To verify whether toroidally asymmetric effects are present directly in front of the biased electrodes, e.g. in the form of a toroidally localized density depletion of the biased flux tube, high resolution measurements could be performed in this region. In a next step, biasing electrodes could be installed at the edge of the limiter and over the full height of TORPEX. This could be used to test possibilities to enlarge the density and temperature scale length in the mode region, which is characterized by steep radial gradients.

Finally, it is planned to install a current carrying toroidal wire inside TORPEX to close the magnetic field lines. This will open many new possibilities to investigate blob physics in a variety of fusion relevant scenarios, such as at the transition from closed to open field lines, in the presence of magnetic shear at the X-point, or with a field curvature that varies along the field lines.

A P P E N D I X

A

Notation

A.1 Repeatedly used symbols/variables

R_0 :	TORPEX major radius
a_0 :	TORPEX minor radius
(r, ϕ, z) :	TORPEX coordinate system (see Fig. 2.1.2)
R :	Radial distance from the center of the torus, i.e. $R = R_0 + r$
B_z :	Vertical magnetic field component
B_ϕ :	Toroidal magnetic field component
B_0 :	Total magnetic field at $r=0$
L_v :	Hight of the TORPEX cross section
N :	Number of toroidal turns of a field line inside TORPEX
Δ :	Vertical shift of a field line after one toroidal turn
L_c :	Connection length (magnetic field line length, wall-to-wall)
P_{rf} :	Injected microwave power
f_{rf} :	Frequency of injected microwaves
p_n :	Neutral gas pressure
n_n :	Neutral denstiy
n_e, n :	Electron/plasma density
T_e :	Electron temperature (" $T_e = k_B T_e$ ")
T_i :	Ion Temperature

V_{pl} :	Plasma potential
L_p :	Pressure scale length
λ_D :	Debye length
v_{the} :	Electron thermal velocity
v_{thi} :	Ion thermal velocity
c_s :	Ion sound speed
ρ_e :	Electron gyro-radius
ρ_i :	Ion gyro-radius
ρ_s :	Ion sound radius
$\omega_{pe} = 2\pi f_{pe}$:	Electron plasma frequency
ω_{pi} :	Ion plasma frequency
$\omega_{ce} = 2\pi f_{ec}$:	Electron cyclotron frequency
ω_{ci} :	Ion cyclotron frequency
ν_{in} :	Ion-neutral collision frequency
ν_{en} :	Electron-neutral collisions frequency
r_p :	Radius of cylindrical LP
V_{pr} :	LP potential
I_{pr} :	LP current drawn from the plasma
I_{sat} :	Ion saturation current
I_{sat}^0 :	Ion saturation current, extrapolated to the floating potential
A_{eff}^0 :	Sheath surface around LP at floating potential
V_{fl} :	Floating potential
α :	Normalized slope of the ion saturation current (see Eg. (3.1.1))
μ :	Parameter in the relation $V_{pl} = V_{fl} + \mu \cdot T_e/e$
$k_z, k_{\parallel}, k_{\phi}$:	Vertical, parallel, and toroidal wave numbers

A.2 Abbreviations

BOX-CAS:	Modified conditional average sampling
CAS:	Conditional Average Sampling
EC:	Electron Cyclotron
ELM:	Edge Localized Mode
GBS:	Global Braginskii Solver
HFS :	High Field Side
ITE :	Intermittent cross-field particle Transport Event
LFS :	Low Field Side
LP :	Langmuir Probe
SMT :	Simple Magnetized Torus
SOL:	Scrape-Off Layer
UH :	Upper Hybrid

A P P E N D I X

B

Estimates of collision frequencies

We discuss here the estimates of ion-neutral and electron-neutral collisions frequencies for momentum transfer used in this thesis. For a rigorous treatment of this subject, we refer the reader to textbooks (e.g. [193]).

B.1 Estimate of the ion-neutral collision frequency

We derive here an approximate expression for the ion-neutral collision frequency for momentum transfer. We assume static neutrals and the case where the ion drift velocity v_d is small compared to the ion thermal velocity v_{thi} . We have in mind collisions between protons and atomic hydrogen, where the most important process for momentum loss at low energy is symmetric charge exchange [91].

The momentum loss of an ion due to a collisions with a neutral can be expressed as [193]

$$\Delta \mathbf{p}_i = -\mu_{in} (1 - \cos \theta) (\mathbf{v}_i - \mathbf{v}_n), \quad (\text{B.1.1})$$

where \mathbf{p}_i is the ion momentum, $\mu_{in} = m_i m_n / (m_i + m_n)$ the reduced mass, θ the deflection angle in the center of mass system, and \mathbf{v}_i and \mathbf{v}_n the velocity of the

ion and the neutral before the collision, respectively. The rate of change of the ion momentum can then be written as

$$\frac{d\mathbf{p}_i}{dt} = -\mu_{in} (\mathbf{v}_i - \mathbf{v}_n) \cdot |\mathbf{v}_i - \mathbf{v}_n| n_n \sigma_{in}^{mt}(E_{CM}), \quad (\text{B.1.2})$$

where we have defined the momentum transfer cross-section σ_{in}^{mt} [91, 193]

$$\sigma_{in}^{mt}(E_{CM}) = \int_{\Omega} (1 - \cos \theta) \frac{d\sigma_{in}}{d\Omega}(E_{CM}, \theta) d\Omega. \quad (\text{B.1.3})$$

This is a function of E_{CM} , the kinetic energy of the colliding particles in the center of mass system. In the following, we consider static neutrals ($v_{thn} \ll v_{thi}$). We can then write σ_{in}^{mt} as a function of the ion velocity v_i . To find the average momentum loss rate, $\langle dp_{i,x}/dt \rangle$, along an arbitrary direction x , we integrate Eq. (B.1.2) over the ion distribution function $f_i(\mathbf{v}_i)$. This gives

$$\left\langle \frac{dp_{i,x}}{dt} \right\rangle = - \int \mu_{in} v_{ix} \cdot v_i n_n \sigma_{in}^{mt}(v_i) \cdot f_i(\mathbf{v}_i) d\mathbf{v}_i. \quad (\text{B.1.4})$$

Assuming a drifting Maxwellian for the ions with a drift $v_d \ll v_{thi}$ along the direction x , we obtain

$$\begin{aligned} \left\langle \frac{dp_{i,x}}{dt} \right\rangle &\approx - \frac{8}{3\sqrt{\pi}} n_n \frac{m_n}{m_i + m_n} \left(\frac{m_i}{2T_i} \right)^{5/2} \\ &\quad \cdot \int_0^\infty v_i^5 \sigma_{in}^{mt}(v_i) \cdot \exp\left(-\frac{m_i v_i^2}{2T_i}\right) dv_i \cdot \langle p_{i,x} \rangle, \end{aligned} \quad (\text{B.1.5})$$

with $\langle p_{i,x} \rangle = m_i v_d$ the average ion momentum along x . For $\sigma_{in}^{mt}(v_i) \approx \text{const.}$, and defining the collision frequency $\nu_{in} = -\langle dp_{i,x}/dt \rangle / \langle p_{i,x} \rangle$, we find

$$\nu_{in} = \frac{16}{3\sqrt{2\pi}} \cdot \frac{m_n}{m_i + m_n} \cdot n_n v_{thi} \sigma_{in}^{mt} \approx n_n v_{thi} \sigma_{in}^{mt}, \quad (\text{B.1.6})$$

where, for the last step, we have assumed $m_i = m_n$.

For $H^+ - H$ collisions, assuming $n_n = 5 \cdot 10^{18} \text{ m}^{-3}$, $T_i \lesssim 1 \text{ eV}$, and $\sigma_{in}^{mt} \approx 10^{-18} \text{ m}^2$ (see [90, 91]), Eq. (B.1.6) gives $\nu_{in} \lesssim 5 \cdot 10^4 \text{ s}^{-1}$.

B.2 Estimate of the electron-neutral collision frequency

We estimate the electron-neutral collision frequency ν_{en} as $\nu_{en} \approx n_n \sigma_{en}^{mt} v_{the}$. For $e - H$ collisions, assuming $n_n = 5 \cdot 10^{18} \text{ m}^{-3}$, $T_e = 5 \text{ eV}$, and $\sigma_{en}^{mt} = 2 \cdot 10^{-19} \text{ m}^2$ (see p. 41 of [91]), this gives $\nu_{en} \approx 10^6 \text{ s}^{-1}$.

The above expression for ν_{en} is an approximation. If we assume for example a drifting Maxwellian for the electrons with a drift velocity $\ll v_{the}$, taking Eq. (B.1.5) and replacing ions by electrons gives a neutral drag given by

$$\left\langle \frac{dp_{e,x}}{dt} \right\rangle \approx -\frac{8}{3\sqrt{\pi}} n_n \left(\frac{m_e}{2T_e} \right)^{5/2} \int_0^\infty v_e^5 \sigma_{en}^{mt}(v_e) \cdot \exp\left(-\frac{m_e v_e^2}{2T_e}\right) dv_e \cdot \langle p_{e,x} \rangle.$$

In this case, defining ν_{en} as $\nu_{en} = -\langle dp_x/dt \rangle / \langle p_x \rangle$ and assuming $\sigma_{en}^{mt}(v) \approx \sigma_{en}^{mt} = \text{const.}$, one obtains $\nu_{en} \approx 2.1 \cdot n_n \sigma_{en}^{mt} v_{the}$.

Bibliography

- [1] C. Suplee, “**The Plasma Universe**,” (Cambridge University Press, 2009).
- [2] D. Meade, “**50 years of fusion research**,” *Nucl. Fusion*, vol. 50, p. 014004, 2010.
- [3] C. M. Braams and P. E. Stott, ***Nuclear fusion: half a century of magnetic confinement fusion research***. Bristol; Philadelphia: IOP; 2002.
- [4] R. Pitts, R. Buttery, and S. Pinches, “**Fusion: The way ahead**,” *Phys. World*, vol. 19, p. 20, 2006.
- [5] C. M. Surko and R. E. Slusher, “**Waves and Turbulence in a Tokamak Fusion Plasma**,” *Science*, vol. 221, pp. 817–822, 1983.
- [6] F. Wagner and U. Stroth, “**Transport in toroidal devices-the experimentalist’s view**,” *Plasma Phys. Control. Fusion*, vol. 35, pp. 1321–1371, 1993.
- [7] W. Horton, “**Drift waves and transport**,” *Rev. Mod. Phys.*, vol. 71, pp. 735–778, 1999.
- [8] A. H. Boozer, “**Physics of magnetically confined plasmas**,” *Rev. Mod. Phys.*, vol. 76, pp. 1071–1141, 2004.
- [9] www.iter.org.
- [10] M. Shimada, D. J. Campbell, V. Mukhovatov, M. Fujiwara, N. Kirneva, K. Lackner, M. Nagami, V. D. Pustovitov, N. Uckan, J. Wesley, N. Asakura, A. E. Costley, A. J. H. Donné, E. J. Doyle, A. Fasoli, C. Gormezano, Y. Gribov, O. Gruber, T. C. Hender, W. Houlberg, S. Ide, Y. Kamada, A. Leonard, B. Lipschultz, A. Loarte, K. Miyamoto, V. Mukhovatov, T. H. Osborne, A. Polevoi, and A. C. C. Sips, “**Progress in the ITER Physics Basis; Chapter 1: Overview and summary**,” *Nucl. Fusion*, vol. 47, p. 1, 2007.
- [11] A. Loarte, B. Lipschultz, A. S. Kukushkin, G. F. Matthews, P. C. Stangeby, N. Asakura, G. F. Counsell, G. Federici, A. Kallenbach, K. Krieger, A. Mahdavi, V. Philipps, D. Reiter, J. Roth, J. Strachan, D. Whyte, R. Doerner, T. Eich, W. Fundamenski, A. Herrmann, M. Fenstermacher, P. Ghendrih,

- M. Groth, A. Kirschner, S. Konoshima, B. La Bombard, P. Lang, A. W. Leonard, P. Monier-Garbet, R. Neu, H. Pacher, B. Pegourie, R. A. Pitts, S. Takamura, J. Terry, E. Tsitrone, t. ITPA Scrape-off Layer, and Divertor Physics Topical Group, “**Progress in the ITER Physics Basis; Chapter 4: Power and particle control**,” *Nucl. Fusion*, vol. 47, p. 203, 2007.
- [12] B. Lipschultz, X. Bonnin, G. Counsell, A. Kallenbach, A. Kukushkin, K. Krieger, A. Leonard, A. Loarte, R. Neu, R. A. Pitts, T. Rognlien, J. Roth, C. Skinner, J. L. Terry, E. Tsitrone, D. Whyte, S. Zweben, N. Asakura, D. Coster, R. Doerner, R. Dux, G. Federici, M. Fenstermacher, W. Fundamenski, P. Ghendrih, A. Herrmann, J. Hu, S. Krasheninnikov, G. Kirnev, A. Kreter, V. Kurnaev, B. Labombard, S. Lisgo, T. Nakano, N. Ohno, H. D. Pacher, J. Paley, Y. Pan, G. Pautasso, V. Philipps, V. Rohde, D. Rudakov, P. Stangeby, S. Takamura, T. Tanabe, Y. Yang, and S. Zhu, “**Plasma surface interaction, scrape-off layer and divertor physics: implications for ITER**,” *Nucl. Fusion*, vol. 47, pp. 1189–1205, 2007.
- [13] P. C. Stangeby, “**The Plasma Boundary of Magnetic Fusion Devices**,” (Institute of Physics, Berkshire, 2000).
- [14] S. J. Zweben, J. A. Boedo, O. Grulke, C. Hidalgo, B. La Bombard, R. J. Maqueda, P. Scarin, and J. L. Terry, “**Edge turbulence measurements in toroidal fusion devices**,” *Plasma Phys. Control. Fusion*, vol. 49, p. 1, 2007.
- [15] J. A. Boedo, “**Edge turbulence and SOL transport in tokamaks**,” *J. Nucl. Mater.*, vol. 390, pp. 29–37, 2009.
- [16] S. Krasheninnikov, “**Multifaceted physics of edge plasma in magnetic fusion devices**,” *Plasma Phys. Control. Fusion*, vol. 53, p. 074017, 2011.
- [17] F. Wagner, “**A quarter-century of H-mode studies**,” *Plasma Phys. Control. Fusion*, vol. 49, p. 1, 2007.
- [18] R. A. Pitts, A. Kukushkin, A. Loarte, A. Martin, M. Merola, C. E. Kessel, V. Komarov, and M. Shimada, “**Status and physics basis of the ITER divertor**,” *Phys. Scr. T*, vol. 138, p. 014001, 2009.
- [19] G. Y. Antar, G. Counsell, Y. Yu, B. Labombard, and P. Devynck, “**Universality of intermittent convective transport in the scrape-off layer of magnetically confined devices**,” *Phys. Plasmas*, vol. 10, pp. 419–428, 2003.
- [20] S. I. Krasheninnikov, D. A. D’Ippolito, and J. R. Myra, “**Recent theoretical progress in understanding coherent structures in edge and SOL turbulence**,” *J. Plasma Physics*, vol. 74, pp. 679–717, 2008.

- [21] R. H. Cohen and D. D. Ryutov, “**Plasma convection induced by toroidal asymmetries of the divertor plates and gas puffing,**” *Nucl. Fusion*, vol. 37, pp. 621–627, 1997.
- [22] D. D. Ryutov, “**Geometrical properties of a “snowflake” divertor,**” *Phys. Plasmas*, vol. 14, p. 064502, 2007.
- [23] F. Piras, S. Coda, I. Furno, J.-M. Moret, R. A. Pitts, O. Sauter, B. Tal, G. Turri, A. Bencze, B. P. Duval, F. Felici, A. Pochelon, and C. Zucca, “**Snowflake divertor plasmas on TCV,**” *Plasma Phys. Control. Fusion*, vol. 51, p. 055009, 2009.
- [24] V. Soukhanovskii, J.-W. Ahn, R. Bell, D. Gates, S. Gerhardt, R. Kaita, E. Kolemen, B. LeBlanc, R. Maingi, M. Makowski, R. Maqueda, A. McLean, J. Menard, D. Mueller, S. Paul, R. Raman, A. Roquemore, D. Ryutov, S. Sabbagh, and H. Scott, “**Taming the plasma–material interface with the ‘snowflake’ divertor in NSTX,**” *Nucl. Fusion*, vol. 51, p. 012001, 2011.
- [25] M. Kotschenreuther, P. M. Valanju, S. M. Mahajan, and J. C. Wiley, “**On heat loading, novel divertors, and fusion reactors,**” *Phys. Plasmas*, vol. 14, p. 072502, 2007.
- [26] T. E. Evans, R. A. Moyer, K. H. Burrell, M. E. Fenstermacher, I. Joseph, A. W. Leonard, T. H. Osborne, G. D. Porter, M. J. Schaffer, P. B. Snyder, P. R. Thomas, J. G. Watkins, and W. P. West, “**Edge stability and transport control with resonant magnetic perturbations in collisionless tokamak plasmas,**” *Nat. Phys.*, vol. 2, pp. 419–423, 2006.
- [27] W. Suttrop, T. Eich, J. C. Fuchs, S. Günter, A. Janzer, A. Herrmann, A. Kallenbach, P. T. Lang, T. Lunt, M. Maraschek, R. M. McDermott, A. Mlynek, T. Pütterich, M. Rott, T. Vierle, E. Wolfrum, Q. Yu, I. Zammuto, and H. Zohm, “**First Observation of Edge Localized Modes Mitigation with Resonant and Nonresonant Magnetic Perturbations in ASDEX Upgrade,**” *Phys. Rev. Lett.*, vol. 106, p. 225004, 2011.
- [28] P. T. Lang, J. Neuhauser, L. D. Horton, T. Eich, L. Fattorini, J. C. Fuchs, O. Gehre, A. Herrmann, P. Ignácz, M. Jakobi, S. Kálvin, M. Kaufmann, G. Kocsis, B. Kurzan, C. Maggi, M. E. Manso, M. Maraschek, V. Mertens, A. Mück, H. D. Murmann, R. Neu, I. Nunes, D. Reich, M. Reich, S. Saarelma, W. Sandmann, J. Stober, U. Vogl, and the ASDEX Upgrade Team, “**ELM frequency control by continuous small pellet injection in ASDEX Upgrade,**” *Nucl. Fusion*, vol. 43, pp. 1110–1120, 2003.
- [29] A. W. Degeling, Y. R. Martin, J. B. Lister, L. Villard, V. N. Dokouka, V. E. Lukash, and R. R. Khayrutdinov, “**Magnetic triggering of ELMs in TCV,**” *Plasma Phys. Control. Fusion*, vol. 45, pp. 1637–1655, 2003.

- [30] M. G. Bell, H. W. Kugel, R. Kaita, L. E. Zakharov, H. Schneider, B. P. Le Blanc, D. Mansfield, R. E. Bell, R. Maingi, S. Ding, S. M. Kaye, S. F. Paul, S. P. Gerhardt, J. M. Canik, J. C. Hosea, G. Taylor, and the NSTX Research Team, “**Plasma response to lithium-coated plasma-facing components in the National Spherical Torus Experiment,**” *Plasma Phys. Control. Fusion*, vol. 51, p. 124054, 2009.
- [31] D. G. Whyte, A. E. Hubbard, J. W. Hughes, B. Lipschultz, J. E. Rice, E. S. Marmar, M. Greenwald, I. Cziegler, A. Dominguez, T. Golfinopoulos, N. Howard, L. Lin, R. M. McDermott, M. Porkolab, M. L. Reinke, J. Terry, N. Tsujii, S. Wolfe, S. Wukitch, Y. Lin, and the Alcator C-Mod Team, “**I-mode: an H-mode energy confinement regime with L-mode particle transport in Alcator C-Mod,**” *Nucl. Fusion*, vol. 50, p. 105005, 2010.
- [32] R. Majeski, R. Doerner, T. Gray, R. Kaita, R. Maingi, D. Mansfield, J. Spaleta, V. Soukhanovskii, J. Timberlake, and L. Zakharov, “**Enhanced Energy Confinement and Performance in a Low-Recycling Tokamak,**” *Phys. Rev. Lett.*, vol. 97, p. 075002, 2006.
- [33] Y. Sarazin and P. Ghendrih, “**Intermittent particle transport in two-dimensional edge turbulence,**” *Phys. Plasmas*, vol. 5, pp. 4214–4228, 1998.
- [34] P. B. Snyder, H. R. Wilson, and X. Q. Xu, “**Progress in the peeling-ballooning model of edge localized modes: Numerical studies of nonlinear dynamics,**” *Phys. Plasmas*, vol. 12, p. 056115, 2005.
- [35] O. E. Garcia, J. Horacek, R. A. Pitts, A. H. Nielsen, W. Fundamenski, J. P. Graves, V. Naulin, and J. J. Rasmussen, “**LETTER TO THE EDITOR: Interchange turbulence in the TCV scrape-off layer,**” *Plasma Phys. Control. Fusion*, vol. 48, pp. L1–L10, 2006.
- [36] U. Frisch, “**Turbulence, The Legacy of A. N. Kolmogorov,**” (Cambridge University Press, 1995).
- [37] S. T. Bramwell, P. C. W. Holdsworth, and J.-F. Pinton, “**Universality of rare fluctuations in turbulence and critical phenomena,**” *Nature*, vol. 396, pp. 552–554, 1998.
- [38] J. A. Krommes, “**The remarkable similarity between the scaling of kurtosis with squared skewness for TORPEX density fluctuations and sea-surface temperature fluctuations,**” *Phys. Plasmas*, vol. 15, p. 030703, 2008.
- [39] J. W. Belcher and L. Davis, Jr., “**Large-amplitude Alfvén waves in the interplanetary medium, 2.,**” *J. Geophys. Res.*, vol. 76, pp. 3534–3563, 1971.

- [40] S. A. Balbus and J. F. Hawley, “**Instability, turbulence, and enhanced transport in accretion disks,**” *Rev. Mod. Phys.*, vol. 70, pp. 1–53, 1998.
- [41] Z. Lin, T. S. Hahm, W. W. Lee, W. M. Tang, and R. B. White, “**Turbulent Transport Reduction by Zonal Flows: Massively Parallel Simulations,**” *Science*, vol. 281, p. 1835, 1998.
- [42] P. H. Diamond, S.-I. Itoh, K. Itoh, and T. S. Hahm, “**TOPICAL REVIEW: Zonal flows in plasma - a review,**” *Plasma Phys. Control. Fusion*, vol. 47, p. 35, 2005.
- [43] A. C. Boxer, R. Bergmann, J. L. Ellsworth, D. T. Garnier, J. Kesner, M. E. Mauel, and P. Woskov, “**Turbulent inward pinch of plasma confined by a levitated dipole magnet,**” *Nat. Phys.*, vol. 6, pp. 207–212, 2010.
- [44] C. Angioni, E. Fable, M. Greenwald, M. Maslov, A. G. Peeters, H. Takenaga, and H. Weisen, “**Particle transport in tokamak plasmas, theory and experiment,**” *Plasma Phys. Control. Fusion*, vol. 51, p. 124017, 2009.
- [45] A. Fasoli, B. Labit, M. McGrath, S. H. Müller, G. Plyushchev, M. Podestà, and F. M. Poli, “**Electrostatic turbulence and transport in a simple magnetized plasma,**” *Phys. Plasmas*, vol. 13, p. 055902, 2006.
- [46] A. Fasoli, A. Burckel, L. Federspiel, I. Furno, K. Gustafson, D. Iraj, B. Labit, J. Loizu, G. Plyushchev, P. Ricci, C. Theiler, A. Diallo, S. H. Mueller, M. Podestà, and F. Poli, “**Electrostatic instabilities, turbulence and fast ion interactions in the TORPEX device,**” *Plasma Phys. Control. Fusion*, vol. 52, p. 124020, 2010.
- [47] M. Podestà, “**Plasma production and transport in a simple magnetised toroidal plasma,**” PhD thesis, EPFL (2007), <http://library.epfl.ch/theses/?nr=3765>.
- [48] S. H. Müller, “**Turbulence in basic toroidal plasmas,**” PhD thesis, EPFL (2006), <http://library.epfl.ch/theses/?nr=3672>.
- [49] G. Plyushchev, “**Interaction of supra-thermal ions with turbulence in a magnetized toroidal plasma,**” PhD thesis, EPFL (2009), <http://library.epfl.ch/theses/?nr=4543>.
- [50] K. L. Wong, M. Ono, and G. A. Wurden, “**ACT-I: A steady-state torus for basic plasma physics research,**” *Rev. Sci. Inst.*, vol. 53, pp. 409–416, 1982.
- [51] E. D. Zimmerman and S. C. Luckhardt, “**Measurement of the Correlation Spectrum of Electrostatic Potential Fluctuations in an ECRH Helimak Plasma,**” *J. Fusion Energy*, vol. 12, p. 289, 1993.

- [52] P. K. Sharma and D. Bora, “**Experimental study of a toroidal magnetized plasma in the presence of a weak vertical magnetic field,**” *Plasma Phys. Control. Fusion*, vol. 37, pp. 1003–1014, 1995.
- [53] K. Gentle, W. and H. He, “**Texas Helimak,**” *Plasma Science and Technology*, vol. 10, pp. 284–289, 2008.
- [54] C. Riccardi, M. Fontanesi, A. Galassi, and E. Sindoni, “**Experimental investigation on ion-Bernstein waves propagation,**” *Plasma Phys. Control. Fusion*, vol. 36, pp. 1791–1803, 1994.
- [55] K. Rypdal and S. Ratynskaia, “**Onset of Turbulence and Profile Resilience in the Helimak Configuration,**” *Phys. Rev. Lett.*, vol. 94, p. 225002, 2005.
- [56] M. Podestà, A. Fasoli, B. Labit, M. McGrath, S. H. Müller, and F. M. Poli, “**Plasma production by low-field side injection of electron cyclotron waves in a simple magnetized torus,**” *Plasma Phys. Control. Fusion*, vol. 47, pp. 1989–2002, 2005.
- [57] L. Federspiel, B. Labit, P. Ricci, A. Fasoli, I. Furno, and C. Theiler, “**Observation of a critical pressure gradient for the stabilization of interchange modes in simple magnetized toroidal plasmas,**” *Phys. Plasmas*, vol. 16, p. 092501, 2009.
- [58] D. Iraj, I. Furno, A. Fasoli, and C. Theiler, “**Imaging of turbulent structures and tomographic reconstruction of TORPEX plasma emissivity,**” *Phys. Plasmas*, vol. 17, p. 122304, 2010.
- [59] D. Iraj, “**Fast imaging of turbulent plasmas in the TORPEX device,**” PhD thesis, EPFL (2011), <http://library.epfl.ch/theses/?nr=5073>.
- [60] I. Furno, M. Spolaore, C. Theiler, N. Vianello, R. Cavazzana, and A. Fasoli, “**Direct Two-Dimensional Measurements of the Field-Aligned Current Associated with Plasma Blobs,**” *Phys. Rev. Lett.*, vol. 106, p. 245001, 2011.
- [61] S. H. Müller, A. Fasoli, B. Labit, M. McGrath, O. Pisaturo, G. Plyushchev, M. Podestà, and F. M. Poli, “**Basic turbulence studies on TORPEX and challenges in the theory-experiment comparison,**” *Phys. Plasmas*, vol. 12, p. 090906, 2005.
- [62] C. Theiler, I. Furno, A. Kuenlin, P. Marmillod, and A. Fasoli, “**Practical solutions for reliable triple probe measurements in magnetized plasmas,**” *Rev. Sci. Inst.*, vol. 82, p. 013504, 2011.

- [63] B. Labit, I. Furno, M. Podestà, and A. Fasoli, “**Two-dimensional time resolved measurements of toroidal velocity correlated with density blobs in magnetized plasmas,**” *Rev. Sci. Inst.*, vol. 79, p. 086104, 2008.
- [64] I. H. Hutchinson, “**Principles of Plasma Diagnostics,**” (Cambridge University Press, Cambridge, England, 2002), 2nd ed.
- [65] J. M. Beall, Y. C. Kim, and E. J. Powers, “**Estimation of wavenumber and frequency spectra using fixed probe pairs,**” *J. Appl. Phys.*, vol. 53, pp. 3933–3940, 1982.
- [66] F. M. Poli, “**Electrostatic instabilities and turbulence in a toroidal magnetized plasma,**” PhD thesis, EPFL (2007), <http://library.epfl.ch/theses/?nr=3849>.
- [67] S.-L. Chen and T. Sekiguchi, “**Instantaneous Direct-Display System of Plasma Parameters by Means of Triple Probe,**” *J. Appl. Phys.*, vol. 36, pp. 2363–2375, 1965.
- [68] K. Rypdal, Å. Fredriksen, O. M. Olsen, and K. G. Hellblom, “**Microwave-plasma in a simple magnetized torus,**” *Phys. Plasmas*, vol. 4, pp. 1468–1480, 1997.
- [69] A. G. Lynn, M. Gilmore, C. Watts, J. Herrea, R. Kelly, S. Will, S. Xie, L. Yan, and Y. Zhang, “**The HelCat dual-source plasma device,**” *Rev. Sci. Inst.*, vol. 80, p. 103501, 2009.
- [70] P. Ricci, B. N. Rogers, and S. Brunner, “**High- and Low-Confinement Modes in Simple Magnetized Toroidal Plasmas,**” *Phys. Rev. Lett.*, vol. 100, p. 225002, 2008.
- [71] P. Ricci and B. N. Rogers, “**Transport scaling in interchange-driven toroidal plasmas,**” *Phys. Plasmas*, vol. 16, p. 062303, 2009.
- [72] P. Ricci and B. N. Rogers, “**Three-dimensional fluid simulations of a simple magnetized toroidal plasma,**” *Phys. Plasmas*, vol. 16, p. 092307, 2009.
- [73] P. Ricci and B. N. Rogers, “**Turbulence Phase Space in Simple Magnetized Toroidal Plasmas,**” *Phys. Rev. Lett.*, vol. 104, p. 145001, 2010.
- [74] P. Ricci, C. Theiler, A. Fasoli, I. Furno, B. Labit, S. H. Müller, M. Podestà, and F. M. Poli, “**Langmuir probe-based observables for plasma-turbulence code validation and application to the TORPEX basic plasma physics experiment,**” *Phys. Plasmas*, vol. 16, p. 055703, 2009.

- [75] P. Ricci, C. Theiler, A. Fasoli, I. Furno, K. Gustafson, D. Iraj, and J. Loizu, **“Methodology for turbulence code validation: Quantification of simulation-experiment agreement and application to the TORPEX experiment,”** *Phys. Plasmas*, vol. 18, p. 032109, 2011.
- [76] S. Brunner, **“Waves and Instabilities in Inhomogeneous Plasmas,”** lecture notes: <https://crppwww.epfl.ch/~brunner/inhomoplasma.pdf>.
- [77] F. M. Poli, S. Brunner, A. Diallo, A. Fasoli, I. Furno, B. Labit, S. H. Müller, G. Plyushchev, and M. Podestà, **“Experimental characterization of drift-interchange instabilities in a simple toroidal plasma,”** *Phys. Plasmas*, vol. 13, p. 102104, 2006.
- [78] F. M. Poli, P. Ricci, A. Fasoli, and M. Podestà, **“Transition from drift to interchange instabilities in an open magnetic field line configuration,”** *Phys. Plasmas*, vol. 15, p. 032104, 2008.
- [79] B. Labit, I. Furno, A. Fasoli, A. Diallo, S. H. Müller, G. Plyushchev, M. Podestà, and F. M. Poli, **“Universal Statistical Properties of Drift-Interchange Turbulence in TORPEX Plasmas,”** *Phys. Rev. Lett.*, vol. 98, p. 255002, 2007.
- [80] B. Labit, A. Diallo, A. Fasoli, I. Furno, D. Iraj, S. H. Müller, G. Plyushchev, M. Podestà, F. M. Poli, P. Ricci, C. Theiler, and J. Horacek, **“Statistical properties of electrostatic turbulence in toroidal magnetized plasmas,”** *Plasma Phys. Control. Fusion*, vol. 49, p. 281, 2007.
- [81] F. Sattin, M. Agostini, P. Scarin, N. Vianello, R. Cavazzana, L. Marrelli, G. Serianni, S. J. Zweben, R. J. Maqueda, Y. Yagi, H. Sakakita, H. Koguchi, S. Kiyama, Y. Hirano, and J. L. Terry, **“On the statistics of edge fluctuations: comparative study between various fusion devices,”** *Plasma Phys. Control. Fusion*, vol. 51, p. 055013, 2009.
- [82] H. M. Mott-Smith and I. Langmuir, **“The Theory of Collectors in Gaseous Discharges,”** *Phys. Rev.*, vol. 28, pp. 727–763, 1926.
- [83] F. F. Chen, **“Langmuir Probe Diagnostics,”** Lecture notes, available online.
- [84] V. I. Demidov, S. V. Ratynskaia, and K. Rypdal, **“Electric probes for plasmas: The link between theory and instrument,”** *Rev. Sci. Instr.*, vol. 73, pp. 3409–3439, 2002.
- [85] F. F. Chen, **“Plasma Diagnostic Techniques,”** (Edited by R.H. Huddleston and S. L. Leonard, Academic, New York, 1965).

- [86] J. D. Swift and M. J. R. Schwar, “**Electrical Probes for Plasma Diagnostics,**” (Lliffe, London, 1970).
- [87] G. Chiodini, C. Riccardi, and M. Fontanesi, “**A 400 kHz, fast-sweep Langmuir probe for measuring plasma fluctuations,**” *Rev. Sci. Inst.*, vol. 70, pp. 2681–2688, 1999.
- [88] L. Giannone, R. Balbin, H. Niedermeyer, M. Endler, G. Herre, C. Hidalgo, A. Rudyj, G. Theimer, and P. Verplanke, “**Density, temperature, and potential fluctuation measurements by the swept Langmuir probe technique in Wendelstein 7-AS,**” *Phys. Plasmas*, vol. 1, pp. 3614–3621, 1994.
- [89] M. Bagatin, D. Desideri, E. Martines, G. Manduchi, G. Serianni, and V. Antoni, “**Automatic fast fitting of single Langmuir probe characteristics on RFX,**” *Rev. Sci. Inst.*, vol. 68, pp. 365–368, 1997.
- [90] A. E. Glassgold, P. S. Krstić, and D. R. Schultz, “**H⁺+H Scattering and Ambipolar Diffusion Heating,**” *Astrophys. J.*, vol. 621, pp. 808–816, 2005.
- [91] “**Atomic and Molecular Processes in Fusion Edge Plasmas,**” edited by R. K. Janev (Plenum, New York, 1995).
- [92] M. Podestá, A. Diallo, A. Fasoli, I. Furno, B. Labit, S. H. Müller, and F. M. Poli, “**Characterization of the electron distribution function in an electron-cyclotron driven toroidal plasma,**” *Plasma Phys. Control. Fusion*, vol. 49, pp. 175–182, 2007.
- [93] P. C. Stangeby, “**A problem in the interpretation of tokamak Langmuir probes when a fast electron component is present,**” *Plasma Phys. Control. Fusion*, vol. 37, pp. 1031–1037, 1995.
- [94] P. C. Stangeby and J. E. Allen, “**Transonic plasma flow past an obstacle,**” *J. Plasma Physics*, vol. 6, p. 19, 1971.
- [95] J. C. McMahon, G. Z. Xu, and J. G. Laframboise, “**The effect of ion drift on the sheath, presheath, and ion-current collection for cylinders in a collisionless plasma,**” *Phys. Plasmas*, vol. 12, no. 6, p. 062109, 2005.
- [96] I. H. Hutchinson, “**Ion Collection by Oblique Surfaces of an Object in a Transversely Flowing Strongly Magnetized Plasma,**” *Phys. Rev. Lett.*, vol. 101, no. 3, p. 035004, 2008.
- [97] B. Labit, C. Theiler, A. Fasoli, I. Furno, and P. Ricci, “**Blob-induced toroidal momentum transport in simple magnetized plasmas,**” *Phys. Plasmas*, vol. 18, p. 032308, 2011.

- [98] D. L. Rudakov, J. A. Boedo, R. A. Moyer, P. C. Stangeby, A. McLean, and J. G. Watkins, “**Effect of electron temperature fluctuations on slowly swept Langmuir probe measurements,**” *Rev. Sci. Inst.*, vol. 75, pp. 4334–4337, 2004.
- [99] J. F. Waymouth, “**Pulse Technique for Probe Measurements in Gas Discharges,**” *J. Appl. Phys.*, vol. 30, pp. 1404–1412, 1959.
- [100] K.-I. Oyama, “**A systematic investigation of several phenomena associated with contaminated Langmuir probes,**” *Planet. Space Sci.*, vol. 24, pp. 183–190, 1976.
- [101] W. E. Amatucci, P. W. Schuck, D. N. Walker, P. M. Kintner, S. Powell, B. Holback, and D. Leonhardt, “**Contamination-free sounding rocket Langmuir probe,**” *Rev. Sci. Inst.*, vol. 72, pp. 2052–2057, 2001.
- [102] R. J. Adrian, “**Conditional eddies in isotropic turbulence,**” *Phys. Fluids*, vol. 22, pp. 2065–2070, 1979.
- [103] H. Johnsen, H. L. Pécseli, and J. Trulsen, “**Conditional eddies in plasma turbulence,**” *Phys. Fluids*, vol. 30, pp. 2239–2254, 1987.
- [104] F. J. Oynes, O.-M. Olsen, H. L. Pécseli, Å. Fredriksen, and K. Rypdal, “**Experimental study of low-frequency electrostatic fluctuations in a magnetized toroidal plasma,**” *Phys. Rev. E*, vol. 57, pp. 2242–2255, 1998.
- [105] I. Furno, B. Labit, A. Fasoli, F. M. Poli, P. Ricci, C. Theiler, S. Brunner, A. Diallo, J. P. Graves, M. Podestà, and S. H. Müller, “**Mechanism for blob generation in the TORPEX toroidal plasma,**” *Phys. Plasmas*, vol. 15, p. 055903, 2008.
- [106] R. B. Lobbia and A. D. Gallimore, “**High-speed dual Langmuir probe,**” *Rev. Sci. Inst.*, vol. 81, p. 073503, 2010.
- [107] H. Y. W. Tsui, R. D. Bengtson, G. X. Li, H. Lin, M. Meier, C. P. Ritz, and A. J. Wootton, “**A new scheme for Langmuir probe measurement of transport and electron temperature fluctuations,**” *Rev. Sci. Inst.*, vol. 63, pp. 4608–4610, 1992.
- [108] A. Kuenlin, “**Sonde électrostatique triple pour TORPEX,**” Semester Project on TORPEX, (2010), supervision: C. Theiler and I. Furno.
- [109] E. O. Johnson and L. Malter, “**A Floating Double Probe Method for Measurements in Gas Discharges,**” *Phys. Rev.*, vol. 80, no. 1, pp. 58–68, 1950.

- [110] E. Powers, “**Spectral techniques for experimental investigation of plasma diffusion due to polychromatic fluctuations,**” *Nucl. Fusion*, vol. 14, p. 749, 1974.
- [111] S. H. Müller, A. Diallo, A. Fasoli, I. Furno, B. Labit, and M. Podestà, “**Plasma blobs in a basic toroidal experiment: Origin, dynamics, and induced transport,**” *Phys. Plasmas*, vol. 14, p. 110704, 2007.
- [112] M. Podestà, A. Fasoli, B. Labit, I. Furno, P. Ricci, F. M. Poli, A. Diallo, S. H. Müller, and C. Theiler, “**Cross-Field Transport by Instabilities and Blobs in a Magnetized Toroidal Plasma,**” *Phys. Rev. Lett.*, vol. 101, p. 045001, 2008.
- [113] D. Goodall, “**High speed cine film studies of plasma behaviour and plasma surface interactions in tokamaks,**” *J. Nucl. Mater.*, vol. 111, pp. 11–22, 1982.
- [114] S. J. Zweben, “**Search for coherent structure within tokamak plasma turbulence,**” *Phys. Fluids*, vol. 28, pp. 974–982, 1985.
- [115] D. C. Robinson and M. G. Rusbridge, “**Turbulent density fluctuations in zeta,**” *Plasma Phys.*, vol. 11, pp. 73–100, 1969.
- [116] S. J. Zweben, D. P. Stotler, J. L. Terry, B. Labombard, M. Greenwald, M. Muterspaugh, C. S. Pitcher, K. Hallatschek, R. J. Maqueda, B. Rogers, J. L. Lowrance, V. J. Mastrocola, and G. F. Renda, “**Edge turbulence imaging in the Alcator C-Mod tokamak,**” *Phys. Plasmas*, vol. 9, pp. 1981–1989, 2002.
- [117] R. J. Maqueda, G. A. Wurden, D. P. Stotler, S. J. Zweben, B. Labombard, J. L. Terry, J. L. Lowrance, V. J. Mastrocola, G. F. Renda, D. A. D’Ippolito, J. R. Myra, and N. Nishino, “**Gas puff imaging of edge turbulence (invited),**” *Rev. Sci. Instr.*, vol. 74, pp. 2020–2026, 2003.
- [118] J. L. Terry, S. J. Zweben, K. Hallatschek, B. Labombard, R. J. Maqueda, B. Bai, C. J. Boswell, M. Greenwald, D. Kopon, W. M. Nevins, C. S. Pitcher, B. N. Rogers, D. P. Stotler, and X. Q. Xu, “**Observations of the turbulence in the scrape-off-layer of Alcator C-Mod and comparisons with simulation,**” *Phys. Plasmas*, vol. 10, pp. 1739–1747, 2003.
- [119] J. A. Boedo, D. L. Rudakov, R. A. Moyer, G. R. McKee, R. J. Colchin, M. J. Schaffer, P. G. Stangeby, W. P. West, S. L. Allen, T. E. Evans, R. J. Fonck, E. M. Hollmann, S. Krashenninnikov, A. W. Leonard, W. Nevins, M. A. Mahdavi, G. D. Porter, G. R. Tynan, D. G. Whyte, and X. Xu, “**Transport by intermittency in the boundary of the DIII-D tokamak,**” *Phys. Plasmas*, vol. 10, pp. 1670–1677, 2003.

- [120] S. J. Zweben, R. J. Maqueda, D. P. Stotler, A. Keesee, J. Boedo, C. E. Bush, S. M. Kaye, B. LeBlanc, J. L. Lowrance, V. J. Mastrocola, R. Maingi, N. Nishino, G. Renda, D. W. Swain, J. B. Wilgen, and the NSTX Team, **“High-speed imaging of edge turbulence in NSTX,”** *Nucl. Fusion*, vol. 44, pp. 134–153, 2004.
- [121] A. Kirk, H. R. Wilson, G. F. Counsell, R. Akers, E. Arends, S. C. Cowley, J. Dowling, B. Lloyd, M. Price, and M. Walsh, **“Spatial and Temporal Structure of Edge-Localized Modes,”** *Phys. Rev. Lett.*, vol. 92, no. 24, p. 245002, 2004.
- [122] O. Grulke, J. L. Terry, B. Labombard, and S. J. Zweben, **“Radially propagating fluctuation structures in the scrape-off layer of Alcator C-Mod,”** *Phys. Plasmas*, vol. 13, no. 1, p. 012306, 2006.
- [123] R. Sánchez, B. P. van Milligen, D. E. Newman, and B. A. Carreras, **“Quiet-Time Statistics of Electrostatic Turbulent Fluxes from the JET Tokamak and the W7-AS and TJ-II Stellarators,”** *Phys. Rev. Lett.*, vol. 90, no. 18, p. 185005, 2003.
- [124] M. Spolaore, V. Antoni, E. Spada, H. Bergsaker, R. Cavazzana, J. R. Drake, E. Martines, G. Regnoli, G. Serianni, and N. Vianello, **“Vortex-Induced Diffusivity In Reversed Field Pinch Plasmas,”** *Phys. Rev. Lett.*, vol. 93, no. 21, p. 215003, 2004.
- [125] I. Furno, B. Labit, M. Podestà, A. Fasoli, S. H. Müller, F. M. Poli, P. Ricci, C. Theiler, S. Brunner, A. Diallo, and J. Graves, **“Experimental Observation of the Blob-Generation Mechanism from Interchange Waves in a Plasma,”** *Phys. Rev. Lett.*, vol. 100, p. 055004, 2008.
- [126] G. Y. Antar, S. I. Krasheninnikov, P. Devynck, R. P. Doerner, E. M. Hollmann, J. A. Boedo, S. C. Luckhardt, and R. W. Conn, **“Experimental Evidence of Intermittent Convection in the Edge of Magnetic Confinement Devices,”** *Phys. Rev. Lett.*, vol. 87, p. 065001, 2001.
- [127] T. A. Carter, **“Intermittent turbulence and turbulent structures in a linear magnetized plasma,”** *Phys. Plasmas*, vol. 13, no. 1, p. 010701, 2006.
- [128] S. I. Krasheninnikov, **“On scrape off layer plasma transport,”** *Phys. Lett. A*, vol. 283, pp. 368–370, 2001.
- [129] D. A. D’Ippolito, J. R. Myra, and S. I. Krasheninnikov, **“Cross-field blob transport in tokamak scrape-off-layer plasmas,”** *Phys. Plasmas*, vol. 9, pp. 222–233, 2002.

- [130] M. V. Umansky, S. I. Krasheninnikov, B. Labombard, and J. L. Terry, **“Comments on particle and energy balance in the edge plasma of Alcator C-Mod,”** *Phys. Plasmas*, vol. 5, pp. 3373–3376, 1998.
- [131] D. A. D’Ippolito, J. R. Myra, and S. J. Zweben, **“Convective transport by intermittent blob-filaments: Comparison of theory and experiment,”** *Phys. Plasmas*, vol. 18, no. 6, p. 060501, 2011.
- [132] H. Biglari, P. H. Diamond, and P. W. Terry, **“Influence of sheared poloidal rotation on edge turbulence,”** *Phys. Fluids B*, vol. 2, pp. 1–4, 1990.
- [133] N. Bisai, A. Das, S. Deshpande, R. Jha, P. Kaw, A. Sen, and R. Singh, **“Simulation of plasma transport by coherent structures in scrape-off-layer tokamak plasmas,”** *Phys. Plasmas*, vol. 11, pp. 4018–4024, 2004.
- [134] C. Theiler, A. Diallo, A. Fasoli, I. Furno, B. Labit, M. Podestà, F. M. Poli, and P. Ricci, **“The role of the density gradient on intermittent cross-field transport events in a simple magnetized toroidal plasma,”** *Phys. Plasmas*, vol. 15, p. 042303, 2008.
- [135] S. H. Müller, C. Theiler, A. Fasoli, I. Furno, B. Labit, G. R. Tynan, M. Xu, Z. Yan, and J. H. Yu, **“Studies of blob formation, propagation and transport mechanisms in basic experimental plasmas (TORPEX and CSDX),”** *Plasma Phys. Control. Fusion*, vol. 51, p. 055020, 2009.
- [136] O. E. Garcia, N. H. Bian, and W. Fundamenski, **“Radial interchange motions of plasma filaments,”** *Phys. Plasmas*, vol. 13, no. 8, p. 082309, 2006.
- [137] J. R. Myra and D. A. D’Ippolito, **“Edge instability regimes with applications to blob transport and the quasicohherent mode,”** *Phys. Plasmas*, vol. 12, no. 9, p. 092511, 2005.
- [138] N. Katz, J. Egedal, W. Fox, A. Le, and M. Porkolab, **“Experiments on the Propagation of Plasma Filaments,”** *Phys. Rev. Lett.*, vol. 101, no. 1, p. 015003, 2008.
- [139] C. Theiler, I. Furno, P. Ricci, A. Fasoli, B. Labit, S. H. Müller, and G. Plyushchev, **“Cross-Field Motion of Plasma Blobs in an Open Magnetic Field Line Configuration,”** *Phys. Rev. Lett.*, vol. 103, p. 065001, 2009.
- [140] S. Sugita, M. Yagi, S. I. Itoh, and K. Itoh, **“Propagation Velocity Analysis of a Single Blob in the SOL,”** *Plasma Fusion Res.*, vol. 3, p. 040, 2008.
- [141] D. Lançon, **“Numerical 2D simulations of seeded blob dynamics in a SMT,”** Semester Project on TORPEX, (2011), supervision: I. Furno and C. Theiler.

- [142] I. Furno, C. Theiler, D. Lançon, A. Fasoli, D. Iraji, P. Ricci, M. Spolaore, and N. Vianello, “**Blob current structures in TORPEX plasmas: experimental measurements and numerical simulations,**” *Plasma Phys. Control. Fusion* (in press), 2011.
- [143] O. E. Garcia, N. H. Bian, V. Naulin, A. H. Nielsen, and J. J. Rasmussen, “**Mechanism and scaling for convection of isolated structures in nonuniformly magnetized plasmas,**” *Phys. Plasmas*, vol. 12, no. 9, p. 090701, 2005.
- [144] G. Q. Yu and S. I. Krasheninnikov, “**Dynamics of blobs in scrape-off-layer/shadow regions of tokamaks and linear devices,**” *Phys. Plasmas*, vol. 10, pp. 4413–4418, 2003.
- [145] D. A. D’Ippolito and J. R. Myra, “**Blob stability and transport in the scrape-off-layer,**” *Phys. Plasmas*, vol. 10, pp. 4029–4039, 2003.
- [146] J. R. Myra, D. A. D’Ippolito, D. P. Stotler, S. J. Zweben, B. P. Leblanc, J. E. Menard, R. J. Maqueda, and J. Boedo, “**Blob birth and transport in the tokamak edge plasma: Analysis of imaging data,**” *Phys. Plasmas*, vol. 13, no. 9, p. 092509, 2006.
- [147] C. Theiler, I. Furno, A. Fasoli, P. Ricci, B. Labit, and D. Iraji, “**Blob motion and control in simple magnetized plasmas,**” *Phys. Plasmas*, vol. 18, no. 5, p. 055901, 2011.
- [148] N. Bian, S. Benkadda, J.-V. Paulsen, and O. E. Garcia, “**Blobs and front propagation in the scrape-off layer of magnetic confinement devices,**” *Phys. Plasmas*, vol. 10, pp. 671–676, 2003.
- [149] J. R. Myra, D. A. D’Ippolito, S. I. Krasheninnikov, and G. Q. Yu, “**Convective transport in the scrape-off-layer by nonthermalized spinning blobs,**” *Phys. Plasmas*, vol. 11, pp. 4267–4274, 2004.
- [150] A. Y. Aydemir, “**Convective transport in the scrape-off layer of tokamaks,**” *Phys. Plasmas*, vol. 12, no. 6, p. 062503, 2005.
- [151] G. Q. Yu, S. I. Krasheninnikov, and P. N. Guzdar, “**Two-dimensional modelling of blob dynamics in tokamak edge plasmas,**” *Phys. Plasmas*, vol. 13, no. 4, p. 042508, 2006.
- [152] R. H. Cohen and D. D. Ryutov, “**Plasma sheath in a tilted magnetic field: Closing of the diamagnetic currents; effect on plasma convection,**” *Phys. Plasmas*, vol. 2, pp. 2011–2019, 1995.

- [153] S. H. Müller, A. Diallo, A. Fasoli, I. Furno, B. Labit, G. Plyushchev, M. Podestà, and F. M. Poli, “**Probabilistic analysis of turbulent structures from two-dimensional plasma imaging**,” *Phys. Plasmas*, vol. 13, p. 100701, 2006.
- [154] B.-W. Koo, N. Hershkowitz, S. Yan, and G.-H. Kim, “**Design and operation of an Omegatron mass spectrometer for measurements of positive and negative ion species in electron cyclotron resonance plasmas**,” *Plasma Sources Sci. Technol.*, vol. 9, pp. 97–107, 2000.
- [155] H. Kojima, “**A mass spectrometer for boundary plasma diagnostics**,” *J. Nucl. Mater.*, vol. 128, pp. 965–968, 1984.
- [156] G. Matthews, R. Pitts, G. McCracken, and P. Stangeby, “**Edge ion analysis in DITE**,” *Nucl. Fusion*, vol. 31, p. 1495, 1991.
- [157] A. Diallo, A. Fasoli, I. Furno, B. Labit, M. Podestà, and C. Theiler, “**Dynamics of Plasma Blobs in a Shear Flow**,” *Phys. Rev. Lett.*, vol. 101, p. 115005, 2008.
- [158] M. Spolaore, N. Vianello, M. Agostini, R. Cavazzana, E. Martines, P. Scarin, G. Serianni, E. Spada, M. Zuin, and V. Antoni, “**Direct Measurement of Current Filament Structures in a Magnetic-Confinement Fusion Device**,” *Phys. Rev. Lett.*, vol. 102, no. 16, p. 165001, 2009.
- [159] P. Piovesan, A. Almagri, B. E. Chapman, D. Craig, L. Marrelli, P. Martin, S. C. Prager, and J. S. Sarff, “**Filamentary current structures in the Madison Symmetric Torus**,” *Nucl. Fusion*, vol. 48, no. 9, p. 095003, 2008.
- [160] J. Lingertat, A. Tabasso, S. Ali-Arshad, B. Alper, P. van Belle, K. Borrass, S. Clement, J. Coad, and R. Monk, “**Studies of giant ELM interaction with the divertor target in JET**,” *J. Nucl. Mater.*, vol. 241, p. 402, 1997.
- [161] R. A. Pitts, S. Alberti, P. Blanchard, J. Horacek, H. Reimerdes, and P. C. Stangeby, “**ELM driven divertor target currents on TCV**,” *Nucl. Fusion*, vol. 43, pp. 1145–1166, 2003.
- [162] A. Kirk, B. Koch, R. Scannell, H. R. Wilson, G. Counsell, J. Dowling, A. Herrmann, R. Martin, and M. Walsh, “**Evolution of Filament Structures during Edge-Localized Modes in the MAST Tokamak**,” *Phys. Rev. Lett.*, vol. 96, no. 18, p. 185001, 2006.
- [163] N. Vianello, V. Naulin, R. Schrittwieser, H. W. Müller, M. Zuin, C. Ionita, J. J. Rasmussen, F. Mehlmann, V. Rohde, R. Cavazzana, and M. Maraschek, “**Direct Observation of Current in Type-I Edge-Localized-Mode Filaments on the ASDEX Upgrade Tokamak**,” *Phys. Rev. Lett.*, vol. 106, no. 12, p. 125002, 2011.

- [164] H. Takahashi, E. D. Fredrickson, and M. J. Schaffer, “**Scrape-Off-Layer Current Model for Filament Structure Observed during Edge-Localized Modes in the DIII-D Tokamak,**” *Phys. Rev. Lett.*, vol. 100, no. 20, p. 205001, 2008.
- [165] P. Migliucci, V. Naulin, and Jet Efda Contributors, “**Magnetic signature of current carrying edge localized modes filaments on the Joint European Torus tokamak,**” *Phys. Plasmas*, vol. 17, no. 7, p. 072507, 2010.
- [166] J. A. van Allen, “**Inference of magnetospheric currents from multipoint magnetic field measurements,**” *Am. J. Phys.*, vol. 74, p. 809, 2006.
- [167] B. Coppi, “**Accretion theory of ‘spontaneous’ rotation in toroidal plasmas,**” *Nucl. Fusion*, vol. 42, pp. 1–4, 2002.
- [168] B. Coppi, D. A. D’Ippolito, S. I. Krasheninnikov, M. Lontano, J. R. Myra, P. Nataf, and D. A. Russell, “**Incentives for and Developments of the Accretion Theory of Spontaneous Rotation,**” *33th EPS Conf. on Controlled Fusion and Plasma Physics (Rome, 2006)*, paper O-4.017, <http://epsppd.epfl.ch/Roma/start.htm>.
- [169] K.-U. Riemann, “**The Bohm criterion and sheath formation,**” *J. Phys. D Appl. Phys.*, vol. 24, pp. 493–518, 1991.
- [170] E. J. Doyle, W. A. Houlberg, Y. Kamada, V. Mukhovatov, T. H. Osborne, A. Polevoi, G. Bateman, J. W. Connor, J. G. Cordey, T. Fujita, X. Garbet, T. S. Hahm, L. D. Horton, A. E. Hubbard, F. Imbeaux, F. Jenko, J. E. Kinsey, Y. Kishimoto, J. Li, T. C. Luce, Y. Martin, M. Ossipenko, V. Parail, A. Peeters, T. L. Rhodes, J. E. Rice, C. M. Roach, V. Rozhansky, F. Rytter, G. Saibene, R. Sartori, A. C. C. Sips, J. A. Snipes, M. Sugihara, E. J. Synakowski, H. Takenaga, T. Takizuka, K. Thomsen, M. R. Wade, H. R. Wilson, ITPA Transport Physics Topical Group, I. Confinement Database, Modelling Topical Group, I. Pedestal, and Edge Topical Group, “**Progress in the ITER Physics Basis; Chapter 2: Plasma confinement and transport,**” *Nucl. Fusion*, vol. 47, p. 18, 2007.
- [171] R. H. Cohen and D. D. Ryutov, “**Dynamics of an Isolated Blob in the Presence of the X-Point,**” *Contrib. Plasma Phys.*, vol. 46, pp. 678–684, 2006.
- [172] R. Chodura, “**Plasma-wall transition in an oblique magnetic field,**” *Phys. Fluids*, vol. 25, pp. 1628–1633, 1982.
- [173] C. Theiler, I. Furno, P. Ricci, A. Fasoli, and B. Labit, “**Study of filament motion and their active control,**” *36th EPS Conf. on Controlled Fusion and Plasma Physics (Sofia, 2009)*, paper O-5.067, <http://epsppd.epfl.ch/Sofia/start.htm>.

- [174] J. Hara, Y. Uesugi, Y. Miura, and H. Kawashima, “**Scrape-off layer broadening by the $E \times B$ convective cell induced by non-axisymmetric divertor biasing,**” *J. Nucl. Mater.*, vol. 241, pp. 338–341, 1997.
- [175] G. F. Counsell, J.-W. Ahn, R. Akers, E. Arends, S. J. Fielding, P. Helander, A. Kirk, H. Meyer, A. Tabasso, H. Wilson, and Y. Yang, “**A review of plasma boundary phenomena in the mega ampere spherical tokamak,**” *J. Nucl. Mater.*, vol. 313-316, p. 804, 2003.
- [176] G. F. Counsell, R. H. Cohen, P. Helander, D. D. Ryutov, and the MAST team, “**Reduction of Divertor Power Loading in MAST,**” *30th EPS Conf. on Controlled Fusion and Plasma Physics (St Petersburg, 2003)*, paper P-3.202, <http://epsppd.epfl.ch/StPetersburg/start.html>.
- [177] J. Stockel, P. Devynck, J. Gunn, E. Martines, G. Bonhomme, I. Voitsekhovitch, G. Van Oost, M. Hron, I. Duran, P. Stejskal, J. Adamek, V. Weinzettl, and F. Zacek, “**Formation of convective cells during scrape-off layer biasing in the CASTOR tokamak,**” *Plasma Phys. Control. Fusion*, vol. 47, pp. 635–643, 2005.
- [178] S. J. Zweben, R. J. Maqueda, A. L. Roquemore, C. E. Bush, R. Kaita, R. J. Marsala, Y. Raitses, R. H. Cohen, and D. D. Ryutov, “**Local scrape-off layer control using biased electrodes in NSTX,**” *Plasma Phys. Control. Fusion*, vol. 51, p. 105012, 2009.
- [179] G. R. Tynan, L. Schmitz, R. W. Conn, R. Doerner, and R. Lehmer, “**Steady-state convection and fluctuation-driven particle transport in the H-mode transition,**” *Phys. Rev. Lett.*, vol. 68, pp. 3032–3035, 1992.
- [180] D. D. Ryutov, P. Helander, and R. H. Cohen, “**On the possibility of inducing strong plasma convection in the divertor of MAST,**” *Plasma Phys. Control. Fusion*, vol. 43, pp. 1399–1423, 2001.
- [181] R. H. Cohen, S. Fielding, P. Helander, and D. D. Ryutov, “**Theory Issues for Induced Plasma Convection Experiments in the Divertor of the MAST Spherical Tokamak,**” *Contrib. Plasma Phys.*, vol. 42, pp. 296–301, 2002.
- [182] V. A. Rozhansky, “**Reviews of Plasma Physics 24,**” chap. 1, Ed. by V. D. Shafranov (Springer-Verlag, Berlin Heidelberg, 2008).
- [183] B.-W. Koo, N. Hershkowitz, and M. Sarfaty, “**Langmuir probe in low temperature, magnetized plasmas: Theory and experimental verification,**” *J. Appl. Phys.*, vol. 86, pp. 1213–1220, 1999.
- [184] V. A. Rozhansky, A. A. Ushakov, and S. P. Voskoboinikov, “**Electric fields and currents in front of a biased electrode (flush mounted probe)**

- and the I - V characteristics of the electrode for various mechanisms of transverse conductivity,” *Nucl. Fusion*, vol. 39, pp. 613–628, 1999.
- [185] K. Rypdal, O. E. Garcia, and J.-V. Paulsen, “**Anomalous Cross-Field Current and Fluctuating Equilibrium of Magnetized Plasmas**,” *Phys. Rev. Lett.*, vol. 79, pp. 1857–1860, 1997.
- [186] K. Rypdal, J. V. Paulsen, and O. E. Garcia, “**Investigation of forced turbulence and transport in toroidal magnetized plasmas**,” *Czech. J. Phys.*, vol. 48, pp. 207–212, 1998.
- [187] C. F. Figarella, P. Ghendrih, Y. Sarazin, G. Attuel, S. Benkadda, P. Beyer, G. Falchetto, E. Fleurence, X. Garbet, and V. Grandgirard, “**Control of long range turbulent transport with biasing in the tokamak scrape-off-layer**,” *J. Nucl. Mater.*, vol. 337, pp. 342–346, 2005.
- [188] P. W. Terry, M. Greenwald, J.-N. Leboeuf, G. R. McKee, D. R. Mikkelsen, W. M. Nevins, D. E. Newman, D. P. Stotler, Task Group On Verification, Validation, U. S. Burning Plasma Organization, and U. S. Transport Task Force, “**Validation in fusion research: Towards guidelines and best practices**,” *Phys. Plasmas*, vol. 15, p. 062503, 2008.
- [189] M. Greenwald, “**Verification and validation for magnetic fusion**,” *Phys. Plasmas*, vol. 17, p. 058101, 2010.
- [190] A. M. Dimits, G. Bateman, M. A. Beer, B. I. Cohen, W. Dorland, G. W. Hammett, C. Kim, J. E. Kinsey, M. Kotschenreuther, A. H. Kritz, L. L. Lao, J. Mandrekas, W. M. Nevins, S. E. Parker, A. J. Redd, D. E. Shumaker, R. Sydora, and J. Weiland, “**Comparisons and physics basis of tokamak transport models and turbulence simulations**,” *Phys. Plasmas*, vol. 7, pp. 969–983, 2000.
- [191] J. Birn, J. F. Drake, M. A. Shay, B. N. Rogers, R. E. Denton, M. Hesse, M. Kuznetsova, Z. W. Ma, A. Bhattacharjee, A. Otto, and P. L. Pritchett, “**Geospace Environmental Modeling (GEM) magnetic reconnection challenge**,” *J. Geophys. Res.*, vol. 106, pp. 3715–3720, 2001.
- [192] R. H. Myers, D. C. Montgomery, and C. M. Anderson-Cook, “**Response Surface Methodology: Process and Product Methodology, Using Designed Experiment**,” 3rd ed., (Wiley, New York, 2009).
- [193] V. E. Golant, A. P. Zhilinsky, and I. E. Sakharov, “**Fundamentals of Plasma Physics**,” (New York: Wiley, 1980).

Acknowledgements

First of all, I would like to thank my advisors Ivo Furno and Ambrogio Fasoli for the excellent supervision and constant support. I very much appreciated the almost daily discussions with Ivo, the many ideas we have developed and sometimes immediately tested on TORPEX, his direct way of attacking a problem, and his broad experience and knowledge of the field. Ambrogio has been a constant motor of motivation. Five minutes of discussion were usually sufficient to arrange my ideas and to continue work with enthusiasm. In the same breath, I would like to thank Paolo Ricci and Benoit Labit. Paolo's analytical and numerical work is invaluable for our understanding of TORPEX plasmas and I have learnt a lot from him. Benoit has been very important for me for all that is related to data treatment and technical aspects of TORPEX. His regular emails with the subject "Paper of interest for us?" have stimulated many ideas.

I am also very grateful to the first generation of PhD students on TOPEX, Stefan Müller, Mario Podestà, and Francesca Poli. This thesis would not have been possible without their excellent work. Very important for me during the second half of my thesis was Joaquim Loizu. The many discussions in the office, on the metro or in front of a beer and the work we have done together were a real pleasure.

I also owe thanks to the technicians: Patrice Gorgerat for the technical drawings and the help on the design of the tilt limiter, the biasing electrodes and the FRIPLE probe, Philippe Marmillod for designing the FRIPLE probe electronics, Pierre Lavanchy for assembling it, William Matthey-Doret, Jean-Pierre Bärtschi, Nelson Reyes, and Christian Maura for fabricating the mechanical parts of the different probes and limiters, and Omar Bartolomeoli for the help during the many openings on TORPEX.

Many thanks also go to my other colleagues and friends, Ahmed, Alessandro, Alex, Aliénor, Andres, Ben, Christian, Davoud, Dusko, Fabio, Federico, Francesco, Fred, Jaime, Jonathan, Juan-Carlos, Kyle, Luca, Mattia, Marcante, Micci, Miiich, PF, Sebi, Sigi, Snjezana, and all the others who made my stay at the CRPP and in Lausanne very enjoyable. Finally, I want to express my deep gratitude to my family and Lorena for their support and love and the good time during the past years.

Curriculum Vitae

Christian Theiler



Personal Data

Jan. 7, 1982 Born in Zurich, Switzerland
Nationality Swiss

Education

Oct. 28, 2011 Ph.D. defense.
Jun. 2007 – Oct. 2011 Research assistant and Ph.D. student at the Centre de Recherche en Physique des Plasmas (CRPP) of the Swiss Federal Institute of Technology Lausanne (EPFL).
Apr. 2007 Diploma in physics from the Swiss Federal Institute of Technology Zurich (ETHZ).
Oct. 2001 – Apr. 2007 Diploma studies of physics, ETHZ.
Oct. 2003 – Jun. 2004 Exchange year at Université Claude Bernard, Lyon 1.

Awards

October 2010 Recognition for exceptional assistantship work at EPFL
July 2009 Itoh Project Prize in Plasma Turbulence: Highly Commended
April 2007 Diploma in physics with distinction from ETHZ

Contributions to conferences (as first author)

”Convective cells and blob control in a simple magnetized torus” (oral presentation), 53rd APS conference on plasma physics, Nov. 14-18, 2011, Salt Lake City, Utah

”Blob motion and control in simple magnetized plasmas” (invited talk), 52nd APS conference on plasma physics, Nov. 8-12, 2010, Chicago, Illinois

”Study of filament motion and their active control” (oral presentation), 36th EPS conference on plasma physics, June 29 - July 3, 2009, Sofia, Bulgaria

”Connected and disconnected blobs in TORPEX and a way to reduce blob induced transport” (poster), 13th EU-US TTF workshop and 1st EFDA Transport Topical Group Meeting, Sept. 1-4, 2008, Copenhagen, Denmark

”Intermittent transport events and blobs in a simple magnetized toroidal plasma” (oral presentation), SPS annual meeting, March 26-27, 2008, Geneva, Switzerland

Peer-reviewed publications

- I. FURNO, **C. Theiler**, A. FASOLI, and B. LABIT. Three-Dimensional Imaging of a Radially Propagating Plasma Blob Using Conditional Sampling Techniques, *IEEE Trans. Plasma Sci.* (in press)
- I. FURNO, **C. Theiler**, D. LANÇON, A. FASOLI, D. IRAJI, P. RICCI, M. SPOLAORE, and N. VIANELLO. Blob current structures in TORPEX plasmas: experimental measurements and numerical simulations, *Plasma Phys. Control. Fusion* (in press)
- C. Theiler**, I. FURNO, A. FASOLI, P. RICCI, B. LABIT, and D. IRAJI. Blob motion and control in simple magnetized plasmas, *Phys. Plasmas* 18, 055901 (2011)
- C. Theiler**, I. FURNO, A. KUENLIN, PH. MARMILLOD, and A. FASOLI. Practical solutions for reliable triple probe measurements in magnetized plasmas, *Rev. Sci. Inst.* 82, 013504 (2011)
- I. FURNO, M. SPOLAORE, **C. Theiler**, N. VIANELLO, R. CAVAZZANA, and A. FASOLI. Direct two-dimensional measurements of the field-aligned current associated with plasma blobs, *Phys. Rev. Lett.* 106, 245001 (2011)
- P. RICCI, **C. Theiler**, A. FASOLI, I. FURNO, K. GUSTAFSON, D. IRAJI, and J. LOIZU. Methodology for turbulence code validation: Quantification of simulation-experiment agreement and application to the TORPEX experiment, *Phys. Plasmas* 18, 032109 (2011)
- B. LABIT, **C. Theiler**, A. FASOLI, I. FURNO, and P. RICCI. Blob-induced toroidal momentum transport in simple magnetized plasmas, *Phys. Plasmas* 18, 032308 (2011)
- J. LOIZU, P. RICCI, and **C. Theiler**. Existence of subsonic plasma sheaths, *Phys. Rev. E* 83, 016406 (2011)
- D. IRAJI, I. FURNO, A. FASOLI, and **C. Theiler**. Imaging of turbulent structures and tomographic reconstruction of TORPEX plasma emissivity, *Phys. Plasmas* 17, 122304 (2010)
- A. FASOLI, A. BURCKEL, L. FEDERSPIEL, I. FURNO, K. GUSTAFSON, D. IRAJI, B. LABIT, J. LOIZU, G. PLYUSHCHEV, P. RICCI, **C. Theiler**, A. DIALLO, S. H. MÜLLER, M. PODESTÀ, and F. M. POLI. Electrostatic instabilities, turbulence and fast ion interactions in the TORPEX device, *Plasma Phys. Control. Fusion* 52, 124020 (2010)
- C. Theiler**, I. FURNO, P. RICCI, A. FASOLI, B. LABIT, S. H. MÜLLER, and G. PLYUSHCHEV. Cross-Field Motion of Plasma Blobs in an Open Magnetic Field Line Configuration, *Phys. Rev. Lett.* 103, 065001 (2009)
- L. FEDERSPIEL, B. LABIT, P. RICCI, A. FASOLI, I. FURNO, and **C. Theiler**. Observation of a critical pressure gradient for the stabilization of interchange modes in simple magnetized toroidal plasmas, *Phys. Plasmas* 16, 092501 (2009)
- S. H. MÜLLER, **C. Theiler**, A. FASOLI, I. FURNO, B. LABIT, G. R. TYNAN, M. XU, Z. YAN, and J. H. YU. Studies of blob formation, propagation and transport mechanisms in basic experimental plasmas (TORPEX and CSDX), *Plasma Phys. Control. Fusion* 51, 055020 (2009)

P. RICCI, **C. Theiler**, A. FASOLI, I. FURNO, B. LABIT, S. H. MÜLLER, M. PODESTÀ, and F. M. POLI. Langmuir probe-based observables for plasma-turbulence code validation and application to the TORPEX basic plasma physics experiment, *Phys. Plasmas* 16, 055703 (2009)

C. Theiler, A. DIALLO, A. FASOLI, I. FURNO, B. LABIT, M. PODESTÀ, F. M. POLI, and P. RICCI. The role of the density gradient on intermittent cross-field transport events in a simple magnetized toroidal plasma, *Phys. Plasmas* 15, 042303 (2008)

A. DIALLO, A. FASOLI, I. FURNO, B. LABIT, M. PODESTÀ, and **C. Theiler**. Dynamics of plasma blobs in a shear flow, *Phys. Rev. Lett.* 101, 115005 (2008)

M. PODESTÀ, A. FASOLI, B. LABIT, I. FURNO, P. RICCI, F. M. POLI, A. DIALLO, S. H. MÜLLER, and **C. Theiler**. Cross-field transport by instabilities and blobs in a magnetized toroidal plasma, *Phys. Rev. Lett.* 101, 045001 (2008)

I. FURNO, B. LABIT, A. FASOLI, F. M. POLI, P. RICCI, **C. Theiler**, S. BRUNNER, A. DIALLO, J. GRAVES, M. PODESTÀ, and S. H. MÜLLER. Mechanism for blob generation in the TORPEX toroidal plasma, *Phys. Plasmas* 15, 055903 (2008)

I. FURNO, B. LABIT, M. PODESTÀ, A. FASOLI, S. H. MÜLLER, F. M. POLI, P. RICCI, **C. Theiler**, S. BRUNNER, A. DIALLO, and J. GRAVES. Experimental Observation of the Blob-Generation Mechanism from Interchange Waves in a Plasma, *Phys. Rev. Lett.* 100, 055004 (2008)

B. LABIT, A. DIALLO, A. FASOLI, I. FURNO, D. IRAJI, S. H. MÜLLER, G. PLYUSHCHEV, M. PODESTÀ, F. M. POLI, P. RICCI, **C. Theiler**, and J. HORACEK. Statistical properties of electrostatic turbulence in toroidal magnetized plasmas, *Plasma Phys. Control. Fusion* 49, B281 (2007)

Employment

Jun. 2007 – Dec. 2011 Research assistant at EPFL, Lausanne, Switzerland.

Feb. 2006 – Jun. 2006 Teaching assistant at ETHZ, Zurich, Switzerland.

Jun. 2004 – Sep. 2004 Trainee at the Research Department Synchrotron Radiation and Nanotechnology of the Paul Scherrer Institute (PSI), Switzerland.